Study of mechanical properties of cathodic arc deposited Ti-Al-N and Ti-Al-Cr-Si-N multi-layered coatings

A thesis

submitted by

Sai Venkata Pramod Kumar P

in partial fulfilment of the requirements for the award of the degree of

Doctor of Philosophy

in

Materials Engineering

School of Engineering Sciences and Technology

University of Hyderabad, India

July 2015

Declaration

I, **Sai Venkata Pramod Kumar P** hereby declare that this thesis work entitled ***"Study of mechanical properties of cathodic arc deposited Ti-Al-N and Ti-Al-Cr-Si-N multi-layered coatings"*** submitted in partial fulfillment of the requirements for the award of Doctor of Philosophy (in Materials Engineering) in the School of Engineering Sciences and Technology (SEST), University of Hyderabad is a bonafide record of the work which was carried out by me under the supervision of **Dr. Koteswararao V. Rajulapati, Dr. S. V. Joshi and Dr. G. Ravi Chandra**. I also declare that this thesis has not been submitted previously in part or in full to this University or any other University or Institution for the award of any degree or diploma.

(Sai Venkata Pramod Kumar P)
Reg. No.: 09ETPM09
School of Engineering Sciences and Technology
University of Hyderabad

Certificate

This is to certify that this thesis work entitled ***"Study of mechanical properties of cathodic arc deposited Ti-Al-N and Ti-Al-Cr-Si-N multi-layered coatings"***, submitted by **Sai Venkata Pramod Kumar P** bearing Reg. No. **09ETPM09** in partial fulfillment of the requirements for the award of the degree of Doctor of Philosophy in Materials Engineering, is a bonafide record of the work that has been carried out by him under my supervision. Dr. S. V. Joshi and Dr. G. Ravi Chandra (ARCI) have also supervised the above mentioned thesis work with me. This thesis has not been submitted previously in part or in full to this or any other University or Institution for the award of any degree or diploma.

Thesis Supervisor

Dr. Koteswararao V. Rajulapati,
Assistant Professor
School of Engineering Sciences and Technology
University of Hyderabad

Approved by

Prof. Rajender Singh
Dean
School of Engineering Sciences and Technology
University of Hyderabad

Certificate

This is to certify that this thesis work entitled ***"Study of mechanical properties of cathodic arc deposited Ti-Al-N and Ti-Al-Cr-Si-N multi-layered coatings"***, submitted by **Sai Venkata Pramod Kumar P** bearing Reg. No. **09ETPM09** in partial fulfillment of the requirements for the award of the degree of Doctor of Philosophy in Materials Engineering, is a bonafide record of the work that has been carried out by him under our supervision. Dr. Koteswararao V. Rajulapati, University of Hyderabad has also supervised the above mentioned thesis work with us. This thesis has not been submitted previously in part or in full to this or any other University or Institution for the award of any degree or diploma.

Thesis Supervisors

Dr. Shrikant V. Joshi,
Additional Director,
ARCI, Hyderabad

Dr. G. Ravi Chandra, Sc- 'F'

Team Leader, Centre for Materials
Characterization and Testing,
ARCI, Hyderabad

Approved by

Dr. Shrikant V. Joshi,
Additional Director, International Advanced Research Centre for Powder Metallurgy and New Materials (ARCI), Hyderabad

Acknowledgements

A PhD is a long journey which is made smoother and worthwhile through association with friends and mentors. I take the opportunity here to thank them. I first profusely thank my supervisors, Dr. G. Ravi Chandra, Dr. Shrikant Joshi, and Dr. Koteswararao Rajulapati who have been supportive of all my research efforts and provided timely guidance and direction to my thesis apart from teaching me the finer nuances of research. I thank the administration at ARCI, the Director, Dr. G. Sundararajan, the Additional Director, Dr. Shrikant Joshi, the Associate Director, Dr. G. Padmanabham, the Administrative and Personnel Officer, Mr. R. Prabhakara Rao and the Chief Finance and Accounts Officer, Mr. R. Vijay Kumar for their support and suggestions. I thank the present Dean, Prof. Rajender Singh and past Deans of the School of Engineering Sciences, Prof. M.Sundaraman, Prof. K. Bhanu Sankara Rao for their support and guidance. I thank my Doctoral Committee members, Dr. VVSS Srikanth and Prof. M. Ghanshyam Krishna for their useful suggestions and encouragement during regular meetings.

While one's parents and family are ever supportive, their encouragement and concern keeps one motivated along the research journey. I thank my mother, P.Saroja, father, P. Krishnaiah and sister, Sai Pradeepa for their ever long support. This journey would have not been possible without the mentorship from my scientist friends at the Centre for Materials Characterization and Testing at ARCI who have not only been instrumental in teaching me various techniques but have also been a tremendous source of support. I am very thankful to Mr. M. Ramakrishna, Mr. L. Venkatesh, Dr. Suresh Koppoju, Dr. P. Suresh Babu, Dr. K. Satya Prasad and Mrs. A Jyothirmayee. Special thanks to Mr. L. Venkatesh and his family for their support in the final stages of my PhD. I also thank Mr. G. Venkata Rao for his assistance in the metallography lab and for his practical tips on handling and troubleshooting any equipment. I thank Mr. GVR Reddy for his assistance in the SEM lab and Mr. K. Ramesh Reddy for assistance with XRD. I thank my scientist friends at the Centre for Engineered Coatings (CEC), notably Dr. Krishna Valleti for his help with regard to the coating deposition and for enlightening discussions. I thank Mr. N. Ravi for his guidance on Residual stress analysis. I also thank Sri. D.S. Rao, Team Leader, CEC for his support in facilitating my experiments at the centre. I thank Mr. Naveen Manhar Chavan for the company and moral support especially during weekends. I also thank Dr. L. Ramakrishna, Dr.Siva Kumar, Dr. Nitin Wasekar and Dr. S. Kumar for their support. I thank Mr. A Jagan for his assistance in the PVD lab. I thank Dr. Joydip Joardar for help and insightful discussions with regard to X-ray measurements. I thank Dr. Gururaj Telasang for his encouragement and PhD tips. I thank Mr. S. B. Chandrasekar for his help with heat treatment and his ever positive approach which has been a source of inspiration. I greatly thank Mr. A. Srinivas, HRD officer for his ever willing support in all administrative aspects and smoothening various formalities for all the students at ARCI.

I thank my friends at ARCI and the University of Hyderabad who have been a source of great support throughout my PhD. I sincerely thank my friends, Puneet, Unnikannan, Pavithra and Archana who have been of great support. I specially thank Puneet for his help at various junctures. I also thank Vinoth, Bolla Reddy, Sreekanth, Murali and many other colleagues at ARCI who have been good friends. I thank Dr. V. Sreedevi for her help in some of the experiments and technical suggestions. Many thanks to Mohan for his help with the final formatting. I also thank Naresh, Rahul, Pardhu, Sampath, Ramana for their help with various matters. I thank Venu and Mallesh for their help with administrative matters at the department.

I also thank my friends at DRDO, Hyderabad who have made my stay at Hyderabad a pleasant one. I especially thank Mr.B. Uma Maheshwararao and Mr. D. Sai Prasad. I also thank Mr. B Jaganmohan and Mr.V.Ramesh Babu for their encouragement.

I thank Mr.Sumanth, IISc for assistance in a few measurements. I also thank the Science and Engineering Research Board (SERB), DST, Govt. of India, for the international travel grant which enabled me to present my work at the ICMCTF conference. Finally, I would like to thank my teachers at my former college, SSSIHL and school, SSSHSS without whose initial support and guidance I would not have chosen research as a career.

Sai Venkata Pramod Kumar P (Sai Pramod Pemmasani)

Dedicated to my Divine Master

and

my dear parents

List of Publications

Peer-reviewed publications from the thesis work

1. **Sai Pramod Pemmasani,** K. Valleti, Ravi C. Gundakaram, K.V. Rajulapati, M. Ramakrishna, S. Koppoju, S.V. Joshi, Effect of microstructure and phase constitution on mechanical properties of $Ti_{1-x}Al_xN$ Coatings, **Applied Surface Science** 313 (2014) 936–946.

2. **Sai Pramod Pemmasani ,** K.V. Rajulapati , M. Ramakrishna , K. Valleti , Ravi C. Gundakaram and S.V. Joshi ,Characterization of multilayer nitride coatings by Electron Microscopy and Modulus mapping , **Materials Characterization** 81 (2013), 7-18

3. **Sai Pramod Pemmasani,** K. Valleti, M. Ramakrishna, K.V. Rajulapati ,G. Ravi Chandra and S.V. Joshi, Structure Property Correlations in Cathodic Arc Deposited TiAlN Coatings, **Materials Science Forum**, 702-703 (2012) pp 967-970

4. Ravi C. Gundakaram, **Sai Pramod Pemmasani**, Characterization of Coatings by SEM Based Micro-diffraction, **Materials Science Forum**, 702-703 (2012) pp 570-573

5. "Effect of Architecture and Composition on life of Multi-layer nitride coatings", (to be submitted to **Advanced Materials Interfaces**)

6. "Nano-impact behaviour of $Ti_{1-x}Al_xN$ coatings: Role of toughness and microstructure", (to be submitted to **Applied Surface Science**)

7. "Investigation on High temperature stability of nitride coatings by Synchrotron XRD", (to be submitted to **Vacuum**)

8. "Role of composition and microstructure on properties of Nanocomposite TiAlCrSiN coatings", (to be submitted to **Ceramics International**)

Contributions in international conferences

i. Influence of Composition and Architecture on Mechanical Properties of Cathodic Arc Deposited Ti-Al-N Coatings, Sai Pramod Pemmasani, Ravi C. Gundakaram, K. V. Rajulapati, K. Valleti, M. Ramakrishna, S. Koppoju, S. V Joshi, Oral Presentation at 40th ICMCTF Conference, April 29th - 3rd May 2013, San Diego, U.S.A.

ii. Microstructural studies of multinary nitride PVD Coatings using TEM and Synchrotron XRD, M. Ramakrishna, Sai Pramod Pemmasani, S. Koppoju, K. V. Rajulapati and K. Valleti, Poster Presentation at 12th International Conference on Surface X-ray and Neutron Scattering (SXNS 12), 25th -28th July 2012, Kolkata, India

iii. Influence of High temperature Exposure on Microstructure and phase constitution of TiAlCrN Coatings, Sai Pramod Pemmasani , S. Koppoju, K.V. Rajulapati, K.Valleti ,M. Ramakrishna, Ravi C. Gundakaram , S.V. Joshi, Oral Presentation at XXXIII Annual Meet of Electron Microscopy Society of India, 2nd -4th July 2012, Bangalore, India

iv. Nanostructured Nitride Coatings for Improved Wear and Corrosion Resistance, Sai Pramod Pemmasani, K. Valleti, A. Jyothirmayi, M. Ramakrishna, K.V. Rajulapati, R. C. Gundakaram, and S.V. Joshi, Poster Presentation at International Conference on Nanoscience and Nanotechnology (ICONSAT 2012), Jan 21st -23rd 2012, Hyderabad, India

v. Structure Property Correlations in Cathodic Arc Deposited TiAlN Coatings, Sai Pramod Pemmasani, Krishna Valleti, M. Ramakrishna, K.V. Rajulapati , Ravi C. Gundakaram and S.V. Joshi, Poster Presentation at International Conference on Textures of Materials (ICOTOM16), Dec 12th -16th 2011, IIT Bombay, India

vi. Characterization of multi-layer coatings by EBSD, Focused ion beam and Transmission Electron Microscopy, Sai Pramod Pemmasani, M. Ramakrishna, K.V. Rajulapati, Ravi C. Gundakaram, S.V. Joshi, Poster Presentation at Workshop on Electron Microscopy (WEM 2011), Nov 23rd -25th 2011, Institute of Physics, Bhubaneswar, India

vii. Dual Beam FIB and Transmission Electron Microscopy Studies on a Multilayer Coating, Sai Pramod Pemmasani, M. Ramakrishna, Krishna Valleti, K.V. Rajulapati, G. Ravi Chandra and S.V. Joshi, Poster Presentation at International Conference on Electron Nanoscopy (EMSI50), July 6th -8th 2011, Hyderabad, India

viii. Microstructural Study Of Wear Resistant Multi-layer Coatings, P.S.V. Pramod ,M. Ramakrishna, K. Valleti, K.V. Rajulapati , G. Ravi Chandra and S.V. Joshi, Oral Presentation at AP Science Congress Convention for Science Technology and Prosperity, Nov 18th -20th, 2010, Hyderabad, India

Table of Contents

List of figures

List of Tables

Abstract

A multi-functional, multi-layer coating with a triple layer structure comprising of an adhesive layer of TiN, a tough, impact resistant TiAlN intermediate layer and a hard, thermally stable TiAlCrSiN top layer was designed and deposited by cathodic arc physical vapour deposition technique. The emphasis of this work was specifically on studying the effect of composition and architecture on the phase constitution and microstructure of the various layers and assessing their impact on the mechanical properties and coating life to gain insight into the role of each constituent on the performance of the overall coating.

Each of the layers was first individually studied and their respective functional properties were optimized. The role of TiN as an adhesive layer was initially studied and an optimum thickness of 100 nm was identified for good adhesion. Monolithic $Ti_{1-x}Al_xN$ coatings were then studied and the effect of varying Al content on mechanical properties (hardness, fracture toughness and impact resistance) of the coatings was specifically assessed and correlated with the crystal structure, phase constitution and microstructure. An optimum composition, $Ti_{0.47}Al_{0.53}N$, was identified for high fracture toughness and impact resistance. The impact resistance showed good correlation with the fracture toughness, with the $Ti_{0.47}Al_{0.53}N$ coating which showed highest fracture toughness also showing the highest impact resistance. The impact resistance was further enhanced by depositing multi-layers comprising two compositions from among the $Ti_{1-x}Al_xN$ coatings and investigating varying bi-layer thicknesses to determine an optimal architecture. Two sets of multi-layer coatings were studied, TiN-TiAlN ML (comprising of TiN and $Ti_{0.35}Al_{0.65}N$ layers) and $Ti_{1-x}Al_xN$ ML (comprising of $Ti_{0.7}Al_{0.3}N$ and $Ti_{0.47}Al_{0.53}N$ layers) with varying bi-layer period thicknesses of 160,100, 80, and 40 nm. The highest impact resistance was achieved with $Ti_{1-x}Al_xN$ multi-layers with the lowest bi-layer thickness of 40 nm, although the coating did not show any hardness increase due to multi-layering. The enhanced impact resistance is attributed to the presence of a large number of interfaces at low bi-layer periods that act as barriers to crack propagation and the absence of a columnar structure in the multi-layer coatings.

The next part of the study focused on the synthesis of nanocomposite coatings of TiAlCrSiN with the desired combination of high hardness, high-temperature resistance and toughness. Monolithic coatings of TiAlCrSiN were first synthesized with different elemental ratios and a maximum hardness of ~37 GPa attained in coatings with a silicon content of 9 at. %. This

composition was also found to show the highest thermal stability as determined from TGA tests. The high hardness and thermal stability at this particular composition is attributed to the desired nanocomposite structure in this coating where nanocrystalline grains of TiAlCrN are surrounded by a thin layer of amorphous Si_3N_4 as confirmed from HRTEM. Multi-layer coatings of TiAlCrSiN were subsequently deposited by choosing two layers, one with high hardness (TiAlCrSiN with 9 % Si) and the other, a softer layer with low crack probability (TiAlCrSiN with 11 % Si) in order to achieve a multi-layer with a combination of toughness and wear resistance. The above multi-layer coatings were deposited with bi-layer periods of 20, 40 and 80 nm. The TiAlCrSiN multi-layer coatings with an intermediate bi-layer period of 40 nm showed the highest impact resistance with a ~35 % improvement in impact resistance over the monolithic TiAlCrSiN coating with 9 % Si and ~55 % and ~66 % improvement over multi-layers with 80 nm and 20 nm bi-layer periods, respectively. This enhancement in impact resistance in the 40 nm bi-layer coating is attributed to the presence of an optimum interface volume in the coating and the the presence of sharp interfaces when compared to 20 nm bi-layer coating. The presence of the softer amorphous layer along with the hard layer in the multi-layers reduces crack propagation and promotes crack re-direction, with the hard layer limiting deformation by providing stiffness and the softer layer accommodating plastic deformation, thereby slowing down crack growth. Thus, an appropriate combination of layers and an optimum bi-layer period were identified and a TiAlCrSiN coating layer with a desirable combination of hardness and toughness was developed.

The final section of the thesis is focused on the optimized multi-functional, multi-layer triple layer coating comprising of a TiN adhesion layer, a tough, impact resistant TiAlN intermediate layer, and a hard, wear resistant TiAlCrSiN top layer. Seven different triple layer coatings were deposited using optimized compositions and configurations which resulted from the initial studies on TiN, TiAlN and TiAlCrSiN layers. Detailed analyses of the microstructure and mechanical properties of the coatings were performed at multiple length scales by SEM, EBSD, XTEM, HAADF-STEM and modulus mapping. The performance of the coatings was evaluated by nano-impact testing. Good interlayer bonding among all the layers in the triple layer coating was observed. The TiN layer was found to comprise of large columnar grains, which progressively become finer with the addition of aluminium as observed in the TiAlN layer. Introduction of Cr did not significantly alter the columnar structure as seen in the gradient layer and the TiAlCrN layer while the introduction of Si disrupted the columnar growth as was seen in the nano-multi-layered region due to amorphous phase formation leading to a layered nano-composite structure. The compositional variation seen within the nano-multi-layers was found to lead to alternating modulus variation in the layers.

Nano-impact studies showed that coatings involving either multi-layers within the individual layers or gradient layers exhibited distinctly improved impact resistance over triple layer coatings with simple monolithic structure and coatings without gradient layers. While multi-layering delays crack propagation in coatings due to deflection of cracks at interfaces, the presence of gradient layers allows a gradual transition of stresses at the interfaces in coating layers and thus prevents any sharp spikes in stress that can lead to cracking-induced failure. The alternating high and low moduli in the multi-layers, as confirmed by modulus mapping, led to the enhanced crack resistance. Hence, the multi-functional, multi-layer coatings developed and studied in this thesis can be expected to lead to improved tool properties and enhance cutting efficiencies in machining applications.

Chapter 1 Introduction

1.1 Background

The manufacturing industry today seeks enhanced productivity to achieve economies of scale, especially in the aerospace and automotive sectors. One of the ways by which this need can be fulfilled is by improving tool life as well as by increasing machining speeds. The application of a coating on a machine tool such as a drill bit or a casting die which leads to pronounced improvement in tool performance as well as tool life is one of the most significant technological advances in the development of modern tools [1]. This is evident from the usage of coated tools in industry where 80 - 90 % of cemented carbide tools [2, 3], 50 % of HSS tools and 40 % of superhard tools are coated [3].

The cutting tool is the component that limits machining performance as it faces high mechanical and thermal stresses during operation. High hardness, wear resistance and high temperature strength are properties which are essential for a cutting tool. However, there is a fundamental contradiction in the ideal properties of a cutting tool such as hardness and strength at high temperatures on one hand, and bending strength and toughness on the other hand as qualitatively shown in Fig. 1.1. Consequently, cutting tools for extreme requirements (as seen in interrupted cutting and in machining of high strength materials) cannot provide ideal performance when made from a single material such as a ceramic or diamond monolith, but can be realized by using a composite material comprised of a hard coating and a tough substrate. Application of coatings on the tool surface brings about an ideal enhancement in properties (strength and toughness) (as in Fig.1.1) and allows the use of tougher, ductile substrates such as cemented carbides and high speed steel (HSS) [4].

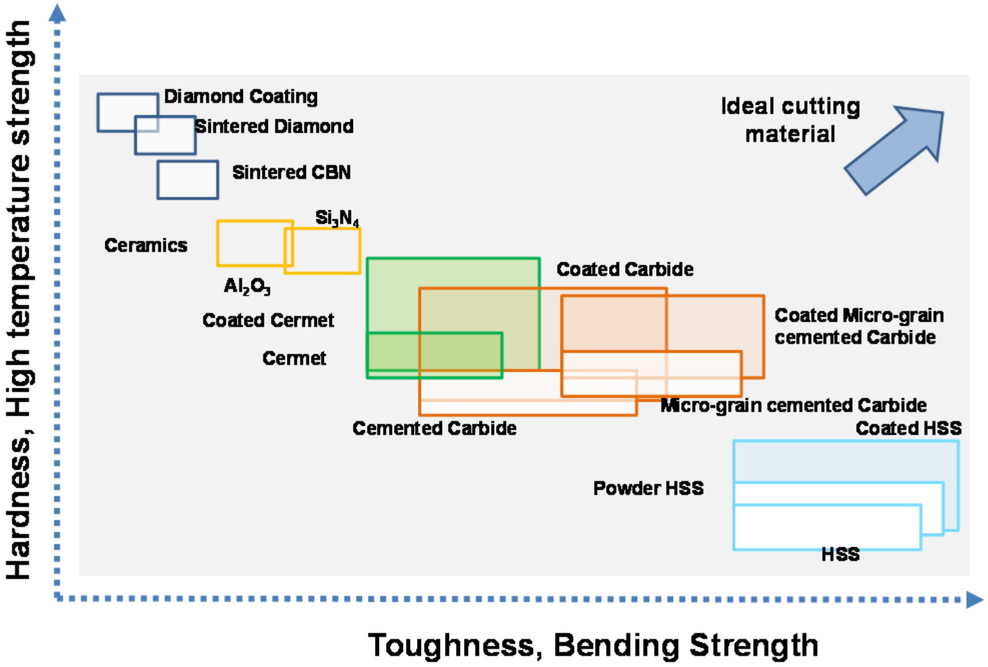

Fig. 1.1 Comparison of hardness and toughness of various cutting tool materials [adapted from, ref. 4].

The formation of thin coatings by deposition from a gaseous phase has been widely employed to improve the service properties of diverse engineering components, mainly the wear resistance of tools [6]. Coating deposition by chemical vapour deposition (CVD) has been practiced for many years, but the last few decades have seen physical vapour deposition (PVD) techniques being increasingly used on account of the lower deposition temperatures and the possibility to control and deposit coatings in multiple configurations. There are a host of variants of PVD techniques, notable among them being thermal or electron beam evaporation, cathodic arc evaporation, magnetron sputtering and more recently, high power impulse magnetron sputtering (HIPIMS).

1.2 Motivation

Coated tools used in machining applications are typically exposed to high temperatures in the range 1100-1200 ^{o}C [7] and undergo extensive fatigue due to repeated contact with the work piece and interrupted cutting conditions [8]. While a hard, ‘oxidation-resistant’ coating would be ideal for use at high temperatures, a tough coating is preferred for achieving long fatigue life. Design of a coating with both the above properties can be possible by depositing a suitable multi-layer, where each layer has one of the above properties and plays a distinct functional role. Multi-layer coatings, which combine properties of individual layers to provide multi-functional attributes, can thus be suitably tailored for numerous diverse applications.

While such coatings have been extensively developed by CVD techniques [9], only a few research reports on new generation PVD multi-layer coatings are available [10,11]. PVD coatings have advantages over CVD coatings, especially for use in finishing operations, in view of the possibility to retain sharp edges of tools along with beneficial compressive stresses and low deposition temperatures [12]. The new generation PVD coatings involve multiple layers comprising nanocomposite and conventional layers, with each layer tailored to discharge a specific function to enhance the durability and performance of the overall coating [13, 14]. Improved performance has been reported even in a number of double layer systems [9]. The use of Ti or TiN interlayers has been widely reported to improve adhesion [15, 16] and adhesive interlayers such as Cr and CrN on tools have been shown to enhance tool life [17]. A multi-layer coating with a three layer design comprising of an adhesive underlayer of TiN and Ti, an intermediate ceramic layer with 90 % Al_2O_3 and 10 % AlN, and a wear resistant top layer that consists of TiAlCrN nanoscale -multi-layers was reported to enhance tool life by about 2.5-8 times when compared to standard coated tools [18]. Enhancement in tool life has also been reported in multi-layer coatings with a hard nanocomposite top layer and a softer underlayer [19].

Notwithstanding the above efforts, no detailed studies exist on the role of individual layers and their microstructure on the performance of such new generation, multi- layer coatings deposited by the PVD technique. In the present study, an attempt has been made to design a multi-functional, multi-layer coating which comprises an adhesive underlayer, a tough intermediate layer followed by a hard, wear resistant top layer. The underlayer was chosen as TiN, the intermediate layer chosen as TiAlN and the top layer chosen as TiAlCrSiN. The technique chosen for deposition of the coatings was cathodic arc deposition. The inherent advantages of cathodic arc technology, such as high deposition rates, high degree of ionization, and presence of ions with high thermal velocities give rise to coatings with a dense structure and superior film adhesion when compared to other conventional PVD techniques [15, 20] and, consequently, has considerable application potential. Apart from comprehensive characterization of all the deposited films in the present study, the performance of these coatings has been evaluated by nano-impact testing. Nano-impact testing is a dynamic technique involving repeated high-strain rate indentation to simulate the interrupted cutting conditions seen in machining applications such as milling. Results from nano-impact tests on hard coatings have been shown to closely match actual tool life evaluation tests in cutting applications such as milling where the tool undergoes repeated fatigue due to interrupted cuts [21].

1.3 Objectives

With the above background, the following objectives were set for the present study in order to develop an in-depth understanding of various aspects associated with the development of a multi-functional, multi-layer coating:

a) Study the function of TiN as an adhesive underlayer.
b) Develop a tough, impact resistant TiAlN coating by composition control and multi-layer optimization
c) Synthesize a hard, thermally stable TiAlCrSiN coating through composition control and multi-layering
d) Develop a multi-functional, multi-layer coating based on the above optimized configurations of TiN, TiAlN and TiAlCrSiN
e) Optimize the mechanical properties and nano-impact resistance of the above coatings, study their microstructure and understand the underlying mechanisms to enhance performance.

Thus, each of the coatings, TiN, TiAlN and TiAlCrSiN were first individually optimized to achieve desired properties in terms of their respective functions as mentioned above and the optimized coatings were finally combined to deposit a multi-functional, multi-layered coating.

1.4 Overview of the thesis

The thesis consists of nine chapters. Chapter 1 presents the motivation, the objectives and overview of the present study. Chapter 2 discusses the evolution of hard coatings deposited by CVD and PVD techniques, the different types of coatings, their architecture and recent developments in the use of nitride coatings for wear resistant applications. Chapter 3 discusses the experimental details pertaining to coating deposition, structural, microstructural characterization and mechanical testing of the coatings.

The results of the thesis are discussed in Chapters 4 to 8. Chapter 4 deals with TiN and discusses results on its function as an adhesive underlayer. Chapters 5 and 6, which are devoted to monolithic $Ti_{1-x}Al_xN$ and multi-layered $Ti_{1-x}Al_xN$ coatings, respectively are focused on improving the toughness of the coatings. Chapter 5 presents the results on $Ti_{1-x}Al_xN$ coatings and discusses the effect of composition and microstructure on the fracture toughness and impact resistance of the coatings. Majority of the results discussed in this chapter have been published in two journal articles; S. P. Pemmasani, K.Valleti, M. Ramakrishna, K.V. Rajulapati, R.C. Gundakaram and S.V. Joshi, *Materials Science Forum*, 702-703 (2012) 967-970 & S. P. Pemmasani, K. Valleti, R. C. Gundakaram, K. V. Rajulapati, R. Mantripragada, S. Koppoju, and S. V. Joshi, *Applied Surface Science* 313 (2014) 936–946. In Chapter 6, results on two sets of multi-layered TiAlN coatings are presented and the effect of bi-layer period and layer composition on their impact resistance is discussed. Chapter 7 deals with nanocomposite TiAlCrSiN coatings, including optimization of composition and multi-layer architecture for superhardness, thermal stability and durability of the coatings. Chapter 8 discusses results of the study on optimized multi-functional, multi-layer coatings which are comprised of the above optimized TiN, TiAlN and TiAlCrSiN coatings as the constituent layers. It first discusses the characterization of the tri-layer coating by orientation imaging microscopy, focused ion beam, cross sectional transmission electron microscopy and modulus mapping of the multi-layers. The chapter then discusses the performance evaluation of these coatings and the effect of different layer combinations on the coating life as studied by nano-impact testing. Part of the results discussed in this chapter have been published in a journal article; S.P. Pemmasani, K.V. Rajulapati, M. Ramakrishna, K. Valleti, Ravi C. Gundakaram and S.V. Joshi, *Materials Characterization* 81 (2013), 7-18. Chapter 9 provides a summary and conclusions, followed by the scope for future work. All the references that have been cited in the thesis have been listed at the end of each chapter. The style of each citation is as follows: Authors names (Last name, Initials), Journal name, Volume number, (Year) page nos.

References

[1] Holmberg K, Matthews A. Coatings tribology – properties, techniques and applications in surface engineering, Tribology Series 28. 1994. Amsterdam: Elsevier.

[2] Paulsson, M., Rich C. The Development Of Coated Grades Of Carbide Tools, American Machinist, 21 December 2007.

[3] Astakhov, VP. Tribology of metal cutting, Vol. 52. 2006 Elsevier.

[4] Knotek O, Löffler F, Barimani C, Kraemer G. Hard coatings for cutting and forming tools by PVD arc processes, Materials Science Forum, 246 (1997) 29-60.

[5] Opiekun, Z.A., Orłowicz, W.A.. Physical vapour deposition coatings on elements of pressure casting dies, Surface engineering, 22(1) (2006) 69-72.

[6] Matthews, A., Holmberg, K. PVD and CVD Coatings, In: Encyclopedia of Tribology, Springer US; 2013, pp. 2705-2711.

[7] Hultman, L., Thermal stability of nitride thin films, Vacuum, 57(1) (2000) 1-30.

[8] Beake, B.D., Fox-Rabinovich, G.S., Veldhuis, S.C., Goodes, S. R. Coating optimisation for high speed machining with advanced nanomechanical test methods, Surface and Coatings Technology, 203(13) (2009) 1919-1925.

[9] Jehn, H. A., Multicomponent and multiphase hard coatings for tribological applications, Surface and Coatings Technology, 131(1) (2000) 433-440.

[10] Vereschaka, A.S., Grigoriev, S. N., Tabakov, V. P., Sotova, E. S., Vereschaka, A. A., Kulikov, M. Y., Improving the efficiency of the cutting tool made of ceramic when machining hardened steel by applying nano-dispersed multi-layered coatings. Key Engineering Materials, 581 (2014) 68-73.

[11] Çalışkan, H., Kurbanoğlu, C., Panjan, P., Čekada, M., Kramar, D., Wear behavior and cutting performance of nanostructured hard coatings on cemented carbide cutting tools in hard milling, Tribology International, 62 (2013) 215-222.

[12] Klocke, F., Krieg, T. Coated tools for metal cutting–features and applications, CIRP Annals-Manufacturing Technology, 48(2) (1999) 515-525.

[13] Veprek S., Veprek-Heijman M.J.G., Industrial applications of superhard nanocomposite coatings, Surface and Coatings Technology, 202 (2008) 5063–5073.

[14] Cselle, T., Coddet, O., Galamand, C., Holubar, P., Jilek, M., Jilek, J., Luemkemann, A., Morstein, M. New Generation of PVD-Coatings for Cutting Tools, Journal of Machine Manufacturing, 1 (2009) 19-25.

[15] PalDey, S., Deevi, S.C., Single layer and multilayer wear resistant coatings of (Ti, Al)N: a review, Materials Science and Engineering A 342 (2003) 58-79.

[16] Hoornaert, T., Hua, Z.K., Zhang JH. In: Luo J, Meng Y, Shao T, and Zhao T, Editors. Advanced Tribology, Berlin Heidelberg: Springer-Verlag Berlin Heidelberg; 2010, p. 774-779.

[17] Bouzakis, K-D., Michailidis, N., Skordaris, G., Bouzakis, E., Biermann, D., M'Saoubi. R., Cutting with coated tools: Coating technologies, characterization methods and performance optimization, CIRP Annals – Manufacturing Technology, 61 (2012) 703–723.

[18] Grigoriev, S.N., Vereschak, A.A., Vereschak, A.S., Kutin, A.A., Cutting tools made of layered composite ceramics with nano-scale multilayer coatings, Procedia CIRP, 1 (2012) 301-306.

[19] Veprek, S., Recent attempts to design new super- and ultrahard solids leads to nano-sized and nano-structured materials and coatings, Journal of Nanoscience and Nanotechnology, 11 (2011) 14-35.

[20] Anders, A., Cathodic Arcs- From Fractal Spots to Energetic Condensation, Springer Series on Atomic, Optical, and Plasma Physics, 2008, Springer.

[21] Beake, B. D., Smith, J. F. Nano-impact testing—an effective tool for assessing the resistance of advanced wear-resistant coatings to fatigue failure and delamination, Surface and Coatings Technology, 188, (2004) 594-598.

Chapter 2 Literature Review

2.1 Hard ceramic coatings

Ceramic thin films based on nitride, carbide, boride, silicide and oxide compounds of metals from the IV, V and VI groups of the periodic table have found wide application as PVD and CVD tribological coatings [1]. These are transition metal nitrides which possess an inherent high hardness as they are covalently bonded. Most of the coatings have the base metal as Ti, with Cr being used in some cases. Different combinations of alloying elements have been added to form Ti- and Cr- based nitride coatings as shown in Fig. 2.1. These coatings have over the last 30 years been found to provide significant enhancement in the tribological performance of tools for cutting and forming applications.

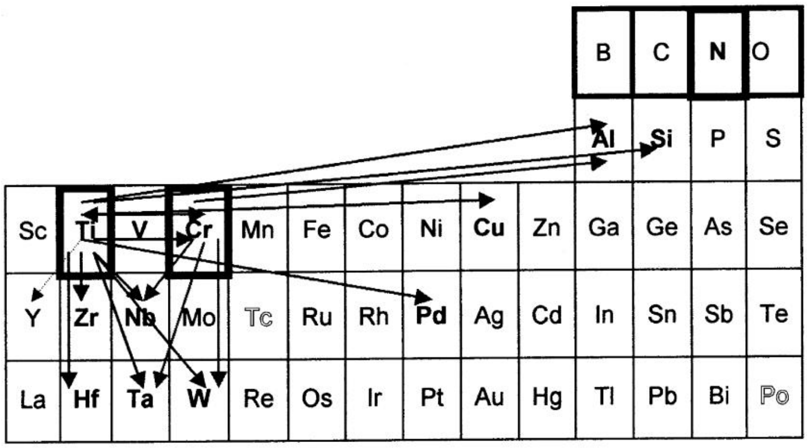

Fig.2.1 Different alloying elements used in ternary Ti and Cr- based nitride coatings [2].

2.2 Evolution of hard coatings

2.2.1 CVD coatings

The first reported hard coatings are based on the TiC and TiN systems which were deposited by CVD in 1957. However, actual application in tooling by deposition on hardened steel or cemented carbides took place around 1967-69 with TiC-coated cemented carbide tools [3]. TiC coatings are often termed the first generation of coatings. However, these coatings had restriction on their usage in applications due to the formation of a brittle η phase at the coating-substrate interface. The η phase could be suppressed by controlling the carbon balance in the CVD process [4]. This resulted in an improvement in ductility and increased film thicknesses which led to increased lifetimes in the second generation of coatings which comprised coatings of TiN, Ti(C, N) and Al_2O_3 apart from TiC. While TiC was suited for abrasive applications due to its high hardness and strength at elevated temperatures, TiN showed better chemical inertness and reduced crater wear due to inhibition of diffusion. A compromise between the high hardness of TiC and the chemical inertness of TiN was achieved in Ti(C, N). Al_2O_3 coatings showed the highest oxidation resistance and were hence suited for cutting applications at high speeds [3].

The third generation of CVD coatings developed between 1972-74 comprised of multi-layer and gradient structures such as TiC/ Ti(C, N)/ TiN and TiN/ Ti(C, N)/ Al_2O_3 where each layer contributed to various functions permitting the use of these coatings in widespread applications. Further developments in the 1980s saw the deposition of more complex multi-layers by CVD such as TiC/Ti(C,N)/TiN/4x(Al-O-N/TiN) where the top layer consists of many fine multi-layers [3].

While CVD coatings found extensive applications in continuous cutting operations such as turning requiring high material removal, their performance was limited due to the brittleness which sets in at high temperatures. The embrittlement observed in CVD coated carbides has been attributed to the following factors: the presence of internal tensile stresses, the partially coarse grained microstructure and the formation of brittle η-phases in the interfacial zone [4]. Also, coatings cannot be deposited by CVD on steel substrates as steel softens beyond 550°C which is much lower than the deposition temperature required in CVD. The above disadvantages of the CVD process have led to PVD gaining increased acceptance for use in cutting tool applications. PVD processes take place at lower temperatures (350-500°C) allowing for deposition on HSS tools and can be used to retain sharp edges apart from generating beneficial compressive stresses, as a result of which the above problems accompanying CVD coatings can be avoided [5].

2.2.2 PVD coatings

2.2.2.1 Binary nitrides

The first material of commercial interest to be deposited by PVD was TiN in the early 1980s [7]. The combination of extreme hardness, high melting point and low coefficient of friction, apart from its golden colour, made TiN an ideal choice for a hard, wear resistant material for coating of cutting tools and wear parts, and as a decorative coating [6]. However, at temperatures beyond 500 °C, TiN was found unsuitable due to its susceptibility to oxidation. Ti (C, N) coatings were developed to enhance the abrasion and erosion resistance of TiN which has a hardness of ~25 GPa. Carbon replaces nitrogen to form a solid solution of TiC_xN_{1-x} leading to a hardness increase up to ~30 GPa and a reduction in friction co-efficient from ~0.6 - 0.8 in TiN to ~0.2 in Ti(C,N) coatings [7]. CrN coatings were developed for use in applications for forming tools such as moulds and dies in view of their higher corrosion resistance and increased adhesion [8].

2.2.2.2 Ternary nitrides

Binary nitrides such as TiN and CrN comprise the first generation of nitride coatings [1], while the second generation ternary coatings are based on TiAlN which were introduced in 1986 where the addition of Al to the TiN lattice created metastable $Ti_{1-x}Al_xN$ solid solutions [9]. TiAlN coatings became the major workhorse for cutting tools in view of their high oxidation resistance and thermal stability up to ~800 °C [6, 10, 11]. The TiAlN coatings have also been reported to show an age hardening phenomenon at high temperatures (700- 800°C) which could explain the improved properties at elevated temperatures [12]. Al-rich compositions such as AlTiN were later developed in order to further improve the high temperature properties of these coatings [13].

More recently in the last decade, nitride coatings based on CrN, mainly CrAlN and AlCrN were also developed, which showed improved oxidation resistance [14]. The introduction of aluminium rich $Al_xCr_{1-x}N$ coatings raised the oxidation onset to temperatures above 1000 °C due to the formation of protective chromium and aluminium oxides [15]. Other ternary nitride coatings such as TiZrN, TiNbN, AlZrN, AlNbN have also been reported [16-19]; however they have not yet found the industrial relevance achieved by the metastable, Al- rich compositions of TiAlN and CrAlN coatings.

2.2.2.3 Quaternary and multinary nitrides

The properties of TiAlN coatings were further improved by development of quaternary and multinary nitrides. Addition of alloying elements such as Cr, Nb, B, Zr, and Y to TiAlN have been shown to further improve the oxidation resistance and mechanical properties at elevated temperatures up to around 900 °C [20-24]. Addition of elements such as V to create coatings such as TiAlVN leads to the formation of self-lubricating oxide phases which improve the tool properties at high operating temperatures [24].

2.2.2.4 Multi-layer and superlattice coatings

The next generation of coatings comprises of the multi-layer and superlattice coatings. Multi-layer coatings, formed by stacking different layers alternatively with individual thickness ranging from few to hundreds of nanometers, show improved tribological properties compared to monolithic coatings. Multi-layer coatings show enhanced properties leading to longer tool lives on account of the beneficial improvements such as hardness increase and crack redirection that arise due to layering. Interestingly, multi-layer structures are also found in nature. Examples are the Cicindela scutellaris beetle where multi-layer structure imparts mechanical protection as well as attractive colour and the Toucan beak where high modulus Keratin fibers are embedded in a lower modulus matrix for efficient load transfer [25, 26].

Superlattice coatings

Superlattice coatings which are comprised of a periodic arrangement of alternating layers of lattice matched nitrides with different individual moduli showed unusual enhancement in hardness, also termed as the superlattice effect. However, these properties are only observed when the thickness of the individual layers is within a specific range and have a large difference in shear modulus. The first reported superlattice coatings were TiN/VN coatings which showed hardness values close to 55 GPa (though hardness for pure single-crystal TiN and VN films were ~22 GPa and 16 GPa, respectively) at a bi-layer period of 5 nm [27]. These coatings were single crystalline and were epitaxially grown on single crystal substrates. Other single-crystalline nitride multi-layer systems with reported superlattice effect are $TiN/V_{0.6}Nb_{0.4}N$ [28] and TiN/NbN [29]. The superlattice effect has also been observed in polycrystalline thin films grown on polycrystalline substrates. Examples of such coatings are TiN/CrN [30], TiN/TaN [31], TiAlN/ZrN [32], TiAlN/CrN [33,34], TiAlN/VN [35,36] TiAlN/TiAlCrN [37], CrAlYN/CrN [38], TiCN/ZrCN [39], and $ZrAlN/ZrB_2$ [40]. Even though no hardening was observed in TiAlCrN/TiAlYN multi-layers, there was a significant improvement in tribological properties reported [34, 35].

Another class of multi-layers is superlattice coatings with epitaxial stabilization. This is observed in the case of a few nano-multi-layer systems where layers with different crystal structures form coherent interfaces by epitaxial stabilization of one layer in the lattice structure of the other [41]. Examples are TiN/AlN multi-layers, where AlN is stabilized in a metastable cubic lattice at low modulation periods of ~3 nm [42], and at a layer thickness below 2 nm [43]. AlN stabilized in the cubic NaCl-type structure has also been reported in other multi-layer systems like AlN/VN [44, 45], AlN/NbN [46], and CrN/AlN [47].

Multi-layer coatings

Various multi-layer systems even without an accompanying superlattice effect show a significant enhancement in properties such as tool life and wear resistance. Improvement in properties has been reported for various multi-layers such as TiAlN/TiN [48], TiAlN/CrN [21], TiAlN/AlCrN [49], TiAlN/TiAlCrN [50], TiN/TiN+TiAlN/TiAlCN [51] as well as in double layer systems such as TiN/TiCN, TiCN/SiCN, TiN/Al_2O_3 and TiAlVN/Al_2O_3 [3]. The properties of these coatings could be further enhanced by depositing them as nanosized layers with coatings comprised of multi-layers with lower bi-layer periods showing better performance [52].

2.2.2.5 Nanocomposite coatings

The fourth generation of coatings comprise of nanocomposite coatings which improved upon the multi-layers. They exhibit a nanocomposite structure which consists of nanocrystallites embedded in an amorphous matrix due to the formation of two or more immiscible phases when elements such as Si and B are co-deposited along with other elements under controlled conditions [53, 54]. Exceptional mechanical properties and high temperature resistance have been reported since the first report on TiN/Si_3N_4 nanocomposite coatings by Veprek et. al [55] where hardness values close to that of diamond were reported with the temperature stability close to 1100°C. While the above values were reported in coatings deposited under stringent thermodynamic conditions at high temperature by plasma assisted CVD, the maximum hardness attainable by PVD was much lower. However, the nanocomposite coatings deposited by PVD still show enhanced properties and high temperature oxidation resistance and have been adopted by the industry. Examples of such coatings are TiSiN (TiN/Si_3N_4) [56, 57], TiAlSiN (TiAlN/Si_3N_4) [58, 59] and more recently CrAlSiN [60, 61] and TiAlCrSiN [62, 63]. Other examples of nanocomposite coatings are TiB_2/TiN and TiN–TiB_x–BN where Boron forms a tissue phase surrounding nanocrystalline grains [64]. As the nanocomposite coatings are superhard, they tend to be brittle and various efforts at improving the toughness of the coatings have been attempted such as nanolayering and addition of ductile metals [65].

Another class of nanocomposite coatings is self-lubricant coatings where a hard phase is embedded in a soft matrix which has lubricant properties. Examples of such nanocomposites are nc-WCx/a-C(:H), nc-TiCx/a-C(:H), or SiC/a-C(:H) which show low values of friction coefficient (0.2–0.3) [66]. Nanocomposite coatings with a transition metal dichalcogenide matrix such as MoS_2 and WS_2 have been reported to show reduced friction and can adapt to changes in environment by regeneration of a new layer and have been called chameleon nanocomposite coatings [67].

2.2.2.6 Gradient coatings

Deposition of graded layers with a continuous variation of the elemental constituents or stress allows tailoring of properties to suit requirements of the substrate or at the coating surface. Such coatings allow a smooth transition between the various coating layers and the substrate, thereby preventing any sudden failures [41].

2.2.2.7 Other hard coatings

Diamond like carbon (DLC) and Alumina based coatings are two other coating classes which also find application for cutting tools. DLC coatings are characterized by an extremely low friction co-efficient in the range 0.007-0.1 and find special application in the automotive industry and can be deposited by either plasma assisted CVD or plasma assisted PVD [7]. While alumina has been extensively coated by CVD on cutting tools, it has only recently been able to be industrially deposited by PVD as it is a challenge mainly due to its electrically insulating nature [68].

Thus, hard coatings for tools have evolved from simple binary carbides and nitrides such as TiC, TiCN and TiN and oxides such as Al_2O_3 to ternary and quaternary nitrides based on TiAlN and CrAlN. The last decade has seen the development of multi-layer coatings and nanocomposite coatings which have further enhanced tool performance. The timescale of the tool coatings development until 2010 is shown in Fig.2.2. The properties of the coatings such as hardness and maximum usage temperature have progressively improved as shown in Table 1. The latter part of the last decade also saw introduction of a new generation of multi-functional, multi-layer coatings which are discussed in section 2.3.2.8.

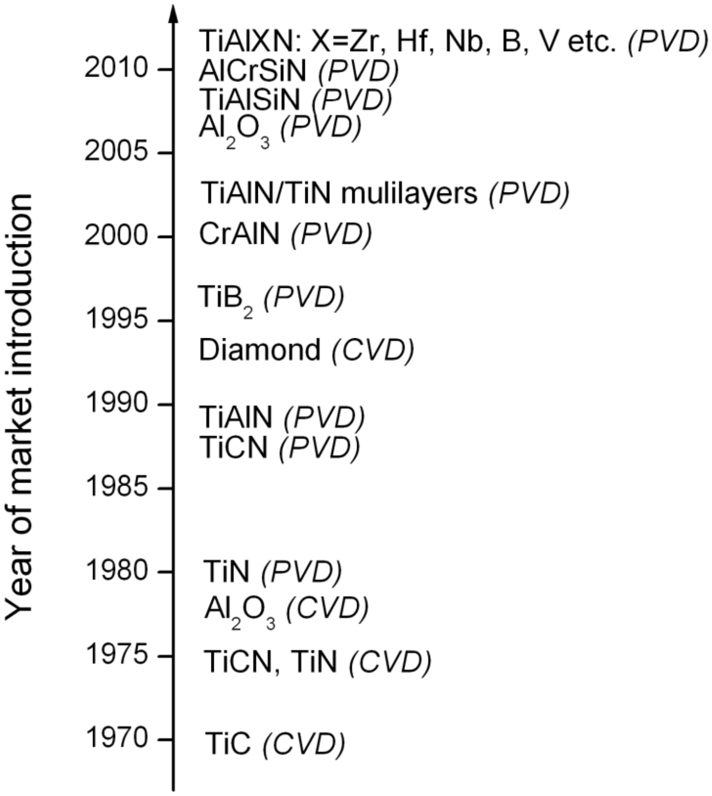

Fig.2.2: Schematic showing timescale of tool coatings adoption in industry [adapted from 68].

Table 1: Properties of various nitride coatings being used in industry [69], * coatings with a nanocomposite structure

Coating	Hardness (GPa)	Friction co-efficient	Max. Usage Temperature (^oC)
TiN	24	0.55	600
TiCN	32	0.2	400
CrN	18	0.3	700
AlTiN	38	0.7	900
TiAlCN	33	0.3	500
ZrN	20	0.4	550
TiAlCrN	40	0.55	850
AlCrN	32	0.6	900
TiAlSiN*	45	0.45	1200
CrAlSiN*	40	0.35	1100
TiAlCrSiN*	42	0.4	1150

2.2.2.8 Multi-functional, Multi-layer coatings

There has been a further improvement in properties through the use of multi-functional, multi-layer coatings [70]. These new generation PVD coatings involve multiple layers comprising of nanocomposite and conventional layers such as TiAlSiN and TiAlN, each layer being tailored to discharge a specific function to enhance the durability and performance of the overall coating [71,72]. These have already begun to be used in industry, especially for cutting tool applications as evident from the increased number of patents reporting such architectures [73]. An enhancement in tool life by almost double when compared with even the high performance nanocomposite coatings has been reported as shown in Fig. 2.3 below.

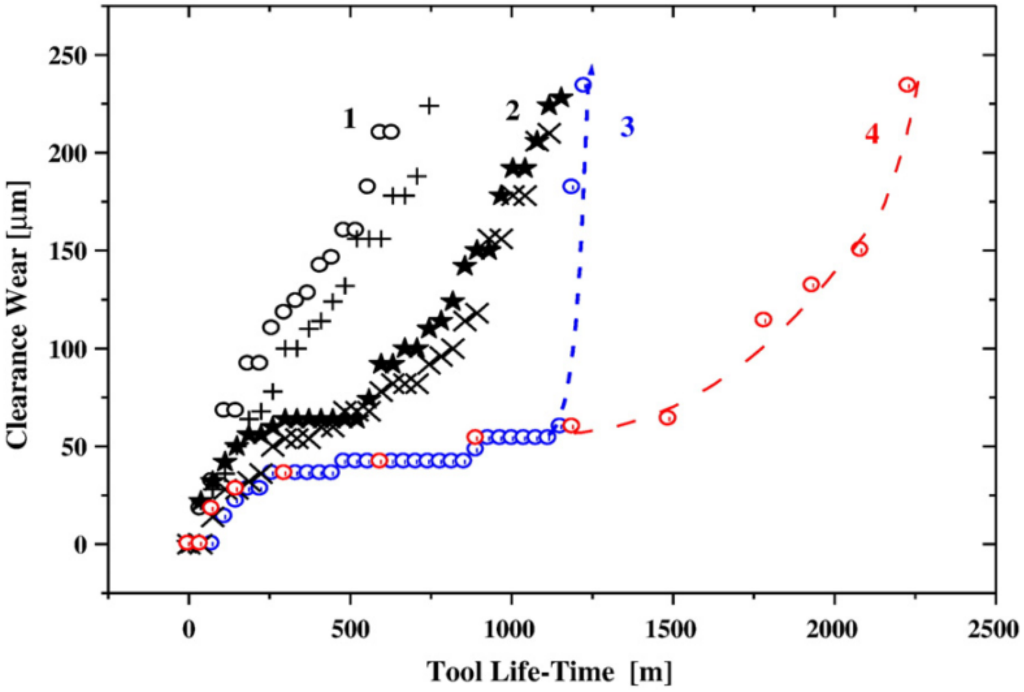

Fig. 2.3 Tool life performance of 1: ($Al_{1-x}Ti_x$) N; 2: AlTiN + TiSiN coatings; 3: first generation of nc-($Ti_{1-x}Al_x$)N/a-Si_3N_4 nanocomposite coatings, and 4: second generation of nanocomposite coatings with a softer under-layer and graded top-nanocomposite layer with higher Si-content [74].

The enhancements in coating development have been made possible (as also shown in Fig.1.5) through:

i) Adoption of newer materials by multi-component alloying,

ii) Improvements in coating processes to enable large scale deposition and

iii) Design of more complex architectures involving multi-layers, nanocomposite coatings, gradient coatings and adaptive coatings.

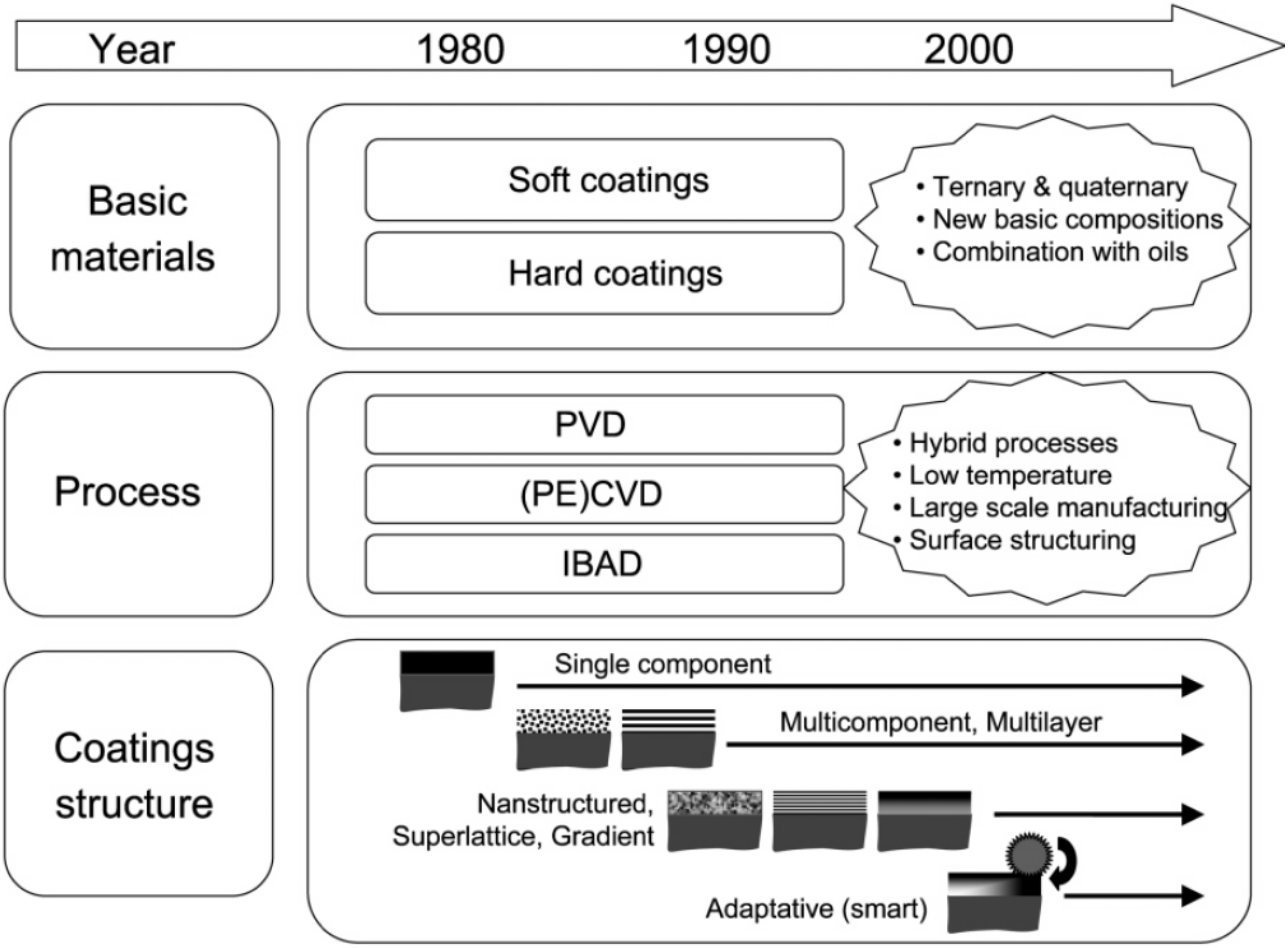

Fig. 2.4 Historical development of tribological coatings [75].

2.3 Microstructural engineering of hard coatings

The properties of a coating are strongly dependent on its structure and microstructure. Most of the coating properties such as hardness and wear resistance are closely related to its microstructure. Thin films often show completely different microstructures compared to their bulk counterparts, e.g., a much smaller grain size, and a higher concentration of other defects on account of the non-equilibrium nature of most vapour deposition methods [76]. As discussed in the earlier section, coatings with varying composition and architecture can be designed and deposited to achieve enhancement in properties. The enhancement in properties comes about due to the unique microstructures present in these coatings. The microstructure can be tailored either by varying the deposition parameters such as bias voltage and temperature, through control of

composition, and in case of multi-layers, the layer thicknesses. Various representative microstructures that have been designed and observed in hard coatings are schematically shown in Fig. 1.6. The microstructure can be varied from columnar grains seen in case of TiN and TiAlN coatings to nanocrystalline grains. Multi-layers can vary from simple double/triple layer systems with large layer spacings as in ZrN/TiN and TiN/Al_2O_3/TiC coatings, respectively, to hard-soft layers such as TiB_2/MoS_2 and superlattice coatings such as CrN/NbN and TiN/VN with layer spacings of 2-5 nm. Nanocomposite coatings with nanocrystalline grains embedded in an amorphous matrix can be designed as seen in TiN/ Si_3N_4, TiN/TiB_2 and h-BN/c-BN coatings.
Gradient coatings such as Ti-TiCN-TiC-DLC with a gradient in composition and adaptive coatings such as YSZ/MoS_2/DLC and TiC/DLC coatings which respond to changing load and contact requirements during operation can also be deposited [73].

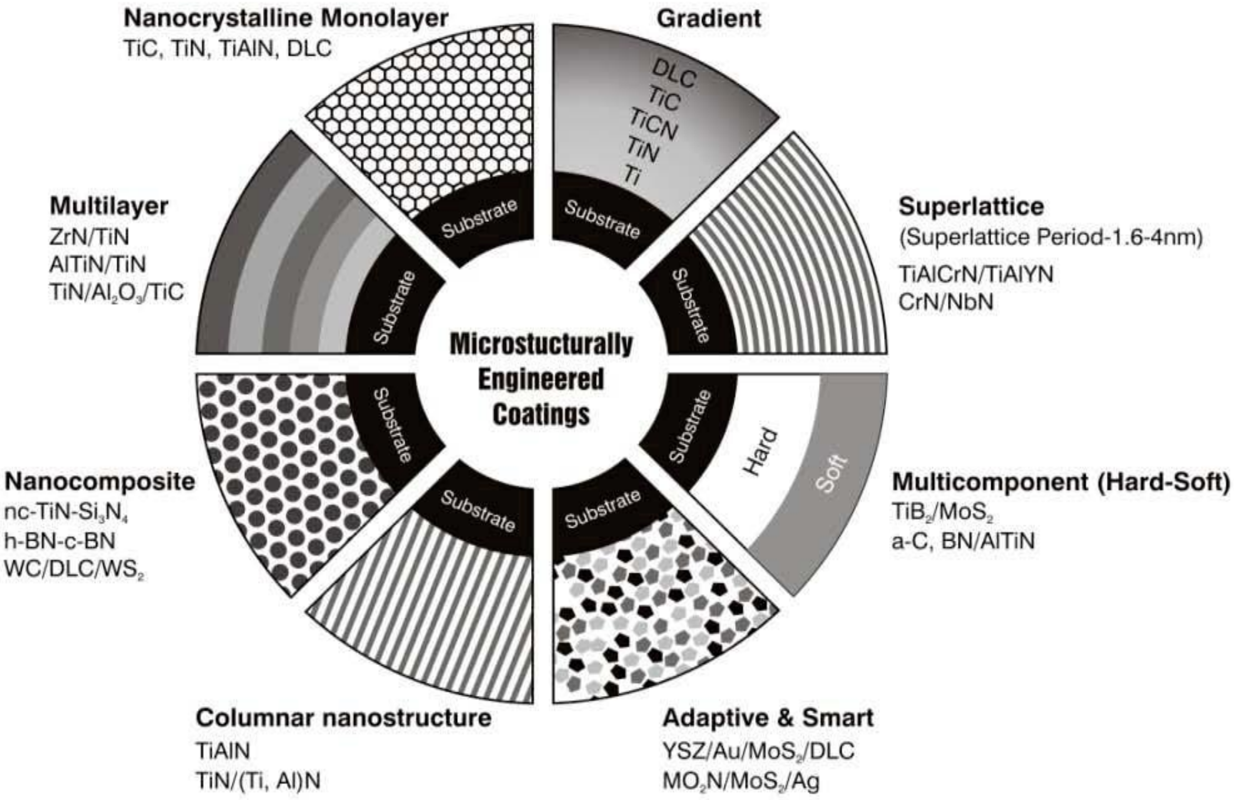

Fig. 2.5 Examples of various microstructures that can be engineered in hard coatings [73].

Thus, design of coating architectures in the form of nanocrystalline, nanocomposite and multi-layer coatings have enabled large improvements in coated tool performance. Combinations involving these different coating types can be used to create multi-functional, multi-layer coatings for further improvements in coated tool performance and life, which is the aim of this thesis.

References

[1] Holmberg K, Matthews A. Coatings tribology – properties, techniques and applications in surface engineering, Tribology Series 28. Amsterdam: Elsevier; 1994.

[2] Jehn, HA. Multicomponent and multiphase hard coatings for tribological applications, Surface and Coatings Technology, 131(1) (2000) 433-440.

[3] Knotek, O, Loffler, F, Kramer, G. Applications to Cutting Tools, In: Handbook of Hard Coatings, RF Bunshah ed. Noyes Publications, New York, USA, 2001, pp. 370-407.

[4] Santhanam, AT, Application of transition metal carbides and nitrides in industrial tools. In: The Chemistry of Transition Metal Carbides and Nitrides, Springer Netherlands. 1996. pp. 28-52.

[5] Knotek O, Löffler F, Barimani C, Kraemer G. Hard coatings for cutting and forming tools by PVD arc processes, Materials Science Forum, 246 (1997) 29-60.

[6] Martin PJ, Mackenzie DR. " Film Growth", in Boxman, R. L., Sanders, D. M., & Martin, P. J. (Eds.). Handbook of vacuum arc science & technology: fundamentals and applications. William Andrew; 1996).

[7] Mitterer, C. PVD and CVD Hard Coatings. In Comprehensive Hard Materials: Elsevier; 2014. pp. 449-467.

[8] Panjan, P, Cvahte, P, Čekada, M, Navinšek, B, Urankar, I. PVD CrN coating for protection of extrusion dies, Vacuum, 61(2) (2001) 241-244.

[9] Münz, WD, Titanium aluminum nitride films: A new alternative to TiN coatings, Journal of Vacuum Science & Technology A, 4(6) (1986) 2717-2725.

[10] Leyendecker, T, Lemmer, O, Esser, S, Ebberink, J. The development of the PVD coating TiAlN as a commercial coating for cutting tools, Surface and Coatings Technology, 48(2) (1991) 175-178.

[11] PalDey S, Deevi SC, Single layer and multilayer wear resistant coatings of (Ti, Al)N: a review, Materials Science and Engineering A 342 (2003) 58-79.

[12] Rachbauer, R, Massl, S, Stergar, E, Holec, D, Kiener, D, Keckes, J, Patscheider J, Stiefel M, Leitner H, Mayrhofer, PH. Decomposition pathways in age hardening of Ti-Al-N films, Journal of Applied Physics, 110(2) (2011) 023515.

[13] Fox-Rabinovich, GS, Endrino, JL, Beake, BD, Kovalev, AI, Veldhuis, SC, Ning, L, Gray, A. Impact of annealing on microstructure, properties and cutting performance of an AlTiN coating, Surface and Coatings Technology, 201(6) (2006) 3524-3529.

[14] Chim, YC, Ding, XZ, Zeng, XT, Zhang, S. Oxidation resistance of TiN, CrN, TiAlN and CrAlN coatings deposited by lateral rotating cathode arc, Thin Solid Films, 517(17) (2009) 4845-4849.

[15] Endrino, JL, Fox-Rabinovich, GS, Reiter, A, Veldhuis, SC, Galindo, RE, Albella, JM, Marco, JF. Oxidation tuning in AlCrN coatings. Surface and Coatings Technology, 201(8) (2007) 4505-4511.

[16] Milošev, I, Strehblow, HH, Navinšek, B. Oxidation of ternary TiZrN hard coatings studied by XPS. Surface and interface analysis, 26(4) (1998) 242-248.

[17] Vasu, K, Krishna, MG, Padmanabhan, KA. Effect of Nb concentration on the structure, mechanical, optical, and electrical properties of nano-crystalline $Ti_{1-x}Nb_xN$ thin films, Journal of Materials Science, 47(8) (2012) 3522-3528.

[18] Franz, R., Lechthaler, M., Polzer, C, Mitterer, C. Oxidation behavior and tribological properties of arc-evaporated ZrAlN hard coatings, Surface and Coatings Technology, 206 (2012) 2337–2345.

[19] Franz, R, Lechthaler, M, Polzer, C, Mitterer, C. Structure, mechanical properties and oxidation behaviour of arc-evaporated NbAlN coatings, Surface and Coatings Technology, 204 (2010) 2447–2453.

[20] Kathrein, M, Michotte, C, Penoy, M, Polcik, P, Mitterer, C. Multifunctional multi-component PVD coatings for cutting tools, Surface and Coatings Technology, 200(5) (2005) 1867-1871.

[21] Luo, Q, Rainforth, WM, Donohue, LA, Wadsworth, I, Münz, WD. Tribological investigation of TiAlCrN and TiAlN/CrN coatings grown by combined steered-arc/unbalanced magnetron deposition, Vacuum, 53(1) (1999) 123-126.

[22] Donohue, LA, Cawley, J, Brooks, JS, Münz, WD. Deposition and characterization of TiAlZrN films produced by a combined steered arc and unbalanced magnetron sputtering technique, Surface and Coatings Technology, 74 (1995) 123-134.

[23] Leyens, C, Peters, M, Hovsepian, PE, Lewis, DB, Luo, Q, Münz, WD. Novel coating systems produced by the combined cathodic arc/unbalanced magnetron sputtering for environmental protection of titanium alloys, Surface and Coatings Technology, 155(2) (2002) 103-111.

[24] Franz, R, Mitterer, C. Vanadium containing self-adaptive low-friction hard coatings for high-temperature applications: A review, Surface and Coatings Technology, 228 (2013) 1-13.

[25] Land, MF. The physics and biology of animal reflectors, Progress in Biophysics and Molecular Biology, 24 (1972) 75-106.

[26] Seki, Y, Schneider, MS, Meyers, MA. Structure and mechanical behavior of a toucan beak, Acta Materialia, 53(20) (2005) 5281-5296.

[27] Helmersson, U, Todorova, S, Barnett, SA, Sundgren, JE, Markert, LC, Greene, JE. Growth of single-crystal TiN/VN strained-layer superlattices with extremely high mechanical hardness, Journal of Applied Physics, 62(2) (1987) 481-484.

[28] Mirkarimi, PB, Hultman, L, Barnett, SA. Enhanced hardness in lattice-matched single-crystal TiN/$V_{0.6}Nb_{0.4}N$ superlattices, Applied Physics Letters, 57 (25) (1990) 2654–2656.

[29] Shinn, M, Hultman, L, Barnett, SA. Growth, structure, and microhardness of epitaxial TiN/NbN superlattices, Journal of Materials Research, 7 (4) (1992) 901–911.

[30] Yashar, P, Barnett, SA, Rechner, J, Sproul, WD. Structure and mechanical properties of polycrystalline CrN/TiN superlattices, Journal of Vacuum Science & Technology, A 16 (5) (1998) 2913–2918.

[31] Xu, J, Li, G, Gu, M. The microstructure and mechanical properties of TaN/TiN and TaWN/TiN superlattice films, Thin Solid Films, 370 (2000) 45-49.

[32] Donohue, LA, Münz, WD, Lewis, DB, Cawley, J, Hurkmans, T, Trinh, T, Petrov, I, Greene, JE. Large-scale fabrication of hard superlattice thin films by combined steered arc evaporation and unbalanced magnetron sputtering, Surface and Coatings Technology, 93 (1997) 69–87.

[33] Münz, WD, Donohue, LA, Hovsepian, PEh. Properties of various large-scale fabricated TiAlN- and CrN-based superlattice coatings grown by combined cathodic arc–unbalanced magnetron sputter deposition, Surface and Coatings Technology, 125 (2000) 269–277.

[34] Hovsepian, PEh, Münz, WD. Recent progress in large-scale production of nanoscale multilayer/superlattice hard coatings, Vacuum, 69 (2002) 27–36.

[35] Hovsepian, PEh, Lewis, DB, Luo, Q, Münz, WD, Mayrhofer, PH, Mitterer, C, Zhou, Z, Rainforth, WM. TiAlN based nanoscale multilayer coatings designed to adapt their tribological properties at elevated temperatures, Thin Solid Films, 485 (2005) 160–168.

[36] Kong, M, Shao, N, Dong, Y, Yue, J, Li, G. Growth, microstructure and mechanical properties of (Ti, Al)N/VN nanomultilayers, Materials Letters, 60 (2006) 874–877.

[37] Hovsepian, PEh, Lewis, DB, Münz, WD. Recent progress in large scale manufacturing of multilayer/superlattice hard coatings, Surface and Coatings Technology, 133–134 (2000) 166–175.

[38] Hovsepian, PEh, Reinhard, C, Ehiasarian, AP. CrAlYN/CrN superlattice coatings deposited by the combined high power impulse magnetron sputtering/unbalanced magnetron sputtering technique, Surface and Coatings Technology, 201 (2006) 4105–4110.

[39] Balaceanu, M, Braic, M., Braic, V., Pavelescu, G. Properties of arc plasma deposited TiCN/ZrCN superlattice coatings, Surface and Coatings Technology, 200 (2005) 1084–1087.

[40] Lee, K.W., Chen, Y.-H., Chung, Y.-W., Keer, L.M., Hardness, internal stress and thermal stability of TiB_2/TiC multilayer coatings synthesized by magnetron sputtering with and without substrate rotation, Surface and Coatings Technology, 177–178 (2004) 591–596.

[41] Stueber, M., Holleck, H., Leiste, H., Seemann, K., Ulrich, S., Ziebert, C., Concepts for the design of advanced nanoscale PVD multilayer protective thin films, Journal of Alloys and Compounds, 483(1) (2009) 321-333.

[42] Setoyama, M., Nakayama, A., Tanaka, M., Kitagawa, N., Nomura, T., Formation of cubic-AlN in TiN/AlN superlattice, Surface and Coatings Technology, 86–87 (1996) 225–230.

[43] Madan, A., Kim, I.W., Cheng, S.C. , Yashar, P., Dravid, V.P., Barnett, S.A., Stabilization of Cubic AlN in Epitaxial AlN/TiN Superlattices, Physical Review Letters, 78 (9) (1997) 1743–1746.

[44] Li, Q., Kim, I.W., Barnett, S.A., Marks, L.D., Structures of AlN/VN Superlattices with Different AlN Layer Thicknesses, Journal of Materials Research, 17 (5) (2002) 1224–1231.

[45] Lao, J., Han, Z., Tian, J., Li, G., Mechanical property investigation of AlN/VN nanomultilayers with microindentation technique, Materials Letter, 58 (2004) 859–862.

[46] Barnett, S.A., Madan, A., Kim, I., Martin, K., Stability of Nanometer-Thick Layers in Hard Coatings, MRS Bulletin, 28 (2003) 169-172.

[47] Kim, G.S., Lee, S.Y., Hahn, J.H., Lee, S.Y., Synthesis of CrN/AlN superlattice coatings using closed-field unbalanced magnetron sputtering process, Surface and Coatings Technology, 171 (2003) 91-95.

[48] Knutsson, A., Johansson, M. P., Karlsson, L., Odén, M., Machining performance and decomposition of TiAlN/TiN multilayer coated metal cutting inserts, Surface and Coatings Technology, 205(16) (2011) 4005-4010.

[49] Liew, W. Y. H., Low-speed milling of stainless steel with TiAlN single-layer and TiAlN/AlCrN nano-multilayer coated carbide tools under different lubrication conditions, Wear, 269(7) (2010) 617-631.

[50] Santana, A. E., Karimi, A., Derflinger, V. H., Schütze, A., Microstructure and mechanical behavior of TiAlCrN multilayer thin films, Surface and Coatings Technology, 177 (2004) 334-340.

[51] Prengel, H. G., Jindal, P. C., Wendt, K. H., Santhanam, A. T., Hegde, P. L., Penich, R. M., A new class of high performance PVD coatings for carbide cutting tools. Surface and Coatings Technology, 139(1) (2001) 25-34.

[52] Inspektor, A., Salvador, P.A., Architecture of PVD coatings for metalcutting applications: A review, Surface and Coatings Technology 257 (2014) 138–153.

[53] Musil, J., Hard and superhard nanocomposite coatings, Surface and Coatings Technology 125(1) (2000) 322-330.

[54] Männling, H. D., Patil, D. S., Moto, K., Jilek, M., Veprek, S., Thermal stability of superhard nanocomposite coatings consisting of immiscible nitrides, Surface and Coatings Technology, 146 (2001) 263-267.

[55] Vepřek, S., Reiprich, S., Shizhi, L., Superhard nanocrystalline composite materials: the TiN/Si_3N_4 system, Applied physics letters, 66(20) (1995) 2640-2642.

[56] Patscheider, J., Nanocomposite hard coatings for wear protection. MRS bulletin, 28(03) (2003) 180-183.

[57] Barshilia, H. C., Deepthi, B., Prabhu, A. A., & Rajam, K. S., Superhard nanocomposite coatings of TiN/Si_3N_4 prepared by reactive direct current unbalanced magnetron sputtering, Surface and Coatings Technology, 201(1) (2006) 329-337.

[58] Jilek, M., Cselle, T., Holubar, P., Morstein, M., Veprek-Heijman, M. G. J., Veprek, S., Development of novel coating technology by vacuum arc with rotating cathodes for industrial production of nc-$(Al_{1-x}Ti_x)N$/a-Si_3N_4 superhard nanocomposite coatings for dry, hard machining. Plasma chemistry and plasma processing, 24(4) (2004) 493-510.

[59] Barshilia, H. C., Deepthi, B., Rajam, K. S., Deposition and characterization of TiAlN/Si_3N_4 superhard nanocomposite coatings prepared by reactive direct current unbalanced magnetron sputtering,Vacuum, 81(4) (2006)479-488.

[60] Ding, X.Z., Zeng, X.T., Liu, Y.C., Structure and properties of CrAlSiN Nanocomposite coatings deposited by lateral rotating cathodic arc, Thin Solid Films, 519(6) (2011) 1894-1900.

[61] Chang, Y. Y., Chang, C. P., Wang, D.Y., Yang, S.M., Wu, W., High temperature oxidation resistance of CrAlSiN coatings synthesized by a cathodic arc deposition process. Journal of Alloys and Compounds, 461(1) (2008) 336-341.

[62] Panich, N., Surinphong, S., Karpov, D. A., Tan, Y. K., Goh, C. F., Ma, J., Mechanical properties of AlCrTiSiN coatings developed by cathodic arc for protection applications, Solid State Phenomena 185 (2012) 81-83.

[63] Rodríguez-Barrero, S., Fernández-Larrinoa, J., Azkona, I., López de Lacalle, L. N., Polvorosa, R. Enhanced Performance of Nanostructured Coatings for Drilling by Droplet Elimination. Materials and Manufacturing Processes, (2015) Article in Press, DOI:10.1080/10426914.2014.973582

[64] Mayrhofer, P. H., Mitterer, C., Hultman, L., Clemens, H. Microstructural design of hard coatings, Progress in Materials Science, 51(8), (2006) 1032-1114.

[65] Zhang, S., Wang, H. L., Ong, S. E., Sun, D., Bui, X. L. Hard yet tough nanocomposite coatings–present status and future trends, Plasma Processes and Polymers, 4(3), (2007). 219-228.

[66] Martínez-Martínez, D. Nanocomposite Coatings. In Encyclopedia of Tribology Springer US. (2013) pp. 2359-2364.

[67] Voevodin, A. A., Zabinski, J.S., Supertough wear-resistant coatings with ‘chameleon’surface adaptation, Thin Solid Films, 370(1) (2000) 223-231.

[68] Bouzakis, K. D., Michailidis, N., Skordaris, G., Bouzakis, E., Biermann, D., M'Saoubi, R., Cutting with coated tools: Coating technologies, characterization methods and performance optimization. CIRP Annals-Manufacturing Technology, 61, (2012) 703-723.

[69] De Lacalle, L. N. L., Lamikiz, A., de Larrinoa, J. F., & Azkona, I. Advanced cutting tools. In: Machining of hard materials, Springer London; 2011. pp. 33-86.

[70] Veprek S, Veprek-Heijman M.J.G, Industrial applications of superhard nanocomposite coatings, Surface and Coatings Technology, 202 (2008) 5063–73.

[71] Cselle T, Coddet O, Galamand C, Holubar P, Jilek M, Jilek J, TripleCoatings^3- New Generation of PVD-Coatings for Cutting Tools. Journal of Machine Manufacturing. 1 (2009) 19-25.

[72] Veprek S, Recent Attempts to Design New Super- and Ultrahard Solids Leads to Nano-Sized and Nano-Structured Materials and Coatings, Journal of Nanoscience and Nantechnology, 11 (2011) 14-35.

[73] Sivudu, K.S., Mahajan, Y.R., Joshi, S.V., Nano-Enabled Tribological Thin Film Coatings: Global Patent Scenario. Recent patents on nanotechnology, 8(2), (2014) 97-116

[74] Veprek, S., Zhang, R.F., Veprek-Heijman, M.G.J., Sheng, S.H., Argon, Superhard nanocomposites: Origin of hardness enhancement, properties and applications Surface and Coatings Technology, 204 (2010) 1898–1906.

[75] Donnet, C., Erdemir, A., Historical developments and new trends in tribological and solid lubricant coatings, Surface and Coatings Technology, 180 -181 (2004) 76–84.

[76] Hultman, L., Sundgren, J. E. Structure-Property Relationships for Hard Coatings, In: Handbook of Hard Coatings. Bunshah, R.F., Ed., Noyes Publications Park Ridge. New Jersey. USA, (2001) pp.159-165

Chapter 3 Experimental details

3.1 Cathodic arc deposition

In the present work, coatings were deposited by cathodic arc evaporation, which comes under the class of arc vapour deposition wherein an arc is created at an electrode to vaporise material and create a plasma. It comprises of an arc generated by application of a high current pulse to the cathode using an anode striker. The arc is controlled and manoeuvred by application of a magnetic field. Arcing occurs when a high current at a low voltage is passed though a gas or vapour of the electrode material with the arc voltage close to the ionization potential of the material. The rapid vapourization generates thermally evaporated atoms along with some percentage of molten droplets or particles from the cathode with a large percentage of the atoms ionized due to the high electron densities [1, 2]. Introduction of a reactive gas into the deposition chamber leads to the formation of stoichiometric compound films.

3.1.1 Cylindrical cathodic arc deposition

In the present study, the coatings were deposited in a Platit cathodic arc unit which uses cylindrical rotating targets as evaporation sources. The arc coating process takes place in an evacuated vacuum chamber where the cylindrical metallic targets act as cathodes in an arc circuit. The arc is generated by a metallic wire called a striker, which strikes the surface of the target, similar to the more commonly known arc welding process. The striker is used only for generation of the arc. The arc, once generated, runs between the cathodes (targets at negative potential) and the anodes and chamber walls on ground potential. The current is concentrated in several μm-sized spots called cathode spots which move randomly on the cathode surface. Very high current densities of 10^6 - 10^8 A/cm^2 are present in these cathode spots which locally melt the surface of the target material. A large number of electrons, metallic ions, clusters and macroparticles are emitted from these hot spots with a high percentage (30 to 100 %) of the evaporated material in the ionized state. The ions exist in several charge states in the plasma, e.g. for Ti cathode- Ti^+, Ti^{2+}, Ti^{3+}. The kinetic energies of the ions are typically in the range of 10 to 100 eV leading to the deposition of dense coatings with excellent adhesion (superior to other types of deposition processes such as magnetron sputtering). High deposition rates of a few micrometers per hour are easily reached. When nitrogen or other reactive gases are introduced into the vacuum chamber during the arc process, stoichiometric compound films, such as TiN, CrN, TiAlN, TiCN are produced [3].

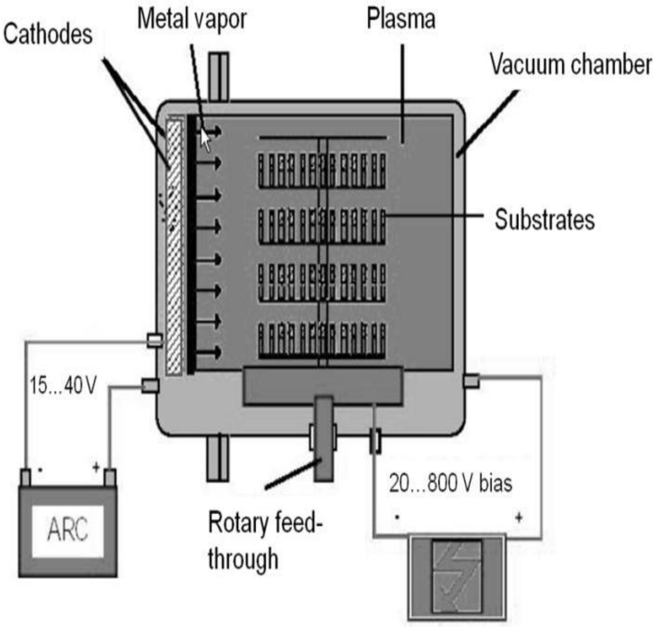

Fig. 3.1 Schematic showing the working principle of cathodic arc deposition.

In the Platit arc deposition unit, the movement of the cathode spots is controlled and steered by a magnetic field generated by inbuilt magnets within the cathodes. The Magnetic Arc Control (MAC) system enables control of the arc stability, the number and the speed of the cathode spots and their size. The presence of macroparticles (droplets), which is the main disadvantage of conventional cathodic arc processes, is reduced by a rapid movement of the arc spot on the cathode surface. The faster the movement of the cathode spot on the surface of the target, the smaller are the melted spots which result in fewer and smaller macroparticles, which leads to smoother coatings. The cylindrical rotational targets increase the usable target area by π*D (where D is the diameter of the target) in comparison to planar targets of width D (both targets of the same height). Further, more uniform target erosion leads to better target utilization and cost efficiency [3]. Fig. 3.2 shows the layout of the four cylindrical cathodes in the Platit π^{300} unit used in the present work with 3 lateral rotating cathodes (LARCs), Cr, Al-Si and Ti, placed in the door, and the fourth central rotating cathode (CERC), Al-Ti, placed in the centre of the sample carousel.

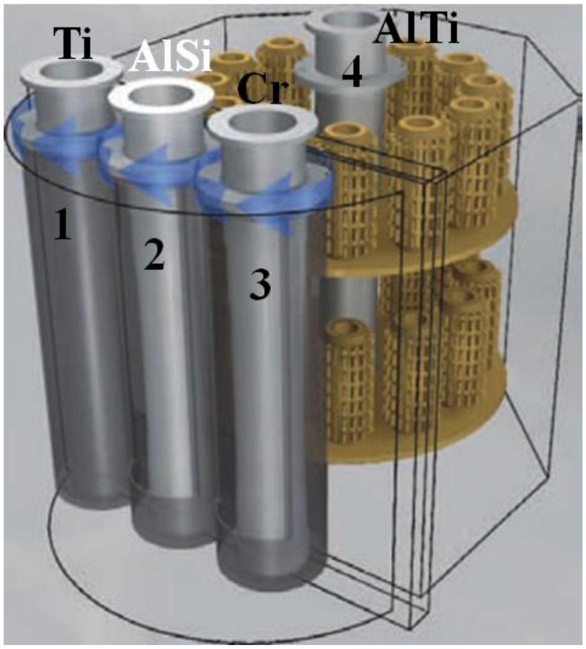

Fig. 3.2 Schematic of the lateral rotating cathodes and central rotating cathode in the Platit π300 system used in the present work.

3.1.2 Coating process

After loading the coating chamber with specimens (substrates and/or tools) for deposition, the chamber is evacuated by vacuum pumps and the specimens are heated up to the preset temperature. During the heating step, all the specimens get uniformly heated and all surfaces inside the chamber get degassed. The heating of the specimens is done in vacuum, argon or nitrogen atmosphere and maintained at the set temperature for an hour. After the heating step, the chamber is kept under vacuum, until a pressure of $< 2x\ 10^{-6}$ mbar is attained.

The coating process is begun once the set temperature is reached. The first step is argon etching where a glow discharge is generated by the bias applied between the specimens and the chamber walls. Positive argon ions are accelerated by the negative potential to the specimens. The argon ions bombard their surfaces and sputter-clean the specimen surface leading to a reduction of adsorbed atoms and molecules and reduction of the naturally formed oxide layer. During the argon etching step, the cathode target shutters close and the arc is ignited (for Ti and Cr cathodes) backwards to the chamber walls effectively cleaning the cathodes. To further enhance the quality of the substrate surface and increase the adhesion of the deposited films, a Metal ion etching step is used. The arc is run on Ti or Cr cathode in the direction of the substrates, which are biased at high voltage (750 to 1200 V). The metal ions at low pressure are accelerated towards the substrates where they get implanted and act as a nucleation layer. This is followed by the coating steps, where single layers, multi-layers and gradient layers can be deposited. The substrates are continually rotated in a threefold planetary motion so that a coating of uniform thickness is deposited. After the desired coating is achieved, the substrates are cooled in vacuum, Ar, nitrogen or fast cooled in helium. The chamber is vented and the specimens unloaded from the chamber once a safe temperature is reached [3].

Pre-coating steps

Prior to loading in the chamber, all the substrates were cleaned in soap solution, followed by ultrasonic agitation and rinsing at a temperature of 60°C in a separate cleaning unit. The substrates were dried using an infrared heater and carefully placed in the chamber and then subjected to argon and metal ion etching in order to remove any residual impurities from the surface prior to the coating.

3.1.3 Deposition parameters

99.99% pure Ti, Cr, AlTi (Al-67% & Ti -33%) and AlSi (Al-82% & Si-18%) cathodes and 99.999 % pure N_2 gas were used for the deposition of the various coatings in this study. The deposition parameters such as the substrate temperature, bias voltage and reactive gas pressure were kept constant throughout the deposition. Details of deposition parameters for the various coatings studied in this work are listed in Table 2. Other specific parameters (cathode powers) are mentioned in the respective sections in the results and discussion. All the coatings were deposited on tool steel substrates with a few specific coatings deposited on silicon (single crystal) substrates for toughness evaluation. The coating deposition time was controlled to obtain a near constant coating thickness of 4 µm; any major deviation is reported in the specific chapter.

Table 2: Deposition parameters used for various coatings.

Coating	Substrate bias (V)	Reactive gas deposition pressure (mbar)	Substrate temperature (°C)	Cathodes utilized
TiN	-50	5×10^{-2}	450	Ti
$Ti_{1-x}Al_xN$	-50	5×10^{-2}	450	Ti, 67Al-33Ti
TiAlCrSiN	-50	5×10^{-2}	475	Ti, Cr,82Al-18Si

3.2 Thickness measurement

Coating thickness was determined from the ball cratering test (Calotest). The Calotest was performed by rotating a steel sphere of 30 mm diameter and at 200 g weight at a speed of 300 rpm for 3 minutes on the sample using a diamond suspension as lubricant, leading to the formation of a hemispherical crater on the coatings. The coating thickness is calculated from a simple geometric equation [4] as below:

$$\boldsymbol{d = \frac{A^2 - B^2}{4D}}$$

where d is the coating thickness, A and B are the respective diameters of the outer and inner circles of the crater and D is the diameter of the steel sphere. This is shown schematically in Fig. 3.3. Fig. 3.4 shows a typical ball crater on a multi-layer coating with an overall thickness of ~ 4 micron measured from the Calotest.

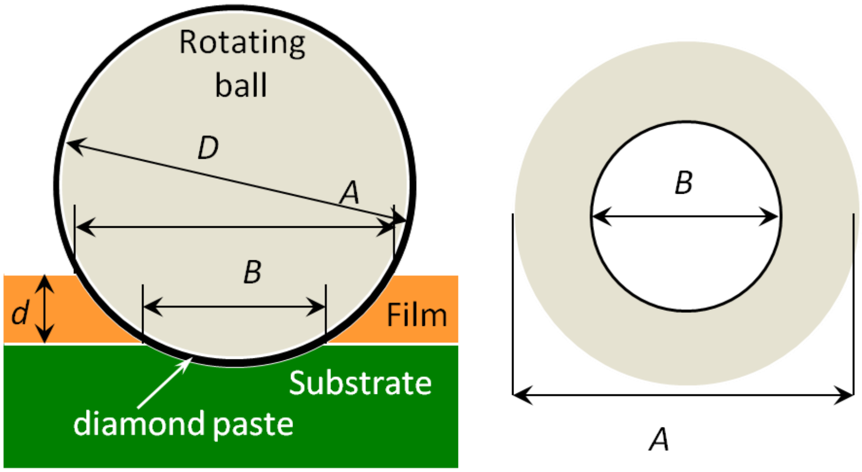

Fig. 3.3 Schematic showing the principle of thickness measurement using a Calotester, where D is the diameter of the steel ball, A and B are the diameters of the outer and inner circles of the crater, respectively and d is the coating thickness.

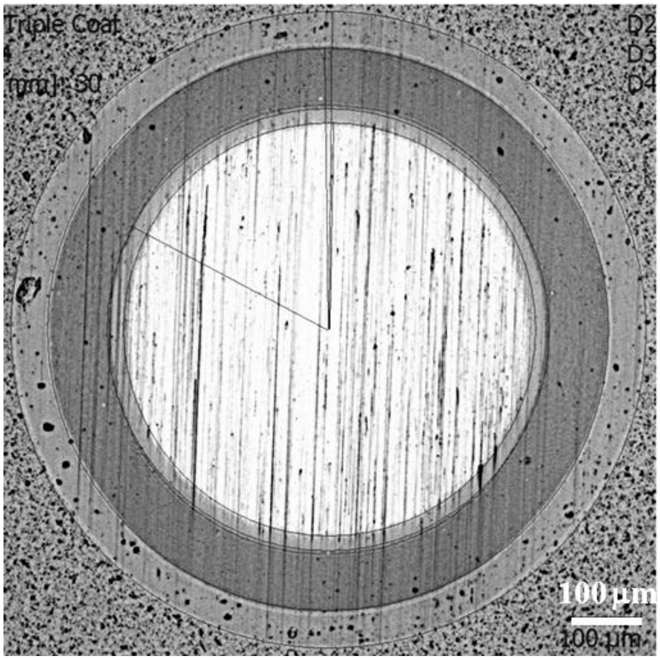

Fig. 3.4 Optical micrograph showing the typical cross section of crater on a multi-layer coating after Calotest.

3.3 Mechanical characterization

3.3.1 Nanoindentation

Instrumented indentation systems (MTS Nanoindentor XP and CSM Nanohardness tester) were used to record the displacement as a function of load and the hardness and modulus of the coatings calculated using the Oliver-Pharr method [5].

A typical load displacement curve along with the measurable parameters is shown in Fig. 3.5. The hardness in nanoindentation (H) is determined from the load-displacement curves, with the value obtained by dividing the peak indentation load by the projected contact area of the indent.

$$\mathrm{H} = \frac{\mathrm{P_{max}}}{\mathrm{A_C}} \tag{3.1}$$

where, P_{max} and A_C represent the maximum load and the projected contact area between the indenter and sample, respectively. The projected contact area is calculated from the contact depth, h_c, and is discussed later.

The elastic modulus of the sample is obtained from the contact stiffness, $S = \frac{dP}{dH}$

which is calculated from the slope of the initial portion of the unloading curve. This is best described by a power law of the type, $P = B(h - h_f)^m$ where B and m are the fitting parameters and h and h_f are the depth of penetration at measured point and the final depth, respectively.

The stiffness is used to calculate the reduced modulus from the Sneddon's relation:

$$S = 2\beta\sqrt{\frac{A}{\pi}}E_r \tag{3.2}$$

where, S is the stiffness, β is a constant that depends on the geometry of the indenter (b = 1.034 for a Berkovich indenter) and E_r is the reduced elastic modulus [6].

The reduced modulus is given by $\frac{1}{E_r} = \frac{1-\nu^2}{E} + \frac{1-\nu_i^2}{E_i}$ (3.3) where, ν and ν_i and E and E_i, denote the Poisson's ratio and Young's modulus for the sample and the indenter, respectively. The Young's modulus (E_i) and Poission's ratio (ν_i) values for the diamond Berkovich tip were assumed to be 1141 GPa and 0.07, respectively [5]

The projected contact area which is a function of the contact depth can be written as:

$$A_c = C_0\, h_c{}^2 + C_1\, h_c{}^1 + C_2\, h_c{}^{\frac{1}{2}} + C_3\, h_c{}^{\frac{1}{4}} + \cdots + C_8\, h_c{}^{\frac{1}{128}} \qquad (3.4)$$

where, C_0 = 24.56 and C_1- C_8 are constants which vary as per the bluntness of the Berkovich tip.

Thus, the projected contact area A_c is used to obtain the hardness from eq. 3.1, while the stiffness S is used to calculate the modulus of the tested specimen from eqs. 3.2 and 3.3.

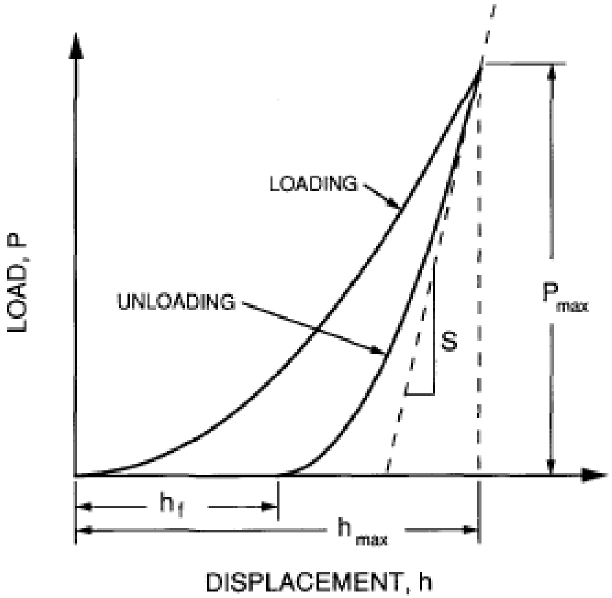

Fig. 3.5 Representation of a typical load-displacement curve. The parameters shown are P_{max}: the peak indentation load; h_{max}: the indenter displacement at peak load; h_f : the final depth of the contact impression after unloading, and S: the initial unloading stiffness [5].

A diamond Berkovich indenter was used for the measurements after carrying out a tip area calibration on a fused silica specimen. All the coating specimens were polished using 0.5 micron diamond paste for a few minutes to remove any droplets on the coating surface since these droplets distort the true value of the mechanical properties. A minimum of 15 indents were then placed at different regions on the surface of each coating sample so as to obtain a statistically significant value. Care was taken to sample only the coating region by limiting the depth of penetration during nanoindentation testing to less than 10 % of the overall coating thickness to avoid the effect of the substrate.

However, the hardness and modulus obtained on multi-layer coatings are a composite value since the individual layers are in the thickness range of 20-100 nm and the effect of multiple layers during the measurements cannot be avoided. The values were also recorded as a function of depth in the coatings by using the continuous stiffness method (CSM). In the CSM method, a small, sinusoidally varying signal is imposed on top of a DC signal that drives the motion of the indenter and a lock-in amplifier is used to analyze the response of the system to obtain the contact stiffness at any point along the loading curve and not just at the point of unloading as in conventional measurements [6].

3.3.2 Modulus mapping

The modulus maps were acquired along with topography data in a Hysitron Triboindentor TI 950 by scanning the diamond tip over the sample with a superimposed small AC sinusoidal force and measuring the resultant amplitude and displacement. The phase and amplitude values were used to calculate the storage stiffness and loss stiffness by applying the known transducer constants of the lock-in amplifier [7]. The storage stiffness and loss stiffness were then used to calculate the complex modulus, which comprises the storage modulus [E'] and loss modulus [E''], using the radius of curvature of the probe determined after mapping the sample [8].

The complex modulus is defined as $E = E' + i\,E''$, (3.5)

where E' is the storage modulus and E'' is the loss modulus and i is the imaginary number, $\sqrt{-1}$. The elastic modulus of coatings is measured in the linear regime under static conditions while the complex modulus is measured under an oscillating force. However, the modulus values measured by both methods were found to match closely [9].

3.3.3 Fracture toughness

Fracture toughness was determined by measuring the lengths of radial cracks generated after Vickers indentation on the coatings, after taking into account the depth of indentation and the coating thickness, based on the formula below [10]:

$$K = \lambda' V^{*} \left(\frac{E}{H}\right)^{\frac{1}{3}} \frac{1}{t} \frac{P}{c^{\frac{1}{2}}} \; ; \; V^{*} = 1 - \frac{(h-t)^{3}}{h^{3}} \qquad (3.6)$$

where $\lambda' = \lambda/\eta$ with $\lambda = 0.013$ in the case of a Vickers indentor and η is the tip shape constant; E is the modulus, H is the hardness, c is the crack length measured from centre of the indent, t is the coating thickness, h is the penetration depth and V^{*} is a multiplication factor.

3.3.4 Adhesion testing

The adhesion of the coatings was studied using a CSM Revetest Nanoscratch tester with a 200 µm spherical diamond tip to carry out progressive load scratch tests in the range 0.9 - 175 N with a fixed scratch length of 4 mm. The ASTM C1624 standard for ceramic coatings was followed during the adhesion testing [11]. The critical loads for failure were determined by identifying the point of first cracking as LC_1- lower critical load and the point of total delamination as the upper critical load- LC_2. These were confirmed from the acoustic and friction signals recorded as well as from direct observation of the scratch track under the optical microscope. Fig. 3.6 shows a typical plot obtained from scratch testing of a coated specimen along with a micrograph of the scratch track. The point of first cracking (LC_1) is marked by a sudden increase in acoustic emission (AE) signal and the point of total delamination (LC_2) is marked by a change in the slope of the friction co-efficient ($f_{co\text{-}eff}$).

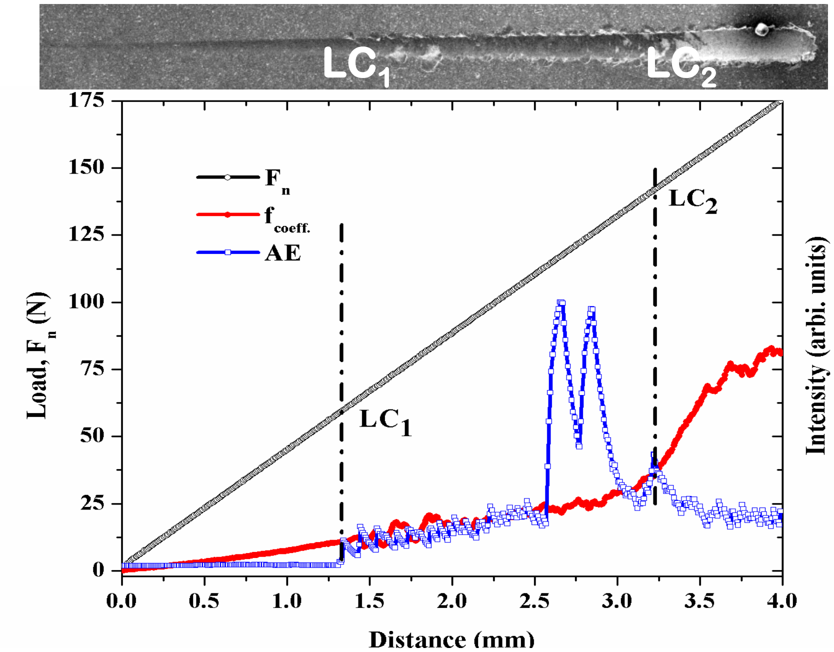

Fig. 3.6 Typical scratch plot showing the variation of acoustic emission and friction co-efficient with increasing load in a progressive load scratch test along with LC1 and LC2.

3.3.5 Nano-impact testing

Nano-impact testing is a rapid indentation technique involving repeated impact at fixed loads for preset time intervals. The high strain rates achievable in this technique can be used to closely simulate actual test conditions, especially in real life applications involving repeated contact such as interrupted cutting during machining where cutting tools experience fatigue due to constant on-off contact with the work piece. This technique has begun to be used to study thin film coatings, especially hard nitride coatings and a close correlation has been found between actual tool life in milling and the impact resistance of these coatings [12]. This provides an advantage as time-consuming industrial machining and testing can be replaced by this simple, laboratory-based impact test which closely simulates conditions seen in real life.

The nano-impact tests were carried out in a Micromaterials Nanotest Vantage unit. The nano-impact test is carried out in the horizontal mode where a diamond indentor fixed to a pendulum is accelerated towards the specimen from a fixed distance at a preset load with the load applied for a preset time. The initial standoff distance can be varied from 1-27 micron by varying the voltage applied to a solenoid electromagnet to pull back the pendulum. This cycle is repeated by setting a fixed frequency which can be varied from 0.25 Hz to several Hz. The capacitor plates measure the penetration depth on the sample at each point which is recorded as a function of the number of impacts and time. Plots of the impact depth vs time (number of impacts) can then be used to identify the final impact depth, the point of cracking and the number of cracking events to estimate the impact resistance of the coatings. The nano-impact tests were carried out with a cube corner indenter at fixed loads ranging from 10 mN to 70 mN for a time period of 180 seconds and a frequency of 0.25 Hz and a distance of 15 μm. A cube corner indenter is used in view of its high sharpness and the ability to generate high strain at low loads.

The crack probability of the coatings can also be estimated in nano-impact tests from the ratio of cracking events to the total number of the tests and is used as a qualitative measure of coating toughness.

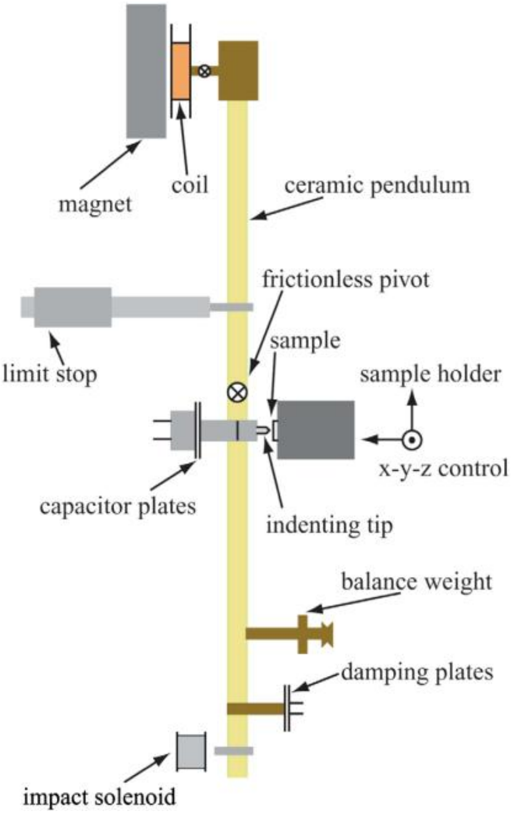

Fig. 3.7 Schematic showing the various parts of the nano-impact module [13].

3.4 Structural characterization

3.4.1 X-ray diffraction

The structural characterization of the coatings was carried out by Grazing Incidence X-Ray Diffraction (GI-XRD) in a Panalytical X′Pert PRO Diffractometer which was also used to estimate the residual stresses in the coatings. Cu-K_α radiation (wavelength 1.54048 Å) was used with the X-ray generator operated at 45 kV at an anode current of 40 mA and a beam size of 2 x 2 mm^2. A PW3011 proportional detector fitted with a parallel plate collimator followed by a Graphite flat plate monochromator was used. The incident angle in GIXRD was chosen after calculating the X-ray penetration depth for the particular coating. The penetration depth was calculated based on the Beer-Lambert's law for a given wavelength λ as below [14]:

$$I(d) = I_0 e^{-\mu\rho d} \qquad (3.7)$$

where d is the length of the path of the X-rays into the material ("distance"), μ is the mass attenuation coefficient ($cm^2.g^{-1}$), which depends on λ, and ρ is the specific mass of the material.

The path length d of the X-rays analyzing a depth x of the sample is given by:

$$d = x.\left(\frac{1}{sin\gamma} + \frac{1}{\sin{(2\theta-\gamma)}}\right) \qquad (3.8)$$

where γ is the angle between the incident beam and the surface of the sample and 2 θ is the deviation of the beam. In the case of Bragg-Brentano geometry, $\gamma = \theta$ so d = 2x/sin θ.

The depth of penetration x is then calculated by substituting for d in equation 3.7:

$$I(x) = I_1.\left[1 - exp\left(-\mu.\rho.x.\left(\frac{1}{sin\gamma} + \frac{1}{\sin{(2\theta-\gamma)}}\right)\right)\right] \qquad (3.9)$$

where I_1 is the total intensity collected by the detector.

The depth of X-ray penetration was calculated after taking into account the coating density and the mass attenuation co-efficient. A glancing incidence angle of 4^o was then chosen to obtain a sufficient intensity for the coating peaks while at the same time avoid any occurrence of substrate peaks.

The interplanar spacings ‘d’ were calculated using Bragg’s law from the 2θ peak positions corresponding to the respective planes. The phases were then identified by comparing and matching the obtained lattice spacings with reference values in the ICDD PDF4+ database.

The precise lattice parameter was determined by using the Nelson-Riley method [15] using the extrapolation function: $\left(\frac{cos^2\,\theta}{\sin\theta} + \frac{cos^2\,\theta}{\theta}\right)$

A linear fit between the lattice parameters and the Nelson-Riley function was obtained for each diffraction angle θ and the intercept on the y axis was considered as the precise lattice parameter.

The crystallite size D was determined from the Scherrer’s formula [16]:

$$B = \frac{k\lambda}{D\ cos\theta}$$

where B is the full width at half maximum of the diffracting peak, , k is a constant, λ is the X-ray wavelength, and θ is the Bragg angle. The crystallite size was calculated after subtracting the contribution from instrumental broadening which was determined from X-ray measurements on LaB_6 powder.

The texture co-efficients were determined using the formula from the Harris Inverse Pole Figure technique as below [17]:

$$\boldsymbol{T}^{*} = \frac{\frac{\boldsymbol{I}_{(\boldsymbol{hkl})}}{\boldsymbol{R}_{(\boldsymbol{hkl})}}}{\left(\frac{\mathbf{1}}{\boldsymbol{n}}\right)\sum_{\mathbf{0}}^{\boldsymbol{n}}\frac{\boldsymbol{I}_{(\boldsymbol{hkl})}}{\boldsymbol{R}_{(\boldsymbol{hkl})}}}$$

where $I_{(hkl)}$ and $R_{(hkl)}$ are the intensities from the (hkl) reflections in the specimen and a random powder, respectively, and n is the number of reflections considered. A T* value of unity denotes a random orientation, while T* values greater than unity imply that the plane has a preferred orientation.

3.4.2 Residual stress

Residual stress measurements were carried out by XRD using the $\sin^2\psi$ method [18]. Strain in the sample due to the presence of stresses is reflected as a change in lattice spacing. Stresses present in the sample can vary about the angle ψ which is the angle between the surface normal and the incident and diffracted beams. Rotation of the sample about ψ can either expand or contract the lattice depending on whether the stress is tensile or compressive. Measuring the change in the angular position of the diffraction peak for atleast two orientations of the sample enables calculation of the stress in the sample surface lying in the plane of diffraction. The stress in different directions at a specific {h,k,l} reflection can be measured by rotating the sample at several (ψ, φ) angles about its surface normal so that the direction coincides with the diffraction plane [19]. The lattice strain $\varepsilon_{\psi,\varphi}^{\mathrm{hkl}} = \frac{(d_{\psi,\varphi}^{\mathrm{hkl}} - \mathrm{d}_0)}{\mathrm{d}_0}$ can be calculated at every tilt and rotation ϕ angle, where $d_{\psi,\varphi}^{\mathrm{hkl}}$ is the interplanar spacing for the {h,k,l} reflection and d_0 is the stress-free interplanar spacing. The stress tensor can then be calculated from classical strain and stress analysis (linear elasticity theory) where the formula for triaxial case is given by [20]:

$$\frac{(d_{\psi,\varphi}^{\mathrm{hkl}} - \mathrm{d}_0)}{\mathrm{d}_0} = \mathrm{S}_1[\sigma_{11} + \sigma_{22} + \sigma_{33}] + \frac{\mathrm{S}_2}{2}\sigma_{33} + \frac{\mathrm{S}_2}{2}[\sigma_{11}\cos^2\varphi + \sigma_{22}\sin^2\varphi + \sigma_{12}\sin(2\varphi) - \sigma_{33}]\sin^2\psi + \frac{\mathrm{S}_2}{2}[\sigma_{13}\cos\varphi + \sigma_{23}\sin\varphi]\sin(2\psi)$$

Where S_1 and $\frac{\mathrm{S}_2}{2}$ are the X-ray elastic constants (XECs).

For a bi-axial stress state $\sigma_{33} = 0$ and the formula reduces to:

$$\frac{(d_{\psi,\varphi}^{\mathrm{hkl}} - \mathrm{d}_0)}{\mathrm{d}_0} = \mathrm{S}_1[\sigma_{11} + \sigma_{22}] + \frac{\mathrm{S}_2}{2}[\sigma_{11}\cos^2\varphi + \sigma_{22}\sin^2\varphi + \sigma_{12}\sin(2\varphi) - \sigma_{33}]\sin^2\psi + \frac{\mathrm{S}_2}{2}[\sigma_{13}\cos\varphi + \sigma_{23}\sin\varphi]\sin(2\psi)$$

which can be written as

$$\frac{(d_{\psi,\varphi}^{\mathrm{hkl}} - \mathrm{d}_0)}{\mathrm{d}_0} = \mathrm{S}_1[\sigma_{11} + \sigma_{22}] + \frac{\mathrm{S}_2}{2}[\tau_{\varphi}]\sin(2\psi) + \frac{\mathrm{S}_2}{2}[\sigma_{\varphi}]\sin^2\psi$$

where , the measured normal stress $\sigma_{\varphi} = \sigma_{11}\cos^2\varphi + \sigma_{22}\sin^2\varphi + \sigma_{12}\sin(2\varphi)$, the measured shear stress $\tau_{\varphi} = [\sigma_{13} \cos \varphi + \sigma_{23} \sin \varphi]$,

and the normal and shear stress tensor components are σ_{ii} and σ_{ij}, respectively.

A plot of $d^{\mathrm{hkl}}_{\psi,\varphi}$ vs $\sin^2\psi$ is used to determine the stress with the slope giving the normal stress. The shear stresses given by $\sigma_{13}$and σ_{23} show up as ψ-splitting in the curve if present. In the absence of shear stresses, a bi-axial stress state is assumed with the normal stress component σ_{33} set to zero. The stresses σ_{φ} and τ_{φ} are evaluated from the X-ray elastic constants with $S_1 = \frac{\nu}{E}$ and $S_2 = \frac{1+\nu}{E}$ where ν is the Poisson's ratio and E the modulus of the material [18]. The stress sum, $[\sigma_{11} + \sigma_{22}]$ is evaluated from S_1 and d_0. The stress-free d-spacing d_0 in the formulae above can be calculated from the corresponding strain-free $\sin^2\psi$ value by interpolation via the fitted straight line in the d_{ψ} vs. $\sin^2\psi$ plot.

Though it is recommended to perform stress measurements for peaks at higher diffraction angles ($2\theta > 100^{o}$) as the angular resolution increases with θ; in the present study, a diffraction angle peak, (220) occurring at 62^{o} was chosen since higher angle reflections were suppressed in the present coatings. The lattice strain was first determined from 15 measurements of the (220) peak at three different φ angles at several ψ tilts in the range ± 60 degrees and the stress calculated from the X-ray elastic constants to obtain the stress tensor. The X-ray elastic constants were calculated using the elastic modulus of each coating as determined from nanoindentation. A biaxial stress state was considered for the coatings with the normal stress component σ_{33} equal to zero, since the stress components σ_{11} and σ_{22} were almost equal and the shear stresses are negligible with no ψ splitting observed and an isotropic in-plane stress was assumed for all the coatings.

3.4.3 Scanning electron microscopy and energy dispersive spectroscopy

Scanning electron microscopy (SEM) was used to study the surface morphology of the coatings and for carrying out energy dispersive spectroscopy (EDS). SEM imaging was carried out in two modes: SE and BSE using the different electrons which are generated on interaction of the incident electron beam with the specimen. SE imaging uses secondary electrons and gives topographic contrast of surface features while BSE imaging uses backscattered electrons which give compositional contrast as the BSE electrons are proportional to the atomic number, Z. EDS was used for identification of the coating composition where the energy of the X-rays generated is measured to identify the elements present in the specimen. Quantification of the elements present was carried out using ZAF standardless quantification. Imaging at lower magnifications was carried out in a conventional SEM with a thermionic tungsten filament (Hitachi S-3400N), while imaging at higher magnifications was carried out in a field emission SEM (Hitachi S-4300 SE/N). The elemental composition of the coatings was determined using a Thermo Electron EDS system. All the elemental composition values reported in the thesis are in atomic %. The reported elemental quantifications for the coatings are only for the cationic species without considering the nitrogen in the coatings since nitrogen quantification is not accurate in EDS.

3.4.4 Electron backscatter diffraction (EBSD)

Electron backscattered diffraction (EBSD), also known as orientation imaging microscopy (OIM) was used to determine the crystallographic orientations of the grains and to carry out electron micro-diffraction. OIM further enables the study of grain shape and size, the angular relationships between different grains and grain boundary character distribution. Electron micro-diffraction provides a simple method for obtaining local crystallographic information without the need for complex synchrotron sources. In electron micro-diffraction, the phases at different regions on the coating cross section were identified by recording EDS data and electron back-scatter patterns (EBSPs) at that location. This was carried out using DELPHI®, proprietary software from EDAX-TSL, where EDS data was first collected and the ICDD Database looked up for phases which are possible with the combination of elements detected. The recorded EBSP is then run and checked against the list of phases generated from the EDS data and the ICDD database for a best possible match.

In OIM, the specimen is first tilted to 70° and the electron beam is scanned across the region of interest with a fixed step size. The EBSPs at each point of the scan recorded on a Phosphor screen connected to a CCD camera. Once the bands are detected, the reflecting planes associated with the detected bands are indentified by comparing the interplanar angles between the bands with a theoretical look up table of interplanar angles to find the most likely reflecting plane by using a voting scheme. In the present study, the EBSD scans were recorded using a Digiview EBSD camera in the Hitachi S-4300 SE/N field emission scanning electron microscope (FE-SEM). The orientation data analysis was carried out using OIM analysis 5.0 software.

3.4.5 Focused ion beam (FIB) milling

Focused ion beam milling was carried out to reveal the cross section of the coating, followed by imaging using the ion beam and the electron beam. Ga^+ ions were used for milling in view of their sufficiently high mass which can give a good sputtering rate and their non-reactive nature with most materials. The use of a FIB permits preparation of cross sections and site-specific TEM specimens from hard coatings for which traditional polishing and ion milling are not well suited [21,22]. The use of FIB for study of the coatings is advantageous in that there is no loss of features in the coating cross section as seen in edge chipping and rounding during mechanical preparation and can also be used to ascertain coating defects and observe their microstructure across the entire coating thickness including the interface with the substrate.

In the present study, the samples were prepared in a Carl Zeiss Neon 40 dual beam microscope equipped with a Ga ion source and a field emission electron source. The specimen was first tilted to 54° to bring it to the eucentric position and to align it with the ion beam. The coatings were then milled with a 2 nA current followed by finer milling at 500 pA to obtain a smooth cross section, which was then imaged by the electron beam at 54°. For imaging with the ion beam, the specimen was brought to the zero tilt position so that the cross section is viewable with the ion beam. Imaging with the ion beam gives rise to images with ion channelling contrast that can be used to distinguish different grains, especially those with different orientations. In channelling, the incident ion beam travels deep into the sample with little hindrance when it is parallel to certain crystal planes. Grain contrast is observed as a result of the variation in the secondary electron yield from different grains. When the ion beam travels parallel to a crystal plane it channels deep into the material and as a result fewer secondary electrons are emitted. Thus, if a grain has a strong channelling orientation, it appears dark and if a grain exhibits little or no channelling it appears bright in the ion image.

The FIB was also used for preparation of site-specific TEM specimens from the final optimized multi-layer coating using the FIB lift out technique [23]. The in-situ lift out technique is especially useful in the preparation of cross sectional specimens from coatings. The steps involved in the preparation of the TEM specimen from the coating are as follows and are also shown in Fig. 3.8. A region of interest (ROI) on the coating was first identified and a protective strip of Pt or W was deposited over it. Trapezoidal trenches were then milled on either side of the

ROI to create a lamella after which rectangular cuts were made at the base of the lamella and at the sides, with one cut on the side that is left incomplete for support. A micromanipulator tip was attached to the lamella by Pt deposition and a final cut made to free the lamella. The freed lamella was attached to a TEM grid and further thinned using the ion beam until electron transparency was achieved.

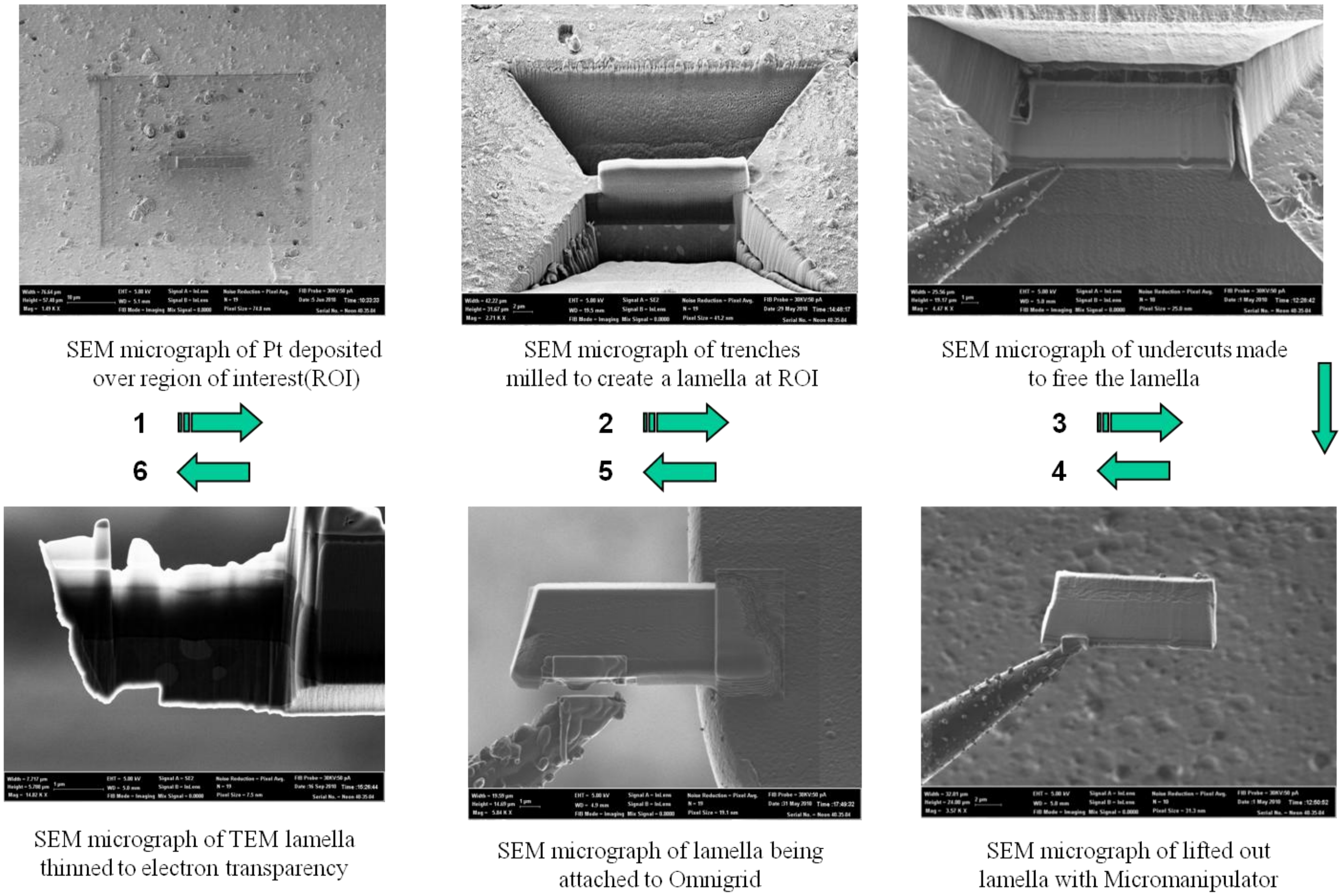
SEM micrograph of Pt deposited over region of interest(ROI)

SEM micrograph of trenches milled to create a lamella at ROI

SEM micrograph of undercuts made to free the lamella

SEM micrograph of TEM lamella thinned to electron transparency

SEM micrograph of lamella being attached to Omnigrid

SEM micrograph of lifted out lamella with Micromanipulator

Fig. 3.8 Micrographs showing the different steps involved in the FIB lift out technique.

3.4.6 Transmission electron microscopy (TEM)

TEM is a powerful tool to obtain high resolution microstructural and structural information and is especially useful in the study of nanostructured PVD coatings. The high resolution of the beam is due to short wavelength of the electrons at high acceleration voltages. In the present study, a 200 kV beam in a FEI Tecnai G^2 microscope was used for both plan view and cross sectional TEM (XTEM) observations of the coatings. Bright field (BF) and dark field (DF) micrographs were recorded by selecting the transmitted beam and the diffracted beams, respectively, using an objective aperture. Selected area diffraction (SAED) patterns were recorded by using an aperture to limit the beam size on the specimen. In the present case, as the coatings are nanocrystalline, ring patterns were obtained and indexed. The interplanar spacings, d were calculated from the ring patterns using the relation [24]:

$$\lambda L = rd$$

where L is the camera length, λ is the wavelength of the electron beam and r is the radius of the ring in the diffraction pattern.

HRTEM imaging was carried out to observe the fine structural details such as the lattice planes, grain boundaries and interfaces of the coatings, especially in case of the nanocomposite coatings. The images were recorded on a bottom-mounted Gatan CCD camera. Fast Fourier Transform (FFT) of the images was carried out using the Digital Micrograph software in order to measure the lattice spacings and identify phases in the coatings.

3.4.7 HAADF-STEM (Z-contrast imaging)

High angle annular dark-field (HAADF) imaging was carried out to obtain Z-contrast images from a few selected coating specimens. As the images are formed from incoherently elastically scattered electrons, the image formed is representative of the atomic number of the elements in the sample. The intensity of the scattered electrons I is directly proportional to the square of the atomic number, Z^2 [25]. The HAADF images were recorded in the scanning transmission electron microscopy (STEM) mode where an annular detector was used to capture the high angle elastically scattered electrons.

3.4.8 X-ray photoelectron spectroscopy (XPS)

X-ray photoelectron spectroscopy (XPS) measurements were carried out in an Omicron system with Argon ion etching prior to acquiring spectra. The obtained spectra were deconvoluted and fitted to identify the binding energy states and the oxidation states of various elements present in the coatings were assigned.

3.4.9 In-situ synchrotron XRD

In-situ Synchrotron XRD studies were carried out at high temperature to ascertain the thermal stability of the nanocomposite TiAlCrSiN coatings. The measurements were carried out at the Indian Beamline 18B, Photon Factory at Tsukuba, Japan. An Anton Paar heating stage was used to heat the coating samples in an Argon atmosphere and measurements were performed at an energy of 13.0 keV, which corresponds to an incident wave length (λ) of 0.95 Å with data collected at room temperature (RT), 40°C, 800°C, 900°C and 1000°C.

3.5 Thermogravimetric analysis (TGA)

The oxidation resistance and thermal stability of the TiAlCrSiN nanocomposite coatings was assessed by carrying out thermogravimetry studies. A differential thermal analyzer (STA 449 F3 Jupiter, NETZSCH), was used to carry out the TGA measurements. The coating samples were heated at a rate of 10°C/min from room temperature up to 1300°C under air and the mass change measured as a function of temperature.

References

[1] Mattox, D. M., Handbook of physical vapor deposition (PVD) processing, (2010) 287–300, William Andrew Publishing.

[2] Anders A, “Cathodic Arcs- From Fractal Spots to Energetic Condensation”, Springer Series on Atomic, Optical, and Plasma Physics, 2008.

[3] Platit π300 Operation Manual.

[4] Fleming M. G., Hashmi M. S. J., A comparison of Magnetron Sputtered and Arc Evaporated PVD thin films for wear applications in multipoint cutting tools, Journal of Materials Processing Technology, 32 (1992) 481-488.

[5] Oliver, W.C. , Pharr, G.M., Improved technique for determining hardness and elastic modulus using load and displacement sensing indentation experiments, Journal of Materials Research, 7 (1992) 1564-1583.

[6] Li, X. , Bhushan, B. A review of nanoindentation continuous stiffness measurement technique and its applications, Materials Characterization, 48 (2002) 11–36.

[7] Syed Asif SA, Wahl KJ, Colton RJ, Nanoindentation and contact stiffness measurement using force modulation with a capacitive load-displacement transducer, Review of Scientific Instruments, 70 (1999) 2408-2413.

[8] Hysitron TI 950 nano-DMA user manual.

[9] Syed Asif SA, Wahl KJ, Colton RJ, Warren OL. Quantitative imaging of nanoscale mechanical properties using hybrid nanoindentation and force modulation, Journal of Applied Physics, 90 (2001) 1192-1200.

[10] Jungk, J.M. , Boyce, B.L., Buchheit, T.E., Friedmann, T.A., Yang, D. W.W. Gerberich, Indentation fracture toughness and acoustic energy release in tetrahedral amorphous carbon diamond-like thin films, Acta Materialia, 54 (2006) 4043–4052.

[11] ASTM Standard Test Method for Adhesion Strength and Mechanical Failure modes of Ceramic Coatings by Quantitative Single Point Scratch Testing: C 1624-05.

[12] Beake B. D., Fox-Rabinovich G. S., Veldhuis S. C., Goodes S. R., Coating optimisation for high speed machining with advanced nanomechanical test methods, Surface and Coatings Technology, 203(13) (2009) 1919-1925.

[13] Wheeler, J.M., Gunner, A.G., Analysis of failure modes under nano-impact fatigue of coatings via high-speed sampling, Surface and Coatings Technology, 232 (2013) 264–268.

[14] AbsorbX Notes, Bruker D8 User manual.

[15] Suryanarayana, C., Grant Norton, M., X-Ray Diffraction- A Practical Approach, New York: Plenum Press; 1998.

[16] H.P. Klug, L.E. Alexander, X-ray Diffraction Procedures for Polycrystalline and Amorphous Materials, New York: John Wiley & Sons, 1974.

[17] Lewis, D.B., Luo, Q., Hovsepian, P.Eh., Munz, W.-D., Interrelationship between atomic species, bias voltage, texture and microstructure of nano-scale multilayers, Surface and Coatings Technology, 184 (2004) 225–232.

[18] Prevey, P. S., X-Ray Diffraction Residual Stress Techniques, in: ASM Hand Book, 10, ASM International, Ohio, 1986, 380-392.

[19] Abadias, G., Stress and preferred orientation in nitride-based PVD coatings, Surface and Coatings Technology, 202 (2008) 2223–2235.

[20] X'Pert Stress Manual, Panalytical X'pert PRO system.

[21] Munroe PR. The Application of Focused Ion Beam Microscopy in the Material Sciences, Materials Characterization, 60 (2009) 2–13.

[22] Cairney JM, Munroe PR, Hoffman M. The application of focused ion beam technology to the characterization of coatings, Surface and Coatings Technology, 198 (2005) 165-168.

[23] Giannuzzi, L. A., Stevie, F. A., A review of focused ion beam milling techniques for TEM specimen preparation. Micron, 30(3) (1999) 197-204.

[24] Brandon DG, Kaplan WD. Microstructural Characterization of Materials.2nd edition. West Sussex: John Wiley and Sons Ltd; 2008.

[25] Pennycook, S. J., Jesson, D. E., High-resolution Z-contrast imaging of crystals, Ultramicroscopy, 37(1) (1991) 14-38.

Chapter 4 Role of TiN as an adhesive layer

4.1 Introduction

PVD coatings on cutting tools have been known to increase the tool life and improve productivity in metal cutting operations during manufacturing. The wear resistance and the life of the coatings is dependent on fundamental coating properties -chemical, thermal, mechanical aspects which further control phenomena such as work piece compatibility, thermal stability and coating adhesion, respectively. Coating to substrate adhesion is an important property, since premature coating chipping due to poor adhesion could create debris which may cause aggravated wear of the substrate material and shortens tool life [1]. In this light, there have been various efforts to enhance the adhesion of coatings including ion etching, addition of interfacial layers, increasing bias voltage and substrate temperatures during deposition and creation of low energy interfaces via structural matching of coating and substrate [2]. Ion etching prior to deposition improves adhesion by removal of any adsorbed impurities from the substrate surface while addition of interlayers enhances adhesion by reducing the mismatch in mechanical and thermal properties between coating and substrate [3]. There have been a few reports where deposition of metallic interlayers such as Ti [4-6], Cr [7, 8] and TiN [9-11] as underlayers for thicker coatings significantly improved adhesion. Nowadays, many commercially available tool coatings make use of an adhesive layer below the main coating layer for improved coating life. However, the role of such a layer, the exact thickness needed and other aspects are usually not disclosed by the manufacturers. In the present chapter, the function of TiN as an adhesive layer was evaluated and an optimum thickness was identified.

4.2 Deposition

Monolithic TiN coatings were first deposited and characterized by XRD and SEM. Scratch testing was used to determine the adhesion strength of the coatings. The role of TiN as an adhesive underlayer was then studied by depositing TiAlN coatings with and without TiN as an underlayer and studying the difference in adhesion. The effect of varying thickness of the TiN layer on the adhesion properties of TiAlN was also evaluated.

TiN coatings were deposited on high speed steel (HSS) substrates with the deposition parameters kept fixed as given in chapter 3. The crystal structure of TiN was found to have a NaCl type FCC structure; more details on the XRD and residual stress analysis are given in chapter 5. The cross section of the TiN coating was studied after FIB milling and is shown in Fig. 4.1(a). The coating showed a columnar grain structure with a smooth interface between the coating and substrate. In order to study the effect and role of TiN on adhesion, TiAlN coatings with three different thicknesses of TiN as an underlayer and a TiAlN coating without a TiN underlayer were then deposited. All the coatings had the initial predeposition steps of argon etching and Ti metal ion etching prior to the actual coating step. Fig.4.1(b) shows the cross section of the TiAlN coating with a ~100 nm thick underlayer. Interlayer bonding between the TiAlN and the TiN layers was found to be good, with the grain structure in the TiAlN layer also being columnar.

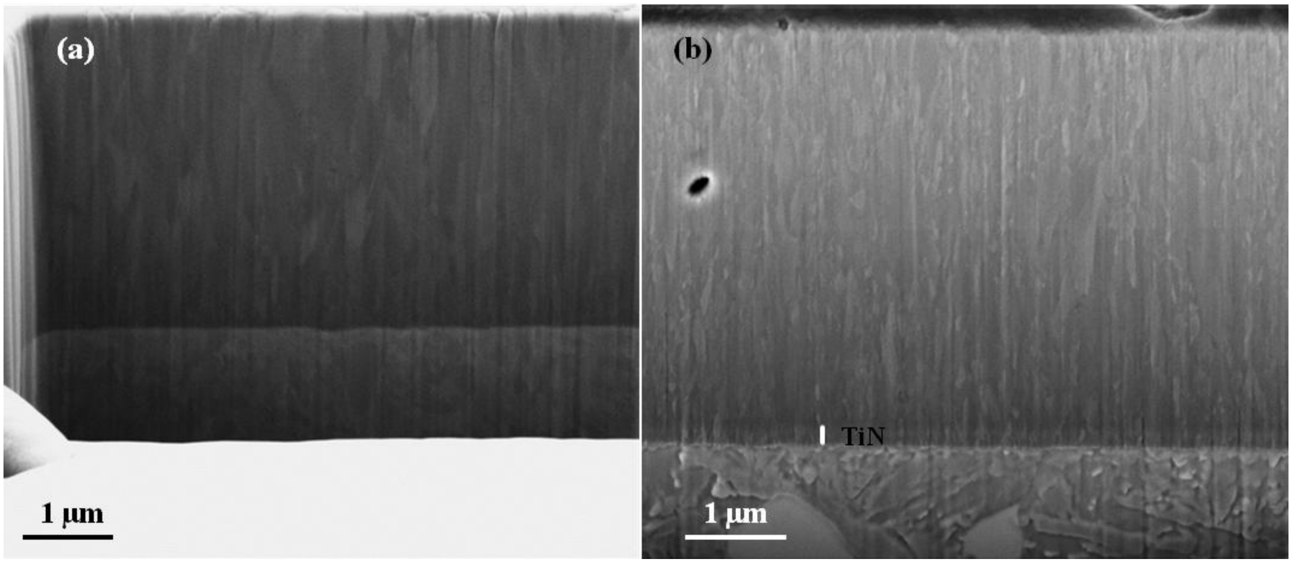

Fig. 4.1 Cross sectional SEM micrographs of (a) TiN coating and (b) TiAlN coating with TiN underlayer showing a columnar grain structure in both the coatings.

4.3 Adhesion studies

Scratch testing was then carried out on three TiAlN coatings with varying thicknesses of the TiN underlayer and on the TiAlN coating without a TiN underlayer. Fig.4.2 shows the variation in adhesion (critical loads) of the TiAlN coating with varying thicknesses of the TiN underlayer and without the TiN underlayer (denoted as TiAlN w. TiN and TiAlN w/o. TiN, respectively). The adhesion increased with increasing TiN layer thickness with the maximum LC_2 value of 134.5

observed at a thickness of 100 nm and a drop of ~ 11 % in LC_2 at a thickness of 200 nm. There was ~ 21 % and ~ 16 % increase in the lower (LC_1) and upper critical load values (LC_2) in case of TiAlN with a 100 nm TiN underlayer over the TiAlN w/o. TiN coating.

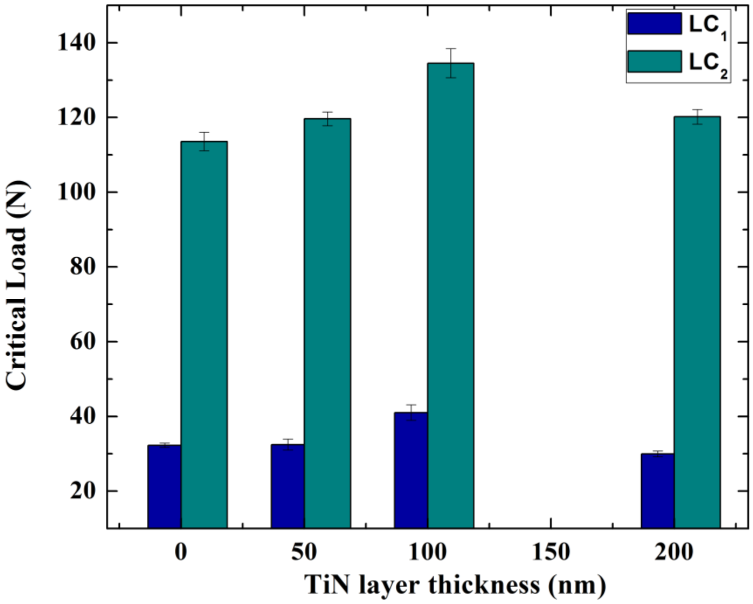

Fig. 4.2 Variation of critical loads (LC_1 and LC_2) in TiAlN with varying TiN underlayer thickness and without a TiN underlayer.

Panoramic images of the scratch tracks were recorded after scratch testing in order to visually observe the point of first cracking (LC_1) and delamination (LC_2) and identify changes in deformation. Fig. 4.4 shows optical micrographs of three TiAlN coatings which illustrate clearly the differences in adhesion as seen from different locations of the LC_1 and LC_2 points on the scratch track. The TiAlN w/o.TiN coating shows the least adhesion (113.6 N) while highest adhesion is shown by the TiAlN coating (134.5 N) with a 100 nm thick TiN underlayer. The coating with a 200 nm thick underlayer showed a reduction in adhesion (120.2 N) as seen in the earlier appearance of delamination on the scratch track.

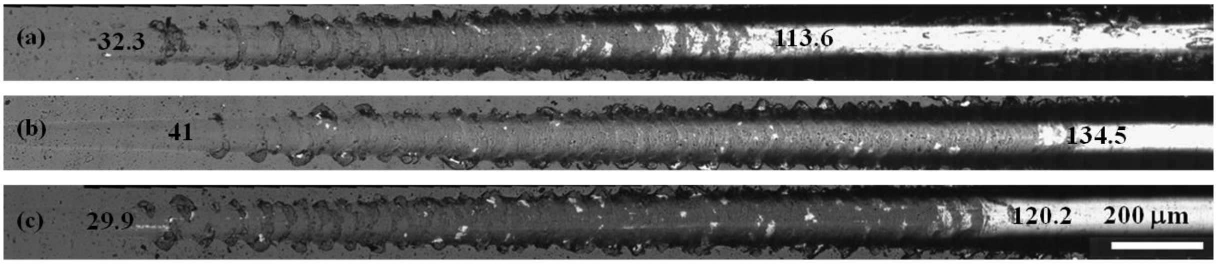

Fig. 4.3 Optical micrographs of scratch tracks showing differences in adhesion (LC_1 and LC_2) in (a) TiAlN coating without a TiN underlayer (b) TiAlN coating with 100 nm thick TiN underlayer and (c) TiAlN coating with 200 nm thick TiN underlayer.

4.4 Conclusions

The improvement in adhesion on addition of the TiN underlayer can be attributed to two effects: i) reduction of thermal expansion mismatch between TiAlN and the HSS substrate (TiN has a co-efficient of thermal expansion (CTE) of $9.4 \times 10^{-6}\ K^{-1}$ with the value in between the CTE of TiAlN ($7.5 \times 10^{-6}\ K^{-1}$) and HSS ($11.7 \times 10^{-6}\ K^{-1}$) [12] and ii) TiN reduces interfacial stresses at the coating–substrate interface by acting as a seed layer for growth of the TiAlN layer [10].

In summary, the presence of TiN was found to distinctly improve adhesion strength by approximately 21 % as determined from scratch testing and a desired thickness of TiN identified for optimum adhesion. A thickness of 100 nm in the TiN underlayer was found to provide good adhesion strength and was fixed as an optimum value for all the subsequent coatings studied. Henceforth, all the TiAlN coatings and the multi-functional, multi-layer coatings in this study were deposited with a 100 nm thick TiN underlayer for good adhesion and, thereby, probably improve the coating life.

References

[1] Hogmark, S., Jacobson, S., Larsson, M., Wiklund, U. Mechanical and tribological requirements and evaluation of coating composites. In : Modern tribology handbook, 2, CRC Press; 2001, p. 931-960.

[2] Holmberg, K., Matthews, A. Tribological properties of metallic and ceramic coatings. In : Modern tribology handbook, 2, CRC Press; 2001, p.827-870.

[3] Helmersson, U., Johansson, B. O., Sundgren, J. E., Hentzell, H. T. G., Billgren, P. Adhesion of titanium nitride coatings on high speed steels. Journal of Vacuum Science and Technology A, 3(2), (1985) 308-315.

[4] Cheng, C. C., Erdemir, A., Fenske, G. R. Correlation of interface structure with adhesive strength of ion-plated TiN hard coatings. Surface and Coatings Technology, 39 (1989) 365-376.

[5] Barshilia, H. C., Yogesh, K., Rajam, K.S., Deposition of TiAlN coatings using reactive bipolar-pulsed direct current unbalanced magnetron sputtering.Vacuum, 83(2) (2008) 427-434.

[6] Gerth, J., Wiklund, U. The influence of metallic interlayers on the adhesion of PVD TiN coatings on high-speed steel. Wear, 264(9) (2008) 885-892.

[7] Barshilia, H. C., Prakash, M. S., Jain, A., Rajam, K. S. Structure, hardness and thermal stability of TiAlN and nanolayered TiAlN/CrN multilayer films. Vacuum, 77(2) (2005)169-179.

[8] Du, H., Zhao, H., Xiong, J., Xian, G. Effect of interlayers on the structure and properties of TiAlN based coatings on WC-Co cemented carbide substrate. International Journal of Refractory Metals and Hard Materials, 37 (2013) 60-66.

[9] Wang, D. Y., Chang, C. L., Wong, K. W., Li, Y. W., Ho, W. Y. Improvement of the interfacial integrity of (Ti, Al) N hard coatings deposited on high speed steel cutting tools. Surface and Coatings Technology, 120 (1999) 388-394.

[10] Wu, S. K., Lin, H. C., Liu, P. L. An investigation of unbalanced-magnetron sputtered TiAlN films on SKH51 high-speed steel. Surface and Coatings Technology, 124(2), (2000) 97-103.

[11] Vereschaka, A. A. Improvement of working efficiency of cutting tools by modifying its surface properties by application of wear-resistant complexes. Advanced Materials Research, Vol. 712 (2013) 347-351.

[12] PalDey, S. C., Deevi, S. C. Single layer and multilayer wear resistant coatings of (Ti, Al) N: a review. Materials Science and Engineering: A, 342(1), (2003) 58-79.

Chapter 5 $Ti_{1-x}Al_xN$ coatings: Role of composition and microstructure on fracture toughness and impact resistance

5.1 Introduction

Titanium and chromium based nitrides find use as wear resistant coatings for cutting and forming tools and also in many other tribological applications [1, 2]. Binary nitrides such as TiN and CrN comprise the first generation of nitride coatings [3], while the second generation ternary coatings like TiAlN are known to provide improved performance due to their superior wear and oxidation resistance as well as thermal stability [3-6]. There have been continuous efforts to further enhance the performance of these coatings through various means, including designing their architecture in the form of nanocrystalline, nanocomposite and/or multi-layer coatings [7, 8]. The mechanical properties of these coatings are also known to be significantly influenced by the crystal structure, composition and microstructure of the coatings [9]. Consequently, there exists an opportunity to enhance the coating performance by either tailoring the composition through addition of alloying elements to achieve different stoichiometries, engineering the microstructure through introduction of nanosized grains or creating a nanocomposite structure.

TiAlN coatings have retained their technological importance by virtue of their high temperature resistance and age hardenability at certain compositions (in the range 52 -70 % Al), which are of both scientific and industrial interest [10-13]. The importance of TiAlN coatings can be gauged from the fact that, even in the use of the new generation nanocomposite coatings such as TiAlN/Si_3N_4, TiAlN is used as an underlayer in order to increase the fatigue and impact resistance of the overall coating system in view of its higher ductility when compared to nanocomposite coatings [14]. Hence, improving the toughness of TiAlN coatings can have important implications in increasing the life of coated tools. The effect of Al content in TiAlN coatings on its mechanical properties has been studied by several researchers [15-22]. Many studies dealing with high temperature behaviour [23, 24] and spinodal decomposition of these coatings [13, 25] as well as on their optical properties [26-29], have also been reported. The percentage of Al in TiAlN is known to influence the crystal structure and lattice parameters which, in turn, determine the hardness and modulus of the coating [3, 6, 10]. Earlier studies on

TiAlN coatings have further reported that the wear resistance [16], residual stress [16, 17] as well as machining life [18] of these coatings is also governed by the Al content.

Notwithstanding the above, only a few detailed studies investigating the toughness and impact resistance of monolithic $Ti_{1-x}Al_xN$ coatings and their variation with Al content are available [20,30,48] although there exist studies on *ab initio* models for improving the toughness through alloying of TiAlN with other transition metals [31] .

As part of the present study, the mechanical properties (indentation, scratch behaviour and toughness) of $Ti_{1-x}Al_xN$ coatings were investigated. The role of bias voltage used during coating deposition as well as the coating composition was specifically assessed and correlated with the crystal structure and microstructure of the coatings. The toughness, sub-surface deformation during scratch testing and impact resistance with changing $Ti_{1-x}Al_xN$ composition has also been studied.

5.2 Effect of bias voltage on coating properties

The bias voltage applied to the substrate during deposition influences the coating properties by affecting its structure [32]. It has been reported that substrate bias affects the mobility of the ionic species during deposition of coatings and, hence, their microstructure and hardness [17]. Assessment of the effect of bias voltage was undertaken as a preliminary study in order to find an optimum value of substrate bias at which good properties could be achieved, so that it could subsequently be used for deposition of all monolithic and multi-layer coatings in the current study.

5.2.1 Crystal structure

The coatings were deposited at fixed negative bias voltages of 50,100, 150 and 200 V with all other conditions being maintained as in Chapter 3. The composition of the coatings as determined from EDS was found to be $Ti_{0.54}Al_{0.46}N$ with no significant variation in elemental concentrations observed with increasing bias. All the coatings discussed in Section 5.2 have a composition close to $Ti_{0.54}Al_{0.46}N$ and are referred to as TiAlN throughout this section. Grazing incidence X-ray diffractograms and texture coefficients of the TiAlN coatings deposited at different bias voltages are shown in Fig.5.1. All the coatings showed a NaCl FCC structure closely matching with FCC $Ti_{0.5}Al_{0.5}N$ [33]. As seen in Fig. 5.1 (a) at – 50V, TiAlN exhibits a dominant (200) peak while coatings deposited at higher bias voltages are characterized by a progressively increasing (111) peak. Comparing the texture co-efficients of the (1 1 1), (2 0 0), (2 2 0) and (311) peaks which are shown in Fig. 5.1 (b), a definite change in texture from (200) at -50 V to (111) at -150 V was noted while there was no texture observed in the coating at -200 V. There is fall in the (200) texture as the (111) texture increases up to -150 V. There appears to be a competition between the growth modes with bias voltage with the texture co-efficients being nearly equal for the (220) and (200) planes at -100 V and the (111) and (220) planes at -150 V.

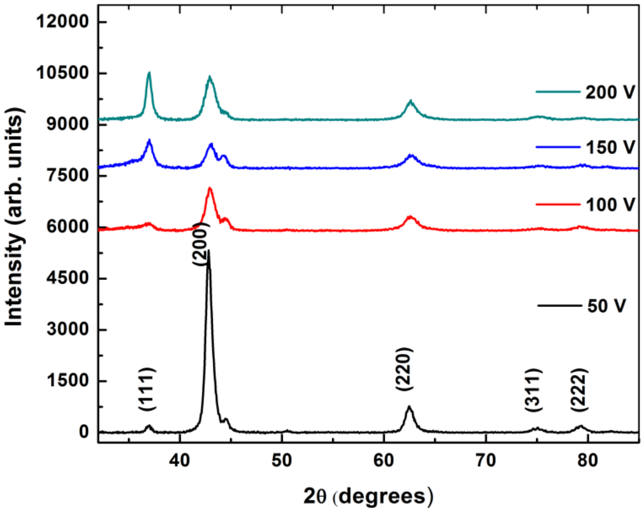

Fig. 5.1 (a) X-ray diffractograms of TiAlN coatings deposited at varied bias voltages.

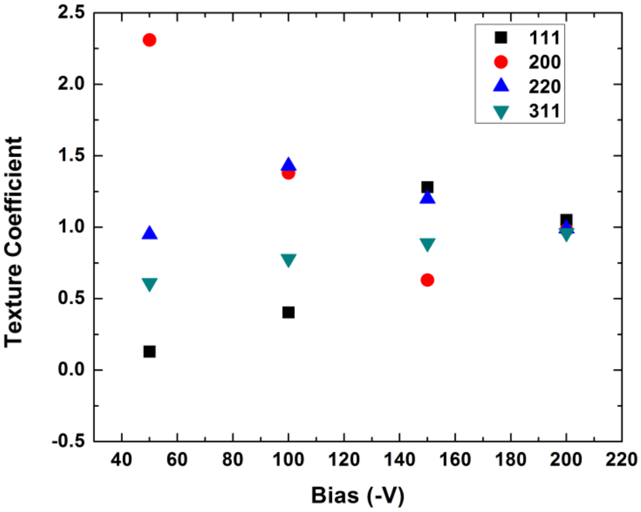

Fig. 5.1 (b) Texture co-efficients of TiAlN coatings deposited at varied bias voltages.

5.2.2 Hardness and modulus

The hardness and modulus of the coatings are shown in Fig. 5.2. At -50 V, the TiAlN coating is found to have a hardness of 34.5 ± 1.15 GPa and a modulus of 416 ± 10.8 GPa. There is a drop in hardness and modulus at -100 V followed by a subsequent gradual increase to a maximum hardness of 35.5 ± 3.25 GPa and modulus of 428 ± 38 GPa seen at -200 V. The higher scatter in the hardness and modulus at -200 V could be due to the formation of non-stoichiometric phases on account of increased ion bombardment at higher bias voltage. The variation in hardness and modulus can be explained on the basis of the variation in grain size and residual stress in the coatings which is discussed in Sec. 5.3.2.

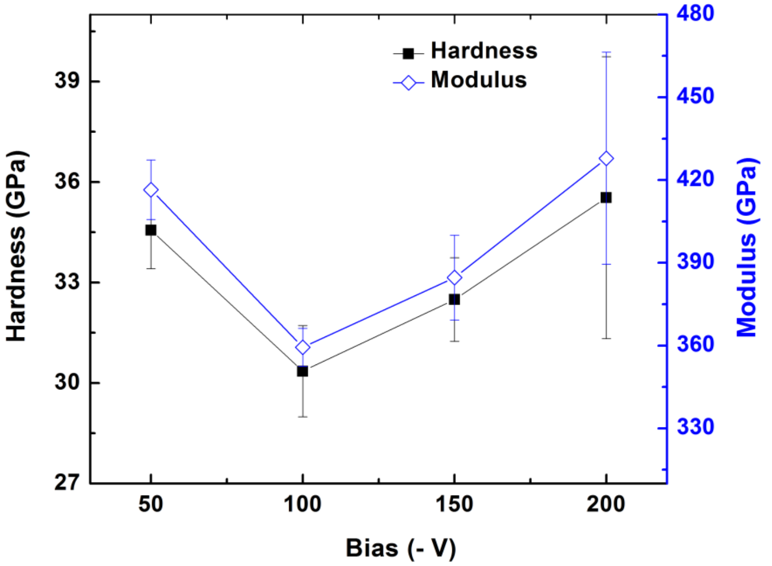

Fig. 5.2 Variation in hardness and modulus of TiAlN coatings with bias voltage.

Fig. 5.3 (a) shows the variation in residual stress with bias voltage. There is a gradual drop in compressive residual stress until -150 V followed by an increase in stress to a maximum of - 5.3 GPa at -200 V. Fig. 5.3 (b) shows the variation in grain size with bias voltage; a gradual decrease with increasing negative bias voltage was seen.

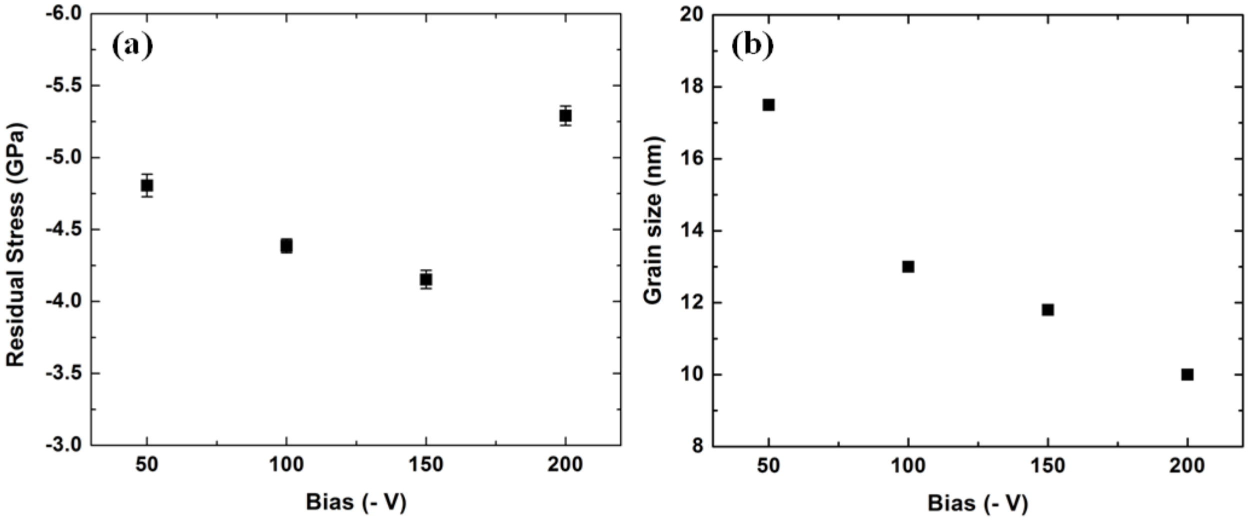

Fig. 5.3 Variation in (a) residual stress and (b) grain size in TiAlN coatings at varying bias voltage.

The high residual stress at -50 V can be attributed to build up of stresses due to defect generation on account of ion bombardment; further ion bombardment due to increasing bias leads to annihilation of the defects which causes a decrease in residual stresses up to -150 V [34, 35]. A further increase in bias up to -200 V saw a maximum in residual stress which could be plausibly due to an increase in bias induced defect density and a denser microstructure [36]. The grain size reduction can be attributed to the reduced mobility of the ion species with increasing bias which leads to higher re-nucleation and hence, smaller grains [37, 17].

The cross sectional focused ion beam images of the coatings are shown in Fig.5.4. A transition to finer grains with increasing negative bias is visible. The grains initially show a columnar structure at -50 V which turns to a more equiaxed structure at higher bias voltages. This was also reflected in the change in texture from (200) at -50 V to (111) at higher bias values; such a change from columnar grain structure with (200) texture at low bias voltages (-40 V) to equiaxed grains with (111) texture at higher bias voltages (-140 and -200 V) has also been reported earlier [38]. To further corroborate the reduction in grain size, TEM studies were also carried out. Fig.5.4 also shows two microdroplets in the TiAlN coating at -50 V, a few of which tend to form in spite of the low droplet density in cylindrical cathodic arc deposition.

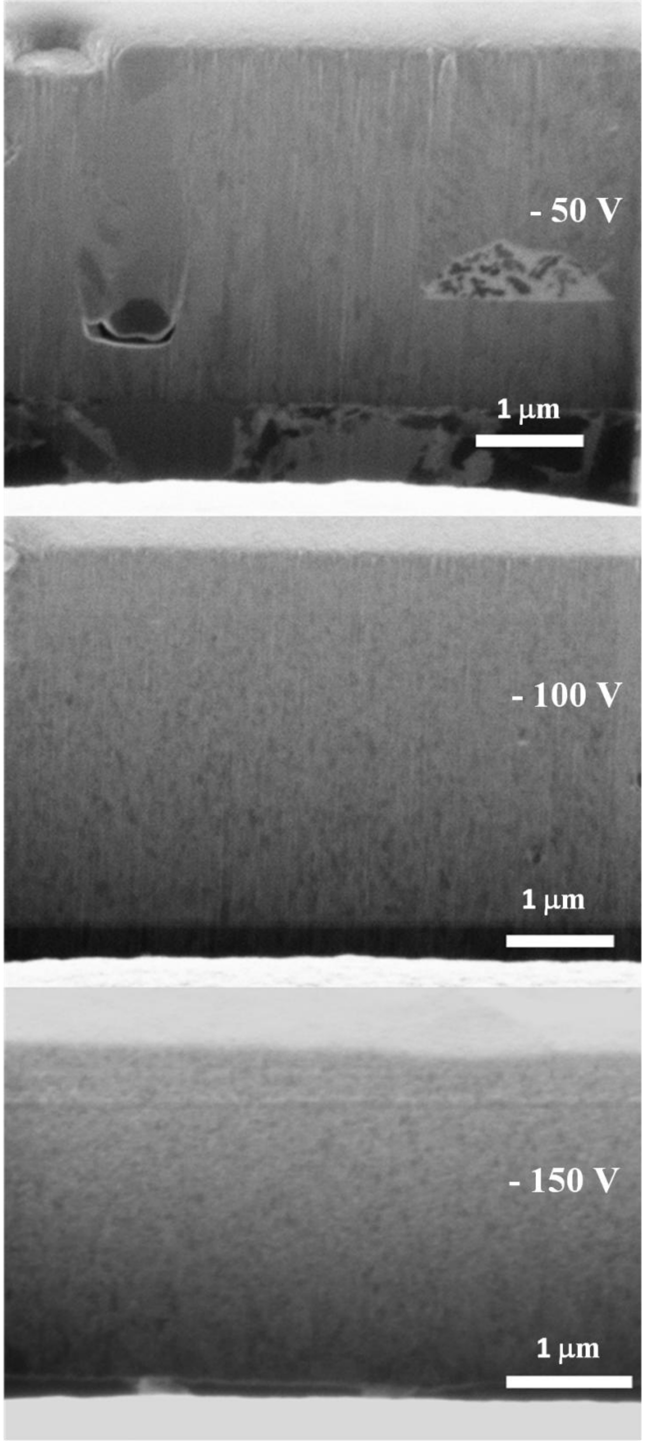

Fig. 5.4 Ion induced secondary electron (ISE) images of TiAlN coating cross section at different bias voltages.

Plan view TEM studies confirm the grain size variation in TiAlN coatings due to changing negative bias voltage. Bright field (BF) and dark field (DF) TEM micrographs of the specimens at different bias voltages are shown in Fig.5.5. All the coatings showed nanocrystalline grains and a gradual reduction in grain size with increasing bias voltage can be observed. SAED patterns showed only a FCC TiAlN phase in all the coatings. A (200) texture was seen in case of the coating deposited at -50 V as evident from the ring pattern corresponding to the (200) plane. The ring patterns also indicate reducing grain size as seen from increasing diffuseness in the rings with increasing bias.

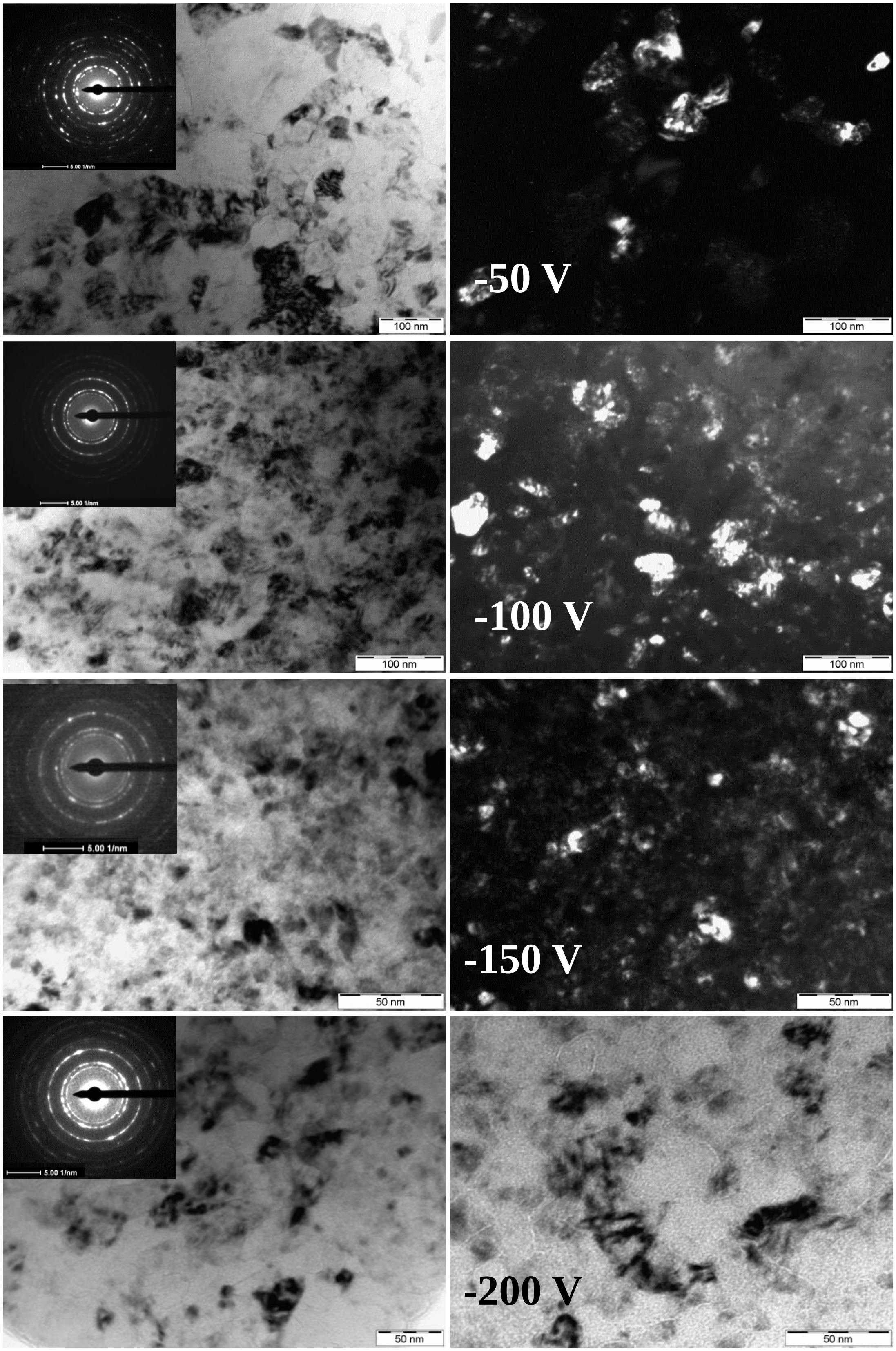

Fig. 5.5 TEM micrographs of TiAlN coating at different bias voltages.

5.2.3 Role of residual stress and grain size on mechanical properties

The hardness of the TiAlN coatings is affected by both the grain size and the residual stress. There is a fall in hardness at -100 V in spite of a lower grain size compared to -50 V due to the fall in residual stress at -100 V. There is an increase in hardness at -150V where the effect of lower grain size has a higher contribution than the effect of lower residual stress. The maximum in hardness seen at - 200 V is due to the small grain size and the highest residual stress observed at this voltage. The value of hardness and residual stress at -50 V is higher compared to the values at -100 and -150 V. This behaviour is probably due to an initial build up of stresses due to defect generation from ion bombardment at -50V which is followed by relaxation due to annihilation of defects at higher bias values of -100 and -150 V. This agrees with other studies on cathodic arc deposited TiAlN coatings where similar build up of stresses with increasing bias followed by a drop in stress at higher bias voltages has been reported [34].

A few other studies on cathodic arc deposited TiAlN coatings report a maximum in hardness observed at different bias values which vary from -40 V to -100 V followed by a drop in hardness and residual stresses [35, 38].Thus, the bias value at which a maximum in hardness is observed varies based on the processing parameters used during deposition. Aliaj *et. al* [34] report a large increase in hardness of cathodic arc deposited TiAlN with increase of negative bias voltage from −25 to −50 V, which is also accompanied by an increase in compressive residual stress by nearly 4 GPa, while further increase in the negative bias voltage to −100 V resulted only in a slight increase in hardness and compressive residual stress. Blomqist and Ahlgren [38] report a 10 % increase in hardness and a large jump in residual stress (~ 38%) from -40 V to -70V for cathodic arc deposited TiAlN coatings after which the above properties are nearly constant up to - 200 V. However, they report a nearly 100 % increase in delamination of the coating from the substrate when bias voltage was increased from -70 to -100 V.

In the present study, the bias voltage of -50 V showed a high hardness and high compressive residual stress while the bias voltage of -200 V showed much higher compressive residual stresses and slightly higher hardness. High compressive stresses beyond a certain point are known to lead to coating delamination [39]. Hence, large bias values during deposition are not advisable. Based on the above study, a bias value of -50 V was determined to be the optimum as it showed the best compromise between hardness and stress and was fixed for deposition of all subsequent coatings reported in the current investigation.

5.3 Effect of composition on properties of $Ti_{1-x}Al_xN$ coatings

5.3.1 Composition and crystal structure of $Ti_{1-x}Al_xN$ coatings

All the deposited coatings had a thickness in the range of 3.6 - 3.7 μm. Specific targeted compositions were attempted to be achieved by varying the currents to the Ti and TiAl cathodes, and the actual film chemistry achieved was determined by EDS. All other deposition conditions were maintained as in Chapter 3. Table 3 summarizes the sample designations representing the chemistries targeted, the corresponding cathode currents employed and the resultant compositions.

Table 3: Sample designations with their corresponding cathode currents and resultant compositions

Sample	**$I_{Cathode}$ (A)**		**Atomic %**	
	Ti	**TiAl**	**Ti**	**Al**
TiN	175	0	100	0
$Ti_{0.70}Al_{0.30}N$	175	130	70.4	29.6
$Ti_{0.60}Al_{0.40}N$	175	225	60.3	39.6
$Ti_{0.54}Al_{0.46}N$	150	275	53.5	46.5
$Ti_{0.47}Al_{0.53}N$	100	275	46.4	53.6
$Ti_{0.35}Al_{0.65}N$	0	275	34.5	64.5

X-ray diffractograms of the $Ti_xAl_{1-x}N$ coatings are shown in Fig.5.6 with the phase and orientation of the diffracting planes marked. As seen in Fig. 5.6 (a), TiN exhibits a dominant (111) peak along with a NaCl type face centred cubic (FCC) structure, while the $Ti_xAl_{1-x}N$ coatings are characterized by a dominant (200) peak with a FCC NaCl type phase that closely matches with FCC $Ti_{0.5}Al_{0.5}N$ [33]. The TiN coating has a (111) texture while the TiAlN coatings show an increasing (200) texture up to an Al content of 53 % followed by a drop at 65 % Al with dominance of (200) texture.

There is a significant peak shift to the right in 2θ with increasing Al content observable in Fig. 5.6 (b) which indicates reducing lattice parameter. Coatings with Al content up to 53 % showed the NaCl FCC structure while coatings with the composition of $Ti_{0.35}Al_{0.65}N$ showed the presence of both FCC and Hexagonal Close Packed (HCP) phases as seen in Fig. 5.6 (c). The crystallinity exhibited a reduction with increasing Al % which was seen in the broadening of the peaks and a decrease in peak sharpness.

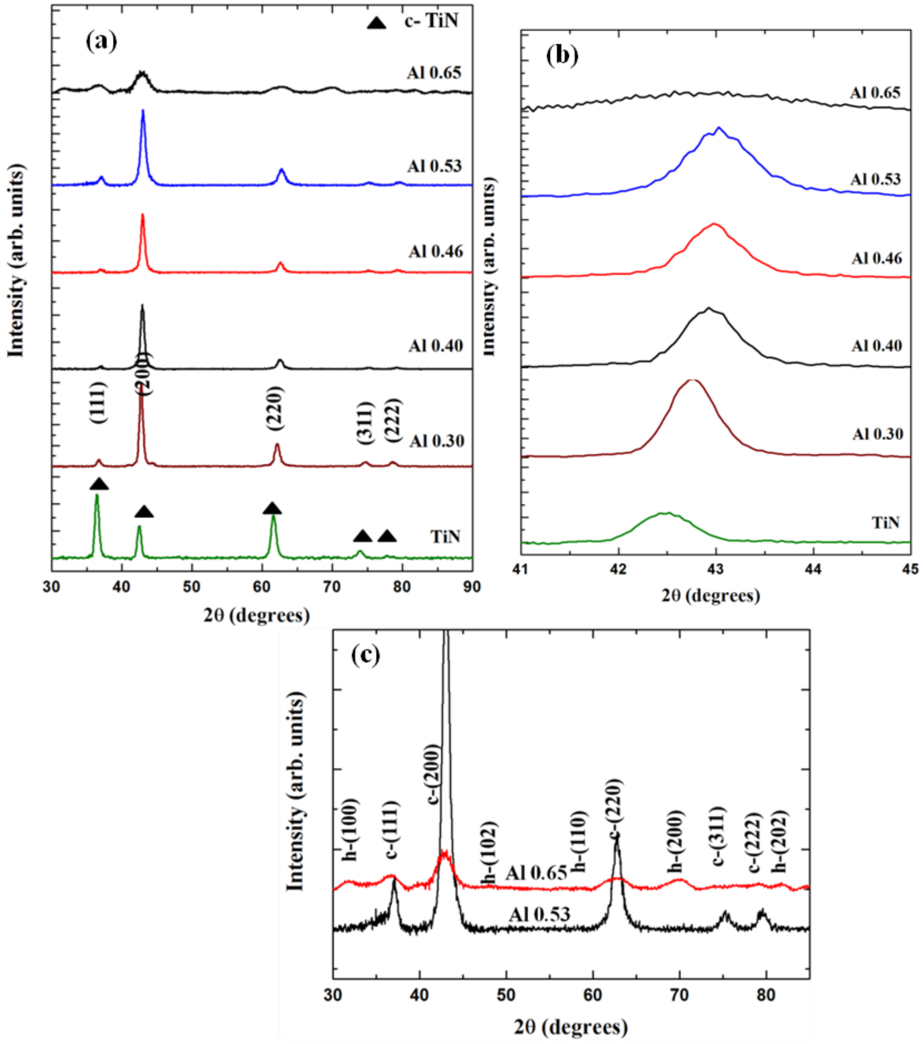

Fig. 5.6 Grazing incidence X-ray diffractograms of (a) Ti_{1-x}AlxN coatings (b) magnified view of 2θ range- 41 to 45 degrees (c) $Ti_{0.35}Al_{0.65}N$ showing the presence of both cubic and HCP phases in comparison with the diffractogram of $Ti_{0.47}Al_{0.53}N$.

The variation of grain size with Al content is shown in Fig. 5.7 (a). The grain size was determined by the Williamson-Hall method after subtraction of instrumental broadening [35] except in case of the $Ti_{0.35}Al_{0.65}N$ where the Scherrer method was used since only a few peaks were available. There is a progressive reduction in grain size with Al content; TiN had the highest grain size while the maximum Al content of 65 % resulted in the lowest grain size. The $Ti_{0.35}Al_{0.65}N$ coating shows a large reduction in grain size to about 13 nm and also shows a broadened peak compared to the other X-ray diffractograms. In order to cross-verify the reduction in grain size, TEM analysis was also carried out and is discussed later in Sec. 5.3.4. All the coatings showed the presence of compressive residual stress, with the trend as shown in Fig. 5.7 (b). After the initial increase in stress in $Ti_{0.7}Al_{0.3}N$ to a maximum of about - 6 GPa compared to -3.84 GPa in TiN, the residual stress values remain nearly constant at 40 % Al, followed by a drop in stress to ~ - 5.3 GPa at an Al content of 46 %. Increase of the Al content to 53 % leads to a large drop in the residual stress to ~ - 4.4 GPa which can be attributed to a lattice relaxation that comes about due to nucleation of the hcp-AlN phase. Since the wurtzite AlN phase has a lower density than the NaCl phase [40], further increase to 65 % of Al will lead to a large fall in stress due to a decrease of strain in the coating. However, the stress in $Ti_{0.35}Al_{0.65}N$ is not shown as the peaks obtained in the $\sin^2\psi$ method were weak and could not be fitted with sufficient accuracy.

The lattice parameters of the above coatings were calculated by extrapolation using the Nelson-Riley function (Fig. 5.7 (c)) and indicate a systematic reduction with Al content upto 53 %, possibly because of the smaller Al atoms replacing Ti in the NaCl type lattice leading to shrinking of the lattice. There is a lattice expansion in case of the coating with Al content of 65 % which can be attributed to the formation of the second phase of h-AlN. Since the above value of the lattice parameter also has a stress contribution, the stress-free lattice parameter (Fig.5.7 (d)) was calculated from the $\sin^2\psi$ plots which showed a similar linear dependence with Al content with a decrease over the values shown in Fig. 5.7 (c). The stress-free lattice parameter calculated for TiN shows a close match to that of the standard JCPDS value.

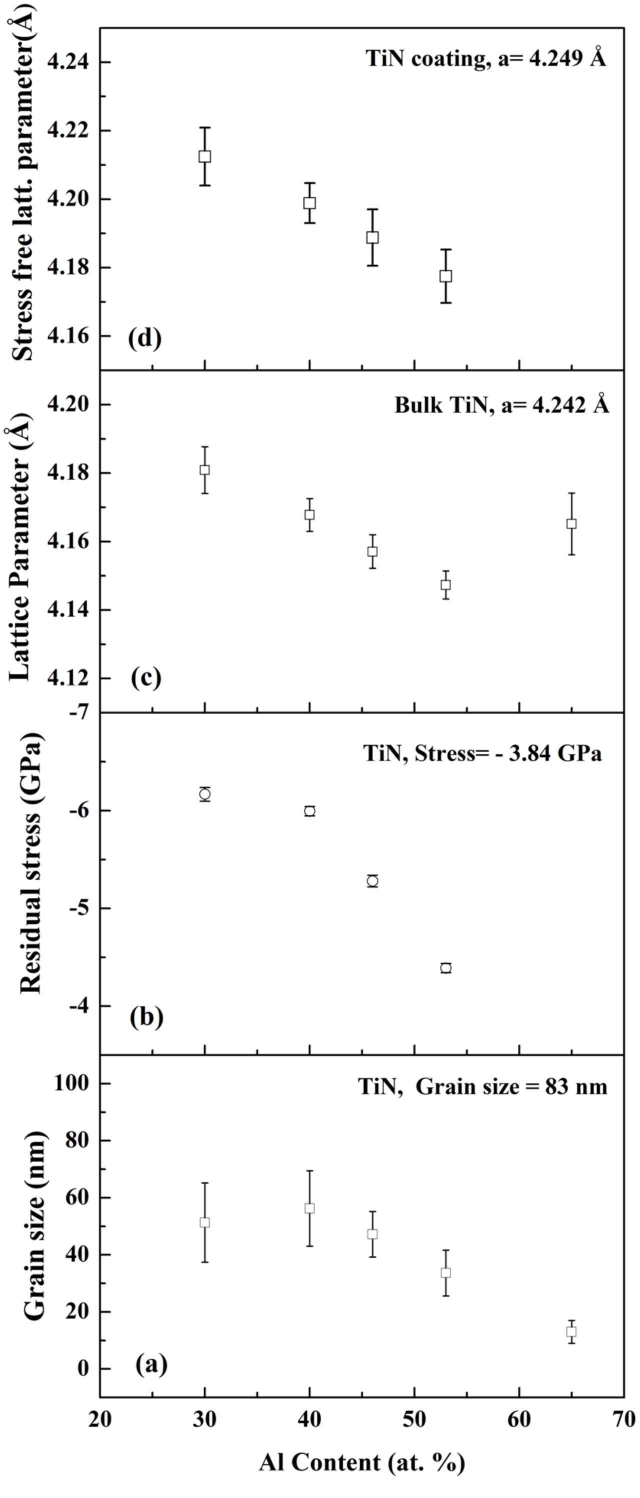

Fig. 5.7 Variation of (a) grain size (b) residual stress and (c) lattice parameter with Al content in the $Ti_{1-x}Al_xN$ coatings.

5.3.2 Hardness and modulus

Fig. 5.8 shows the variation in hardness and modulus of the $Ti_xAl_{1-x}N$ coatings with Al content. However, a closer look at the hardness and modulus values revealed that the coatings corresponding to compositions with Al content of 30 at. % and 65 at. % showed a much higher scatter. This is more clearly illustrated in Fig. 5.9 which depicts hardness values from all measurements made on coatings with the two above Al contents. $Ti_{0.7}Al_{0.3}N$ showed a large spread in the values while $Ti_{0.35}Al_{0.65}N$ results were grouped around two values. The above observation cannot be attributed to experimental error since the difference between the values is nearly 5 GPa and their frequency of occurrence is also significant. The bunching is distinct in case of $Ti_{0.35}Al_{0.65}N$ where two sets of data points are grouped very closely together which can be attributed to the presence of two distinct phases whereas in case of $Ti_{0.7}Al_{0.3}N$ the data has a lot more scatter, which is most likely due to the random distribution of non-stoichiometric phases. An average of 20 measurements made on each coating shown in Fig. 5.8 reveals a trend similar to that generally reported earlier [18] which shows hardness and modulus values with larger error bars. Possible causes for the above behaviour are discussed in more detail in Sec. 5.4.1.

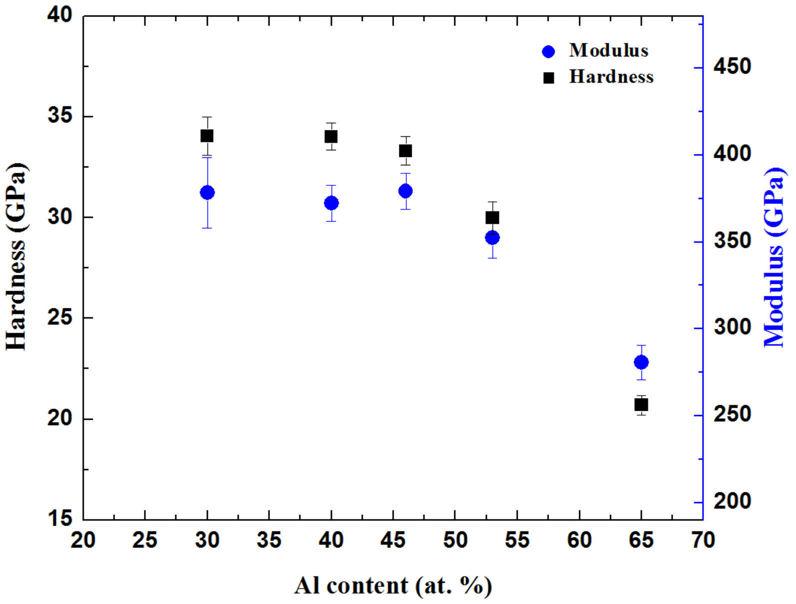

Fig. 5.8 Average hardness and modulus of the $Ti_{1-x}Al_xN$ coatings.

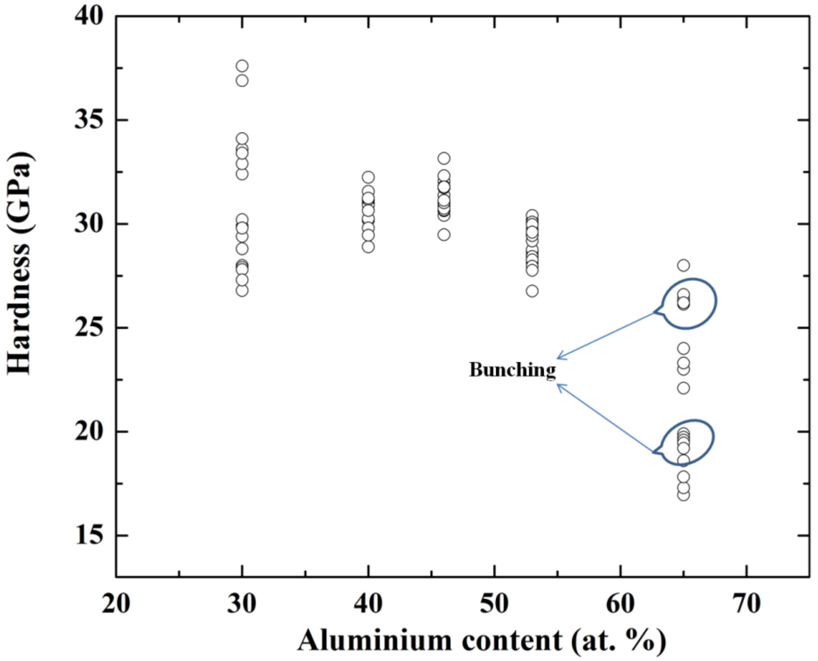

Fig. 5.9 Hardness distribution showing the large variation in $Ti_{0.7}Al_{0.3}N$ and bunching of data in $Ti_{0.35}Al_{0.65}N$.

5.3.3 Fracture toughness measurements

Fracture toughness was determined by measuring the lengths of radial cracks generated after Vickers indentation on the coatings, after taking into account the depth of indentation and the coating thickness, based on the formula below [41]:

$$K = \lambda' V^{*} \left(\frac{E}{H}\right)^{\frac{1}{3}} \frac{1}{t} \frac{P}{c^{\frac{1}{2}}} \; ; \; V^{*} = 1 - \frac{(h-t)^{3}}{h^{3}}$$

where $\lambda' = \lambda/\eta$ with $\lambda = 0.013$ in the case of a Vickers indentor and η– the tip shape constant; E –modulus; H-Hardness, c- the crack length measured from centre of the indent, t- coating thickness, h- penetration depth and V^{*} is a multiplication factor.

The fracture toughness values are plotted as a function of Al content in Fig. 5.10. The highest toughness was observed in the $Ti_{0.47}Al_{0.53}N$ coating followed by $Ti_{0.35}Al_{0.65}N$ while $Ti_{0.6}Al_{0.4}N$ showed a lower toughness with the lowest toughness (6.5 $MPam^{1/2}$, not shown in graph) observed in case of TiN. The variations in toughness can be explained on the basis of the microstructure of the coatings and the crystal structure of the phases formed, as discussed in sections 5.3.4 and 5.4.

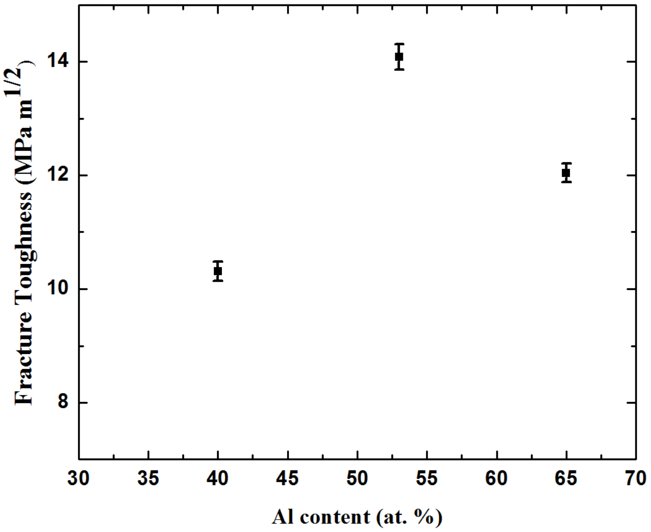

Fig. 5.10 Variation of fracture toughness with Al content in the $Ti_{1-x}Al_xN$ coatings.

5.3.4 Microstructural studies

The cross sectional microstructure of TiAlN coatings was studied using a dual beam SEM. Fig. 5.11 shows images from three representative coatings, namely TiN, $Ti_{0.54}Al_{0.46}N$ and $Ti_{0.35}Al_{0.65}N$, where trenches were milled by FIB to reveal the cross section. Fig. 5.11(a) reveals long columnar grains in the TiN coating while Fig. 5.11(b) shows a near columnar structure in the $Ti_{0.54}Al_{0.46}N$ coating with much smaller grains than in TiN. Fig. 5.11(c) shows no columnar grains being present in the $Ti_{0.35}Al_{0.65}N$ coating, with fine nanocrystalline grains being visible. Fig.5.12 shows plan view TEM micrographs of $Ti_{0.7}Al_{0.3}N$, $Ti_{0.47}Al_{0.53}N$ and $Ti_{0.35}Al_{0.65}N$ along with their corresponding SAED patterns. A clear gradual reduction in grain size can be seen from $Ti_{0.7}Al_{0.3}N$ to $Ti_{0.35}Al_{0.65}N$. Also, the SAED patterns highlight the reducing crystallinity with increasing Al content, with the $Ti_{0.35}Al_{0.65}N$ coating showing a nearly amorphous signature along with a dual phase of hcp-AlN and cubic-TiAlN as seen in the ring patterns. However, $Ti_{0.7}Al_{0.3}N$ showed abnormal grain growth in some regions. High resolution TEM micrographs of $Ti_{0.47}Al_{0.53}N$ and $Ti_{0.35}Al_{0.65}N$ are shown in Fig. 5.13 where the $Ti_{0.35}Al_{0.65}N$ coating shows a nanocomposite structure which is absent in the $Ti_{0.47}Al_{0.53}N$ coating. This is in agreement with earlier reports on $Ti_{1-x}Al_xN$ coatings [21, 42].

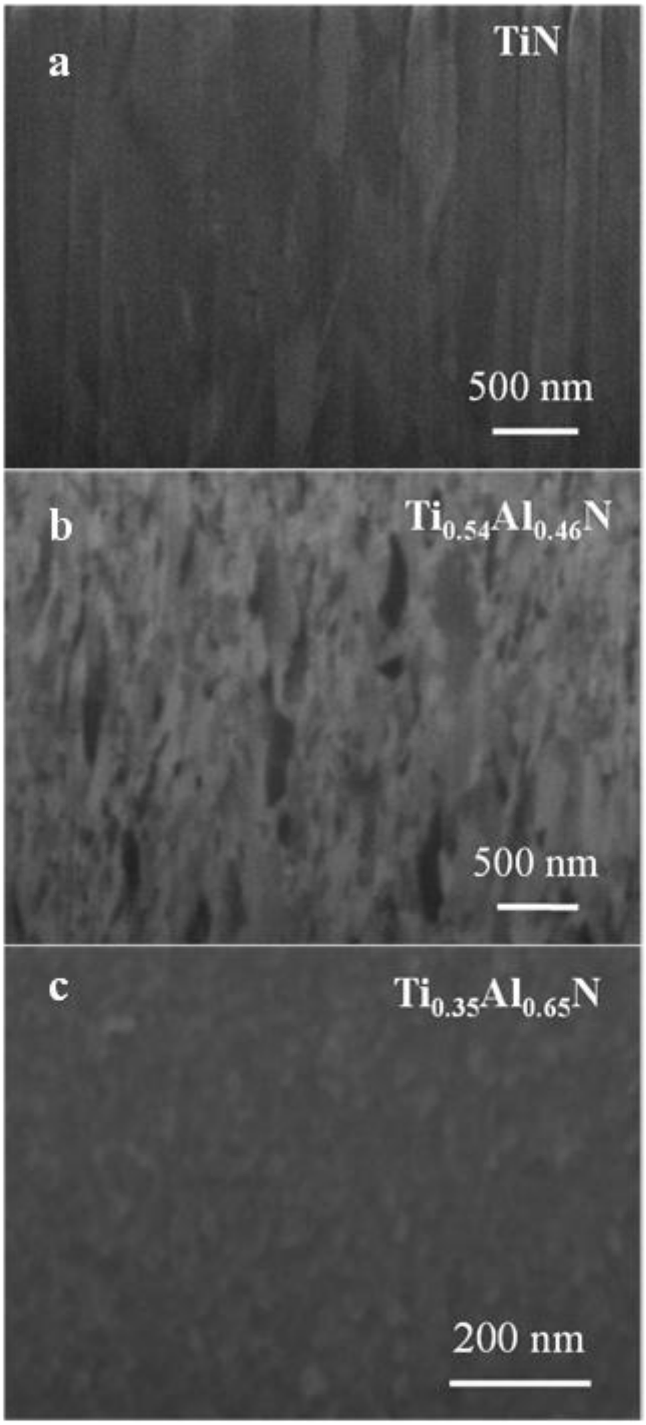

Fig. 5.11 Cross sectional SEM images after FIB milling of (a) TiN showing columnar grains (b) $Ti_{0.54}Al_{0.46}N$ showing finer columnar grains and (c) $Ti_{0.35}Al_{0.65}N$ showing equiaxed nanocrystalline grains.

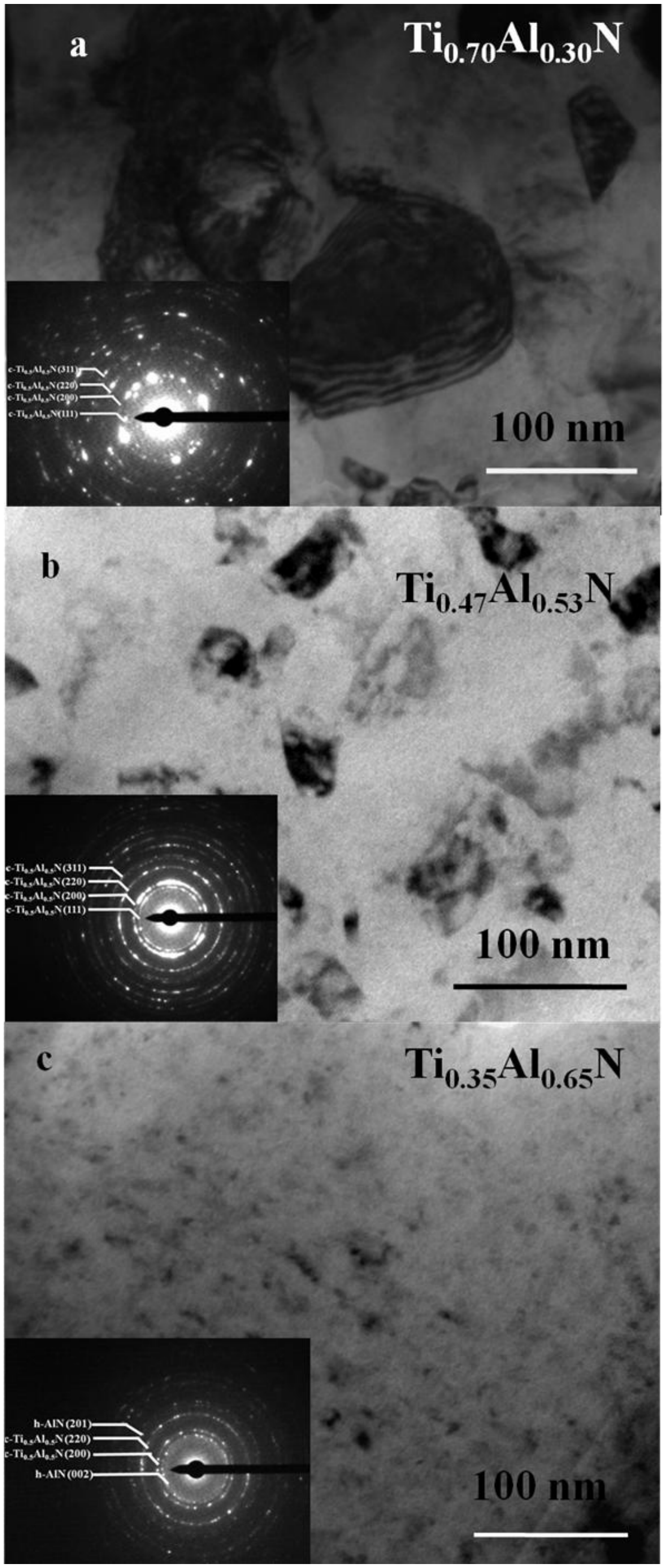

Fig. 5.12 Plan view TEM micrographs of (a) Ti$_{0.7}$Al$_{0.3}$N, (b) Ti$_{0.47}$Al$_{0.53}$N and (c) Ti$_{0.35}$Al$_{0.65}$N along with their corresponding SAED patterns.

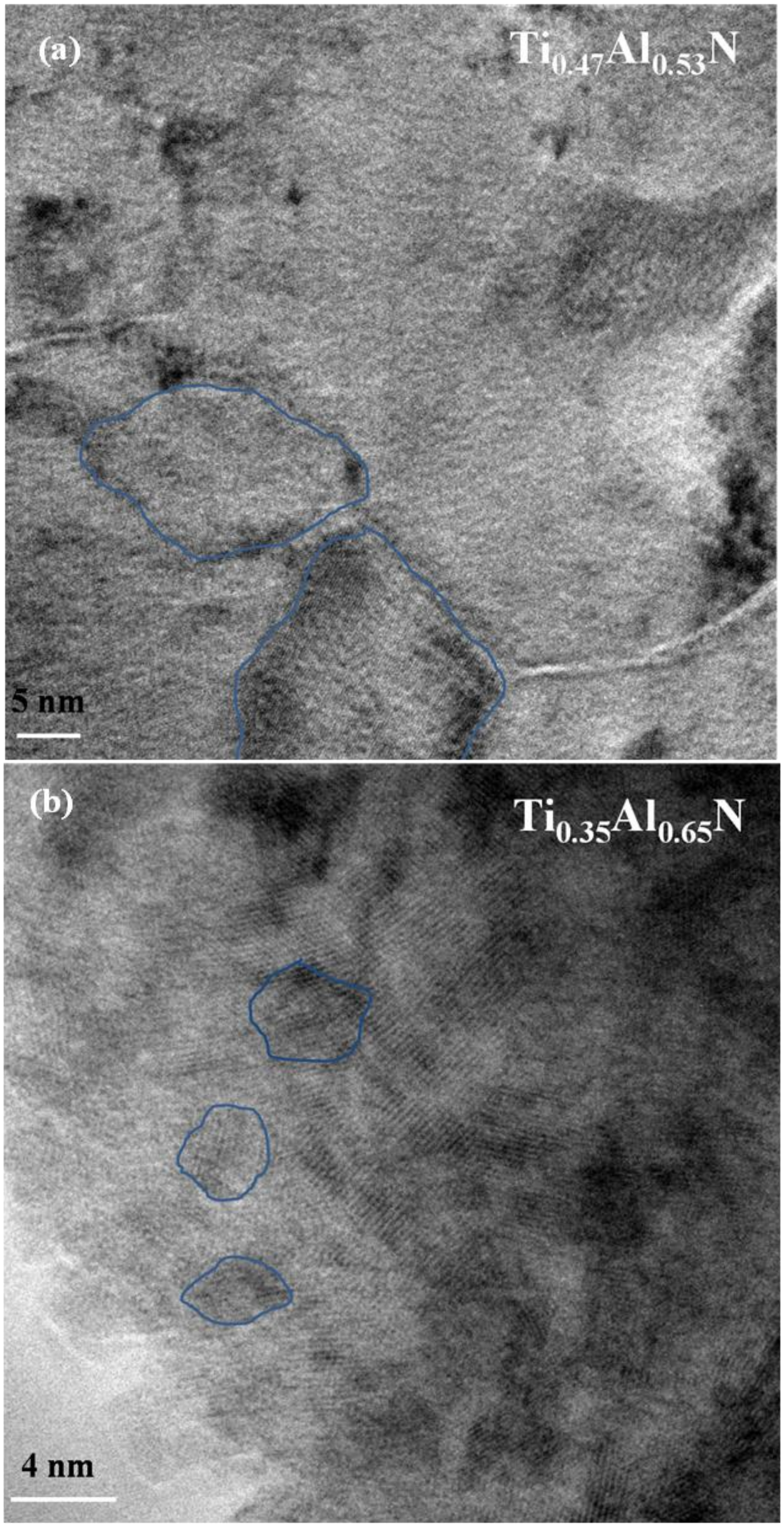

Fig. 5.13 High resolution TEM micrographs of (a) $Ti_{0.47}Al_{0.53}N$ and (b) $Ti_{0.35}Al_{0.65}N$ showing the nanocrystalline grains and nanocomposite structure, respectively (a few grains in the coatings are demarcated by markings).

5.3.5 Scratch testing and post-scratch observations

Progressive load scratch tests were carried out to determine the adhesion and also, more importantly, to observe the deformation modes as a function of Al content. The scratch tracks were examined under the scanning electron microscope to ascertain the mechanism of deformation in the coatings. The deformation modes were identified by comparing the observed scratch deformation with the damage modes and the scratch atlas given in the ASTM standard C1624 [43].

Fig. 5.14 shows representative SEM images of the post scratch deformation seen in the $Ti_{1-x}Al_xN$ coatings at the point of first chipping or crack formation. The scratch tracks in $Ti_{0.7}Al_{0.3}N$, $Ti_{0.6}Al_{0.4}N$ and $Ti_{0.54}Al_{0.46}N$ show tensile arc cracks followed by recovery spallation with reduced crack density as we progress from an Al content of 0.3 to an Al content of 0.46. The scratch track in $Ti_{0.47}Al_{0.53}N$ shows mild wedging spallation while the scratch track in the $Ti_{0.35}Al_{0.65}N$ coating shows complete wedging spallation. The TiAlN coatings (up to an Al content of 53 %) show a gradually increasing brittleness on account of the increase in covalent nature with the increase in Al leading to a reduction in ductility. $Ti_{0.35}Al_{0.65}N$ shows a brittle failure as seen from the annular spallation in the scratch track. The number of cracks in the scratch track can give a rough indication of toughness [44]. In the above coatings, a gradual reduction in the crack density with Al content in the scratch tracks is visible (Fig. 5.14) with the $Ti_{0.47}Al_{0.53}N$ coating showing reduced number of cracks and larger inter-crack spacing compared to the $Ti_{0.7}Al_{0.3}N$, $Ti_{0.6}Al_{0.4}N$ and $Ti_{0.54}Al_{0.46}N$ coatings. The $Ti_{0.35}Al_{0.65}N$ coating showed a slightly higher crack density compared to $Ti_{0.47}Al_{0.53}N$. This indicates increasing toughness in $Ti_{1-x}Al_xN$ with increasing Al content in the range up to 53 at. %. The toughness enhancement was also confirmed from FIB studies. FIB milling was used to probe the region below the scratch track in order to understand the exact nature of cracking.

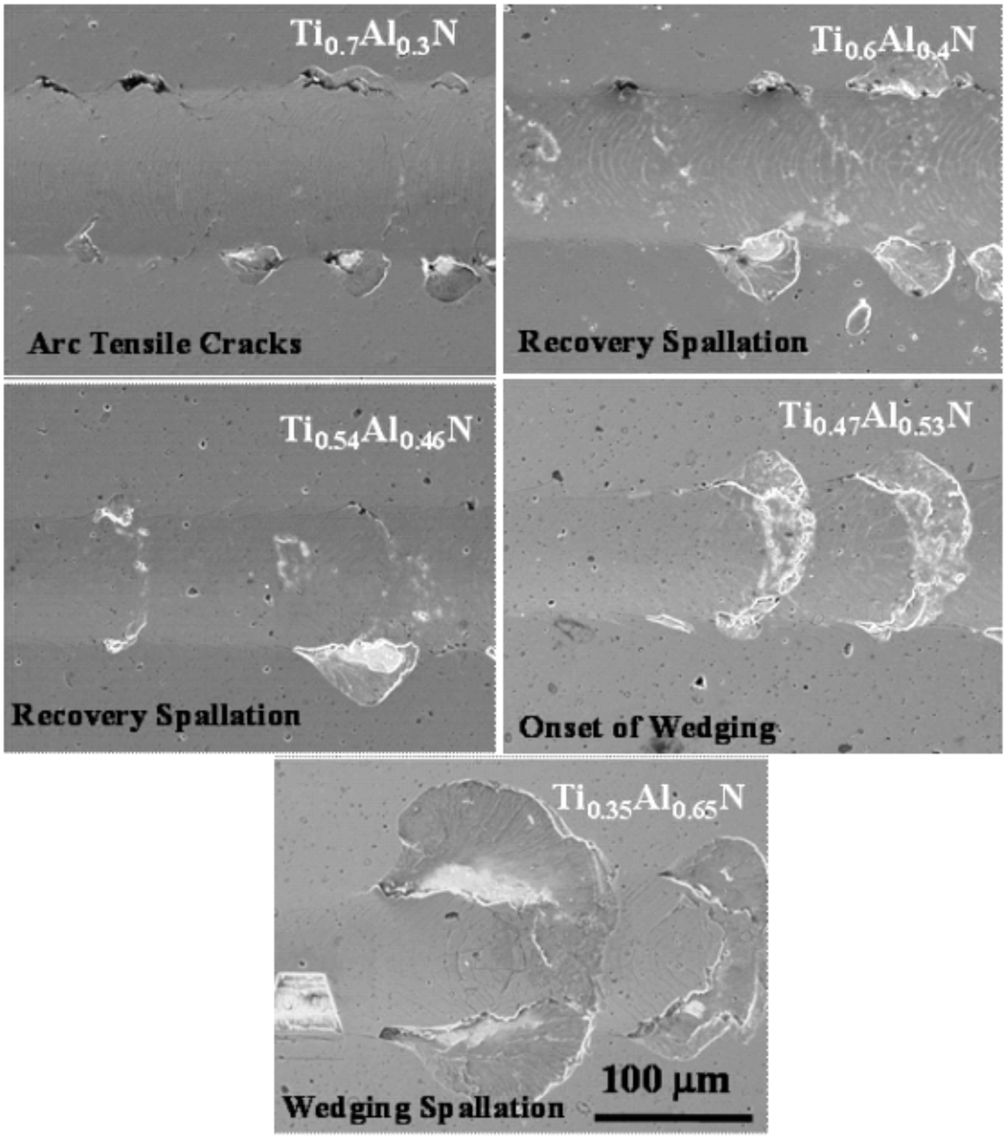

Fig. 5.14 Representative SEM images of the post scratch deformation seen in the Ti1-xAlxN coatings at the point of first chipping and crack formation.

The use of FIB milling has been proven to be useful to study the subsurface deformation in PVD coatings [45]. All coatings studied were sectioned using FIB milling in the region of first chipping along the centre of the scratch track so as to have a uniform reference point for comparison. Figures.5.15 (a-c) show the sub surface deformation at the point of first chipping in TiN, $Ti_{0.54}Al_{0.46}N$ and $Ti_{0.35}Al_{0.65}N$ coatings, respectively. Both TiN and $Ti_{0.54}Al_{0.46}N$ show through-thickness cracks during scratch deformation while $Ti_{0.35}Al_{0.65}N$ shows deflection of cracks which could be attributed to its dual phase fine grained nanocomposite structure. As seen in the FIB cross sections, the number of cracks progressively reduced and the distance between them increased with increasing Al content which also indicates an increase in toughness.

\

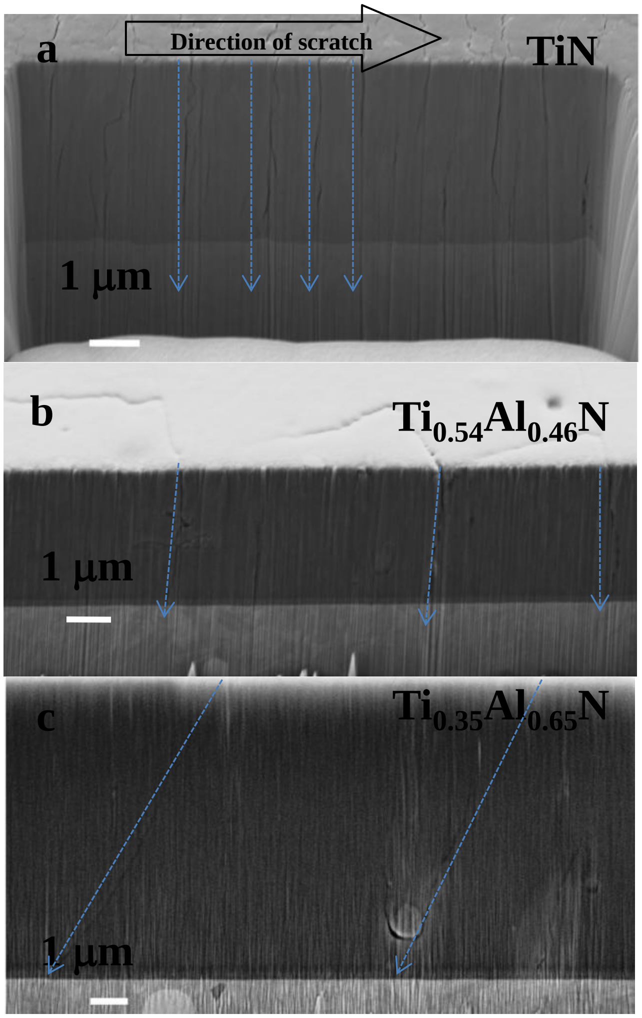

Fig. 5.15 FIB milled cross sections along scratch tracks at the point of first chipping showing (a) long vertical columnar cracks in TiN coating (b) shorter columnar cracks in $Ti_{0.54}Al_{0.46}N$ coating (c) deflected cracks in $Ti_{0.35}Al_{0.65}N$ coating.

5.3.6 Nano-impact testing of $Ti_{1-x}Al_xN$ coatings

Nano-impact tests were carried out in order to evaluate the behaviour of the $Ti_{1-x}Al_xN$ coatings under dynamic loading conditions which simulates the repeated contact and loading seen in real life machining. Tests were carried out with a cube corner indenter at fixed loads ranging from 10 mN to 70 mN for a time period of 180 seconds and a frequency of 0.25 Hz. Fig. 5.16 shows typical impact depth vs. time plots obtained at 10 mN on the $Ti_{1-x}Al_xN$ coatings. Fig.5.17 shows representative impact curves with varying Al content at loads of 10 mN, 20 mN and 30 mN.

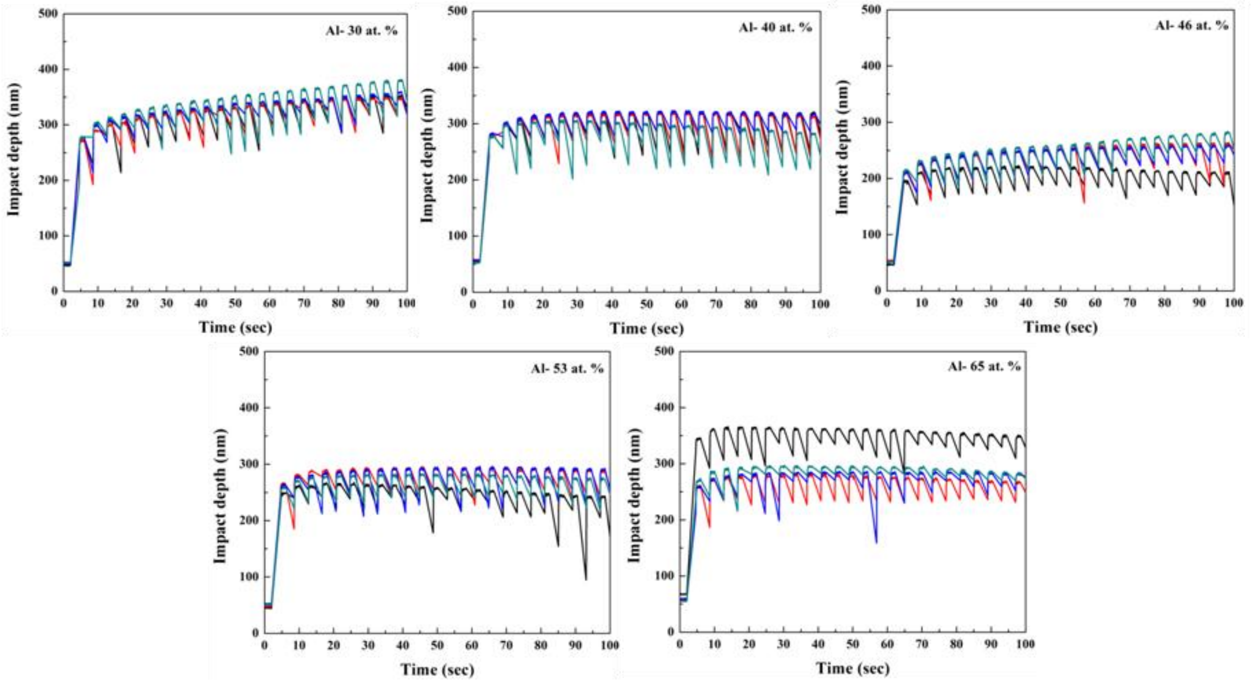

Fig. 5.16 Impact depth vs. time plots at 10 mN with varying Al % in TiAlN.

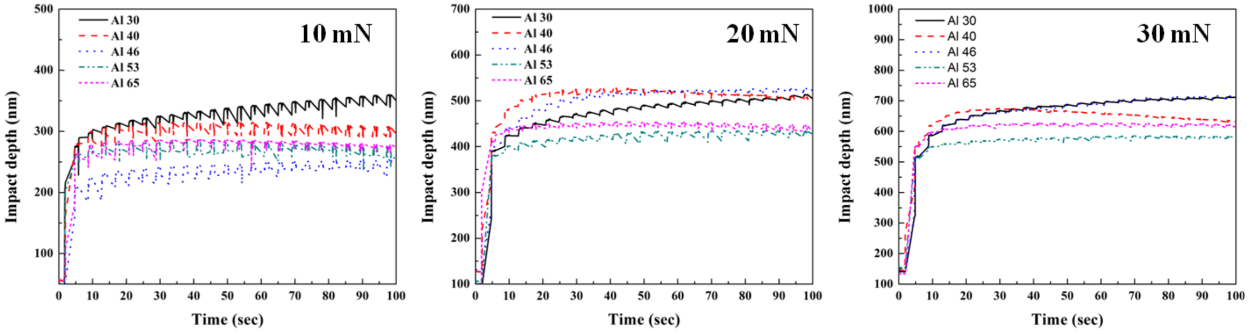

Fig. 5.17 Representative impact depth vs. time plots with varying Al % in TiAlN at loads of 10, 20 and 30 mN.

The average final impact depth at each load was plotted as a function of composition and is shown in Fig. 5.18. At 10 mN, there is a gradual reduction in impact depth i.e. an increase in impact resistance as the Al content increases up to 46 % and is nearly constant in the range 46 to 65 %. At 20 mN and 30 mN, the least impact depth is shown at an Al content of 53 % and is followed closely by the coating with 65 % of Al. Beyond 30 mN, fracture begins in most of the coatings and results in abnormal values of impact depth, hence loads above 30 mN were not considered. However, $Ti_{0.35}Al_{0.65}N$ shows lower cracking compared to the other coatings, this anomalous behaviour is discussed in section 5.4.2. The impact depths in TiN are nearly double the value of the depths seen at $Ti_{0.7}Al_{0.3}N$ and are not shown in the graph.

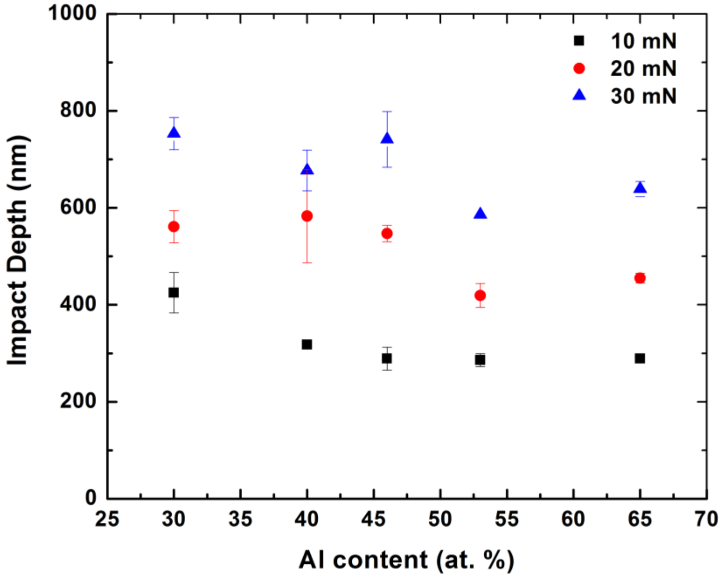

Fig. 5.18 Average impact depth with varying Al % in TiAlN at loads of 10, 20 and 30 mN.

5.4 Discussion

5.4.1 Effect of stoichiometry and phase on mechanical properties

The variation in hardness and toughness with varying Al in the $Ti_{1-x}Al_xN$ coatings can be explained on the basis of the microstructure, phase constitution and the residual stress. The hardness enhancement on introduction of Al, as seen in the large increase from TiN (~ 24 GPa) to $Ti_{0.7}Al_{0.3}N$ (~ 31 GPa), could be attributed to solid solution formation where Al substitutes Ti atoms in the NaCl type TiN lattice which is evident from the reduction in lattice parameter from 4.25 Å (TiN) to 4.22 Å ($Ti_{0.7}Al_{0.3}N$) (Fig.5.7(c)). The build-up of residual stress, which is probably due to the presence of non-stoichiometric phases and defects, is also expected to play a significant contributory role [16, 18].

Hardness variation in PVD coatings is known and attributed to the non-equilibrium nature of the deposition process [46]. Regardless of the above, there was a distinctly large spread in case of $Ti_{0.7}Al_{0.3}N$ and bunching of values in $Ti_{0.35}Al_{0.65}N$ as shown in Fig.5.9. $Ti_{0.7}Al_{0.3}N$ and even TiN showed hardness and modulus values that had a large scatter, which is probably due to the presence of both stable cubic phases of TiAlN and TiN and non-stoichiometric phases such as Ti_2N. As a second phase was not detected in XRD scans, XPS analysis was carried out to ascertain non-stoichiometry which showed the presence of multiple oxidation states of Ti as shown in Fig. 5.18. An increase in the hardness of TiN coatings due to non-stoichiometric phases has been reported to arise due to the accompanying lattice defects and microstructural changes [47]. Further increase in the Al content up to 53 % did not result in a significant drop in hardness but was accompanied by a gradual fall in stress. The near stable hardness in the composition range 40 to 53 % can be attributed to the hardness increase due to reduction in grain size, offsetting the drop in hardness due to the reduction in stress. The reduction in stress can be attributed to the stabilization of the cubic phases and the negligible presence of non-stoichiometric phases. Further increase in the Al content to 65 % saw a dramatic change in the microstructure and mechanical properties due to the formation of a hcp-AlN phase in addition to the cubic TiAlN phase.

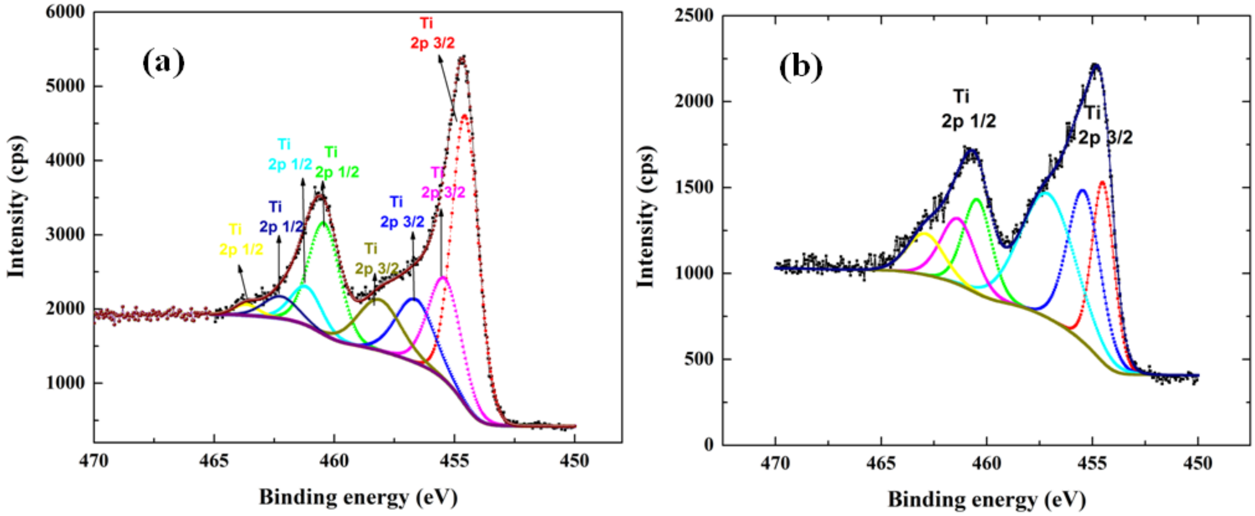

Fig. 5.19 XPS spectrums of (a) TiN showing multiple oxidation states (TiN and Ti_2N are the possible phases) and (b) $Ti_{0.54}Al_{0.46}N$ showing oxidation states corresponding to the bonding states of TiAlN (a minor peak of Ti_2N is also seen).

The co-existence of more than one phase in $Ti_{0.35}Al_{0.65}N$ could be responsible for the very pronounced grain size refinement. The change in the microstructure with increasing Al is evident in the change from large columnar grains to smaller grains and finally to an equiaxed type of structure is in agreement with earlier studies [15, 16, 48, 49]. The above two phase structure seen in coatings deposited with $Ti_{0.33}Al_{0.67}$ cathodes has been reported in prior studies [17, 40, 50]; though other studies also report the existence of a single phase cubic structure with this cathode composition [18,42]. This difference arises due to the metastable nature of TiAlN in the Al composition range- 52 to 70 % [3, 15], with a minor change in deposition conditions leading to phase separation.A recent study also reports that increasing the Al content from $x = 0.55$ to $x = 0.66$ leads to an increase in wurtzite formation on account of the reduced energetic difference which increases the probability of forming both phases simultaneously [40]. Other studies where $Ti_{0.33}Al_{0.67}$ cathodes were used have also reported a two phase structure, e.g. Aliaj *et. al.* [50] observed this in TiAlN coatings deposited in a Platit cathodic arc PVD while Wüstefeld *et. al* [17] reported this in coatings deposited in a Balzers RCS cathodic arc system. These authors also report that the formation of the hexagonal phase is suppressed when a higher negative bias voltage is applied to the substrates during deposition. The presence of the hexagonal phase of AlN in the present study might be due to the fact the bias voltage used was a relatively low value of -50 V which is close to the value at which the hexagonal phase was observed in the study by Wüstefeld *et. al* [17].

The $Ti_{0.35}Al_{0.65}N$ coating shows two different values of the hardness and modulus which may be attributed to the presence of the hard cubic TiAlN phase along with the h-AlN phase that has a lower hardness. The noted bunching of hardness measured around two distinct values of ~ 19 and 27 GPa could be attributed to AlN which has a hardness value of 19 GPa [51] and cubic TiAlN which has a value of ~ 28 GPa [52,3]. There were a few intermediate data points with a hardness of ~ 23 GPa, which probably result from an unequal distribution of the AlN and TiAlN phases; where the local distribution of the phases determines the hardness and modulus at that particular point. The overall hardness of the $Ti_{0.35}Al_{0.65}N$ coating is lower than the coatings with other Al contents, which is due to the presence of the h-AlN phase. A similar grouping of hardness has been reported earlier in PVD coatings of TaN and was attributed to the presence of agglomerations of different phases formed due to anisotropic diffusion of nitrogen in Ta [53]. While the large scatter in hardness seen in $Ti_{0.7}Al_{0.3}N$ could be a result of non-stoichiometric phases which can be attributed to the non-equilibrium nature of the cathodic arc deposition, the hardness distribution about two values seen in $Ti_{0.35}Al_{0.65}N$ is most likely due to the presence of two phases, cubic TiAlN and h-AlN. The effect of non-stoichiometry and second phases is significant as they too contribute to the final properties of the coating.

5.4.2 Effect of composition and microstructure on fracture toughness and impact resistance

The toughness of the films was found to initially increase with Al content, with the highest fracture toughness of ~14 MPa $m^{1/2}$ seen at an Al content of approx. 53% and was followed by the coating with 65 % Al which showed a fracture toughness that was lower by about 15 % (Fig. 5.10). This value is still higher than the fracture toughness seen at an Al content of 40 % or in the case of TiN. The maximum fracture toughness at the Al content of 53 % can be attributed to the reduction in grain size and stress which inhibits crack propagation. The fracture toughness decreased in the case of the coating with Al content of 65 %, in spite of the much lower grain size, due to the presence of the hcp-AlN phase. However, the fall in toughness is not steep on account of the nanocomposite structure seen in the coating and the presence of a cubic phase.

The impact resistance of TiN is low and nearly doubles at 30 % Al after which there is a gradual increase in resistance up to 46 % Al with a maximum seen at 53 % Al followed closely by 65 % Al. As seen in Fig. 5.18, at 10 mN the impact resistance of the coatings with Al % - 46, 53 and 65 % are nearly equal while at loads of 20 mN and 30 mN, the coating with 53 % Al shows the maximum. The increase in impact resistance as Al content increases can be attributed to the microstructure; there is a change from large columnar grains in TiN to finer grains which become equiaxed as the Al content is close to 60 % with the fracture toughness increasing as the grains become finer. The impact resistance is found to show a dependence on the toughness of the coatings with the coating showing the highest fracture toughness (Al 53%) also showing the highest impact resistance. The coating with 65 % Al showed a slightly lower impact resistance with the impact depth higher by 9 % at 30 mN. However, at higher loads the cracking seen at 65 % Al was lower than that at 53 % Al. This could be due to the close match in the modulus of the coating (280 GPa) and the HSS substrate (300 GPa) and the nanocomposite structure of the coating.

Earlier studies on TiAlN with Al content of about 65 % have reported enhanced inhibition of crack propagation due to a nanocomposite structure [42] and reduced cracking even in the presence of a hexagonal phase, provided that a cubic nature still exists [54,55]. A rather high hardness of ~ 47 GPa was reported in the case of a TiAlN nanocomposite coating which was attributed to the presence of nanocrystalline TiAlN grains surrounded by an x-ray amorphous AlN phase. In the present study, while $Ti_{0.35}Al_{0.65}N$ shows both cubic and hexagonal phases and a nanocomposite structure, there is a fall in hardness due to the higher content of the hexagonal phase. The cubic phase of TiAlN has been reported to be more beneficial for increased wear resistance [55, 56]. To achieve an oxidation resistant TiAlN, a high Al content is desired while for improved wear resistance and toughness, a cubic nanocomposite structure is found most suitable. Hence, tailoring of Al content and deposition conditions to obtain an Al-rich TiAlN with a near cubic, nanocomposite structure will provide a coating with an optimum combination of toughness, impact and oxidation resistance.

5.4.3 Effect of composition and phase on deformation behaviour and fracture toughness

The nature of deformation of the coatings during scratch testing, as inferred from the post-scratch FIB study (Fig. 5.15) is discussed below. Cross sections along the scratch track showed large vertical cracks and large substrate penetration in TiN while reduced cracks and lower substrate penetration were seen in TiAlN with intermediate Al content (46 %). Cross section of the scratch track in the case of $Ti_{0.35}Al_{0.65}N$ coating showed deflected cracks, along with negligible substrate penetration. The deformation seen in TiN where deep, inter-columnar cracks appeared which could be due to grain boundary mediated processes involving the columnar grains sliding against each other and penetrating into the substrate. The deformation in $Ti_{0.54}Al_{0.46}N$ was found to be lesser with the cracks spread out due to bending of the fine, columnar grains while the deformation in $Ti_{0.35}Al_{0.65}N$ was further minimized on account of crack deflection which can be attributed to arresting of cracks by the amorphous phase at grain boundaries.

Earlier studies on TiAlN coatings also reflect the above with Ti-rich and Al-rich nitrides reported to behave differently under indentation [20, 42, 54]. The deformation in columnar TiAlN coatings was explained by means of grain boundary sliding and inter-columnar cracking, while an inhibition of crack propagation was reported in nanocomposite TiAlN on account of the enhanced capacity for plastic deformation. The presence of a cubic symmetry in the case of Al-rich $Ti_{0.32}Al_{0.68}N$ films with a major hexagonal phase has also been reported to reduce the deformation, preventing disintegration of the entire film as seen in AlN [54].

There have been conflicting reports on toughness of $Ti_{1-x}Al_xN$ coatings. The fracture toughness increases vary widely with the enhancements reported at vastly different Al contents. While a few studies report high toughness and impact resistance at compositions around 65 % of Al [42, 48], another study reports enhanced toughness in Ti-rich coatings [30]. These differences are probably due to variation in deposition conditions. A previous study on $Ti_{0.5}Al_{0.5}N$ and $Ti_{0.33}Al_{0.67}N$ reported that the coating with higher Al content showed better impact resistance, lower fracture and higher tool life in spite of a lower hardness and modulus [57]. However, the difference in impact resistance between $Ti_{0.5}Al_{0.5}N$ and $Ti_{0.33}Al_{0.67}N$ was found to be minimal at

500°C which was attributed to an optimum ratio of H/E at that temperature; the $Ti_{0.33}Al_{0.67}N$ coating has also been reported to show lower hardness at elevated temperatures due to the hexagonal phase of AlN when compared with TiAlN coatings with a cubic structure [55]. However, since enhanced tool life is the final desired property, the coating should possess a high wear resistance along with good toughness and impact resistance. $Ti_{1-x}Al_xN$ coatings with high Al content have shown better abrasive wear resistance, attributed to finer grains in these coatings, apart from a higher plasticity index which could result in better toughness and reduced cracking [16]. In the present study, the $Ti_{0.35}Al_{0.65}N$ coating showed a reasonable toughness as seen in lower cracking during impact and crack deflection during scratch testing which could be attributed to the nanocomposite structure along with the presence of the cubic phase. Hence, a fairly high Al content in TiAlN is desirable for both wear resistance and toughness while for hot hardness a high Al content is desirable along with a cubic crystal structure.

On comparing the toughness and hardness of $Ti_{1-x}Al_xN$ coatings in this study, it can be seen that the highest toughness corresponded neither to the high hardness seen at an Al content of 40% nor to the least hardness seen at an Al content of 65 %. The highest toughness corresponded to $Ti_{0.47}Al_{0.53}N$ which showed a reasonably high hardness and reasonably uniform hardness. It could be inferred that the non-stoichiometry and the formation of hexagonal phase that were formed at the above compositions probably led to the drop in toughness. Therefore a fully stoichiometric composition aided by a nanocomposite structure would be ideal for coatings with high hardness and reasonable toughness.

The presence of amorphous phases at grain boundaries of nanocrystalline grains is known to lead to dissipation and arresting of propagating cracks thereby enhancing mechanical properties such as toughness [58]. Hence, a reduced grain size along with a nanocomposite structure will lead to higher toughness and impact resistance; which in the case of TiAlN can probably be achieved by choosing a critical Al content in the range 50 to 65 % where one can obtain a nanocomposite structure while at the same time retaining the basic cubic nature without formation of the hexagonal phase.

5.5 Conclusions

A preliminary study was undertaken to examine the effect of bias voltage on the mechanical properties of TiAlN coatings. An optimum value of hardness and residual stress was obtained at a bias voltage of – 50 V. This bias value was fixed for the deposition of all subsequent coatings.

The effect of varying Al content on the microstructure, phase constitution, mechanical properties and impact resistance of $Ti_{1-x}Al_xN$ coatings has been studied. The Al content played a role in the residual stress and microstructure of the coatings which further affected their hardness and toughness. The fracture toughness gradually increased with Al content with the maximum in $Ti_{0.47}Al_{0.53}N$ which was followed by a small drop in case of $Ti_{0.35}Al_{0.65}N$ due to the presence of the hexagonal phase of AlN. The impact resistance shows a close relation to the fracture toughness with the coating showing highest fracture toughness also showing the highest impact resistance. It was found that a cubic structure along with a fine grain size contributed to toughness enhancement while a nanocomposite structure limited the decrease in toughness. Thus, design of a TiAlN coating with a high content of Al while retaining the cubic nature and a good control of the amount of second phase (amorphous AlN) to realize a nanocomposite structure can lead to coatings with high toughness and impact resistance.

References

[1] Zhang, S., Zhu, W., TiN coating of tool steels: a review, J. Mater. Process. Technol. 39 (1993) 165-177.

[2] Navinšek, B., Panjan, P., Milošev, I. Industrial applications of CrN (PVD) coatings deposited at high and low temperatures, Surf. Coat. Technol. 97 (1997) 182–191.

[3] PalDey, S., Deevi, S.C. Single layer and multi-layer wear resistant coatings of (Ti,Al)N:

a review, Mater. Sci. Eng., A 342 (2003) 58-79.

[4] Jehn, H.A. Multicomponent and multiphase hard coatings for tribological applications, Surf. Coat. Technol. 131 (2000) 433-440.

[5] Kim, C. W., Kim, K. H. Anti-oxidation properties of TiAlN film prepared by plasma-assisted chemical vapor deposition and roles of Al, Thin Solid Films 307 (1997) 113-119.

[6] Leyendecker, T., Lemmer, O, Esser, S., Ebberink, J. The development of the PVD coating TiAlN as a commercial coating for cutting tools, Surf. Coat. Technol. 48 (1991) 175-178.

[7] Stueber, M., Holleck, H., Leiste, H., Seemann, K., Ulrich, S., Ziebert, C. Concepts for the design of advanced nanoscale PVD multi-layer protective thin films, J Alloys Compd. 483 (2009) 321-333.

[8] Pemmasani, S.P., Valleti, K., Ramakrishna, M., Gundakaram, R. C., Rajulapati, K.V., Joshi, S.V. Characterization of multi-layer nitride coatings by electron microscopy and modulus mapping, Mater. Charact. 81 (2013) 7-18.

[9] Mayrhofer, P.H., Mitterer, C., Hultman, L., Clemens, H. Microstructural design of hard coatings, Prog. Mater. Sci. 51 (2006) 1032-1114.

[10] Kalss, W., Reiter, A., Derflinger, V., Gey, C., Endrino, J. L. Modern coatings in high performance cutting applications, Int. J. Refract. Met. Hard Mater. 24 (2006) 399-404.

[11] Jindal, P. C., Santhanam, A. T., Schleinkofer, U., Shuster, A. F. Performance of PVD TiN, TiCN, and TiAlN coated cemented carbide tools in turning, Int. J. Refract. Met. Hard Mater. 17 (1999) 163-170.

[12] Mayrhofer, P. H., Horling, A., Karlsson, L., Sjolen, J., Larsson, T., Mitterer, C., Hultman, L. Self-organized nanostructures in the Ti–Al–N system, Appl. Phys. Lett. 83 (2003) 2049-2051.

[13] Rachbauer, R., Massl, S., Stergar, E., Holec, D., Kiener, D., Keckes, J., Mayrhofer, P. H. Decomposition pathways in age hardening of Ti-Al-N films, J. Appl. Phys. 110 (2011) 023515.

[14] Veprek, S., Veprek-Heijman, M.J.G. Industrial applications of superhard nanocomposite coatings, Surf. Coat. Technol. 202 (2008) 5063–5073.

[15] Kimura, A., Hasegawa, H., Yamada, K., Suzuki, T. Effects of Al content on hardness, lattice parameter and microstructure of $Ti_{1-x}Al_xN$ films, Surf. Coat. Technol. 120 (1999) 438-441.

[16] Ding, X., Bui, C.T., Zeng, X.T. Abrasive wear resistance of $Ti_{1-x}Al_xN$ hard coatings deposited by a vacuum arc system with lateral rotating cathodes, Surf. Coat. Technol. 203 (2008) 680-684.

[17] Wüstefeld, Ch., Rafaja, D., Klemm, V., Michotte, C., Kathrein, M. Effect of the aluminium content and the bias voltage on the microstructure formation in $Ti_{1-x}Al_xN$ protective coatings grown by cathodic arc evaporation, Surf. Coat. Technol. 205 (2010) 1345-1349.

[18] Horling, A. Hultman, L. M. Oden, J. Sjolen, L. Karlsson, Mechanical properties and machining performance of $Ti_{1-x}Al_xN$-coated cutting tools, Surf. Coat. Technol. 191 (2005) 384-392.

[19] Mayrhofer, P. H., Music, D., Schneider, J. M. Influence of the Al distribution on the structure, elastic properties, and phase stability of supersaturated $Ti_{1-x}Al_xN$, J. Appl. Phys. 100 (2006) 094906.

[20] Gîrleanu, M., Pac, M. J., Louis, P., Ersen, O., Werckmann, J., Rousselot, C., Tuilier, M. H. Characterisation of nano-structured titanium and aluminium nitride coatings by indentation,

transmission electron microscopy and electron energy loss spectroscopy, Thin Solid Films 519 (2011) 6190-6195.

[21] Musil, J., Hrubý, H. Superhard nanocomposite $Ti_{1-x}Al_xN$ films prepared by magnetron sputtering, Thin Solid Films 365 (2000) 104-109.

[22] Kutschej, K., Mayrhofer, P. H., Kathrein, M., Polcik, P., Tessadri, R., Mitterer, C. Structure, mechanical and tribological properties of sputtered $Ti_{1-x}Al_xN$ coatings with $0.5 \leq x \leq 0.75$, Surf. Coat. Technol. 200 (2005) 2358-2365.

[23] Barshilia, H.C., Prakash, M. S., Jain, A., Rajam, K. S. Structure, hardness and thermal stability of TiAlN and nanolayered TiAlN/CrN multi-layer films, Vacuum 77 (2005) 169-179.

[24] Fox-Rabinovich, G. S., Beake, B. D., Endrino, J. L., Veldhuis, S. C., Parkinson, R., Shuster, L. S., Migranov, M. S. Effect of mechanical properties measured at room and elevated temperatures on the wear resistance of cutting tools with TiAlN and AlCrN coatings, Surf. Coat. Technol. 200 (2006) 5738-5742.

[25] Oden, M., Rogstrom, L., Knutsson, A., Terner, M. R., Hedstrom, P., Almer, J., Ilavsky, J. In situ small-angle x-ray scattering study of nanostructure evolution during decomposition of arc evaporated TiAlN coatings, Appl. Phy. Lett. 94 (2009) 053114-053114.

[26] Schüler, A., Thommen, V., Reimann, P., Oelhafen, P., Francz, G., Zehnder, T., Düggelin, M., Mathys, D., Guggenheim, R. Structural and optical properties of titanium aluminum nitride films ($Ti_{1-x}Al_xN$), J. Vac. Sci. Technol. A. 19 (2001) 922-929.

[27] Valleti, K., Krishna, D. M., Joshi, S. V. Functional multi-layer nitride coatings for high temperature solar selective applications, Sol. Energy Mater. Sol. Cells 121 (2014) 14–21.

[28] Barshilia, H. C., Selvakumar, N., Rajam, K. S., Biswas, A. Optical properties and thermal stability of TiAlN/AlON tandem absorber prepared by reactive DC/RF magnetron sputtering, Sol. Energy Mater. Sol. Cells 92 (2008) 1425-1433.

[29] Jose, F., Ramaseshan, R., Dash, S., Sundari, S. T., Jain, D., Ganesan, V., Raj, B. Significance of Al on the morphological and optical properties of $Ti_{1-x}Al_xN$ thin films, Mater. Chem. Phys. 130 (2011) 1033-1037.

[30] Henry, P., Pac, M.J., Rousselot, C., Tuilier, M. H. Wear mechanisms of titanium and aluminium nitride coatings: A microtribological approach, Surf. Coat. Technol. 223 (2013) 79-86.

[31] Sangiovanni, D. G., Chirita, V., Hultman, L. Toughness enhancement in TiAlN-based

quarternary alloys, Thin Solid Films 520(11) (2012) 4080-4088.

[32] Bull, S. J. Correlation of microstructure and properties of hard coatings, Vacuum, 43(5), (1992) 387-391.

[33] Powder Diffraction File (PDF) No. 04-005-5251, PDF-4+ Database, International Centre for Diffraction Data (ICDD), Newton Square, PA, USA; USA 2010.

[34] Aliaj, F., Syla, N., Avdiaj, S., and Dilo, T. Effect of bias voltage on microstructure and mechanical properties of arc evaporated (Ti, Al) N hard coatings. Bulletin of Materials Science, 36(3), (2013) 429-435.

[35] Sato, K., Ichimiya, N., Kondo, A., Tanaka, Y. Microstructure and mechanical properties of cathodic arc ion-plated (Al, Ti) N coatings. Surface and Coatings Technology, 163, (2003) 135-143.

[36] Vlasveld, A. C., Harris, S. G., Doyle, E. D., Lewis, D. B., Munz, W. D. Characterisation and performance of partially filtered arc TiAlN coatings. Surface and Coatings Technology, 149(2), (2002) 217-224.

[37] Cheng, Y. H., Tay, B. K., Lau, S. P., Shi, X. Influence of substrate bias on the structure and properties of (Ti, Al) N films deposited by filtered cathodic vacuum arc. Journal of Vacuum Science & Technology A, 19(3), (2001) 736-742.

[38] Ahlgren, M., Blomqvist, H. Influence of bias variation on residual stress and texture in TiAlN PVD coatings. Surface and Coatings Technology, 200(1), (2005)157-160.

[39] Hogmark, S., Jacobson, S., Larsson, M. Design and evaluation of tribological coatings. Wear, 246(1), (2000) 20-33.

[40] Andersson, J.M., Vetter, J., Müller, J., Sjölén, J. Structural effects of energy input during growth of $Ti_{1-x}Al_xN$ ($0.55 \leq x \leq 0.66$) coatings by cathodic arc evaporation, Surf. Coat. Technol. 240 (2014) 211-220.

[41] Jungk, J.M., Boyce, B.L., Buchheit, T.E., Friedmann, T.A., Yang, D., Gerberich, W.W. Indentation fracture toughness and acoustic energy release in tetrahedral amorphous carbon diamond-like thin films, Acta Mater. 54 (2006) 4043–4052.

[42] Santana, A. E., Karimi, A., Derflinger, V. H., Schütze, A. Relating hardness-curve shapes with deformation mechanisms in TiAlN thin films enduring indentation, Mater. Sci. Eng., A, 406(1) (2005) 11-18.

[43] ASTM Standard Test Method for Adhesion Strength and Mechanical Failure modes of Ceramic Coatings by Quantitative Single Point Scratch Testing: C 1624-05.

[44] Bull, S. J. Failure mode maps in the thin film scratch adhesion test, Tribol. Int. 30 (1997) 491-498.

[45] Xie, Z.H., Hoffman, M., Munroe, P., Singh, R., Bendavid, A., Martin, P.J. Microstructural response of TiN monolithic and multi-layer coatings during microscratch testing, J. Mater. Res. 22 (2007) 2312-2318.

[46] Schwaller, P., Haug, F. J., Michler, J., Patscheider, J. Nanocomposite hard coatings: Deposition issues and validation of their mechanical properties, Adv. Eng. Mater. 7 (2005) 318-322.

[47] Sundgren, J. E. Structure and properties of TiN coatings, Thin Solid Films 128 (1985) 21-44.

[48] Hernandez-Torres, J., Garcia-Gonzalez, L., Zamora-Peredo, L., Hernandez-Quiroz, T., Sauceda-Carvajal, A., Garcia-Ramirez, P. J., Flores-Ramirez, N. Analysis of hardness of nanocrystalline coatings of aluminum-rich $Ti_{1-x}Al_xN$, Bull. Mater. Sci. 35 (2012) 733-738.

[49] Wahlstrom, U., Hultman, L., Sundgren, J.E., Adibi, F., Petrov, I., Greene, J.E. Crystal growth and microstructure of polycrystalline $Ti_{1-x}Al_xN$ alloy films deposited by ultra-high-vacuum dual-target magnetron sputtering, Thin Solid Films 235 (1993) 62-70.

[50] Aliaj, F., Syla, N., Dilo, T., Avdiaj, S. The effect of Aluminum on the Microstructure and Mechanical properties of arc-evaporated $Ti_{1-x}Al_xN$ Coatings deposited on Cemented Carbide substrates, Physica Macedonica 61 (2012) 113-119

[51] Yonenaga, I., Shima, T., Sluiter, M. H. Nano-indentation hardness and elastic moduli of bulk single-crystal AlN, Jpn. J. Appl. Phys. 41 (2002) 4620-4621.

[52] Klostermann, H., Böcher, B., Fietzke, F., Modes, T., Zywitzki, O., Nanocomposite oxide and nitride hard coatings produced by pulse magnetron sputtering, Surf. Coat. Technol. 200 (2005) 760-764.

[53] Valleti, K., Subrahmanyam, A., Joshi, S. V., Phani, A. R., Passacantando, M., Santucci, S. Studies on phase dependent mechanical properties of dc magnetron sputtered TaN thin films: evaluation of super hardness in orthorhombic Ta_4N phase, J. Phys. D: Appl. Phys. 41 (2008) 045409.

[54] Gîrleanu, M., Pac, M. J., Ersen, O., Werckmann, J., Arnold, G., Rousselot, C., Tuilier, M. H. The role of structural properties on damage behaviour of titanium and aluminium nitride coatings: An EXAFS and TEM study, Surf. Coat. Technol. 204 (2010) 2042-2045.

[55] Ohnuma, H., Nihira, N., Mitsuo, A., Toyoda, K., Kubota, K., Aizawa, T. Effect of aluminum concentration on friction and wear properties of titanium aluminum nitride films, Surf. Coat. Technol. 177 (2004) 623-626.

[56] Mayrhofer, P. H., Music, D., Schneider, J. M., Ab initio calculated binodal and spinodal of cubic $Ti_{1-x}Al_xN$, Appl. Phys. Lett. 88 (2006) 071922.

[57] Beake, B. D., Smith, J. F., Gray, A., Fox-Rabinovich, G. S., Veldhuis, S. C.,Endrino, J. L. Investigating the correlation between nano-impact fracture resistance and hardness/modulus ratio from nanoindentation at 25–500° C and the fracture resistance and lifetime of cutting tools with $Ti_{1-x}Al_xN$(x= 0.5 and 0.67) PVD coatings in milling operations, Surface and Coatings Technology, 201(8), (2007) 4585-4593.

[58] Guo, J., Liu, Z., Wang, S., Shen, Y. The grain refining effect of energy competition and the amorphous phase in nanocomposite materials, Scri. Mater. 69 (2013) 662-665.

Chapter 6 Multi-layered TiAlN coatings: Effect of layer composition and architecture on toughness and impact resistance

6.1 Introduction

The performance and life of tools and their components have shown noticeable improvement with the application of Titanium Aluminium nitride based coatings [1, 2]. There have been increasing efforts to further improve the performance of these coatings through multi-layering and/or nanostructuring. In this respect, there have been numerous studies on TiAlN based multi-layer coatings where TiAlN was co-deposited along with various nitrides or metals to obtain improved properties when compared with monolithic TiAlN coatings. Various multi-layer combinations with TiAlN found in literature are TiAlN/TiAlCN [3], TiAlN/TiNbN [4], TiAlN/TiN [5-9], AlN/TiN/TiAlN [10], TiAlN/CrN [11-13], TiAlN/Ti [14-16], TiAlN/Al [16], TiAlN/Mo [17-18], TiAlN/Zr [19], TiAlN/Ta [20]. While the multi-layers comprising TiAlN and metal layers show high ductility and low residual stresses due to which they can be built up to large thicknesses, they are not suitable for use at high temperatures as they tend to get oxidized. TiAlN/ nitride multi-layers are more widely used as they are more stable and show good mechanical strength at high temperatures. Among these, TiN- TiAlN multi-layer coatings have been widely studied. These coatings have been reported to lead to improvements in hardness [21], thermal stability [5, 6], wear resistance [8, 10], corrosion resistance [22] and machining life [21, 23, 24].

The improvement in properties have been attributed to different factors, which include hardening on account of dislocation pileup at the interfaces between two layers, increased crack deflection at layer interfaces and modulus differences between layers in multi-layers leading to dislocation pinning (dislocation remains in lower modulus layer) due to the varying stress fields between the layers. While there have been many reports on the mechanical properties of TiN-TiAlN multi-layers, only a few studies exist on the underlying mechanisms [25-27] and on actual machining studies in TiN-TiAlN multi-layers which report improved cutting performance with reduced bi-layer periods [7, 21, 28]. There are a few studies which propose mechanisms of crack deflection at interfaces during machining [28, 29]. Bouzakis *et. al.* correlated machining tests with nano-impact tests and attributed the improvement in multi-layers due to the increased number of interfaces, creating barriers to crack growth and leading to reduction in brittleness [29]. However, the above reports did not study the underlying deformation behaviour during machining tests. In the present study, an attempt has been made to develop an impact resistant TiAlN based multi-layer coating and understand its behaviour in nano-impact testing. A study of sub-surface deformation behaviour was carried out by observing the microstructural changes in the coatings after indentation. Since the purpose of the TiAlN layer in the multi-functional, multi-layer coating is for improved fatigue and impact resistance, the layers comprising the multi-layer were chosen so as to enhance the impact resistance and toughness of the TiAlN coating. The rationale behind the choice of layers is explained in section 6.1. Two sets of multi-layer coatings were deposited, the first one comprising TiN and $Ti_{0.35}Al_{0.65}N$ layers (designated TiN-TiAlN ML) while the second set comprising $Ti_{0.7}Al_{0.3}N$ and $Ti_{0.47}Al_{0.53}N$ layers (designated $Ti_{1-x}Al_xN$ ML).

6.2 Deposition

The TiN-TiAlN ML multi-layer coatings were deposited with the composition of the layers chosen based on the measured modulus of the individual monolithic TiAlN coatings such that there is a large variation in the modulus of the two layers. TiN and $Ti_{0.35}Al_{0.65}N$ were chosen as the two alternating layers in view of the large difference in the modulus values of 415 GPa and 258 GPa for TiN and $Ti_{0.35}Al_{0.65}N$, respectively. $Ti_{1-x}Al_xN$ ML coatings are comprised of $Ti_{0.7}Al_{0.3}N$ and $Ti_{0.47}Al_{0.53}N$ layers with modulus values of 411 and 360 GPa, respectively. These two layers were chosen in view of their same crystal structure and the presence of Al in both the layers. Both sets of multi-layer coatings were deposited with varying bi-layer period (Λ) thicknesses of 160,100, 80, and 40 nm and designated as Λ-160, Λ-100, Λ-80 and Λ-40, with the individual layer thicknesses being equal to $\Lambda/2$, i.e. 80, 50, 40 and 20 nm, respectively. The actual layer thicknesses varied slightly from the above values. The bi-layer repeat period (Λ) mentioned above is the combined thickness of the two alternating layers in the multi-layer coating. The deposition conditions were the same as in Sec.3.1, except for a cyclic variation of the cathode on-off times and cathode currents to achieve the multi-layer structure; details of which are given in Table 4. Deposition of TiN-TiAlN ML coatings comprised an on-off cycle of the Ti and $Ti_{0.33}Al_{0.67}$ cathodes while the $Ti_{1-x}Al_xN$ ML coatings were deposited by a cyclic variation of the Ti and $Ti_{0.33}Al_{0.67}$ cathode currents; the currents used for the respective layer compositions are as earlier mentioned in Table 3. All the coatings had a thickness in the range 3.7 - 3.8 µm, except in case of TiN-TiAlN ML Λ-40 which had a thickness of 2.7 µm.

Table 4: Sample designations and deposition times for each of the layers in TiN-TiAlN ML and $Ti_{1-x}Al_xN$ ML coatings corresponding to different bi-layer periods

Coating	**Deposition time (sec)**	
	Layer 1 (TiN)	Layer 2 ($Ti_{0.35}Al_{0.65}N$)
TiN-TiAlN ML Λ-160	434	192
TiN-TiAlN ML Λ-100	228	120
TiN-TiAlN ML Λ-80	217	96
TiN-TiAlN ML Λ-40	108	46
	Layer 1 ($Ti_{0.7}Al_{0.3}N$)	Layer 2 ($Ti_{0.47}Al_{0.53}N$)
$Ti_{1-x}Al_xN$ ML Λ-160	247	175
$Ti_{1-x}Al_xN$ ML Λ-100	171	118
$Ti_{1-x}Al_xN$ ML Λ-80	114	80
$Ti_{1-x}Al_xN$ ML Λ-40	57	40

6.3 Crystal structure

Grazing incidence X-ray diffractograms of the TiN-TiAlN ML and $Ti_{1-x}Al_xN$ ML coatings are shown in Fig. 6.1 (a) and (b), respectively. Both the TiN-TiAlN ML and $Ti_{1-x}Al_xN$ ML coatings show a structure that corresponds to FCC TiAlN [JCPDS no 004-55-460].

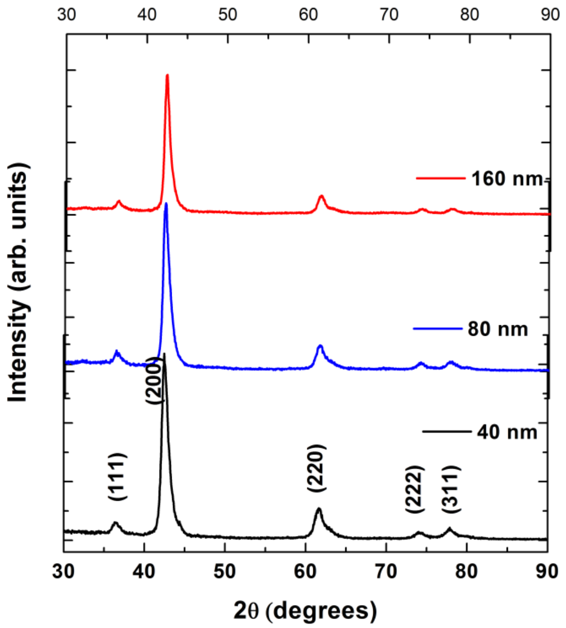

Fig. 6.1 (a) Grazing incidence x-ray diffractograms of TiN-TiAlN ML coatings at different bi-layer periods showing the presence of FCC TiAlN.

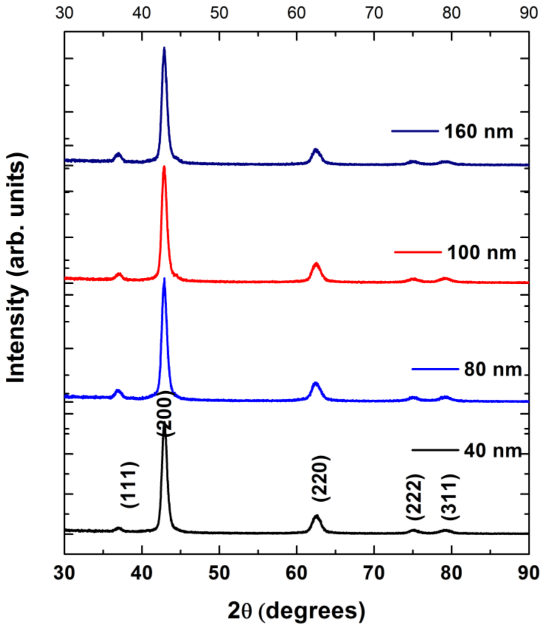

Fig. 6.1 (b) Grazing incidence x-ray diffractograms of $Ti_{1-x}Al_xN$ ML coatings at different bi-layer periods showing the presence of FCC TiAlN.

Residual stress

Both the sets of multi-layer coatings showed presence of compressive residual stresses, with the trend as shown in Fig. 6.2. The stress variation with bi-layer period is higher in case of the TiN-

TiAlN ML coatings (- 8 to - 6.6 GPa) than the $Ti_{1-x}Al_xN$ ML (- 6.3 to - 5.9 GPa) coatings. The higher stress seen in case of the TiN-TiAlN ML coatings can be attributed to interlayer stresses due to the high difference in modulus apart from the different thermal expansion co-efficients of TiN (9.4 x 10^{-6} K^{-1}) and TiAlN (7.5 x 10^{-6} K^{-1}) [1]. There is an increase in residual stress with reducing bi-layer period in case of the TiN-TiAlN ML (Fig. 6.2 (a)) coatings while there is no significant variation in case of the $Ti_{1-x}Al_xN$ ML coatings (Fig. 6.2 (b)). A maximum compressive stress of 8 GPa was observed in case of the TiN-TiAlN ML coating with 40 nm bi-layer period. The high values of stress seen at lower bi-layer periods could be attributed to epitaxial stress contributions at interfaces which is dominant at lower bi-layer periods [30].

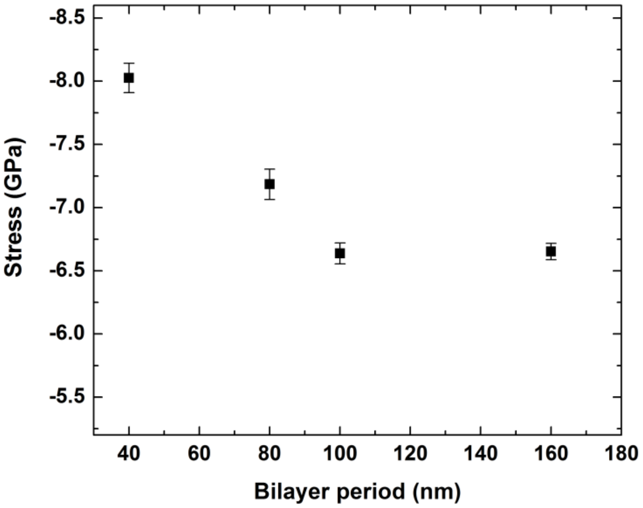

Fig. 6.2 (a) Variation of residual stress with bi-layer period in TiN-TiAlN ML coatings.

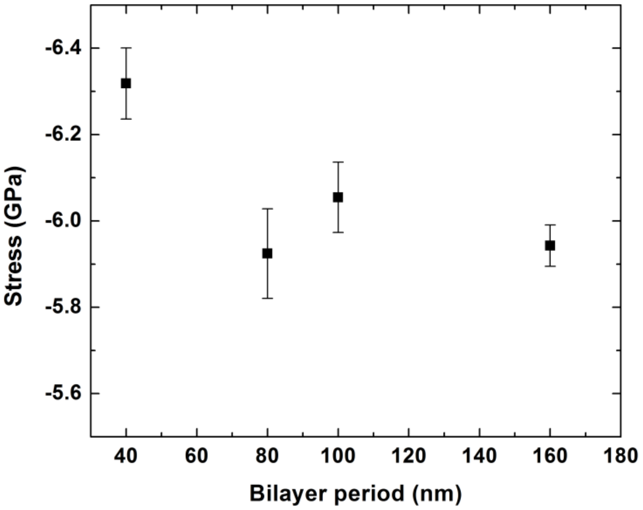

Fig. 6.2 (b) Variation of residual stress with bi-layer period in $Ti_{1-x}Al_xN$ ML coatings.

6.4 Mechanical properties

Hardness and modulus

Figs. 6.3 (a) and (b) show the variation in hardness and modulus of the TiN-TiAlN ML and $Ti_{1-x}Al_xN$ ML coatings, respectively. The TiN-TiAlN ML coatings show a linear increase in hardness and modulus with reducing bi-layer period while the $Ti_{1-x}Al_xN$ ML coatings do not show much variation with bi-layer period. The values of hardness (H) and modulus (E) in the TiN-TiAlN ML coatings are in the range 26.2 ± 1 GPa to 29.6 ± 0.8 GPa and 342 ± 11 GPa to 376 ± 9 GPa for the bi-layer period range 160 nm to 40 nm, respectively. These values are higher than the composite H and E values of 23.6 GPa and 333 GPa, respectively, measured in the constituent layers. The increase in H and E could be attributed to stresses due to the modulus difference and increasing interfacial strain between the layers with reducing bi-layer period. Some contribution to the hardness due to the Hall-Petch effect on account of reducing bi-layer period is also expected. The values of H and E in the $Ti_{1-x}Al_xN$ ML coatings are in the range 32 ± 1.3 GPa to 33 ± 1.26 GPa and 421 ± 14 GPa to 431 ± 15.34 GPa, respectively, while the composite H and E values of the constituent layers are 31.7 GPa and 414 GPa, respectively. Thus, there is no hardening due to multi-layering taking place in case of the $Ti_{1-x}Al_xN$ ML coatings.

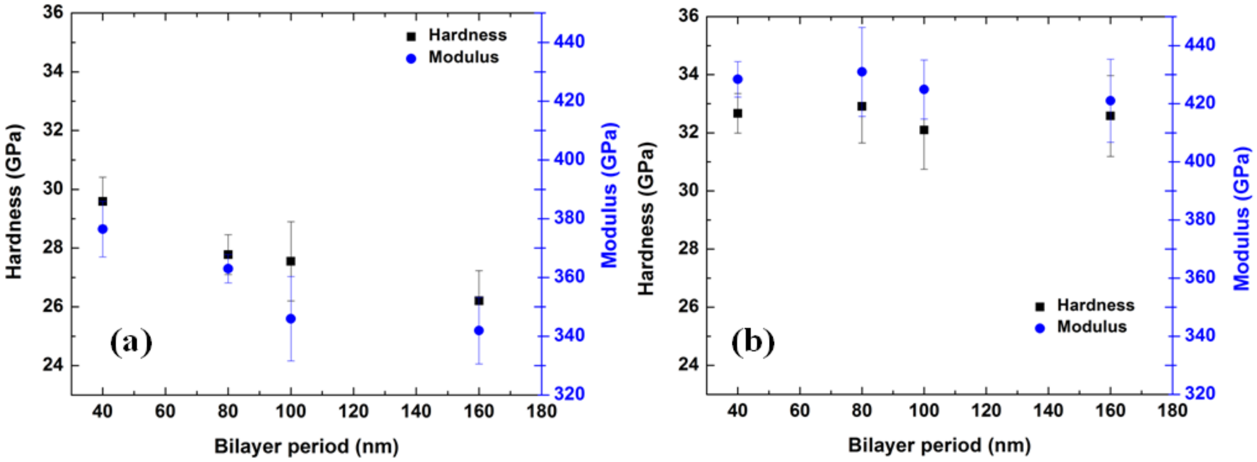

Fig. 6.3 Variation of hardness and modulus with bi-layer period in (a) TiN-TiAlN multi-layers (b) $Ti_{1-x}Al_xN$ multi-layers.

6.5 Microstructural studies

The cross section of the multi-layer coatings was studied in the dual beam SEM while the surface microstructure after scratch testing and the cross section of the deformed track were observed in the SEM and FIB, respectively. Details of the procedure followed for FIB milling and observation are given in Chapter. 3. Figs. 6.4 and 6.5 show the cross sections of representative TiN-TiAlN ML and $Ti_{1-x}Al_xN$ ML coatings with various bi-layer periods, respectively. The cross sections show good interfacial bonding between the substrate and the TiN adhesion layer and among the individual layers as well in both the sets of coatings.

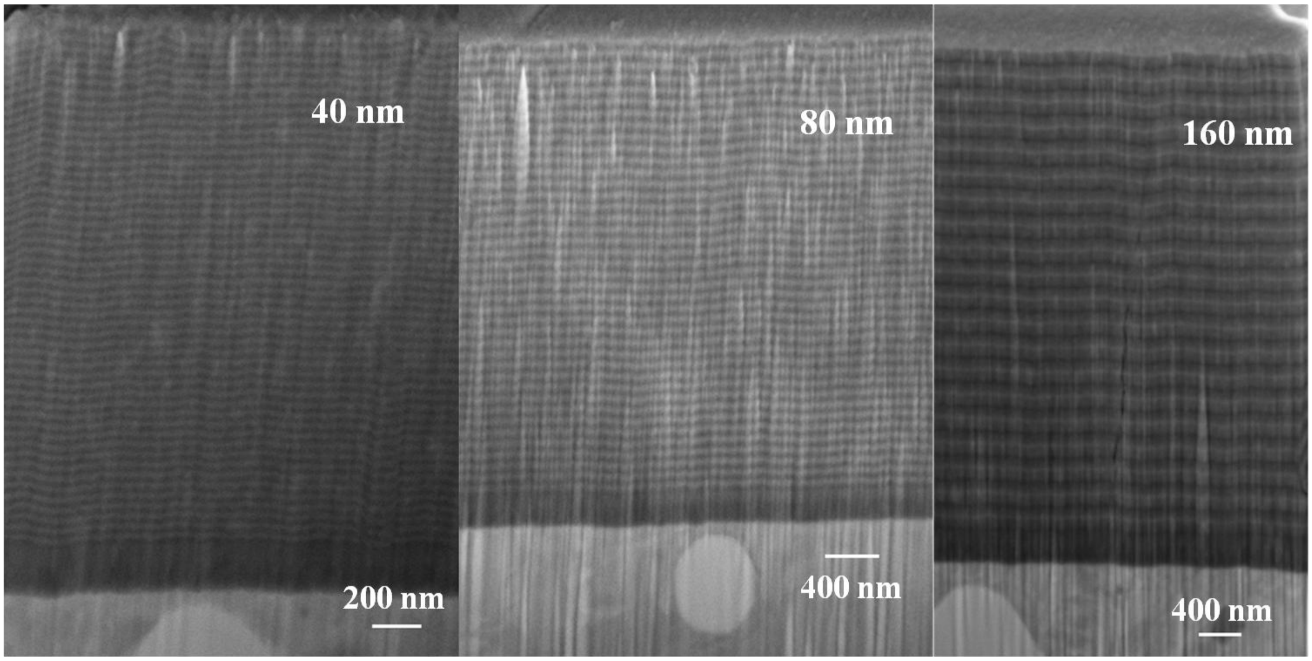

Fig. 6.4 Cross sectional SEM images of TiN-TiAlN ML coatings (a) Λ-40 nm, (b) Λ-80 nm, and (c) Λ-160 nm.

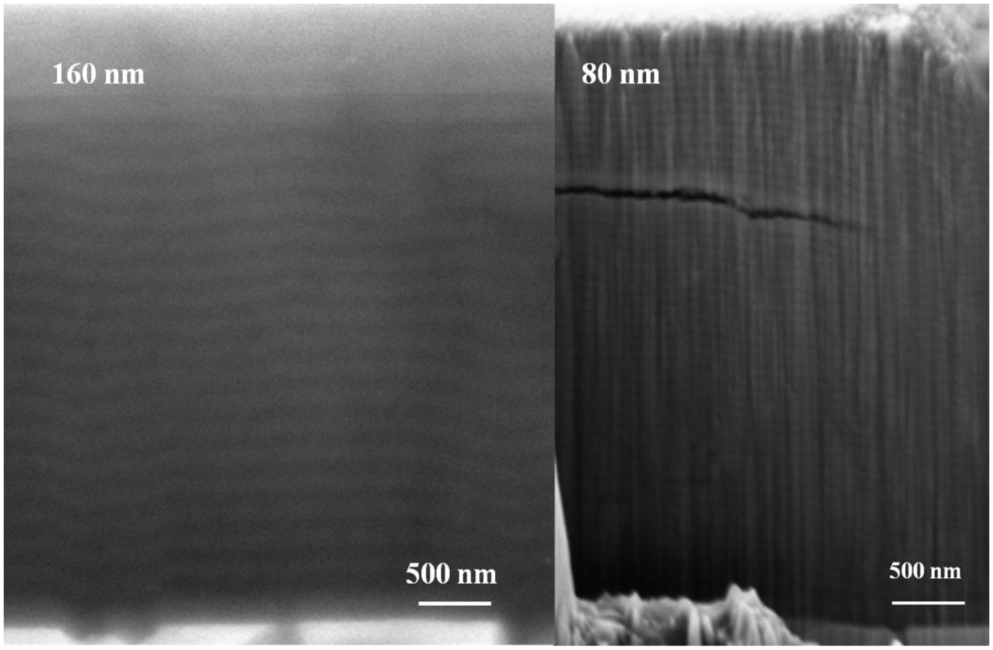

Fig. 6.5 Cross sectional SEM images of $Ti_{1-x}Al_xN$ ML coatings (a) Λ-160 nm and (b) Λ-80 nm.

Scratch testing and post-scratch observation

Progressive load scratch tests were carried out to determine the adhesion and to observe the deformation modes in the multi-layer coatings. The multi-layer coatings showed good adhesion with the critical load (LC_2) for the multi-layer coatings found to be in the range of 120-140 N. The scratch tracks were examined under SEM. Fig. 6.6 shows representative SEM images of the post scratch deformation seen in the TiN-TiAlN ML coatings at the point of first chipping or crack formation.

The scratch tracks in the multi-layer coatings show Chevron tensile cracks along with small lateral cracks at the initial stage followed by conformal and buckling cracks at higher loads. Though there was chipping observed, there was minimal buckling spallation or wedging spallation unlike the large spallation observed in a few of the monolithic $Ti_{1-x}Al_xN$ coatings. The degree of chipping also decreased with reducing bi-layer period in the TiN-TiAlN ML coatings as seen in Fig. 6.6. Large chipping seen in case of Λ-160 coating gave way to moderate chipping at Λ-80 with a further reduction in chipping seen in case of Λ-40 coating. The width of the scratch tracks in the multi-layer coatings at the point of first chipping (LC_1) was also found to decrease with reducing bi-layer period (Table 5) when compared to the individual monolithic coatings indicating an increase in resistance to deformation with multi-layering.

Table 5: Width of scratch tracks at LC_1 in monolithic and multi-layer TiN-TiAlN coatings

Coating	**Width of track at LC_1** (μm)
TiN	109
$Ti_{0.35}Al_{0.65}N$	94
TiN-TiAlN Λ-160	85
TiN-TiAlN Λ-80	77

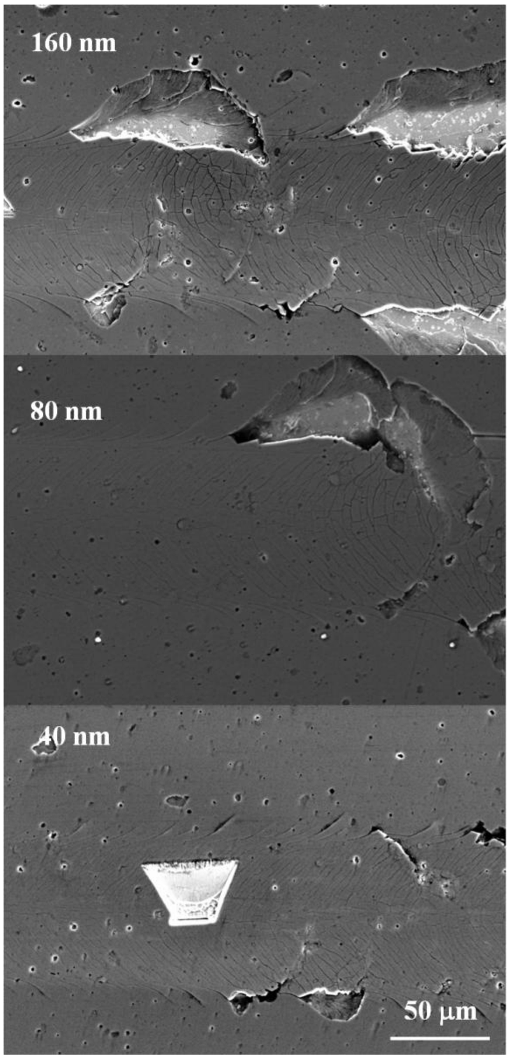

Fig. 6.6 Representative SEM images of scratch deformation in the TiN-TiAlN ML coatings.

FIB cross sections of the scratch tracks in three TiN-TiAlN ML coatings are shown in Fig. 6.7 All the three coatings exhibit crack deflection as a result of scratch deformation. The crack deflection in the Λ-160 coating is much less compared to the Λ-80 and Λ-40 coatings and the crack openings were wider than in the latter two coatings. The Λ-80 and Λ-40 coatings also show crack redirection at the interlayer interfaces with the deflection being more prominent in the Λ-40 coating as seen in Fig. 6.7(b). This suggests that the resistance to deformation at lower bi-layer periods is enhanced.

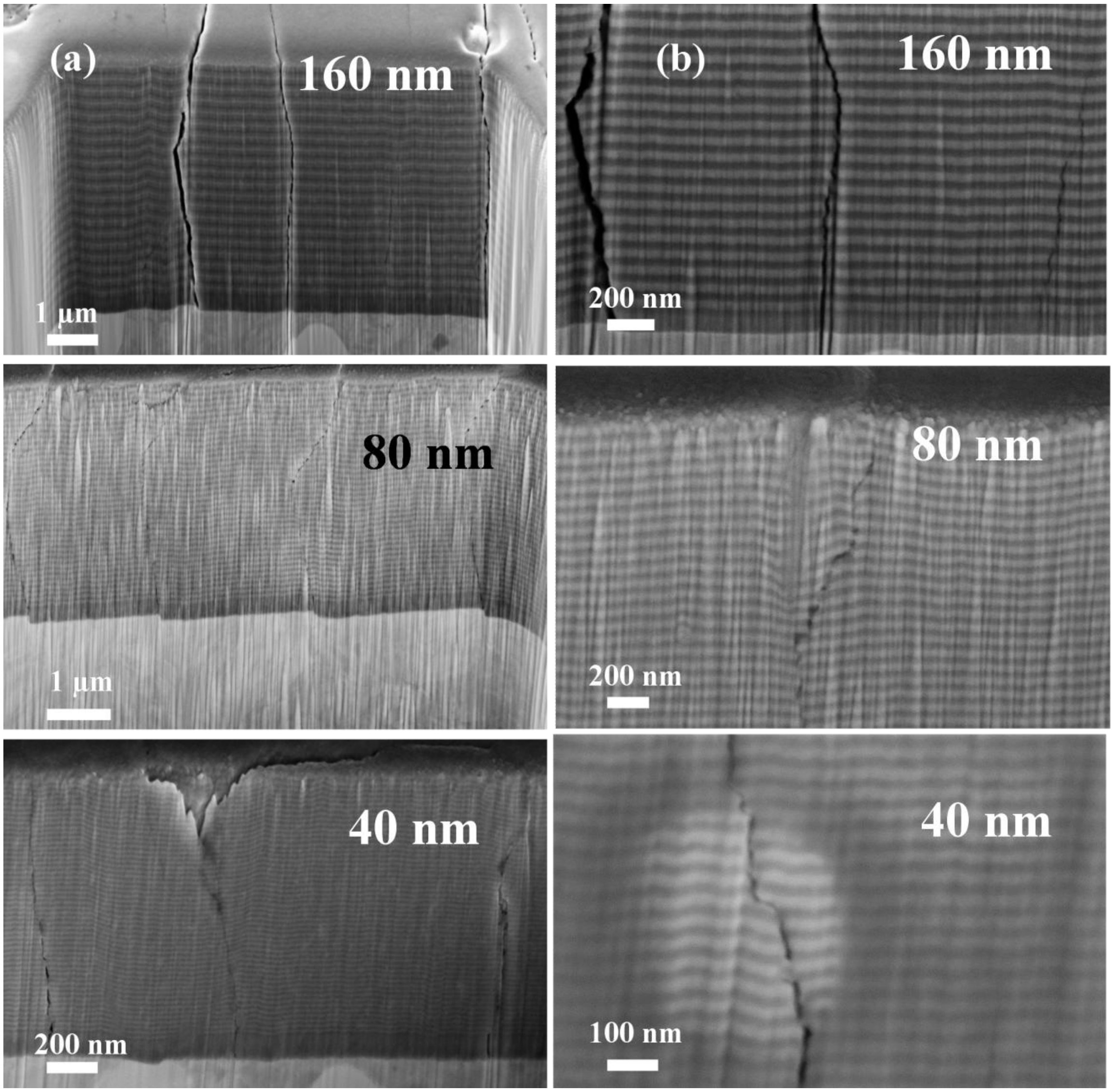

Fig. 6.7 SEM micrographs of cross section below scratch track in TiN-TiAlN ML coatings at various bi-layer periods (a) Entire coating cross section and interface with substrate (b) Magnified images of cross section showing crack redirection at layer interfaces.

6.6 Nano-impact testing

Nano-impact tests were carried out to estimate the impact resistance of the multi-layer coatings. The tests were carried out on both sets of multi-layer coatings with a cube corner indenter at the same parameters that were used in testing the monolithic TiAlN coatings. The final impact depths and cracking probability were calculated and plotted to study their variation with bi-layer period. Fig. 6.8 shows representative plots of impact depth vs. time obtained at a load of 10 mN on the multi-layer coatings. From the curves, it can be inferred that the impact resistance at lower bi-layer periods is higher as seen from the lower final depths and fewer cracking events (seen as abrupt steps in the impact curves).

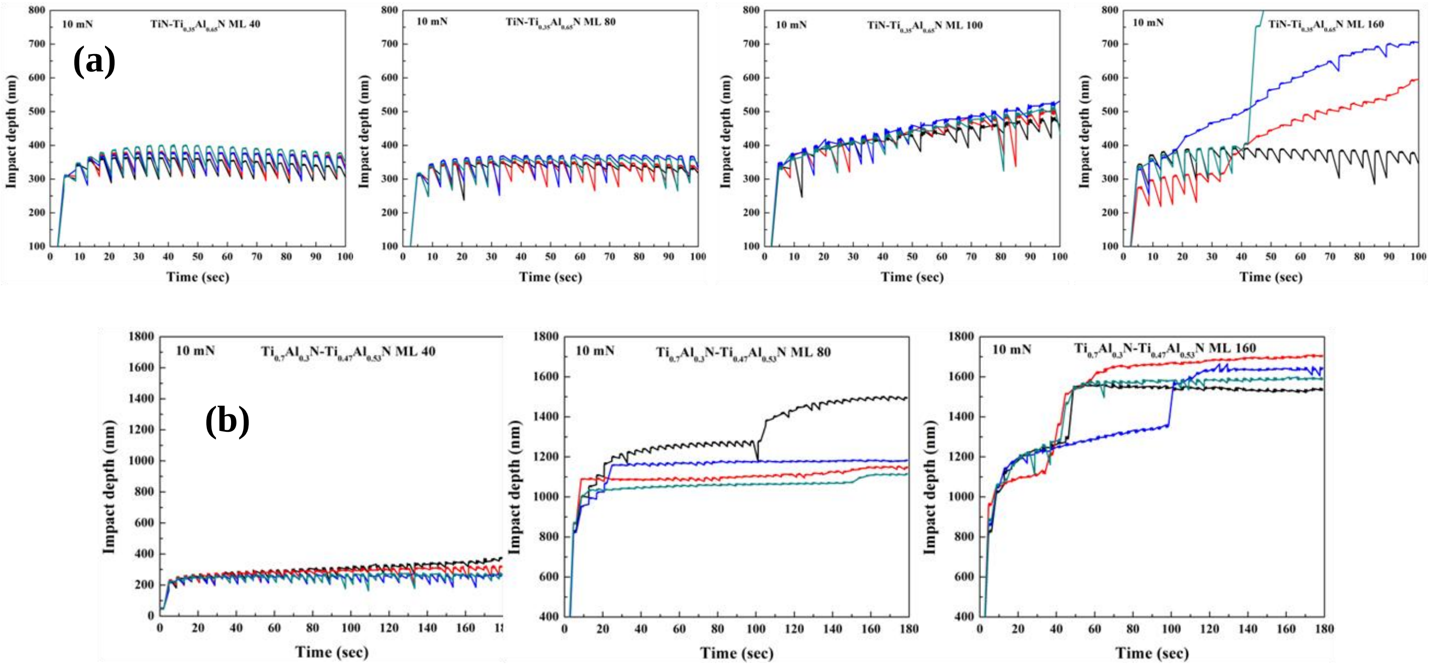

Fig. 6.8 Representative plots showing variation of impact depth with time in (a) TiN-TiAlN ML coatings and (b) $Ti_{1-x}Al_xN$ ML coatings.

The variation in final impact depth with bi-layer period in both sets of multi-layer coatings is shown in Fig. 6.9. The final impact depth showed a reduction with bi-layer period, indicating an increase in impact resistance with decreasing bi-layer period. The reduction in impact depth at lower bi-layer periods was more prominent in case of the $Ti_{1-x}Al_xN$ ML coatings. Comparing both sets of coatings, the highest impact resistance was shown by the Λ-40 $Ti_{1-x}Al_xN$ ML coating followed closely by the Λ-80 and Λ-40 TiN-TiAlN ML coatings, respectively.

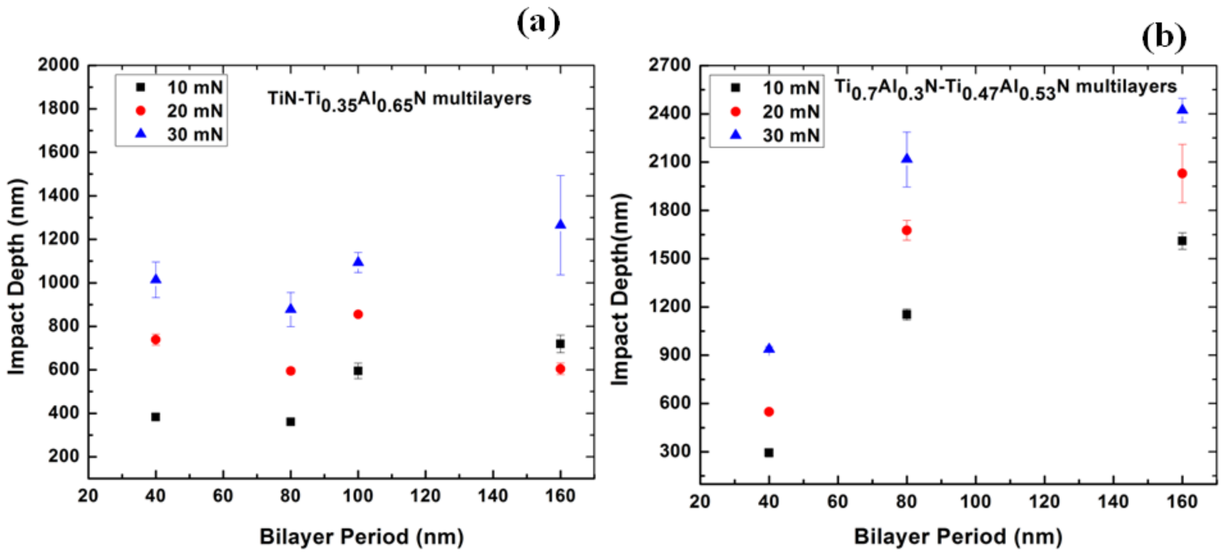

Fig. 6.9 Variation of impact depth with bi-layer period in (a) TiN-TiAlN ML and (b) $Ti_{1-x}Al_xN$ ML coatings at different loads.

The crack probability in the coatings was estimated from the ratio of cracking events to the total number of the tests and is shown in Fig. 6.10. The Λ-40 TiN-TiAlN ML coating showed the least number of cracking events followed by the Λ-40 $Ti_{1-x}Al_xN$ ML, Λ-80 TiN-TiAlN ML and Λ-100 TiN-TiAlN ML coatings. The crack probability was lower at lower bi-layer periods in both the sets of coatings, with the TiN-TiAlN ML coatings showing lower propensity for cracking compared to the $Ti_{1-x}Al_xN$ ML coatings. This can be attributed to higher ductility in case of the former on account of the presence of TiN (which is more ductile compared to TiAlN) as one of the constituent layers. However, the Λ-40 $Ti_{1-x}Al_xN$ ML coating shows low cracking probability even though the constituent layers are less ductile, which can be explained on the basis of the enhanced strain accommodation due to the increased number of interfaces.

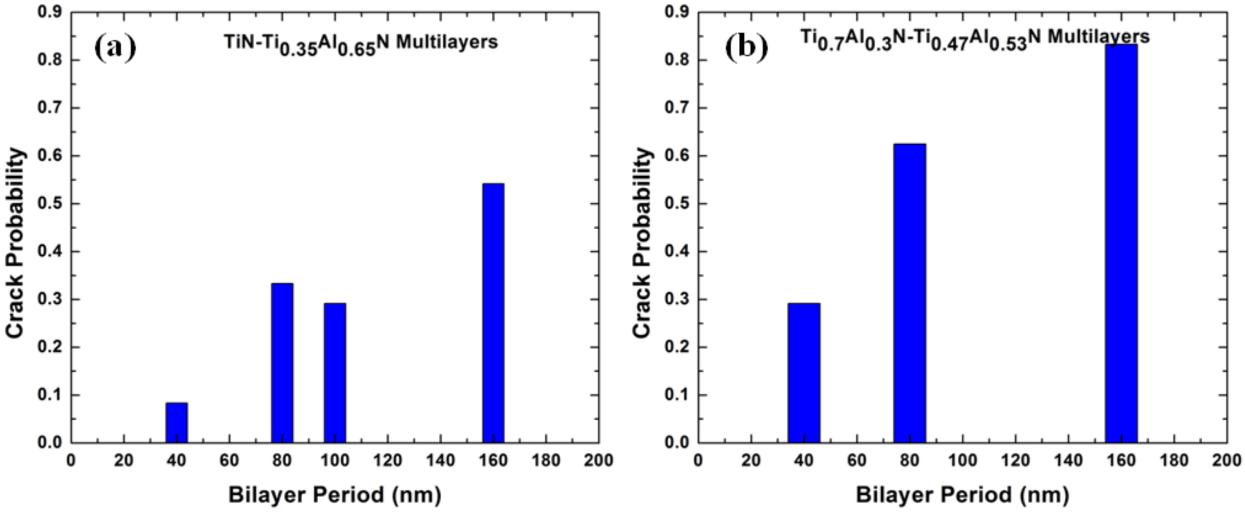

Fig. 6.10 Crack probability at different bi-layer periods in (a) TiN-TiAlN ML and (b) $Ti_{1-x}Al_xN$ ML coatings.

6.7 Discussion

6.7.1 Mechanical properties: Role of interlayer modulus and multi-layering

The TiN-TiAlN ML coatings showed a linear increase in hardness and modulus with reducing bi-layer period with the values much above the composite values expected from the rule of mixtures. Such a behaviour was not seen in case of the $Ti_{1-x}Al_xN$ ML coatings which did not show significant variation with change in bi-layer period and also did not show any hardening above the values expected from the rule of mixtures.

This difference seen in TiN-TiAlN ML coatings can be explained on the basis of the large modulus differences which can lead to Kohler hardening [31] and the presence of coherency strains on account of the large difference in lattice parameters between the TiN and $Ti_{0.35}Al_{0.65}N$ layers which leads to stress fields that restrict dislocation movements [32]. Contribution due to Hall-Petch strengthening is not significant since there was no hardness increase seen even at lower bi-layer periods in case of the $Ti_{1-x}Al_xN$ ML coatings. The requirement for an increased hardness for improved performance is not necessarily true in all cases as the $Ti_{1-x}Al_xN$ ML coatings showed improved impact resistance at low bi-layer periods even though an hardness increase was not observed. This agrees with earlier studies which also reported improvement in properties for multi-layers even in the absence of a hardness enhancement [8, 10, 24, 25].

6.7.2 Deformation behaviour: Effect of multi-layering and layer composition

Indentation tests were carried out on multi-layer coatings and monolithic coatings of the constituent layers and observed under SEM to understand the nature of deformation in the above coatings. SEM micrographs of indentation impressions on the above coatings are shown in Fig.6.11. The TiN-TiAlN ML coatings show major pileup with negligible chipping at the indent edge due to higher ductility of the coatings (since TiN is one of the layers) while the $Ti_{1-x}Al_xN$ ML coatings show some chipping at the indent edges with minor pileup. The monolithic $Ti_{0.7}Al_{0.3}N$ and $Ti_{0.47}Al_{0.53}N$ coatings show radial cracks and extensive chipping at the indent edges. The reduced chipping and cracking in case of $Ti_{1-x}Al_xN$ ML coatings, which comprise of the same above two coatings as alternating layers, is due to the increased plasticity and toughness on account of the increase in interfaces.

To further understand the reasons behind the above differences during indentation and impact testing, FIB milling was carried out at the centre of the indent to observe the nature of subsurface deformation.

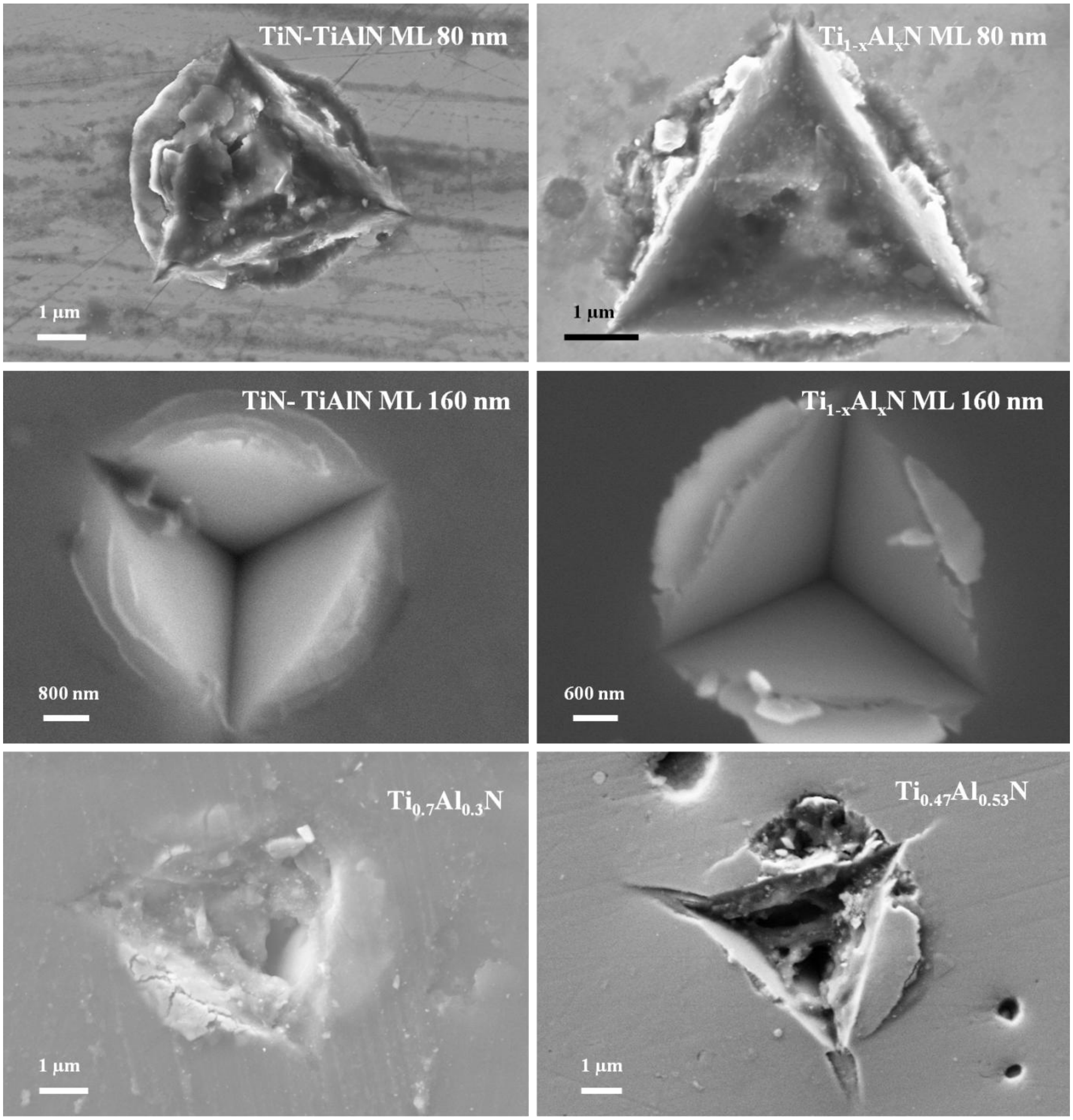

Fig. 6.11 SEM micrographs of indents on TiN-TiAlN ML, $Ti_{1-x}Al_xN$ ML and individual monolithic coatings.

FIB cross sections of indents carried out at a fixed load of 400 mN on a $Ti_{0.47}Al_{0.53}N$ monolithic coating, as well as TiN-TiAlN ML and $Ti_{1-x}Al_xN$ ML coatings having an identical bi-layer period of 80 nm, are shown in Fig. 6.12. The monolithic $Ti_{0.47}Al_{0.53}N$ coating shows open radial cracks below the substrate. Both the TiN-TiAlN ML and $Ti_{1-x}Al_xN$ ML coatings show bending of the multi-layers around the indent edge, with the amount of bending being higher by about

30% in case of the TiN-TiAlN ML coating. The TiN-TiAlN ML coatings can accommodate more strain on account of their inherent ductility due to the presence of TiN as one of the constituent layers. The TiAlN multi-layers showed improved resistance to deformation over monolithic TiAlN coatings, even in the absence of an increase in hardness which can be attributed to the increased number of interfaces that act as barriers to deformation and lead to crack deflection.

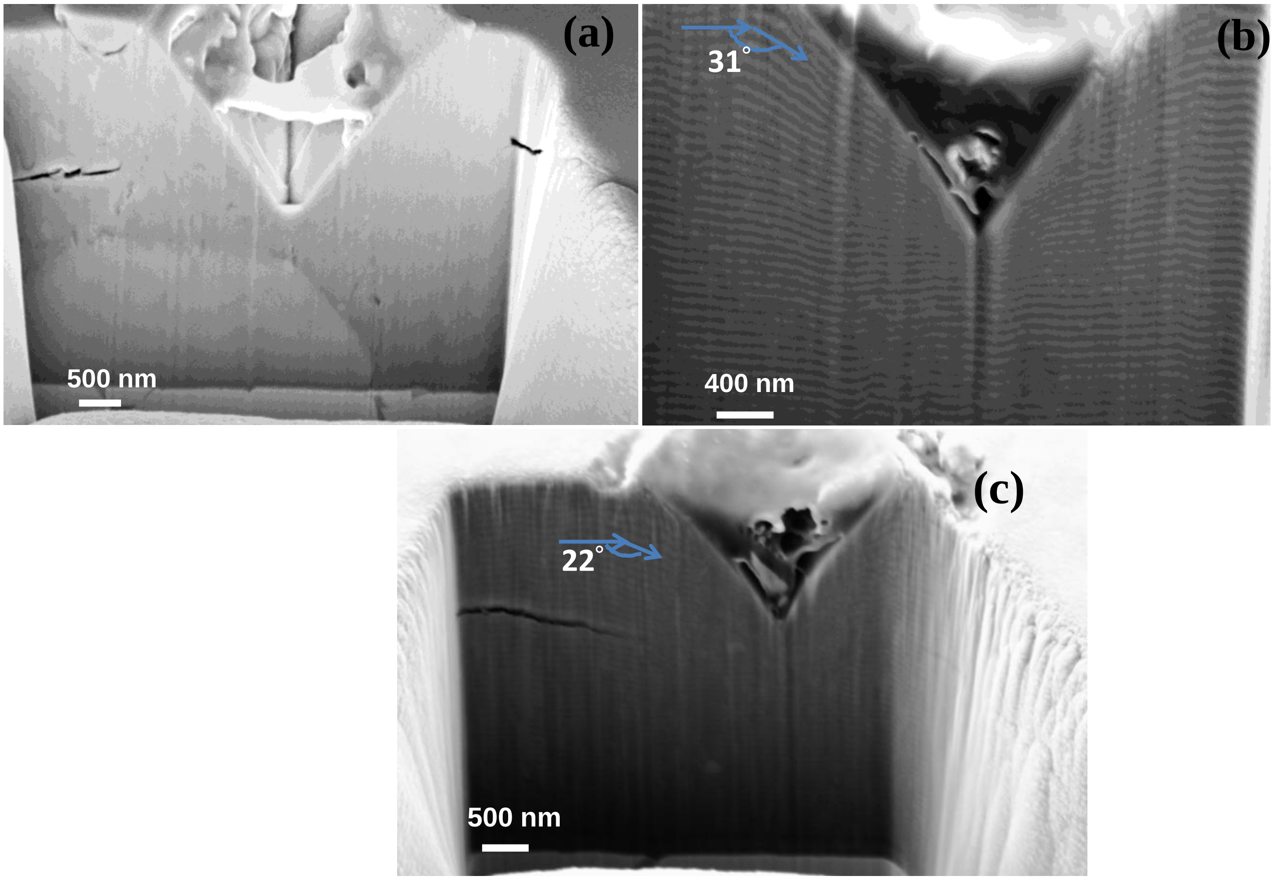

Fig. 6.12 Cross sectional SEM images of indents on (a) $Ti_{0.47}Al_{0.53}N$ (b) TiN-TiAlN ML Λ-80 and (c) $Ti_{1-x}Al_xN$ Λ-80 coatings.

An earlier report [26] also showed increased pile up at finer layer spacings in TiAlN-TiN multi-layers during indentation as a result of material flow beneath the indenter due to the interfaces which provide an additional mechanism of material transfer. Though the multi-layer coatings had a columnar grain structure, the presence of multi-layers led to distributed columnar sliding and interfacial slip while increased density of interfaces led to increased stress accommodation.

In the present study, there was a change in deformation modes from vertical cracking in monolithic TiAlN (Fig.4.15) to reduced, deflected cracking in case of the multi-layer coatings (Fig.6.7) as seen from the cross sections below scratch tracks. The multi-layers also showed enhanced strain accommodation as seen from the bending of layers in the region below indents. This difference can be attributed to the structure of the coatings which leads to the change in deformation modes. The monolithic coatings have a columnar grain structure while the multi-layer coatings inhibit columnar grain growth on account of the disruption of grain growth at each layer interface (Fig. 6.13). The cracking in monolithic and multi-layer coatings takes place as in the schematic below (Fig.6.14). Monolithic coatings show vertical cracks at columnar boundaries as shown in Fig. 6.14(a) while the multi-layer coatings interrupt cracks at interfaces (Fig. 6.14(b)). Increasing the number of interfaces further by creating nano-multi-layered coatings as shown in Fig. 6.14 (c) prevents crack growth and leads to improved life of the coatings as the time to failure due to cracking is also increased.

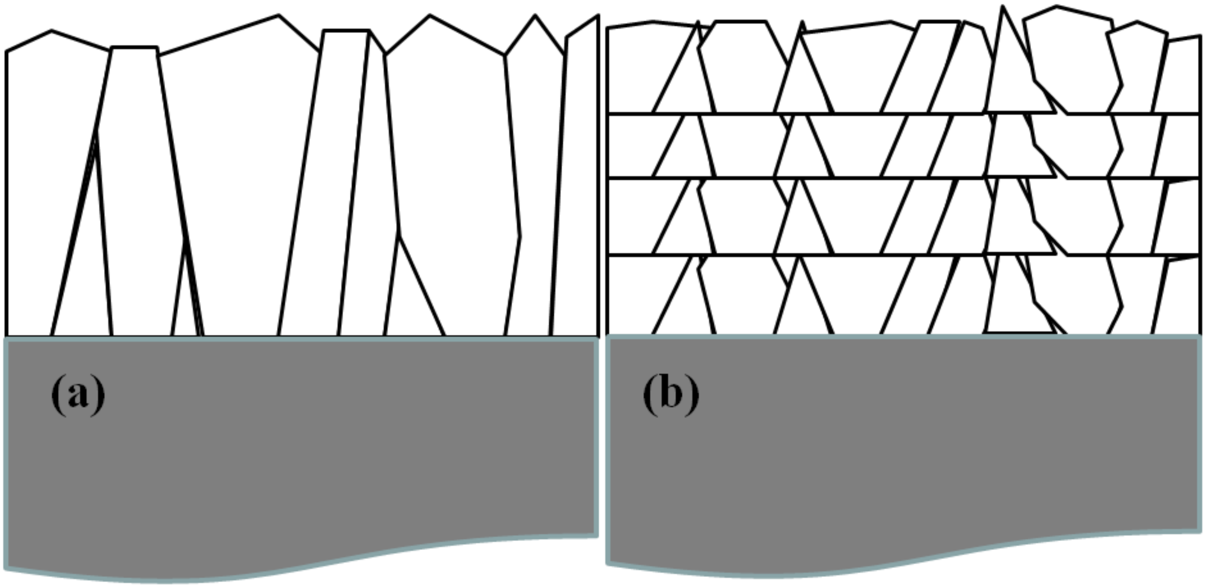

Fig. 6.13 Schematic showing grain structure in (a) monolithic and (b) multi-layer coatings.

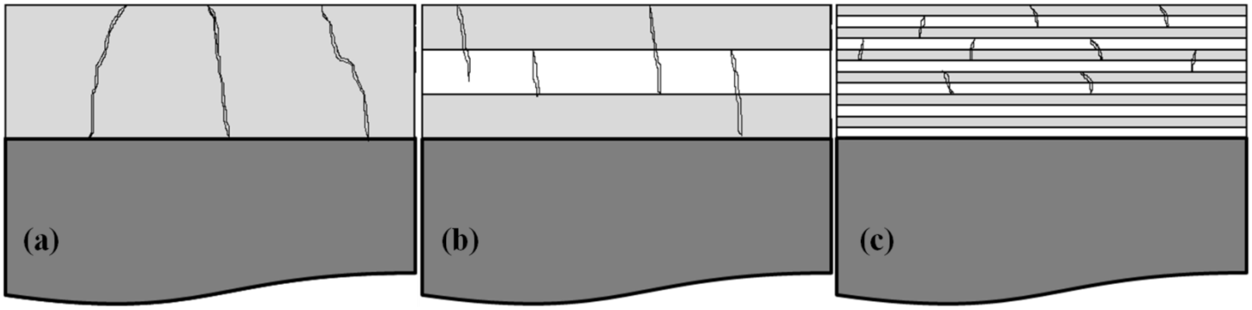

Fig. 6.14 Schematic showing changes in crack propagation in (a) monolithic coatings, (b) multi-layer coating with three layers and (c) nano-multi-layered coating with many interfaces [adapted from ref. 29].

6.8 Conclusions

Comparing the impact resistance of all the multi-layer coatings, it was found that the least impact depth was exhibited by the Λ-40 $Ti_{1-x}Al_xN$ ML coating followed by the Λ-80 TiN-TiAlN ML coating. Though the least cracking probability was observed in the Λ-40 TiN-TiAlN ML coating, it showed higher impact depths. Although the Λ-40 $Ti_{1-x}Al_xN$ multi-layer coating did not show any hardness increase on account of multi-layering, it shows the highest impact resistance apart from a low cracking probability when compared to the TiN-TiAlN ML coatings. It may also be noted that the hardness of the Λ-40 $Ti_{1-x}Al_xN$ ML coating is higher by about 3 GPa compared to the TiN-TiAlN ML coatings. This indicates that the above approach can be utilized to improve the impact resistance by increasing the number of interfaces in the multi-layer coating and choosing alternate layers with varying moduli even when the coating has a high hardness.

Realizing such a combination of high impact resistance along with a low cracking probability through appropriate control of coating architecture can have important implications in enhancing the performance and life of coated tools. From an industrial viewpoint, coatings which have a high Al content are preferred for the purpose of high oxidation resistance. Hence, the $Ti_{1-x}Al_xN$ ML coatings are better suited for applications which involve high temperatures than the TiN-TiAlN ML coatings which have TiN as one of the layers as TiN gets oxidized at lower temperatures than TiAlN. It is relevant to point out that such multi-layer coatings can be conveniently deposited by programming an appropriate processing sequence to simplify the deposition protocol and also make it cost-effective for industrial applications.

References

[1] PalDey S, Deevi SC, Single layer and multilayer wear resistant coatings of (Ti, Al)N: a review, Materials Science and Engineering A 342 (2003) 58-79.

[2] Münz, W. D. Titanium aluminum nitride films: A new alternative to TiN coatings, Journal of Vacuum Science & Technology A, 4 (1986) 2717-2725.

[3] Han, J.G., Nam, K.H., Choi, I.S., The shear impact wear behavior of Ti compound coatings, Wear, 214 (1998) 91-97.

[4] Petrov, I., Losbichler, P., Bergstrom, D., Greene, J.E., Munz, W.D., Hurkmans, T., Trinh, T. Ion-assisted growth of $Ti_{1-x}Al_xN/Ti_{1-y}Nb_yN$ multilayers by combined cathodic-arc/magnetron-sputter deposition, Thin Solid Films, 302 (1997) 179-192.

[5] Knutsson, A., Johansson, M.P., Karlsson, L., Oden, M., Thermally enhanced mechanical properties of arc evaporated $Ti_{0.34}Al_{0.66}N/TiN$ multilayer coatings, Journal of Applied Physics. 108 (2010) 044312.

[6] Knutsson, A., Johansson, M.P., Persson, P.O.A., Hultman, L., Oden, M. Thermal decomposition products in arc evaporated TiAlN/TiN multilayers, Applied Physics Letters, 93 (2008) 143110.

[7] Knutsson, A., Johansson, M.P., Karlsson, L., Oden, M., Machining performance and decomposition of TiAlN/TiN multilayer coated metal cutting inserts, Surface and Coatings Technology. 205 (2011) 4005-4010.

[8] Andersen, K.N., Bienk, E.J., Schweitz, K.O., Reitz, H., Chevallier, J., Kringshoj, P., Bottiger, J. Deposition, microstructure and mechanical and tribological properties of magnetron sputtered TiN/TiAlN multilayers, Surface and Coatings Technology, 123(2-3) (2000) 219-226.

[9] Barshilia, H. C., Rajam, K. S., Jain, A., Gopinadhan, K., Chaudhary, S, A comparative study on the structure and properties of nanolayered TiN/NbN and TiAlN/TiN multilayer coatings prepared by reactive direct current magnetron sputtering, Thin Solid Films, 503(1) (2006) 158-166.

[10] Hsieh, J.H., Liang, C., Yu, C.H., Wu, W. Deposition and characterization of TiAlN and multi-layered TiN/TiAlN coatings using unbalanced magnetron sputtering, Surface and Coatings Technology. 108-109 (1998) 132-137.

[11] Barshilia, H. C., Prakash, M. S., Jain, A., Rajam, K. S, Structure, hardness and thermal stability of TiAlN and nanolayered TiAlN/CrN multilayer films, Vacuum, 77(2) (2005) 169-179.

[12] Luo, Q., Rainforth, W.M., Donohue, L.A., Wadsworth, I., Munz, W.D. Tribological investigation of TiAlCrN and TiAlN/CrN coatings grown by combined steered-arc/unbalanced magnetron deposition, Vacuum, 53(1-2) (1999) 123-126.

[13] Lembke, M.I., Lewis, D.B., Munz, W.D. Localised oxidation defects in TiAlN/CrN superlattice structured hard coatings grown by cathodic arc/ unbalanced magnetron deposition on various substrate materials, Surface and Coatings Technology, 125 (2000) 263-268.

[14] Tillmann, W., Vogli, E., Momeni, S. Mechanical and tribological properties of Ti/TiAlN duplex coatings on high and low alloy tool steels, Vacuum, 84(3) (2009) 387-392.

[15] Vogli, E., Tillmann, W., Selvadurai-Lassl, U., Fischer G., Herper, J, Influence of Ti/TiAlN-multilayer designs on their residual stresses and mechanical properties, Applied Surface Science, 257(20) (2011) 8550-8557.

[16] Castanho, J. M., Vieira, M. T. Effect of ductile layers in mechanical behaviour of TiAlN thin coatings, Journal of Materials Processing Technology, 143 (2003) 352-357.

[17] Tavares, C.J., Rebouta, L., Alves, E., Cavaleiro, A., Goudeau, P., Riviere, J.P., Declemy, A. A structural and mechanical analysis on PVD-grown (Ti,Al)N/Mo multilayers. Thin Solid Films, 377–378 (2000) 425-429.

[18] Taveres, C.J., Rebouta, L., Andritschky, M., Guimaraes, F., Cavaleiro, A. Mechanical and surface analysis of $Ti_{0.4}Al_{0.6}N$/Mo multilayers, Vacuum, 60 (2001) 339-346.

[19] Xian, G., Zhao, H. B., Fan, H. Y., Du, H. The Structure and Adhesion of Zr/TiAlN Coatings on High-Speed Steel and Cemented Carbide Substrates, Applied Mechanics and Materials, 459 (2014) 46-50.

[20] Shang, H., Li, J., Shao, T, Mechanical properties and thermal stability of TiAlN/Ta multilayer film deposited by ion beam assisted deposition, Applied Surface Science, 310 (2014) 317-320.

[21] Bejarano Gaitan, G., Caicedo, J. C., Balogh, A. G., Gottschalk, S. Cutting tools performance enhancement by using a TiN/TiAlN multilayer coating system, Physica status solidi (c), 4(11) (2007) 4260-4266.

[22] Ananthakumar, R., Subramanian, B., Kobayashi, A., Jayachandran, M, Electrochemical corrosion and materials properties of reactively sputtered TiN/TiAlN multilayer coatings, Ceramics International, 38(1) (2012) 477-485.

[23] Chen, L., Du, Y., Yin, F., Li, J, Mechanical properties of (Ti, Al)N monolayer and TiN/(Ti, Al)N multilayer coatings, International Journal of Refractory Metals and Hard Materials, 25(1) (2007) 72-76.

[24] Ducros C., Benevent V., Sanchette F., Deposition, characterization and machining performance of multilayer PVD coatings on cemented carbide cutting tools, Surface and Coating Technology, 163-164 (2003) 681-688.

[25] Suresha, S. J., Math, S., Jayaram, V., Biswas, S. K., Toughening through multilayering in TiN–AlTiN films, Philosophical Magazine, 87 (2007) 2521- 2539.

[26] Verma. N, Cadambi. S, Jayaram V., Biswas S. K, Micromechanisms of damage nucleation during contact deformation of columnar multilayer nitride coatings, Acta Materialia, 60(6) (2012) 3063-3073.

[27] Carvalho, N.J.M., De Hosson, J.T.M., Deformation mechanisms in TiN/(Ti,Al)N multilayers under depth-sensing indentation, Acta Materialia, 54(7) (2006) 1857-1862.

[28] Prengel, H. G., Jindal, P. C., Wendt, K. H., Santhanam, A. T., Hegde, P. L., Penich, R. M., Deposition, characterization and machining performance of multilayer PVD coatings on cemented carbide cutting tools, Surface and Coatings Technology, 139(1) (2001) 25-34.

[29] Skordaris, G., Bouzakis, K. D., Charalampous, P., Bouzakis, E., Paraskevopoulou, R., Lemmer, O., Bolz, S., Brittleness and fatigue effect of mono- and multi-layer PVD films on the cutting performance of coated cemented carbide inserts, CIRP Annals-Manufacturing Technology, 63(1) (2014) 93-96.

[30] Mendibide, C., Steyer, P., Esnouf, C., Goudeau, P, Thiaudière, D., Gailhanou, M., Fontaine, J. X-ray diffraction analysis of the residual stress state in PVD TiN/CrN multilayer coatings deposited on tool steel, Surface and Coatings Technology. 200 (2005) 165–169.

[31] Koehler, J.S. Attempt to Design a Strong Solid, Physical Review B, 2 (1970) 547-551.

[32] Xu. J, Kamiko. M., Zhou. Y., Yamamoto. R., Li. G., Gu. M. Superhardness effects of heterostructure NbN/TaN nanostructured multilayers, Journal of Applied Physics, 89(7) (2001) 3674-3678.

Chapter 7 Nanocomposite TiAlCrSiN coatings: Optimization of composition and architecture for superhardness, thermal stability and durability

7.1 Introduction

The use of TiAlN coatings has been reported to increase the tool life; however these coatings are only stable up to a temperature of ~ 800^{o}C [1,2]. There have been efforts to improve the properties of these coatings through alloying with additional elements or/and multi-layering. The addition of Cr to TiAlN has been reported to improve the high temperature stability and oxidation resistance up to 900^{o}C [3]. Aluminium-rich compositions such as AlCrN have also been reported to further improve the high temperature resistance [4]. The addition of Si has been reported to greatly improve the performance and high temperature stability of coatings up to about 1200^{o}C on account of the formation of a nanocomposite structure [5, 6]. Various coating systems with reported nanocomposite structures include TiSiN, TiAlSiN, AlSiN, CrAlSiN and TiAlCrSiN [7-11]. Among these, TiSiN was one of the first reported nanocomposite coatings with TiN grains surrounded by an amorphous phase of Si_3N_4 which impeded grain sliding during deformation and led to a high crack resistance [5]. Further developments in nanocomposite coatings saw the introduction of TiAlSiN coatings which comprised of TiAlN grains in an amorphous Si_3N_4 matrix [8, 12, 13]. Chromium based nanocomposite coatings such as CrAlSiN comprise of CrAlN grains in amorphous Si_3N_4 and have been reported to show better oxidation resistance over TiAlSiN [14, 15]. Addition of Si and Ti along with Cr to synthesize TiAlCrSiN nanocomposite coatings has been reported to show an ideal combination of high temperature strength and ductility [16]. It has been reported that though the nanocomposite coatings have a high crack nucleation resistance they do not necessarily show high fracture resistance once an initial crack is nucleated [17]. There have been increasing efforts on improving the toughness of nitride coatings through various means [18]. In the present study, an attempt is made to synthesize nanocomposite coatings of TiAlCrSiN with a desirable combination of high hardness, high temperature resistance and toughness, by studying the role of composition and architecture on the microstructure and the resultant properties. The coatings were studied in both monolithic and multi-layer configurations. Monolithic coatings of TiAlCrSiN were first synthesized with different compositions of silicon and an optimum concentration of silicon arrived at to obtain high hardness and high temperature stability. Based on the initial study, multi-layer coatings of TiAlCrSiN were subsequently deposited by choosing two appropriate compositions in order to achieve a good combination of hardness and toughness.

7.2 Monolithic TiAlCrSiN coatings

7.2.1 Deposition

The coatings were deposited by varying the cathode currents in fixed ratios to obtain different targeted compositions as shown in Table 6 below. All the pre-deposition steps involving the base vacuum and the cleaning procedures for the substrates are as mentioned in chapter 3 with the substrate temperature kept at 475^{o}C. The composition of the coatings was determined by EDS as shown in Table 6. The sample nomenclature indicates the atomic percentage of silicon present in each of the deposited coatings, e.g. Si-4 refers to TiAlCrSiN coatings with 3.9 at. % of Si present in the coatings while Si-9 refers to TiAlCrSiN with 8.7 at. % Si, with 3.9 % and 8.7 % truncated to 4 and 9 at. %, respectively. The mechanical characterization carried out by nanoindentation and nano-scratch testing. The structural and microstructural characterization was carried out by XRD, SEM and TEM. Nano-impact tests were then carried out to evaluate the performance of the coatings.

Table 6: Sample designations along with cathode power ratios and obtained compositions of TiAlCrSiN

Sample Nomenclature	**Cathode Power Ratio**	**Elemental Concentration (Atomic %)**			
	Ti + Cr /Al + Si	**Si**	**Al**	**Ti**	**Cr**
Si-4	3	3.9	15.8	40.3	40
Si-6	2	5.8	24.3	35.5	34.4
Si-7	1.75	7	30.4	31.6	30.9
Si-9	1.5	8.7	38.5	27.4	25.4
Si-11	1	11.1	48.2	20.3	20.4

7.2.2 Crystal structure

X-ray diffractograms of the TiAlCrSiN coatings are shown in Fig.7.1. The coatings showed a FCC $Ti_{0.5}Al_{0.5}N$ phase up to a Si content of 9 at. %. Coating with a Si content of 11 at. % showed a different XRD pattern with broad peaks corresponding to h-AlN and c-AlN and minor peaks of c-TiAlN. The broad peak at 36° is most likely due to overlap of peaks from hcp-AlN and Si_3N_4. There was a gradual shift in peak position to higher 2θ (Fig. 7.1(b)) indicating a reduction in lattice parameter with increasing Si and Al. Fig. 7.2 shows the variation in residual stress, lattice parameter and grain size with Si content.

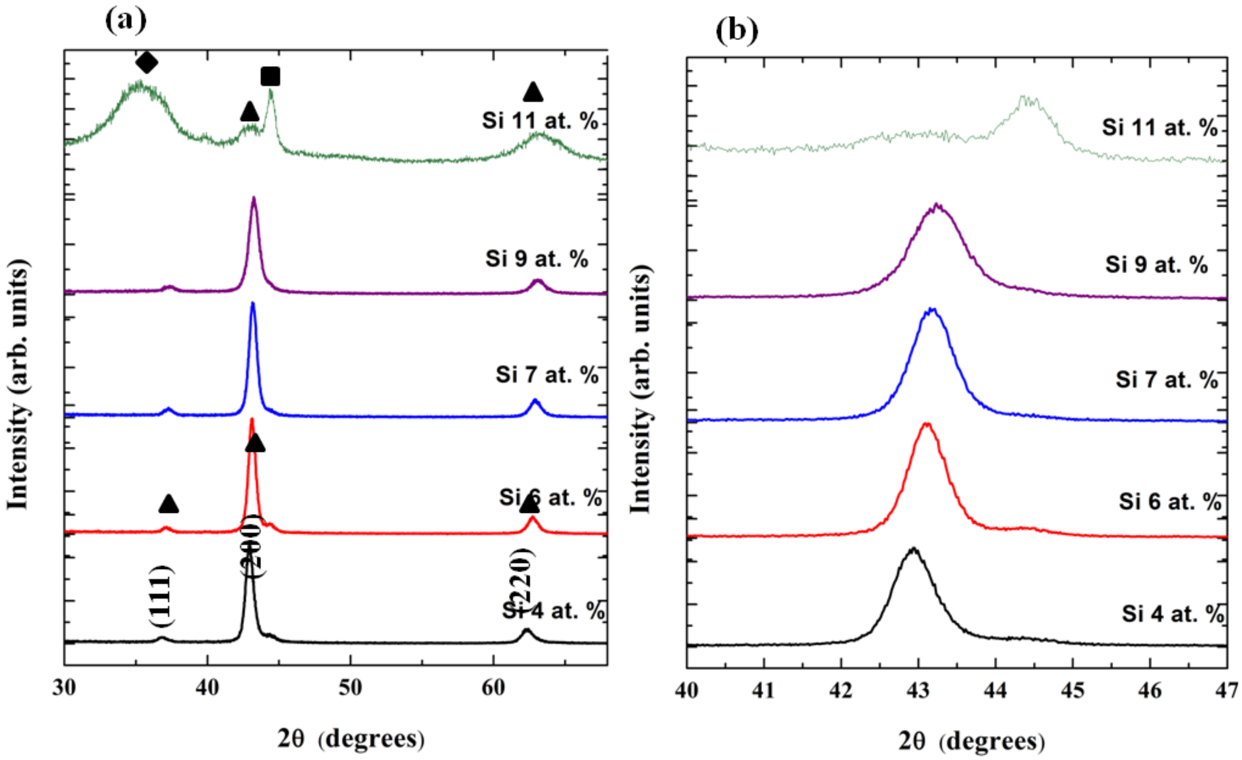

Fig. 7.1 (a) X-ray diffractograms of TiAlCrSiN coatings at different Si at. % (b) Magnified view of X-ray diffractograms from Fig. 7.1(a) (where ◆ corresponds to h- AlN, ■ to c- AlN and ▲ to c- $Ti_{0.5}Al_{0.5}N$).

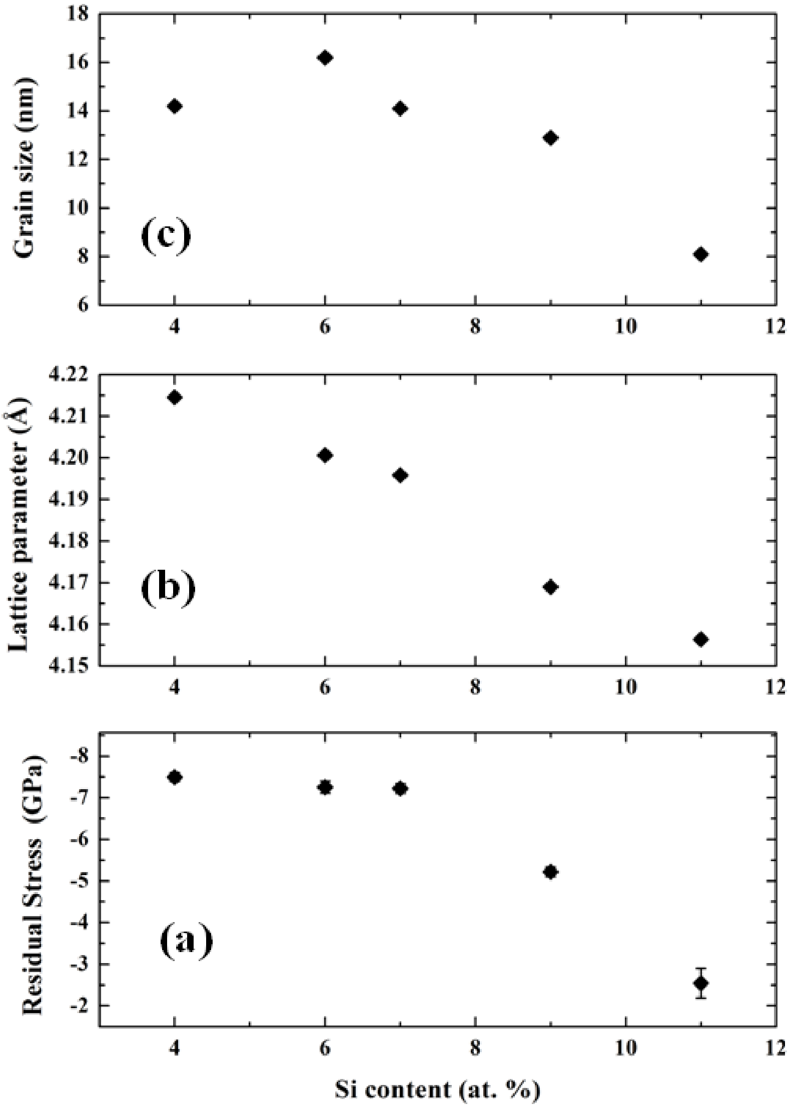

Fig. 7.2 Variation of (a) residual stress (b) lattice parameter and (c) grain size with Si content.

The residual stress was compressive in nature and nearly constant (~ - 7 GPa) up to a Si content of 7 at. %, decreased to ~ - 5.1 GPa at 9 at. % Si and was followed by a drastic reduction in stress to ~ - 2.5 GPa at 11 at. % Si (Fig.7.2 (a)). The high stress seen at low Si concentrations could be attributed to high lattice strains arising on account of the defects due to competition in growth between the Ti and the Cr containing phases (since Ti and Cr are high at low Si). The reduction in stress at 9 at. % Si could be attributed to stabilization of the microstructure due to formation of a silicon nitride phase. The large drop in residual stress observed at 11 at. % of Si is due to the increase in both the Si and Al content which led to an increase in the presence of amorphous Si_3N_4 and nucleation of the hcp-AlN phase along with a minor phase of c-AlN. The lattice parameter showed a linear reduction with increasing Si (Fig.7.2 (b)), which can be attributed to lattice shrinkage as Si replaces other elements in the TiAlN lattice. Fig. 7.2 (c) shows the variation in grain size (crystallite size) with Si content. Variation of the grain size in the Si composition range 4-9 at. % is not significant with only a minor decrease in grain size with increasing Si up to 9 at. %. There was a prominent reduction observed only in case of Si-11 which shows a grain size of ~8 nm in comparison with ~13 nm in case of Si-9. The difference could be attributed to grain growth inhibition due to a gradual increase in the amorphous Si_3N_4 phase which reaches a maximum at 11 at. % of Si. The nucleation of the hcp-AlN phase due to increased Al content (since both Al and Si increase simultaneously) is also expected to play a contributory role.

7.2.3 Mechanical Properties

Hardness and modulus:

The variation in hardness and modulus of the coatings with Si content is shown in Fig. 7.3. The hardness was found to increase to a maximum of ~37 GPa at Si content of 9 at. % followed by a drastic fall to ~27 GPa at Si content of 11 at. %. The modulus followed a somewhat similar trend, with a significant drop being noted from 9 at. % Si to 11 at. % Si. This variation could be due to microstructural and phase changes accompanying the change in Si content within the film. The high hardness in case of Si-9 could be attributed to the formation of a nanocomposite structure while the drastic fall in hardness in case of Si-11 is due to the high content of the amorphous phase of Si_3N_4 [17, 19] and the presence of the hcp AlN phase [20]. Microstructural studies were carried out to ascertain this.

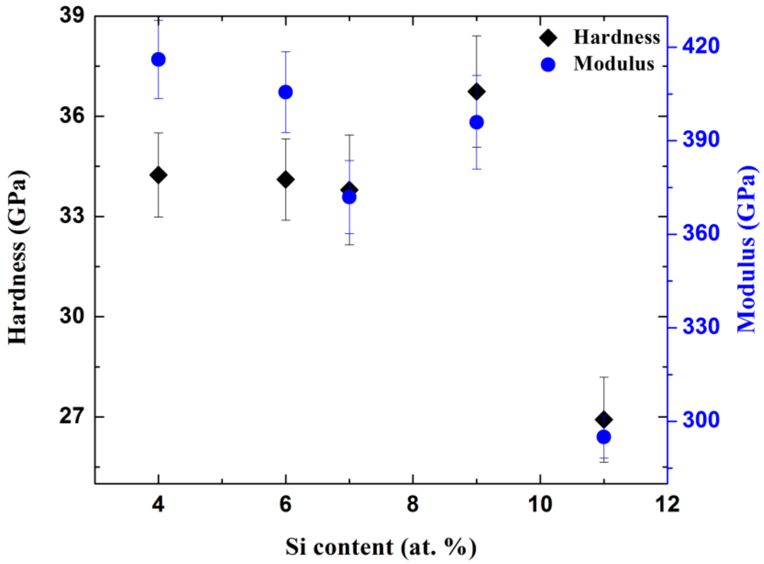

Fig. 7.3 Hardness and modulus variation with Si at. %.

7.2.4 Microstructural studies

The cross section of the coatings was studied in the dual beam SEM while the surface morphology after scratch testing was observed by SEM. Fig.7.4 shows the cross section of the Si-9 and Si-11 coatings. Both the coatings show contrasting microstructures; the Si-9 coating has a crystalline, columnar type structure while the Si-11 coating shows a microstructure with fine grains and low crystallinity. The coatings were later observed in the TEM for more detailed studies of the microstructure.

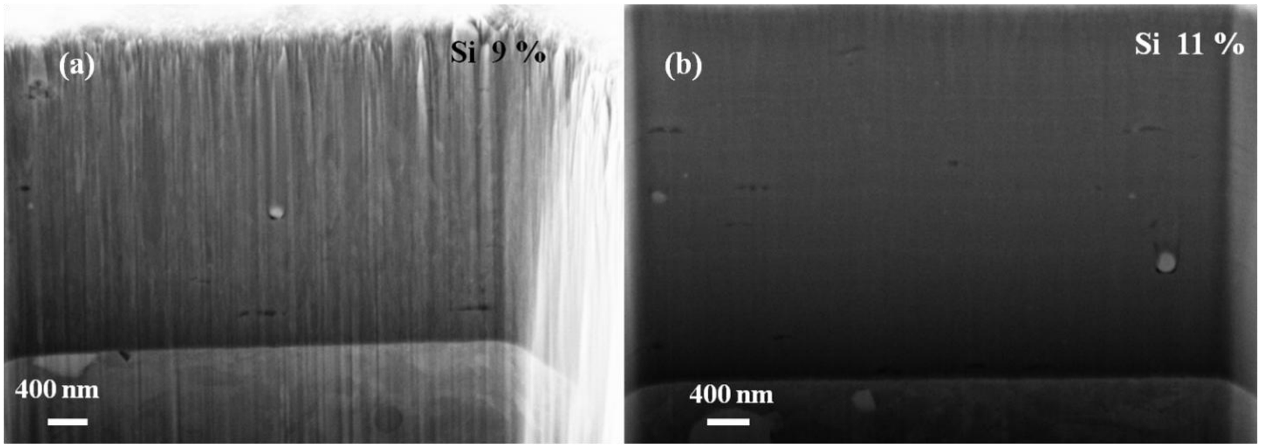

Fig. 7.4 SEM micrographs of FIB milled cross sections of (a) Si-9 and (b) Si-11 coatings.

Scratch testing was carried out to determine the adhesion of the coatings and observe the nature of deformation. All the coatings showed good adhesion with the critical load (LC_2) found to be in the range of 130-140 N. The deformation during scratch testing was found to vary with coating composition, with the cracking modes changing with Si at. % as shown in Fig. 7.5. While the Si-6 coating shows chipping due to forward cracks, the Si-9 coating shows buckling cracks and minor spallation and the Si-11 coating shows wedging spallation which could be due to the large content of amorphous phase present. There is a clear change in the deformation modes in coatings with composition, particularly between 9 at. % and 11 at. % Si.

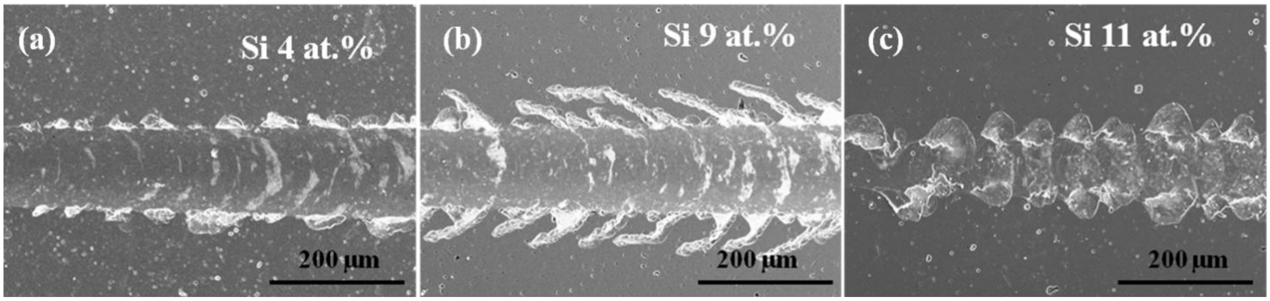

Fig. 7.5 SEM micrographs of scratch tracks in TiAlCrSiN coatings with (a) 4 at. % Si, (b) 9 at. % Si and (c) 11 at. % Si.

Plan view TEM studies showed a clear difference in microstructure with Si variation. Fig. 7.6 shows bright field and dark field TEM micrographs along with SAED patterns of Si-6, Si-9 and Si-11 coatings. Si-6 coating shows the presence of many crystalline grains (diffracting domains); Si-9 shows a reduction in the number of diffracting domains while Si-11 coating shows further reduction in crystallinity as also seen in the diffraction pattern which shows diffused rings. SAED patterns of Si-6 and Si-9 coatings showed only a cubic phase of TiAlN while Si-11 showed rings corresponding to cubic-TiAlN and a hcp-AlN phase. In order to get a clearer picture, HRTEM was also undertaken. Fig. 7.7 shows HRTEM micrographs of the above coatings. Si-9 shows a nanocomposite structure with crystalline grains of TiAlCrN embedded in an amorphous Si_3N_4 phase. Si-6 does not show a nanocomposite structure while Si-11 shows a large amorphous phase along with a few crystalline grains. Fast Fourier Transform (FFT) of the HRTEM images showed the presence of a hcp-AlN phase along with a cubic phase of TiAlN in case of Si-11 while the other coatings showed the presence of only cubic TiAlN.

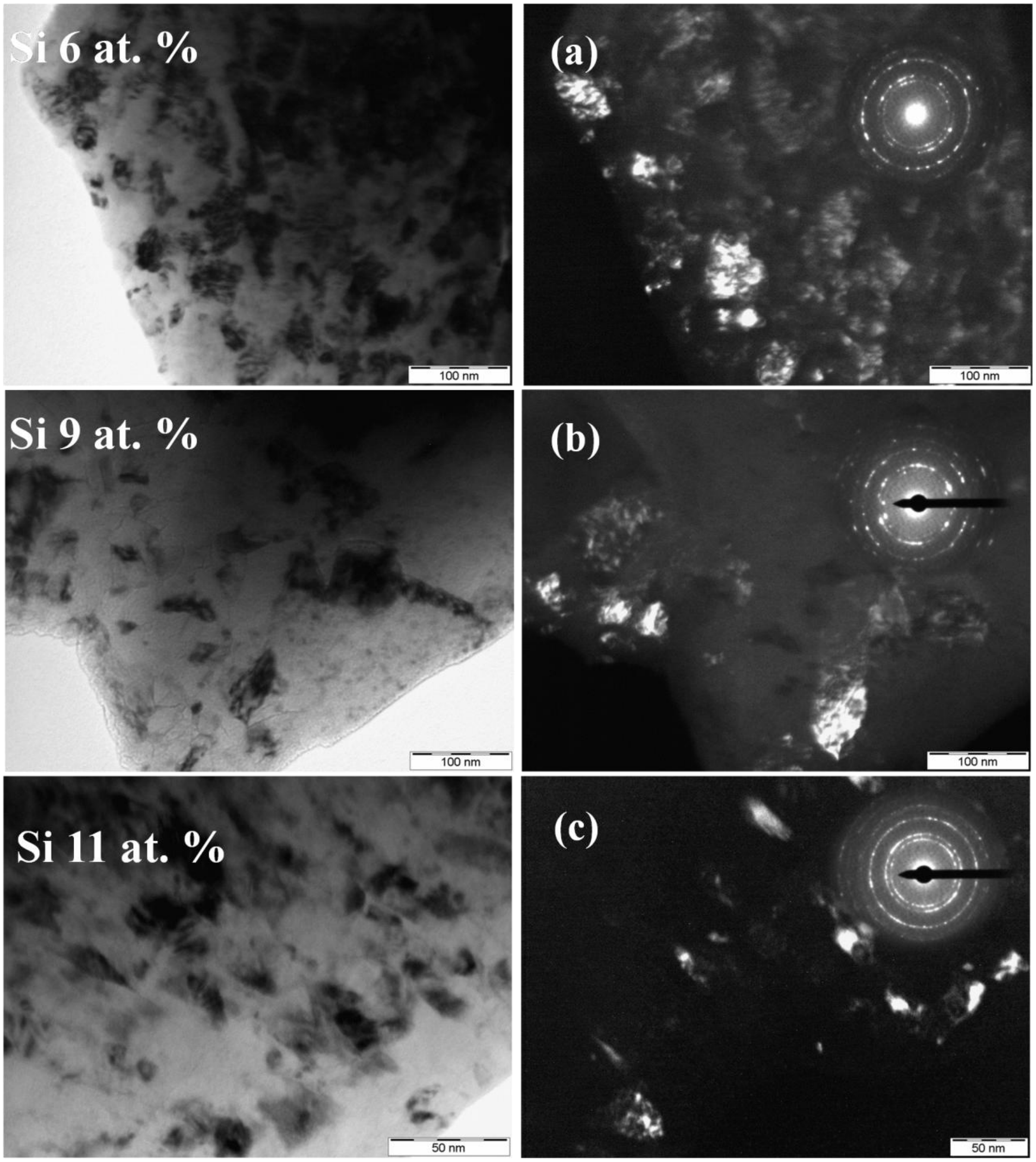

Fig. 7.6 Bright field and dark field micrographs along with the corresponding SAED patterns of (a) Si-6, (b) Si-9 and (c) Si-11 coatings.

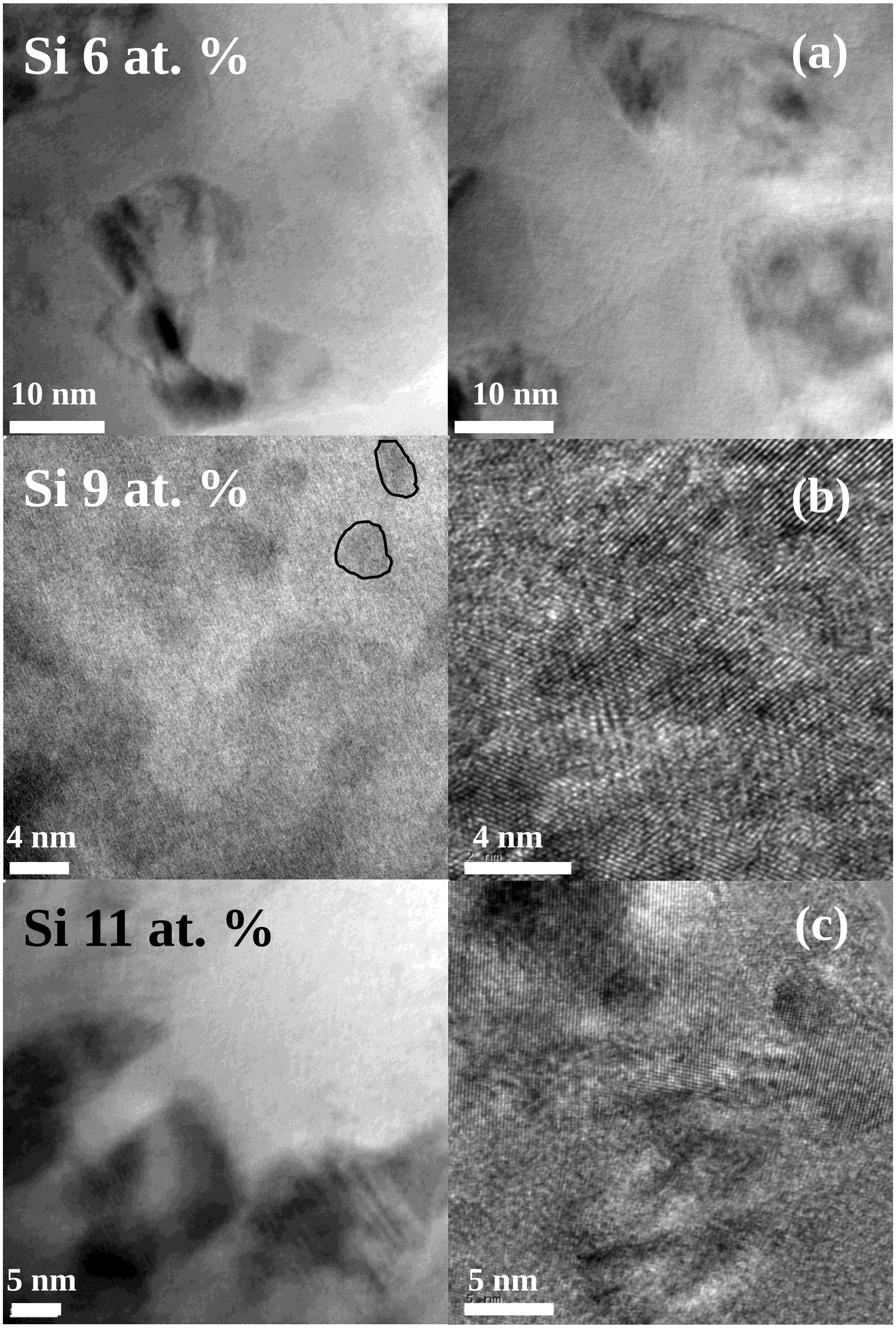

Fig. 7.7 HRTEM micrographs of (a) Si-6, (b) Si-9 and (c) Si-11 coatings, an optimum nanocomposite structure is visible in Si-9 with nanocrystalline grains in an amorphous matrix.

7.2.5 Nano-impact testing

Nano-impact tests were carried out on the coatings, beginning with a load of 10 mN and increasing the load for subsequent tests in steps of 10 mN. The TiAlCrSiN coatings were found to be more brittle compared to the TiAlN coatings due to the presence of Si and began to show cracking events even at 10 mN. Hence, to enable comparison between the coatings, only low loads and low times were considered during testing. Fig. 7.8 (a) shows the variation of impact depth with Si content while Fig. 7.8 (b) shows representative impact curves corresponding to the above coatings. There is a gradual reduction in impact depth with increasing Si content with the least depth seen in the case of Si-9. Si-11 showed a slightly higher impact depth than Si-9. It can be inferred that the highest impact resistance is seen at 9 at. % Si (Si-9) followed closely by the coating with 11 at. % Si (Si-11). Fig.7.9 shows all the impact depth vs. time curves corresponding to the above coatings. On comparing the impact depth vs. time curves, it was found that, while 9 at. % Si showed a low impact depth, the number of cracking events in case of 11 at. % Si were low. It was felt that combining the above two layers (Si-9 and Si-11) in a multi-layer configuration would, thus, be beneficial in terms of achieving both wear resistance and toughness. Multi-layer coatings comprising of the two layers above were later deposited in order to improve the toughness of the nanocomposite coatings and the details are discussed in Sec. 7.3.

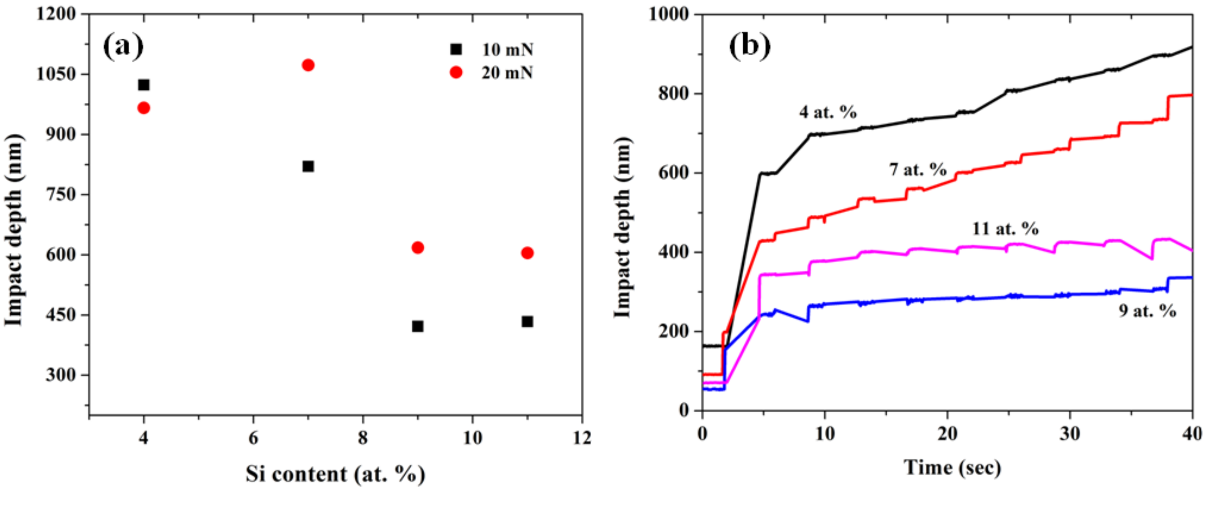

Fig. 7.8 (a) Variation of impact depth with Si content and (b) representative impact curves corr. to above coatings.

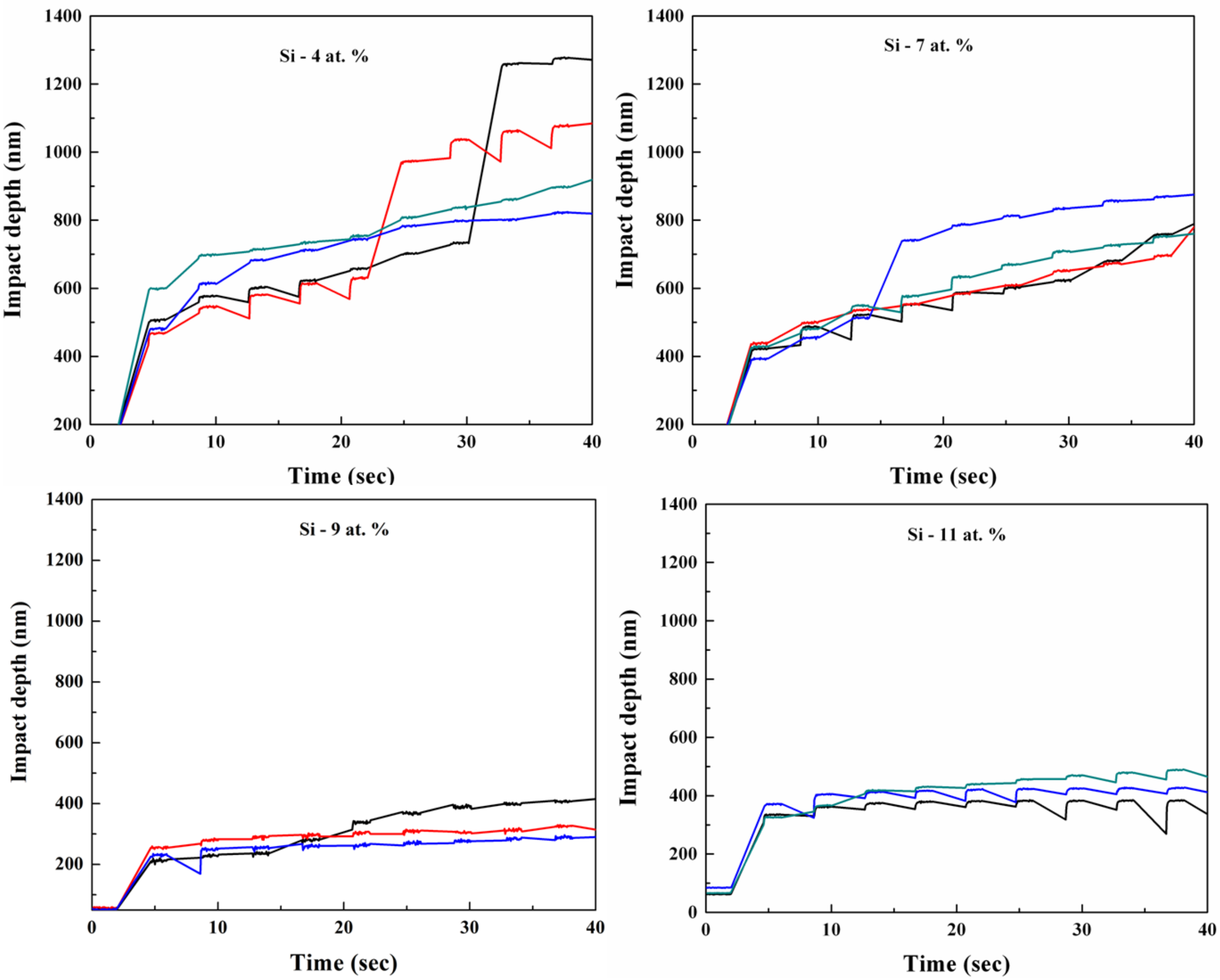

Fig. 7.9 Impact depth vs time curves corresponding to TiAlCrSiN at different compositions, lower depths in case of Si-9 and lower cracking in case of Si-11 can be observed.

7.2.6 High temperature resistance

7.2.6.1 TGA tests

Since the TiAlCrSiN coatings are most suitable for use at high temperatures, TGA tests and high temperature XRD analysis were also carried out to ascertain their thermal stability. The plots of weight gain with temperature at various Si contents in TiAlCrSiN, along with a blank tungsten carbide substrate as reference, are shown in Fig.7.10. The coating with 9 at. % Si showed lowest weight gain compared to all other compositions, which could be attributed to its nanocomposite structure which is discussed in Sec. 7.4. The onset of weight gain also began much later (around

1030 °C) in this coating. All the coatings showed good thermal stability up to about 1000 °C, which can be attributed to the presence of both Si and Cr in the coatings. Most of the weight gain measured in this experiment was due to the formation of Tungsten oxide from the underlying substrate which was the major phase detected during XRD measurements of the coatings after TGA tests.

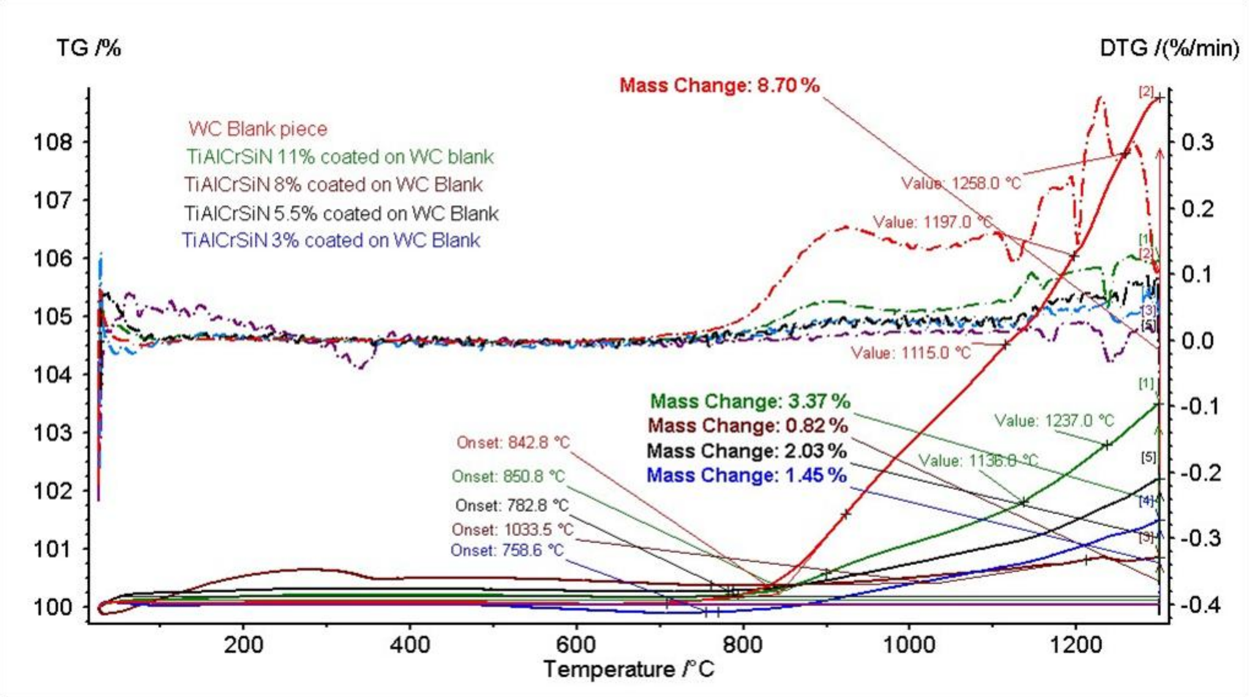

Fig. 7.10 TGA plot showing weight gain with temperature at different Si contents in TiAlCrSiN.

7.2.6.2 High temperature XRD analysis

High temperature XRD measurements were carried out in an Ar atmosphere using an in-situ heating stage in a synchrotron XRD to ascertain the thermal stability of these coatings. Details of the measurements are given in Chapter 3. In view of the limited beam time, only the coating with 9 at. % Si could be analyzed at fixed temperatures of 40, 800, 900 and 1000 °C. The resultant X-ray diffractograms are shown in Fig.7.11. There was no evidence of nucleation of a new phase up to 1000°C. These results suggest that coatings with 9 at. % Si content could be suitable for use in high temperature applications.

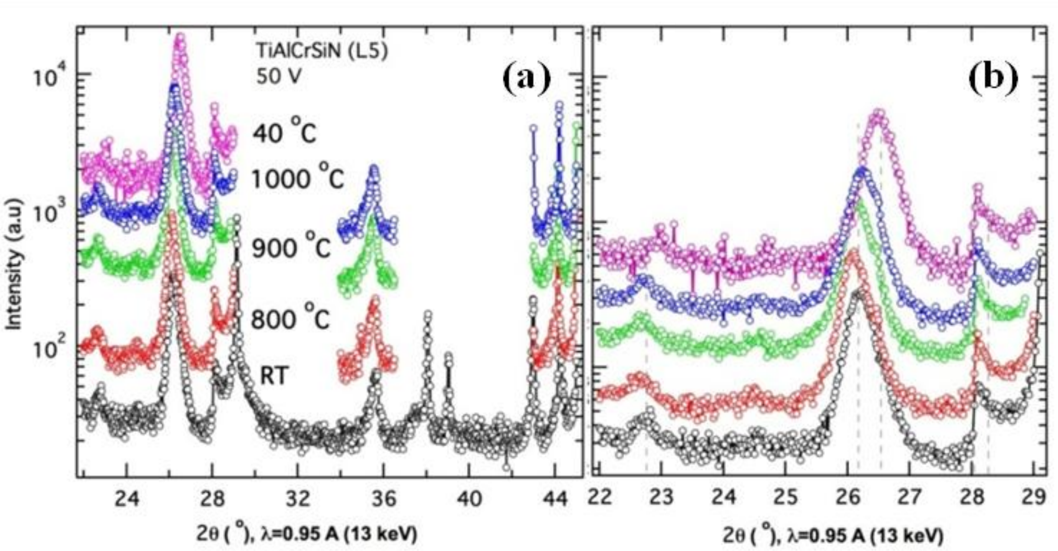

Fig.7.11 Synchrotron X-ray diffractograms of TiAlCrSiN at elevated temperatures up to 1000 °C

7.3 Multi-layered TiAlCrSiN coatings

Though Si based nanocomposite nitride coatings show superior wear resistance on account of their superhardness and oxidation resistance, the toughness of the coatings is low due to the inherent brittleness of the coating. Multi-layered coatings have been reported to show longer life and better performance. Various systems studied include AlTiCrN/TiSiCN, TiAlCrSiYN/TiAlCrN, TiAlSiN/CrAlN, TiSiN/TiAlN, TiSiN/TiN, TiCrN/AlSiN, CrAlN/AlSiN [22-27]. Multi-layers comprising of nano-layers having a modulating chemical composition but with similar crystal structure and hardness have been reported to show enhanced wear performance [22]. In the present study, a multi-layer coating based on TiAlCrSiN was designed by choosing two layers, one with high hardness and the other a softer layer with low crack probability in order to achieve a multi-layer with a combination of toughness and wear resistance for enhanced life. Based on the study on monolithic TiAlCrSiN coatings (Sec 7.2), multi-layers comprising of alternating layers with compositions of 9 at. % Si and 11 at. % Si were deposited. The multi-layers were deposited with bi-layer periods of 20, 40 and 80 nm and designated as Si ML Λ-20, Si ML Λ-40 and Si ML Λ-80, respectively. The deposition times are given in Table 7 and the other deposition parameters were the same as those in Sec 7.1.

Table 7: Deposition times used for different bi-layer periods in the TiAlCrSiN multi-layer coatings

Coating	**Deposition time (sec)**	
	Layer 1 (Si 11 at. %)	Layer 2 (Si 9 at. %)
Si ML Λ-20	32	29
Si ML Λ-40	64	58
Si ML Λ-80	128	116

7.3.1 Crystal structure

Grazing incidence X-ray diffractograms of the TiAlCrSiN multi-layers are shown in Fig. 7.12. The coatings showed a crystal structure corresponding to FCC TiAlN along with minor peaks corresponding to hcp-AlN and cubic AlN.

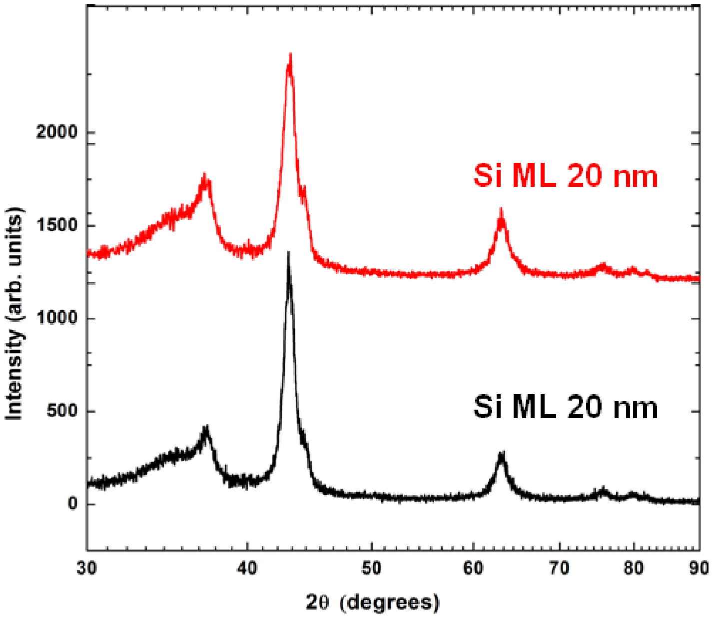

Fig. 7.12 Grazing incidence X-ray diffractograms of TiAlCrSiN multi-layers at bi-layer periods of 20 and 80 nm.

Residual stress

The multi-layer coatings showed the presence of compressive residual stresses with the stress variation in the range - 4.2 to - 5.2 GPa (Fig. 7.13). A maximum in residual stress was observed at the intermediate bi-layer period of 40 nm with the lowest stress seen in case of the 20 nm bi-layer period. The high values of stress seen at bi-layer periods of 40 nm and 80 nm could be attributed to stress build up at interfaces while the lower stress in case of 20 nm bi-layer period could be due to compositional variations at interfaces reported in case of multi-layers with low layer spacings [28]. Possible reasons for the above behaviour and correlation with mechanical properties are discussed in Sec.7.4.2.

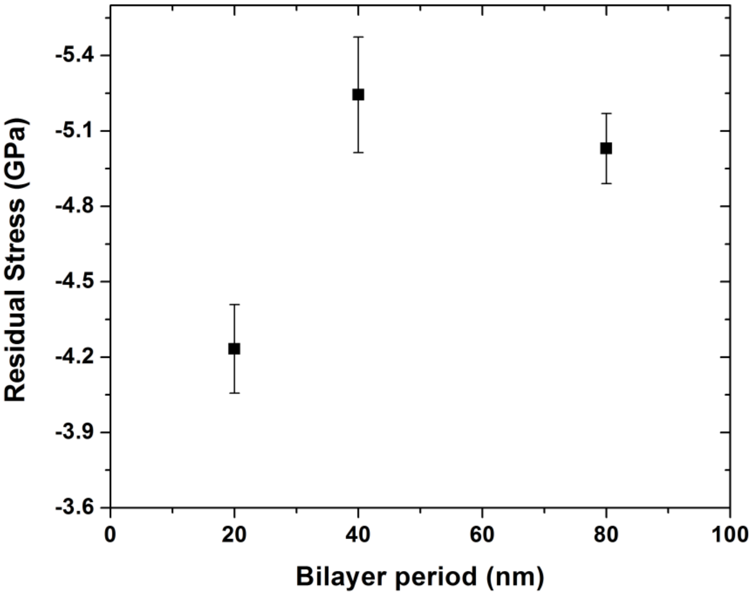

Fig. 7.13 Variation of residual stress with bi-layer period in TiAlCrSiN multi-layers.

7.3.2 Mechanical properties

The hardness and modulus values of the above multi-layer coatings are shown in Fig. 7.14. There is no significant hardening seen due to multi-layering, with the hardness values being very close to the composite hardness of the individual layers. The coating with 40 nm bi-layer period showed a minor increase in hardness and modulus compared to the other two coatings. This may be related to the nature and volume of interfaces in the multi-layers [29]. Sharp interfaces are required for a hardening effect to take place [28, 30] whereas in the present multi-layer coatings the lower bi-layer period of 20 nm may not have a sharp interface due to the decreasing composition modulation at lower bi-layer periods. The hardening in case of the 40 nm bi-layer could probably be explained on the basis of the presence of an optimum volume of interfaces and is discussed in Sec. 7.4.2.

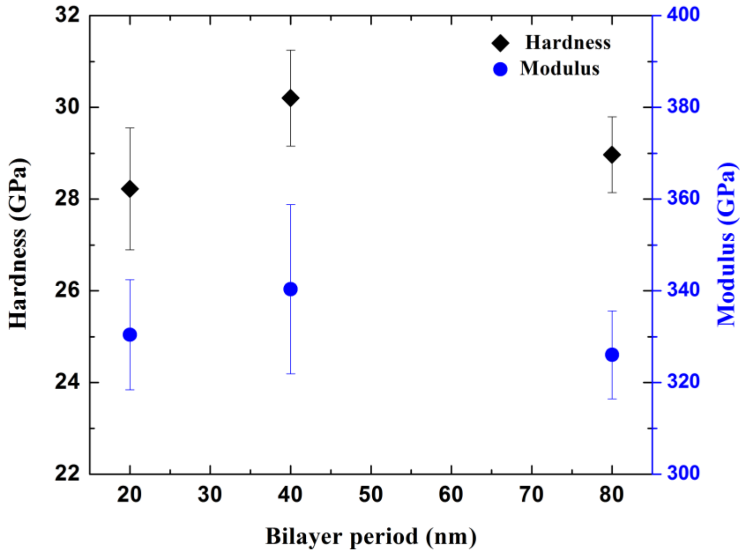

Fig. 7.14 Variation in hardness and modulus with bi-layer period in TiAlCrSiN multi-layers.

7.3.3 Nano-impact testing

Nano-impact tests were carried out on the three multi-layer coatings under identical conditions as those used during testing of the monolithic TiAlCrSiN coatings. Only low loads and times were considered in view of the high number of cracking events. Fig. 7.15 shows the variation in impact depth with bi-layer period at 10 mN and 20 mN. The coating with 40 nm bi-layer period shows the best impact resistance (least impact depth), with the impact depth at 10 mN also lower than the least impact depth seen in the monolithic TiAlCrSiN coatings. The reason behind the higher impact resistance of the 40 nm bi-layer coating when compared to the 20 nm and 80 nm bi-layer coatings is discussed in Sec. 7.4.2.

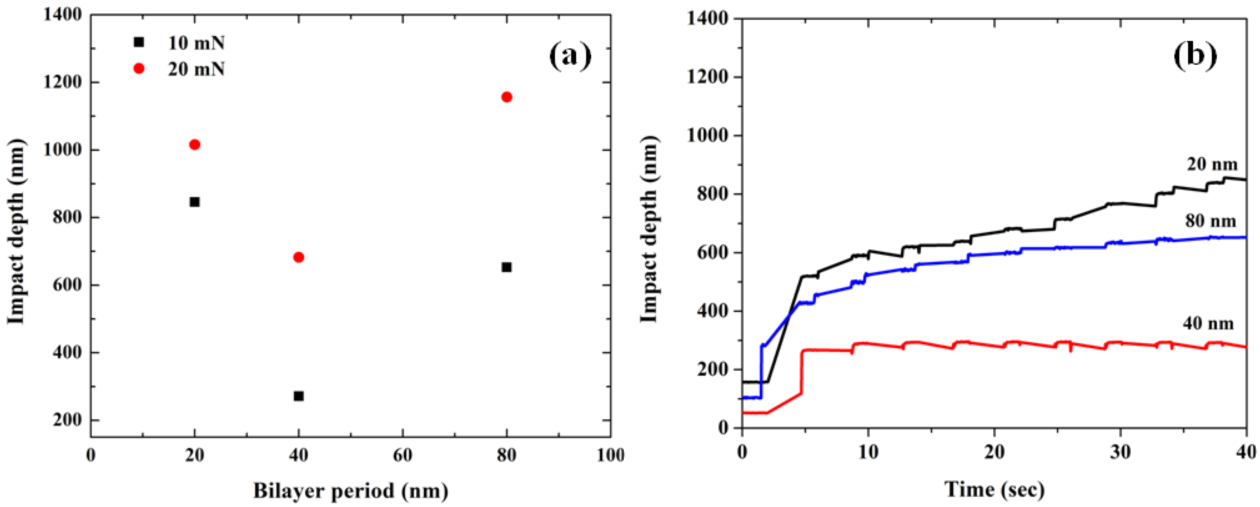

Fig. 7.15 (a) Variation in impact depth with bi-layer period and (b) Impact depth vs time curves at load of 10 mN in TiAlCrSiN multi-layers.

7.4 Discussion

7.4.1 Effect of Si content on microstructure and resultant properties

The amount of silicon present in the coatings controlled the microstructure and phase which in turn had an effect on the mechanical properties of the TiAlCrSiN coatings. The coatings with low Si content did not show the presence of a nanocomposite structure which was seen only in coatings with Si content of 9 at. % and 11 at. %. There have been various reports in literature on the optimum value of Si for the formation of a nanocomposite structure with a wide variation of Si concentrations reported [31]. This is due to the different deposition conditions and techniques used. In the present study, the coating with 9 at. % of silicon showed the best properties in terms of hardness and high temperature resistance as it had an optimum quantity of both nanocrystalline grains and the amorphous Si_3N_4 phase. Though the coating with 11 at. % Si showed a nanocomposite structure, it showed poor properties due to the excessive presence of amorphous phase and the hcp-AlN phase. The Al content is also expected to play a contributory role on the coating properties with high Al content seen in case of Si-11 leading to formation of the hcp-AlN phase which degrades mechanical properties. A probable model for the nanocomposite structure obtained is shown in Fig. 7.16. While the ideal nanocomposite structure is one where a single monolayer of the amorphous phase surrounds nanocrystalline grains, confirmation of such a structure is not feasible due to the difficulty involved in obtaining an ultra-thin TEM specimen of the coating.

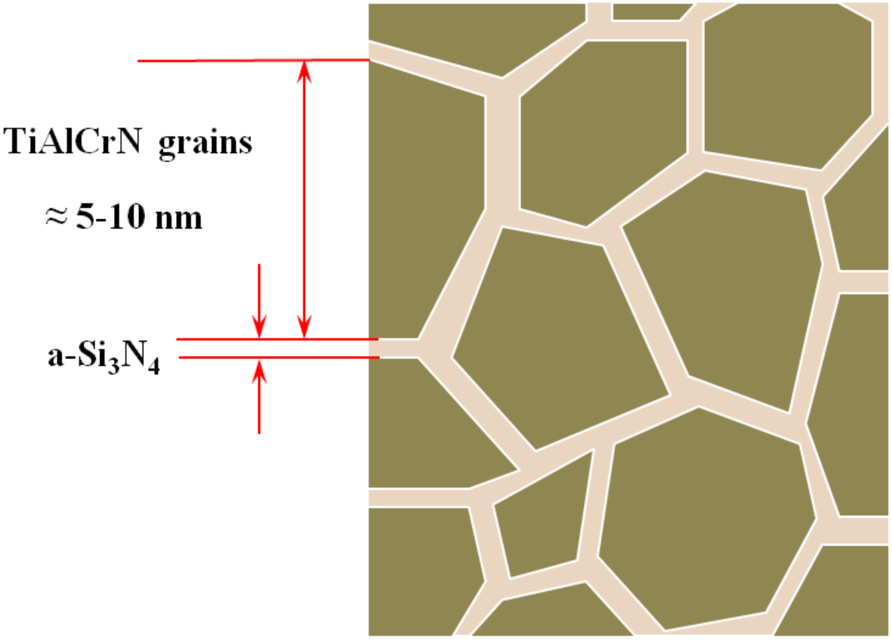

Fig. 7.16 Schematic representation of probable nanocomposite structure formed at optimum concentration of Si.

Fig. 7.17 shows TEM micrographs corresponding to the Si-9 coating showing a near ideal nanocomposite structure with nanocrystalline grains of TiAlCrN surrounded by an amorphous Si_3N_4 phase. The interface between the matrix and the grains also influences the mechancial properties and thermal stability. It has been reported that the highest hardness in nitride nanocomposite coatings is obtained when one monolayer of Si_3N_4 covers a grain of the nitride as the decohesion strength of one Si_3N_4 monolayer bonded with a nitride layer is higher than that of bulk Si_3N_4 [32]. The presence of a similar desired nanocomposite structure in case of the Si-9 coating could be the reason behind the combination of high hardness, thermal stability and impact resistance observed.

The thermodynamic conditions which depend on the deposition temperature, composition as well as the inter cathode distance also play a role with the optimum nanocomposite structure reported when spinodal decomposition takes place. This has been reported to take place when conditions of fast diffusion (high temperature) and a high driving force for the solid solution to decompose are met causing the segregation of Si_3N_4 to the grain boundaries [33]. Many of the above thermodynamic conditions are probably met in case of the coating with Si 9 at. % leading to the formation of an optimum nanocomposite structure and an enhancement in properties.

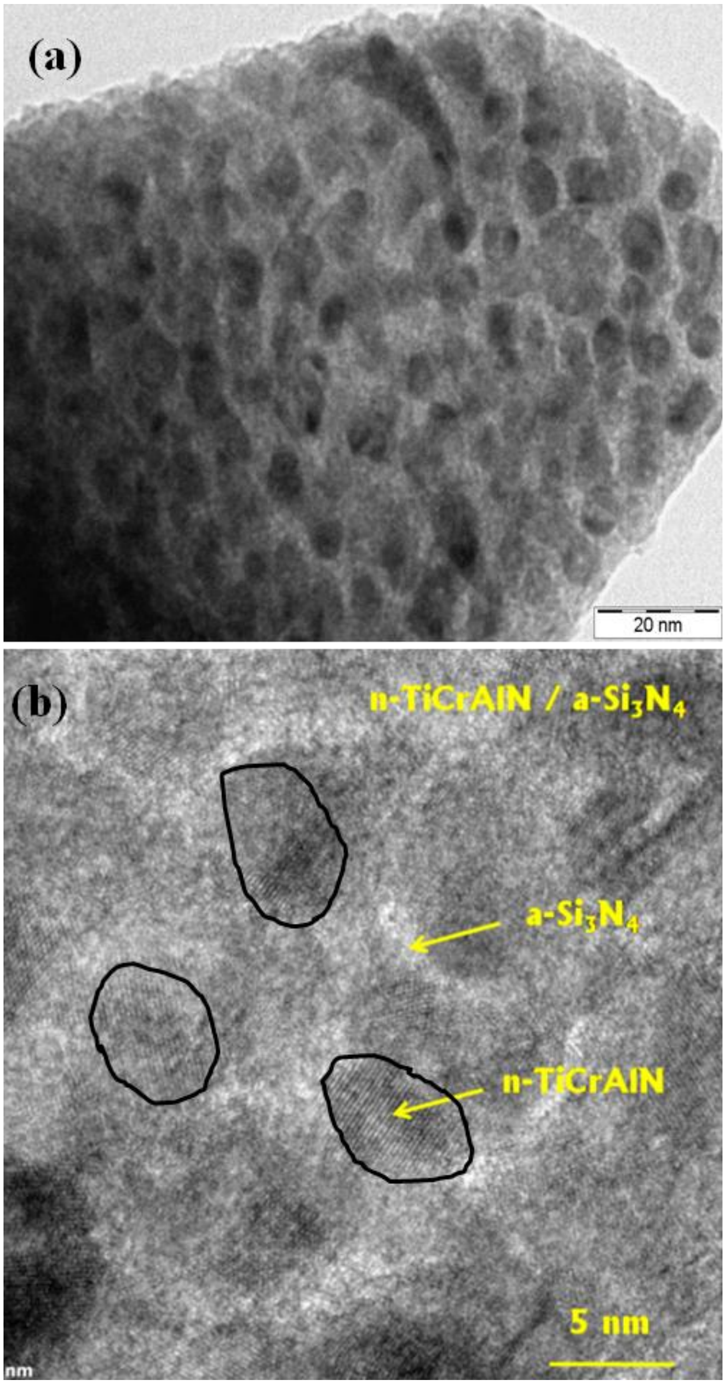

Fig. 7.17 (a) TEM micrograph of Si-9 coating showing nanocrystalline grains in an amorphous matrix (b) HRTEM image showing nanocrystalline grains surrounded by amorphous Si_3N_4.

7.4.2 Effect of layer composition and bi-layer period on impact resistance

The two layers comprising of the TiAlCrSiN multi-layers (hard Si-9 coating and softer Si-11 coating) were chosen in order to improve the toughness and the impact resistance of the coatings. Though the hardness of the multi-layer coatings did not show any increase over the monolithic coatings, there was a significant increase in impact resistance in the multi-layer coatings. The Si ML Λ-40 coating showed ~35 % reduction in impact depth compared to Si-9 coating which showed the highest impact resistance among the monolithic TiAlCrSiN coatings. The presence of the softer amorphous layer (Si-11) along with the hard layer (Si-9) in the multi-layers prevents crack propagation where the hard layer limits the deformation by providing stiffness and the softer layer accommodates plastic deformation, thereby slowing down the crack growth.

Among the TiAlCrSiN multi-layers, there was a large variation seen in impact resistance with variation in bi-layer period. The coating with intermediate bi-layer period of 40 nm showed a nearly 55 % reduction in impact depth over the 80 nm bi-layer coating and a ~66 % reduction in impact depth over the coating with 20 nm bi-layer period. This variation is most likely due to differences in the interface volume and stress build up at the interfaces between the two layers in the multi-layer coatings. The lower impact resistance in case of the 20 nm bi-layer period is probably due to the high number of interfaces leading to a drop in mechanical properties and/ or a lack of sharp interfaces due to compositional variations at the interfaces in lower bi-layer periods [28, 30] which was also reflected in the lower stresses. The higher impact resistance in case of the 40 nm and 80 nm bi-layer coatings could be due to two reasons: i) the volume of interfaces and ii) the presence of sharp interfaces when compared to 20 nm bi-layer. The higher impact resistance in case of the 40 nm bi-layer coating over 80 nm bi-layer could be due to the number of layers meeting the requirement of an optimum volume of interfaces for enhancement in properties of multi-layers. This is in agreement with an earlier report on multi-layer coatings where tool life showed a gradual increase with increasing no of layers (increasing interface volume) with a maximum observed at an intermediate number of layers and a drop in life seen at higher number of layers [34].

7.5 Conclusions

A high temperature-resistant and superhard Ti-Al-Cr-Si-N coating was developed, with a Si content of 9 % showing the maximum in hardness and high temperature resistance due to the presence of the desired nanocomposite structure. The toughness and impact resistance of the coatings could be enhanced by multi-layering with an intermediate bi-layer period of 40 nm showing the best impact resistance due to the enhanced crack redirection at the interfaces on account of the presence of alternating hard and softer amorphous layers which led to crack dissipation. Thus, an optimum combination of layers and bi-layer period was identified and a coating with a desirable combination of hardness and toughness that could enable enhanced performance was developed.

References

[1] Kalss, W., Reiter, A., Derflinger, V., Gey, C., Endrino, J. L. Modern coatings in high performance cutting applications. International Journal of Refractory Metals and Hard Materials, 24(5), (2006) 399-404.

[2] Barshilia, H. C., Prakash, M. S., Jain, A., Rajam, K. S. Structure, hardness and thermal stability of TiAlN and nanolayered TiAlN/CrN multilayer films. Vacuum, 77(2), (2005) 169-179.

[3] Kovalev, A. I., Wainstein, D. L., Rashkovskiy, A. Y., Fox-Rabinovich, G. S., Yamamoto, K., Veldhuis, S., M. Aguirre, Beake, B. D. Impact of Al and Cr alloying in TiN-based PVD coatings on cutting performance during machining of hard to cut materials. Vacuum, 84(1), (2009) 184-187.

[4] Reiter, A. E., Derflinger, V. H., Hanselmann, B., Bachmann, T., Sartory, B. Investigation of the properties of $Al_{1-x}Cr_xN$ coatings prepared by cathodic arc evaporation. Surface and Coatings Technology, 200(7), (2005) 2114-2122.

[5] Veprek, S., Veprek-Heijman, M. J. Industrial applications of superhard nanocomposite coatings. Surface and Coatings Technology, 202(21), (2008) 5063-5073.

[6] Veprek, S., Männling, H. D., Jilek, M., Holubar, P. Avoiding the high-temperature decomposition and softening of $(Al_{1-x}Ti_x)N$ coatings by the formation of stable superhard

nc-($Al_{1-x}Ti_x$)N/a-Si_3N_4 nanocomposite. Materials Science and Engineering: A, 366(1), (2004) 202-205.

[7] Vepřek, S., Reiprich, S., Shizhi, L. Superhard nanocrystalline composite materials: the TiN/Si3N4 system. Applied physics letters, 66(20), (1995) 2640-2642.

[8] Holubar, P., Jilek, M., Sima, M. Present and possible future applications of superhard nanocomposite coatings. Surface and Coatings Technology, 133, (2000) 145-151.

[9] Pélisson, A., Parlinska-Wojtan, M., Hug, H. J., Patscheider, J. Microstructure and mechanical properties of Al–Si–N transparent hard coatings deposited by magnetron sputtering. Surface and Coatings Technology, 202(4), (2007) 884-889.

[10] Polcar, T., Cavaleiro, A. High-temperature tribological properties of CrAlN, CrAlSiN and AlCrSiN coatings. Surface and Coatings Technology, 206(6), (2011 1244-1251.

[11] Dehlinger, A. S., Lapostolle, F., Lamy, S., Rapaud, O., Meunier, C., Brien, V, Didier Klein, Coddet, C. Influence of Cr and Si addition on structural and mechanical properties of TiAlN coatings reactively sputter deposited. Plasma Processes and Polymers, 4(S1), (2007) S588-S592.

[12] Carvalho, S., Ribeiro, E., Rebouta, L., Tavares, C., Mendonca, J. P., Monteiro, A. C, N. J. M. Carvalho, J. Th M. De Hosson, Cavaleiro, A. Microstructure, mechanical properties and cutting performance of superhard (Ti, Si, Al) N nanocomposite films grown by dc reactive magnetron sputtering. Surface and Coatings Technology, 177, (2004) 459-468.

[13] Kim, S. K., Vinh, P. V., Kim, J. H., Ngoc, T. Deposition of superhard TiAlSiN thin films by cathodic arc plasma deposition. Surface and Coatings Technology, 200(5), (2005) 1391-1394.

[14] Chang, Y. Y., Hsiao, C. Y. High temperature oxidation resistance of multicomponent Cr–Ti–Al–Si–N coatings. Surface and Coatings Technology, 204(6), (2009) 992-996.

[15] Chang, Y. Y., Chang, C. P. High Temperature Stability of Multicomponent TiAlSiN and CrAlSiN Coatings. Journal of nanoscience and nanotechnology, 10(7), (2010) 4762-4766.

[16] Wheeler, J. M., Raghavan, R., Chawla, V., Morstein, M., Michler, J. Deformation of Hard Coatings at Elevated Temperatures. Surface and Coatings Technology, 254, (2014) 382-387.

[17] Zhang, S., Wang, H. L., Ong, S. E., Sun, D., Bui, X. L. Hard yet tough nanocomposite coatings–present status and future trends. Plasma Processes and Polymers, 4(3), (2007) 219-228.

[18] Zhang, S., Sun, D., Fu, Y., Du, H. Toughening of hard nanostructural thin films: a critical review. Surface and Coatings Technology, 198(1), (2005) 2-8.

[19] Patscheider, J., Zehnder, T., Diserens, M. Structure–performance relations in nanocomposite coatings. Surface and Coatings Technology, 146, (2001) 201-208.

[20] Ezura, H., Ichijo, K., Hasegawa, H., Yamamoto, K., Hotta, A., Suzuki, T. Micro-hardness, microstructures and thermal stability of (Ti, Cr, Al, Si) N films deposited by cathodic arc method. Vacuum, 82(5), (2008) 476-481.

[21] Imamura, S., Fukui, H., Shibata, A., Omori, N., Setoyama, M Properties and cutting performance of AlTiCrN/TiSiCN bilayer coatings deposited by cathodic-arc ion plating. Surface and Coatings Technology,202(4), (2007) 820-825.

[22] Fox-Rabinovich, G. S., Beake, B. D., Yamamoto, K., Aguirre, M. H., Veldhuis, S. C., Dosbaeva, G., A. Elfizy, A. Biksa, Shuster, L.S. Structure, properties and wear performance of nano-multilayered TiAlCrSiYN/TiAlCrN coatings during machining of Ni-based aerospace superalloys. Surface and Coatings Technology, 204(21), (2010) 3698-3706.

[23] Fukumoto, N., Ezura, H., Suzuki, T. Synthesis and oxidation resistance of TiAlSiN and multilayer TiAlSiN/CrAlN coating. Surface and Coatings Technology, 204(6), (2009) 902-906.

[24] Chang, C. L., Chen, W. C., Tsai, P. C., Ho, W. Y., Wang, D. Y. Characteristics and performance of TiSiN/TiAlN multilayers coating synthesized by cathodic arc plasma evaporation. Surface and Coatings Technology, 202(4), (2007) 987-992.

[25] Wo, P. C., Munroe, P. R., Zhou, Z. F., Li, K. Y., Xie, Z. H. Effects of TiN sublayers on the response of TiSiN nanocomposite coatings to nanoidentation and scratching contacts. Materials Science and Engineering: A,527(16), (2010) 4447-4457.

[26] Nguyen, T. D., Kim, S. K., Lee, D. B. High-temperature oxidation of nano-multilayered TiAlCrSiN thin films in air. Surface and Coatings Technology, 204(5), (2009) 697-704.

[27] Zhang, S., Wang, L., Wang, Q., Li, M. A superhard CrAlSiN superlattice coating deposited by multi-arc ion plating: I. Microstructure and mechanical properties. Surface and Coatings Technology, 214, (2013) 160-167.

[28] Chu, X., Barnett, S. A. Model of superlattice yield stress and hardness enhancements. Journal of applied physics, 77(9), (1995) 4403-4411.

[29] H. Holleck, V. Schier, Multilayer PVD coatings for wear protection Surface and Coatings Technology 76-77 (1995) 328-336

[30] Oberle, R. R., Cammarata, R. C. Dependence of hardness on modulation amplitude in electrodeposited Cu-Ni compositionally modulated thin films, Scripta metallurgica et materialia, 32(4), (1995) 583-588.

[31] Guo, J., Liu, Z., Wang, S., Shen, Y. The grain refining effect of energy competition and the amorphous phase in nanocomposite materials, Scr. Mater. 69 (2013) 662-665.

[32] Veprek, S., Zhang, R. F., Veprek-Heijman, M. G. J., Sheng, S. H., Argon, A. S. Superhard nanocomposites: Origin of hardness enhancement, properties and applications. Surface and Coatings Technology, 204(12), (2010) 1898-1906.

[33] Veprek, S. Recent search for new superhard materials: Go nano!.Journal of Vacuum Science & Technology A, 31(5), (2013) 050822.

[34] Ulrich, S., Ziebert, C., Stueber, M., Nold, E., Holleck, H., Goken, M., Schweitzer, E., Schlobmacher, P. Correlation between constitution, properties and machining performance of TiN/ZrN multilayers, Surface & Coatings Technology 188–189 (2004) 331– 337.

Chapter 8 Optimized multi-functional, multi-layer coatings: Characterization and performance evaluation

8.1 Introduction

The new generation PVD coatings which involve multiple layers comprising both nanocomposite and conventional layers, with each layer tailored to discharge a specific function to enhance the durability and performance of the overall coating are already available in the industry, especially for cutting tool applications [1, 2]. As discussed in Chapter 1, there have been earlier studies which report enhancement in coating properties when interlayers or adhesive underlayers are used. However, there are only a few studies on the new generation multi-layer coatings with reports on tool life enhancement in triple layer coatings such as Ti-TiN-TiCrAlN, TiCN-TiZrN-TiN, TiAlN-TiCrN-TiCrAlN, and TiAlSiN/TiSiN/TiAlN [3-6]. There have been a few studies which report improved properties using functionally gradient coatings [7-8]. Notwithstanding the above efforts, no detailed study exists on the role of individual layers and their microstructure on the performance of such new generation, multi-layer coatings deposited by the PVD technique.

In the present chapter, a multi-functional, multi-layer coating which is a triple layer comprising of a TiN adhesion layer, a tough, impact resistant TiAlN intermediate layer, and a hard, wear resistant TiAlCrSiN top layer was designed and deposited in various configurations. Layer combinations as per the schematic shown in Fig. 8.1 were deposited. As part of the preceding optimization studies (Chapters 4-7), TiN which comprises layer C at the base of the coating was optimized for adhesion while TiAlN which forms the middle layer B was optimized for toughness and impact resistance and TiAlCrSiN which forms layer A at the top was optimized for hardness, thermal stability and durability. Seven different multi-functional, multi-layer coatings were deposited using the optimized compositions and configurations which resulted from the above studies and their microstructural details and mechanical properties were evaluated.

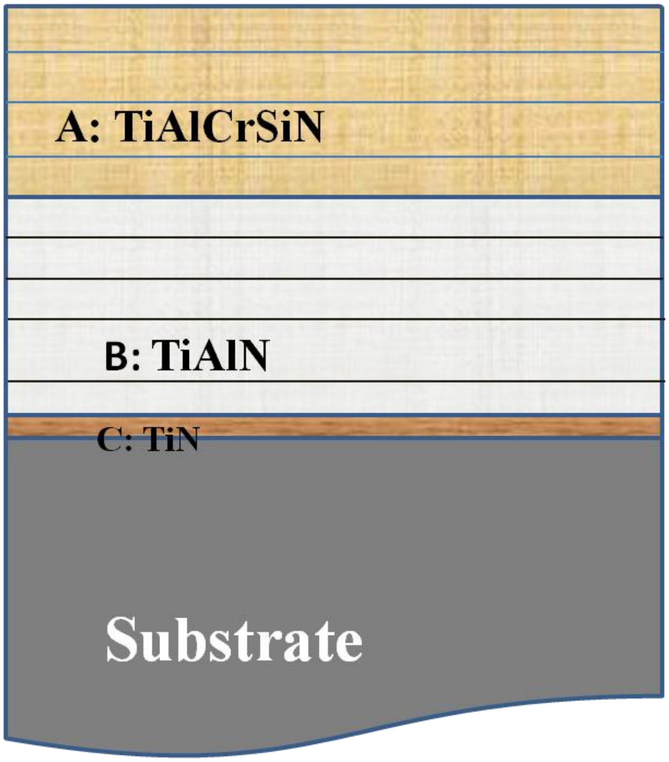

Fig. 8.1 Schematic illustration of optimized multi-functional, multi-layer coating with triple layer architecture.

The coatings along with their constituent layers and nomenclatures are given in Table 8. Layer 1 in all the coatings was fixed as TiN with the optimized thickness of ~ 100 nm; layer 2 was comprised of different optimized combinations of TiAlN- monolithic $Ti_{0.47}Al_{0.53}N$, $Ti_{0.35}Al_{0.65}N$ and $Ti_{1-x}Al_xN$ multi-layers ($Ti_{0.7}Al_{0.3}N$ and $Ti_{0.47}Al_{0.53}N$) and layer 3 comprised of optimized monolithic TiAlCrSiN (Si-8) and Si ML multi-layers (TiAlCrSiN- 8 at. % and TiAlCrSiN -11 at. %). Gradient layers (denoted as Grad.) between layers were also used in some of the coatings with details given in Table 8. The coatings in this chapter are henceforth referred to by the nomenclature as given in Table 8.

Table 8: Various configurations of multi-functional, multi-layered coatings studied along with their constituent layers

Coating nomenclature	Layer 1	Layer 2	Layer 3	Thickness (μm)
Coat-1	TiN	$Ti_{0.47}Al_{0.53}N$	Si-8	3.4
Coat-2	TiN	$Ti_{0.47}Al_{0.53}N$	Si ML 40‡ + Grad. TiAlCrSiN	3.5
Coat-3	TiN	Grad. $Ti_{0.47}Al_{0.53}N$+ Grad. TiCrN	Si ML 40*	3.91
Coat-4	TiN	TiAlN ML 80$^{\#}$ + Grad. TiCrN	Si ML 40 + Grad. TiAlCrSiN	4.05
Coat-5	TiN	TiAlN ML 80	Si ML 40	3.82
Coat-6	TiN	$Ti_{0.35}Al_{0.65}N$	Si ML 40‡ + Grad. TiAlCrSiN	5.4
Coat-GL	TiN	Grad. $Ti_{0.47}Al_{0.53}N$+ Grad. TiCrN	Si ML 40‡ + Grad. TiAlCrSiN	3.84

[*] Si ML 40 corresponds to TiAlCrSiN multi-layers with a bi-layer period of 40 nm, with 20 nm thick layers of TiAlCrSiN 8 at. % Si and TiAlCrSiN 11 at. % Si

[#] TiAlN ML 80 corresponds to $Ti_{1-x}Al_xN$ multi-layers with a bi-layer period of 80 nm, with 40 nm thick layers of $Ti_{0.7}Al_{0.3}N$ and $Ti_{0.47}Al_{0.53}N$

[‡] Si ML 40‡ corresponds to TiAlCrSiN multi-layers with bi-layers comprising of 25 nm thick TiAlCrSiN 8 at. % Si layer and 40 nm thick TiAlCrSiN 11 at. % Si layer

8.2 Deposition

The coatings were deposited as per the schematic illustrated in Fig. 8.1 and in various configurations as in Table 8 with the deposition conditions as mentioned in Chapter 3. A typical design of the triple layer coating deposited involves a TiN underlayer on the substrate followed by a thick TiAlN layer with a gradient layer in between. The gradient layer comprises a varying concentration of the elements Ti, Al and Cr in order to allow for a smooth transition between different layers. The TiAlN layer is followed by another gradient layer over which TiAlCrSiN multi-layers were deposited with alternating Si contents of 8.5 and 11 at. % within the layers.

Comprehensive characterization of the coatings was carried out followed by evaluation of their performance by nano-impact testing. Detailed microstructural investigations on one of the coating configurations (Coat-GL) are presented followed by results from the performance evaluation tests of all the coatings. Coatings of different thicknesses (2, 4 and 7 μm, designated as ML1, ML2 and ML3, respectively) were initially deposited and characterized.

8.3 Characterization

The coatings were characterized using a combination of SEM based micro-diffraction, FIB milling, TEM and scanning probe microscopy (SPM) techniques that cumulatively enable a comprehensive investigation. Multi-scale characterization was carried out where the preliminary coating thickness was inferred from optical microscopy, while more accurate measurements were performed in the SEM and FIB, with the latter allowing a detailed observation of the multi-layer coating cross section and the various layers. EBSD provided a simple method for location-specific phase identification by electron micro-diffraction in addition to enabling orientation imaging (OIM) of the coating cross section. TEM permitted identification of the nano-layered structure of the multi-layers apart from providing phase information through SAED. SPM enabled probing of mechanical properties to obtain maps of the complex modulus apart from enabling study of fine topographic details and interfaces at the nanometre scale [9].

The cross section of all the three coating specimens was studied in the FIB. However, the phase and crystal orientation mapping using EBSD was undertaken only on the 7 micron-thick coating specimen since an EBSD scan on a coating with lower thickness was not easy to carry out due to charging at the coating edge. Similarly, the cross sectional TEM study was carried out only on the 2 micron thick coating as due to experimental constraints associated with the FIB liftout procedure; uniform thinning of thicker coatings in the final milling at low currents was difficult. The SPM imaging was carried out on the same specimen that was prepared for EBSD since a smooth polished surface was needed for modulus mapping.

8.4. Microstructural studies

8.4.1 Scanning electron microscopy and energy dispersive spectroscopy

The cross sections of the coatings were observed in the SEM after mounting and metallographic polishing. Fig. 8.2 (a) shows a typical secondary electron micrograph and Fig. 8.2 (b), the corresponding backscattered electron micrograph of ML3 with the insets showing the nano-multi-layer region of the coating. Fig. 8.2 (c) shows the EDS elemental maps acquired across the entire coating along with a schematic of the elements present in each layer. The elemental constituents in the different layers were identified and confirmed. As shown in the schematic in Fig. 8.1, the maps confirm that the nano-multi-layers are Cr and Si rich, along with the presence of Ti and Al (the exact variation between individual nano-multi-layers in this region was not detectable in the above EDS maps). While the middle layer is Ti and Al rich, the gradient layer comprises of Ti, Al, and Cr, with a gradual increase in the concentration of Ti and Al and a gradual decrease in the Cr concentration. The underlayer shows the presence of Ti and Cr corresponding to the TiCrN layer and Ti which corresponds to the TiN adhesion layer. The tool steel substrate showed the presence of Fe and Cr.

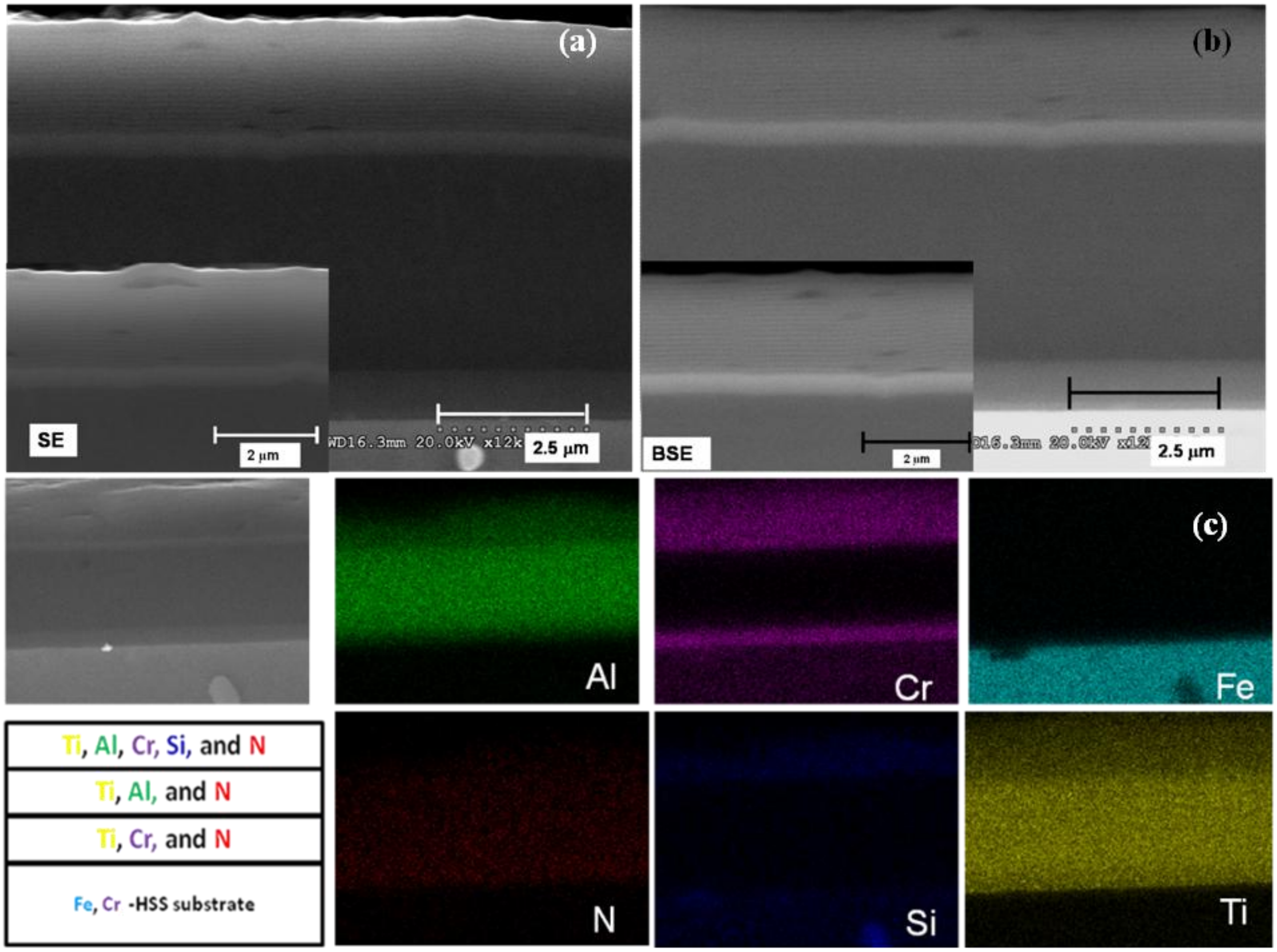

Fig. 8.2 (a) Secondary electron (SE) image of the coating cross section, (b) backscattered electron (BSE) image of the same area as in (a) [Insets show the nano-multi-layer region of the coating] and (c) EDS maps and schematic of coating cross section showing elements present in each layer.

8.4.2 Electron micro-diffraction

The coating cross section was prepared for EBSD using standard metallographic procedures. The different layers in the multi-layer coating were observed and the electron beam was focused in each region to obtain an EBSP. Patterns could not be obtained in the TiAlCrSiN nano-multi-layers possibly due to the presence of nanocrystalline grains interspersed with amorphous regions, which could be resolved in the XTEM study and are shown later. The TiAlN middle layer and the TiN base layer did show patterns which were indexed to identify the phases present. The patterns appeared diffused probably due to the presence of nanocrystalline grains which lead to superposition of patterns from several grains at a time, or the presence of strain in the deposited coatings as has been reported earlier [10]. Fig. 8.3 shows the different representative spots (shown as green stars) from where EBSPs were obtained, the patterns from the respective spots and the corresponding phases which were indexed based on the patterns. Fig. 8.3 (a) corresponding to the middle layer indicates the presence of the cubic phase- $Ti_{0.5}Al_{0.5}N$ at the location of the spot while Fig. 8.3(b) corresponds to a tetragonal phase- $TiN_{0.61}$ at the location of the spot in the Titanium nitride adhesion layer. EBSPs were recorded at several locations along the coating cross section so as to identify the dominant phase within each layer. It was found that the TiAlN layer had a dominant phase of FCC $Ti_{0.5}Al_{0.5}N$ [11] although a few weak patterns that appeared to belong to a hexagonal phase were also seen, while the TiN layer showed the presence of a dominant tetragonal phase [12]. The co-existence of both FCC and HCP phases in TiAlN has been reported earlier and attributed to a structural change from FCC to HCP [13]. The identified phase, which showed a high confidence index apart from the maximum number of occurrences, corresponded to FCC $Ti_{0.5}Al_{0.5}N$ and was used as an input to set up EBSD scans across the coating. Prior to the scan, a phase information file corresponding to FCC $Ti_{0.5}Al_{0.5}N$ was created using the lattice parameters, Wyckoff positions and the site occupancy factors [11]. The confidence index (CI) is a measure of the degree of confidence that an identified pattern is correct and a CI value of 0.1 is used as the minimum cutoff to determine if an EBSD pattern is acceptable or not. This value is used since it has been reported that, in the plot of the fraction of correct solutions vs CI, the solutions were correct 95 % of the times for patterns with a CI value of 0.1 and above [14].

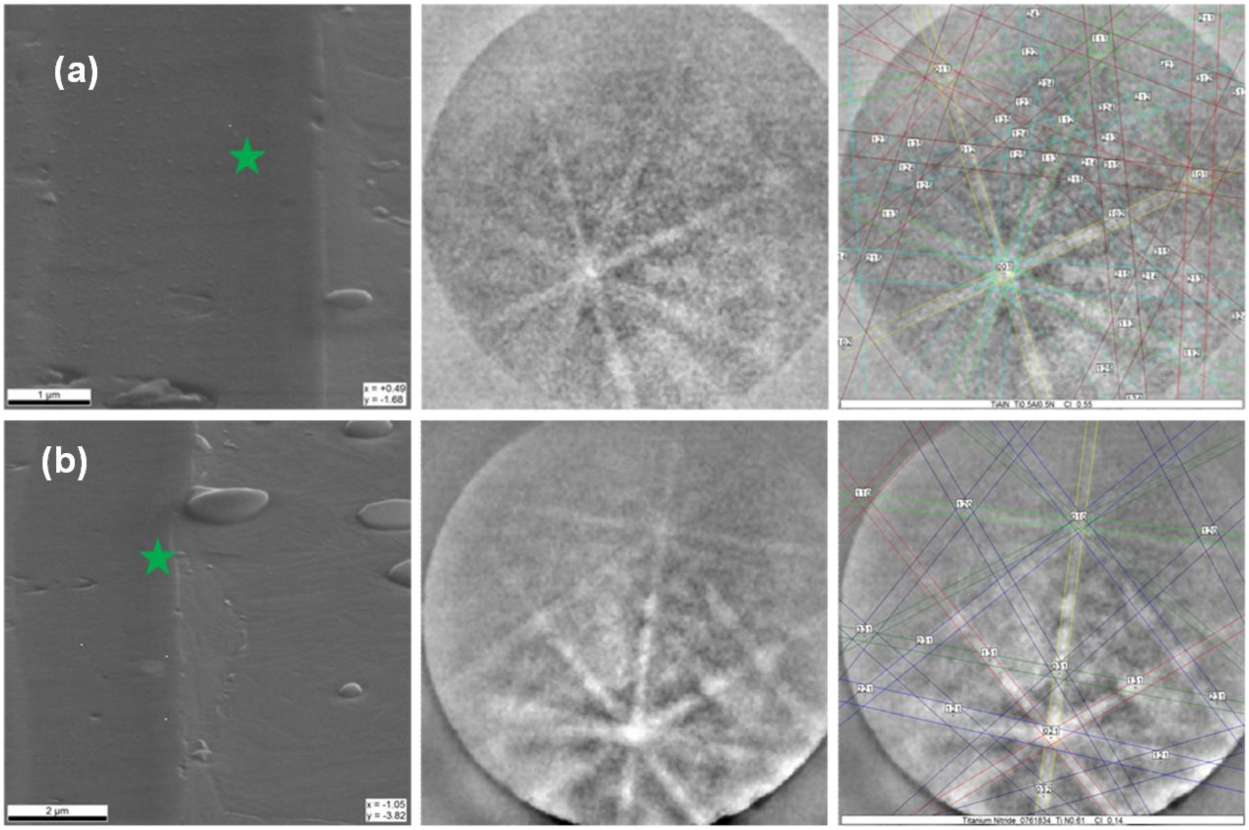

Fig. 8.3 (a) EBSP from the TiAlN layer (corresponding to the green star in the SEM image) in the coating with the phase indexed as FCC $Ti_{0.5}Al_{0.5}N$ (b) EBSP from the adhesion layer with the phase indexed as tetragonal $TiN_{0.61}$.

Fig. 8.4 shows a crystal orientation map (COM) of the coating with its inverse pole figure (IPF), along with a SEM image of the mapped region and the corresponding elemental maps that were obtained in tandem during the EBSD scan. The advantage of EDS maps recorded in the EBSD configuration with 70^o tilt over conventional EDS mapping (which is done at zero tilt), is that the maps are at a higher resolution due to the reduced interaction volume of the electron beam at higher angles of tilt [15]. The middle layer corresponds to TiAlN and shows columnar-like grains while the top layer corresponds to nano-multi-layers which did not give rise to any patterns. The elemental maps of the region provide a picture of the compositional variation in the multi-layer coating and could help in finding the exact stoichiometry of the different layers. As an example, in Fig. 8.4.(c), the maps show the middle layer to be Ti and Al rich as expected for the TiAlN layer, while the nano-multi-layers of TiAlCrSiN were confirmed to be Si and Cr rich with nitrogen being uniformly present in all the layers. However, in the present case, the exact variation in Si and Cr percentage within the nano-multi-layers was not detectable during the above scan. A technique with a higher resolution such as electron energy loss spectroscopy (EELS) or high-angle annular dark-field scanning transmission electron microscopy (HAADF-STEM) could probably help to resolve the exact elemental variation.

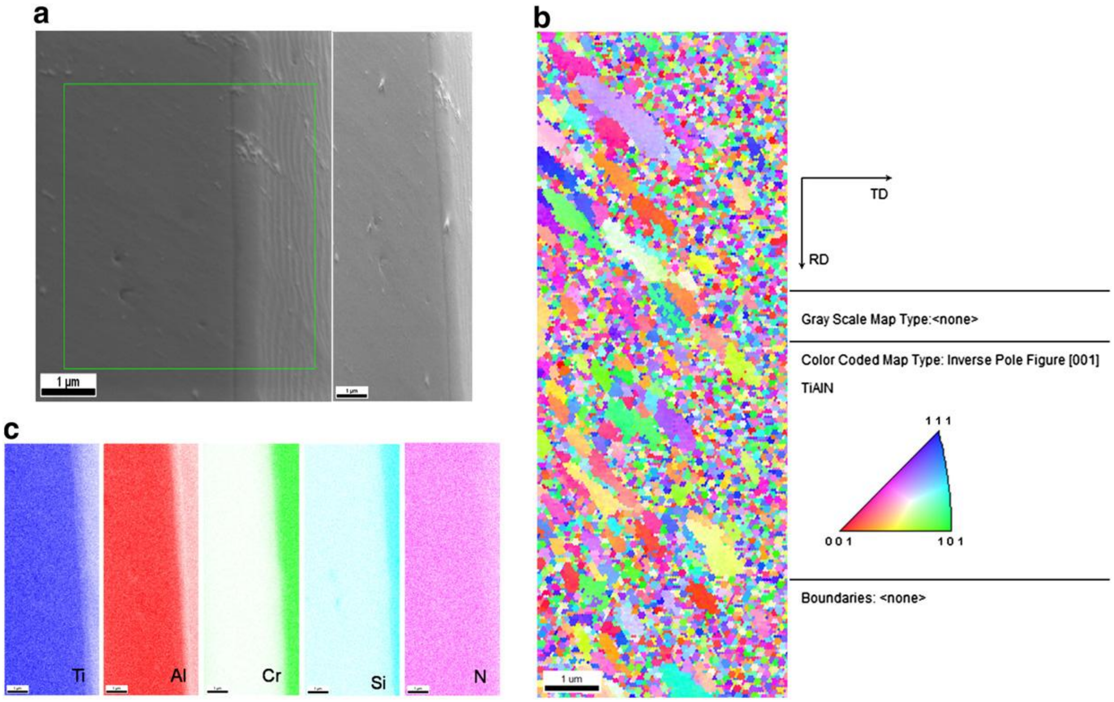

Fig. 8.4 (a) SEM image of the mapped TiAlN region showing nano-multi-layers in the coating, (b) the corresponding crystal orientation map (COM) along with its IPF and (c) elemental maps obtained in tandem during the above EBSD scan.

8.4.3 FIB study of coating cross section

To reveal the cross-sectional microstructure of the coatings as shown in Fig. 8.5, trenches were milled on all the three coating samples, ML1, ML2 and ML3 at an angle of 54^o with respect to the sample surface and at an ion current of 2 nA. The thickness of the various layers in the coatings and the total coating thickness were then measured as in Fig. 8.5. The measurements were found to agree with the expected thickness of each layer estimated based on the duration of each step in the deposition cycle for a given set of processing conditions. The three samples studied differed only in their total thickness, with the individual layer thicknesses being in proportion to the total thickness. The nano-multi-layered region has an increased number of

TiAlCrSiN sublayers with increasing overall thickness, with the sublayer period (thickness) remaining constant. The middle layer (TiAlN) and the gradient layers have an increased thickness proportionate to the increased coating thickness. However, the thicknesses of the TiN-TiCrN underlayer and the TiAlCrN layer at the top of the coating do not vary across the three samples.

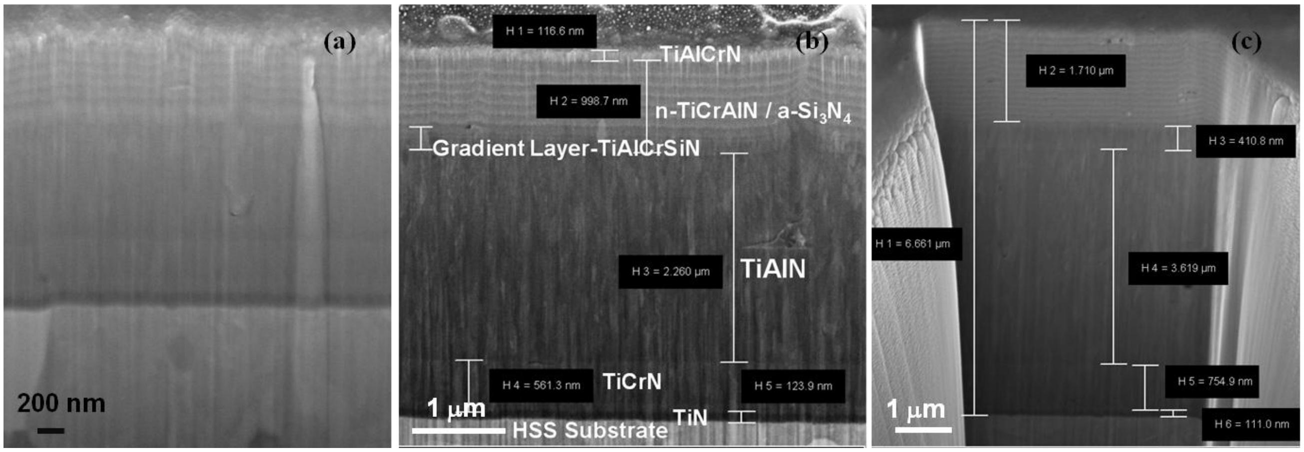

Fig. 8.5 Cross sectional SEM images obtained after FIB milling of (a) ML1, (b) ML2 (different layers in the coating have been labelled and the thickness of each layer has been marked), and (c) ML3.

The FIB study showed that the adjacent interlayers were closely bonded without any discontinuities and no porosity was present within all the three coatings or at the substrate-coating interface. The TiAlN layer was found to consist of fine columns, which was subsequently also confirmed by the TEM studies.

8.4.4 Cross sectional transmission electron microscopy (XTEM) and diffraction

8.4.4.1 Specimen preparation

A XTEM specimen was prepared from the 2 μm thick multi-layer coating (ML1) by the FIB liftout technique which has been discussed in detail in Chapter 3. The specimen lamella after attachment to a TEM grid is shown in Fig.8.6. The lamella prior to thinning is shown in Fig. 8.6 (a) and the electron transparent lamella is shown in Fig. 8.6 (b).

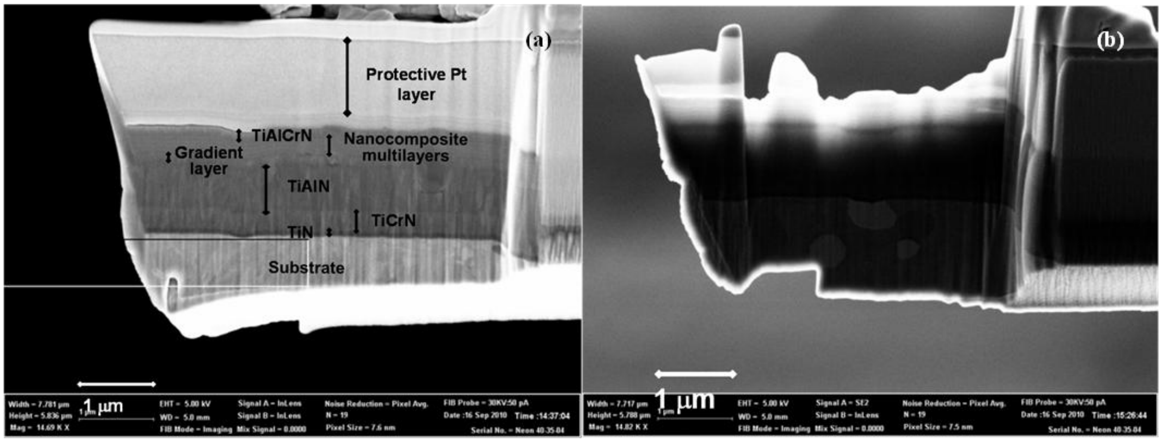

Fig. 8.6 (a) SEM micrograph of TEM lamella lifted out from the coating and (b) micrograph of the same lamella after thinning to electron transparency.

8.4.4.2 XTEM studies

The lifted-out specimen was studied at different magnifications in TEM. The different layers in the coating and their dimensions are labelled as shown in the TEM micrographs in Fig. 8.7 (a). Fig. 8.7 (b) shows a XTEM image of the TiAlCrSiN nano-multi-layers along with its selected area diffraction pattern; the compositional variation due to low Si and high Si in the 40 nm and 25 nm thick alternating layers can be seen as difference in black and white contrast in the image. The 25 nm layer consists of higher Cr % while the 40 nm layer has higher Si %, this difference being seen as a variation in crystallinity between the two layers with the 40 nm layer having a more amorphous nature (Fig.8.7 (c)). As mentioned earlier, an optimum percentage of silicon leads to the formation of a nanocomposite structure due to the amorphous phase as seen above in the 40 nm layer [16]. The SAED pattern also shows diffused rings due to the presence of the amorphous phase. Finer sub-layers could be seen within these layers but were not clearly resolvable due to the amorphous structure. The interface between the layers in TiAlCrSiN nano-multi-layers as seen in Fig.8.7 (c) is coherent and sharp which could explain the high impact resistance observed in multi-layers (Chap. 7, sec. 7.2) with this composition and similar bi-layer periods.

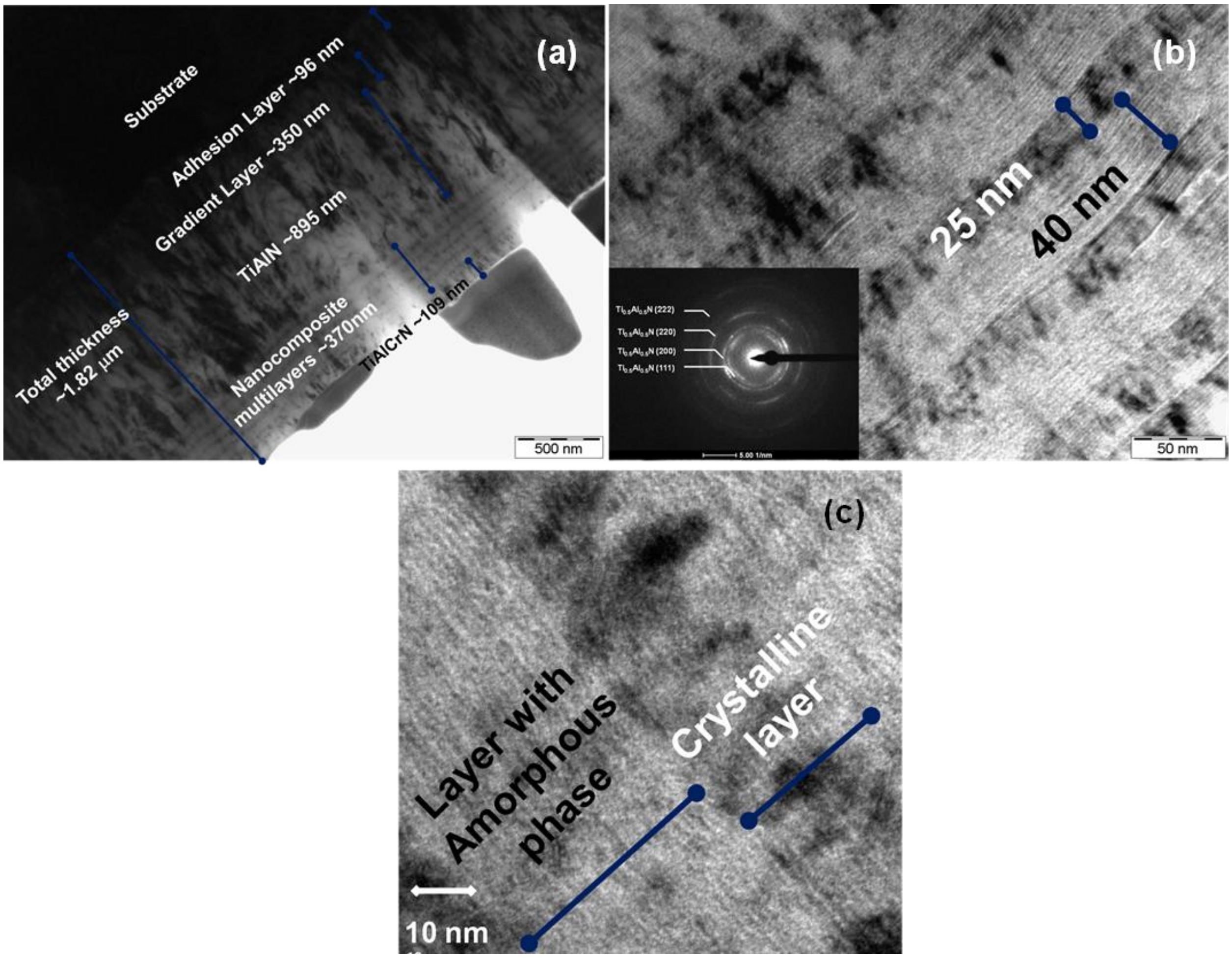

Fig. 8.7 (a) XTEM image of the entire multi-layer coating, (b) XTEM image of nano-multi-layers and corresponding SAED pattern of multi-layers and (c) XTEM image at higher magnification showing the crystalline and amorphous regions.

Fig. 8.8 shows XTEM micrographs and SAED pattern of the TiAlN layer. The columnar grains of TiAlN can be observed while the ring diffraction pattern shows that the columnar grains are nanocrystalline (Fig. 8.8 (a)). In addition, fine nano-layers of approximately 2 nm within the TiAlN layer (Fig. 8.8 (b)) were observed. A similar observation has also been made in other reports on cathodic arc deposited coatings and attributed to the asymmetric arrangement of the cathode with respect to the rotating substrate holder [17].

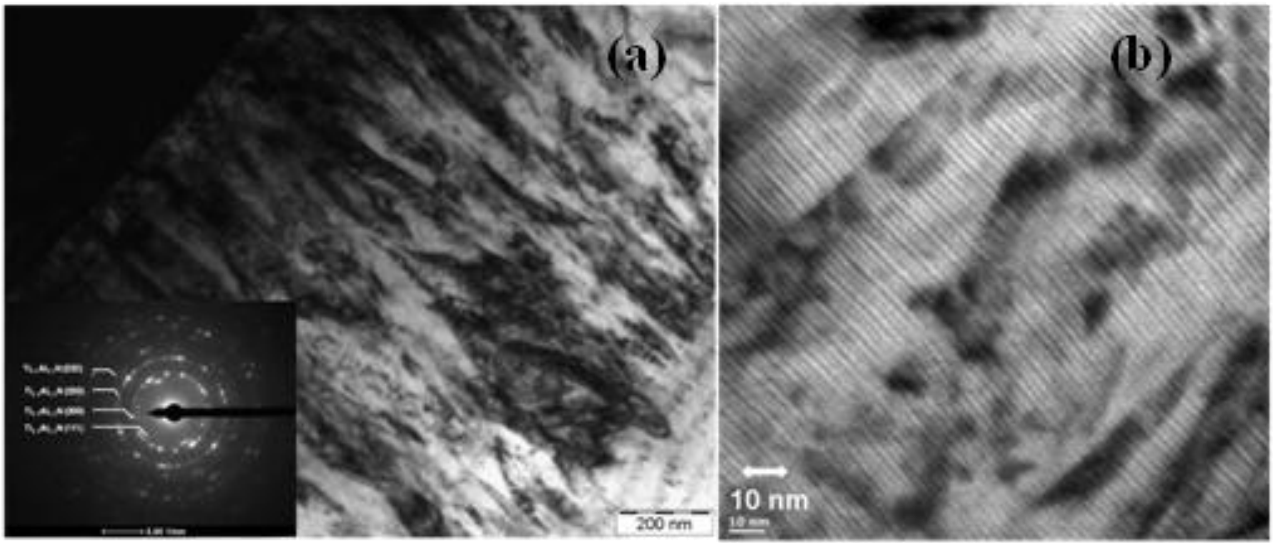

Fig. 8.8 XTEM micrographs of (a) TiAlN layer and corresponding SAED pattern and (b) At higher magnification showing the nano-layers within the TiAlN layer.

Fig. 8.9 (a) shows the XTEM micrograph and SAED pattern of the topmost TiAlCrN layer revealing a ring diffraction pattern along with a weak diffused ring and a micrograph showing fine columns with nano-layers. The presence of the diffused ring could imply the presence of very fine nanocrystalline grains in this layer. Fig. 8.9 (b) shows the XTEM micrograph and SAED pattern of the TiN adhesion layer with the diffraction rings indicating larger grains within the layer.

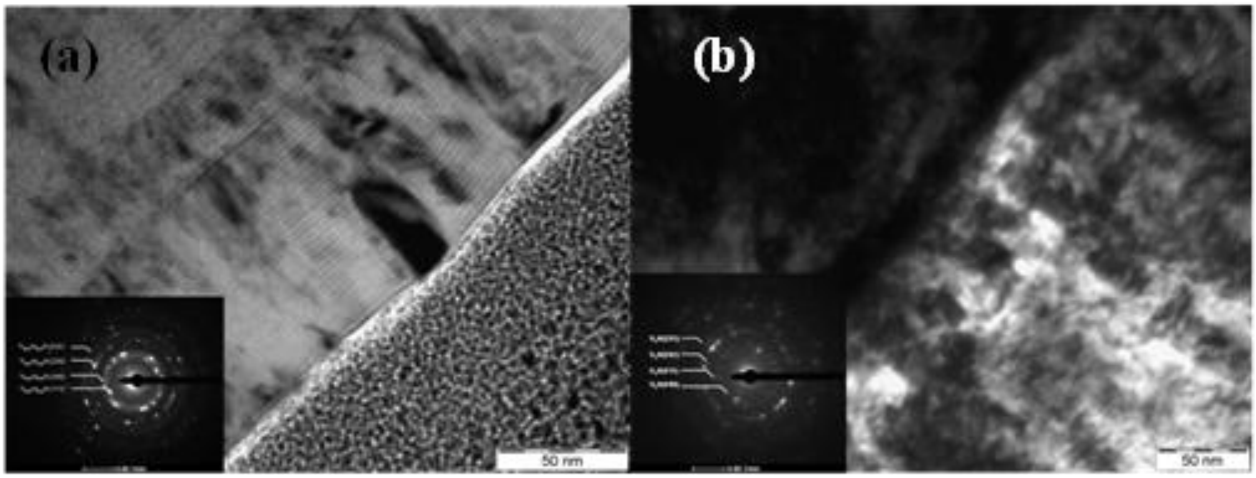

Fig. 8.9 XTEM micrograph and corresponding SAED pattern of (a) TiAlCrN layer and (b) TiN adhesion layer.

The measured interplanar spacings (d) from the SAED patterns match closely with that of TiAlN. The interplanar spacings corresponding to different layers are shown in Table 9. These reveal that all the layers, except the adhesion layer which had a tetragonal structure, had similar 'd' values close to that of FCC $Ti_{0.5}Al_{0.5}N$. The adhesion layer showed a 'd' value close to that of tetragonal Ti_2N. The similar interplanar spacings observed in the different layers above is in agreement with an earlier study which reported minimal variation in interplanar spacings with Si or Al incorporation in TiN [18].

The adhesion layer comprises of large grains while the TiAlN layer comprises of smaller columnar grains. The nano-multi-layered region shows a clear absence of any columnar grains which can be attributed to the formation of a nanocomposite structure due to the presence of silicon [17]. The top layer which comprises of TiAlCrN shows a columnar structure which can be attributed to the absence of silicon in the layer.

Table 9: Interplanar spacings (d) corresponding to different layers in the multi-layer coating ML1 (values for the adhesion layer correspond to the listed planes from tetragonal Ti_2N; all other layers correspond to FCC $Ti_{0.5}Al_{0.5}N$)

Coating Layer	**d (Å) (111)**	**d (Å) (200)**	**d (Å) (220)**	**d (Å) (222)**
TiAlCrN	2.41	2.08	1.47	1.29
TiAlCrSiN multi-layers	2.36	2.07	1.46	1.20
TiAlN	2.42	2.08	1.48	1.19
Adhesion layer	2.40 (200)	2.28 (111)	1.46 (301)	1.24 (321)

8.4.5 HAADF-STEM and EDS study

The cross-section of the above specimen was also observed using a HAADF-STEM detector in the TEM in order to differentiate the various layers of the multi-layer coating. Fig.8.10 (a) shows a HAADF-STEM micrograph of the entire coating with each of the layers showing Z-contrast. The TiN and TiCrN layers at the base appear brighter compared to the adjacent TiAlN layer due to their higher average atomic number. The TiAlCrSiN multi-layers show alternating bright and dark layers due to the Z-contrast generated as a result of the high Cr (low Si) and high Si (low Cr) concentrations, respectively. The columnar grain structure of the TiAlN, TiN and TiAlCrN layers is also visible in the micrographs while the TiAlCrSiN multi-layers do not show any columnar grains. Figs. 8.10 (b) and (c) show the nano-multi-layer region of the coating and the corresponding EDS line scan taken using the STEM detector. Alternating Cr and Si peaks can be noticed across the multi-layers that correspond to the Cr-rich 25 nm (bright) and Si-rich 40 nm (dark) thick layers, respectively. It can also be noticed that the Cr-rich layers are rich in Ti while the Si-rich layers are rich in Al. The gradient layer below the multi-layer region is rich in Cr and Ti along with a moderate content of Al while the middle layer shows only the presence of Ti and Al corresponding to TiAlN. The line scan confirms the oscillatory change in the percentage of Cr and Si between alternate layers in the nano-multi-layers as expected from the coating design.

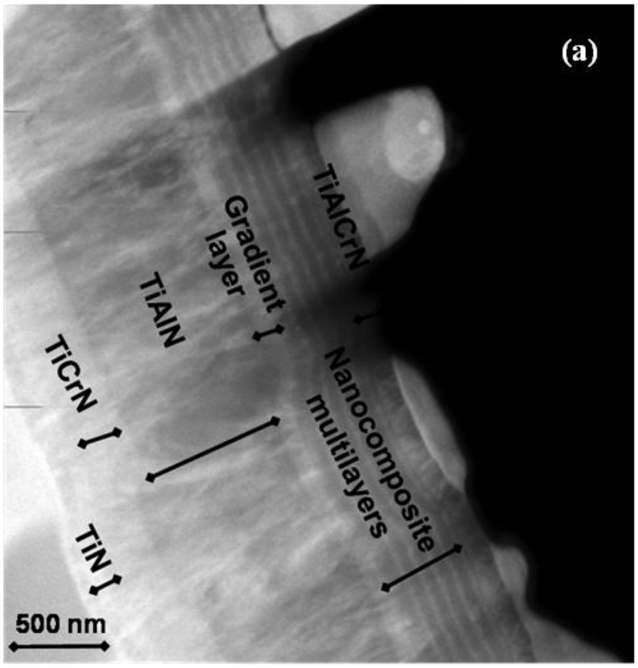

Fig. 8.10 (a) HAADF-STEM micrograph of the coating showing the Z-contrast across the layers.

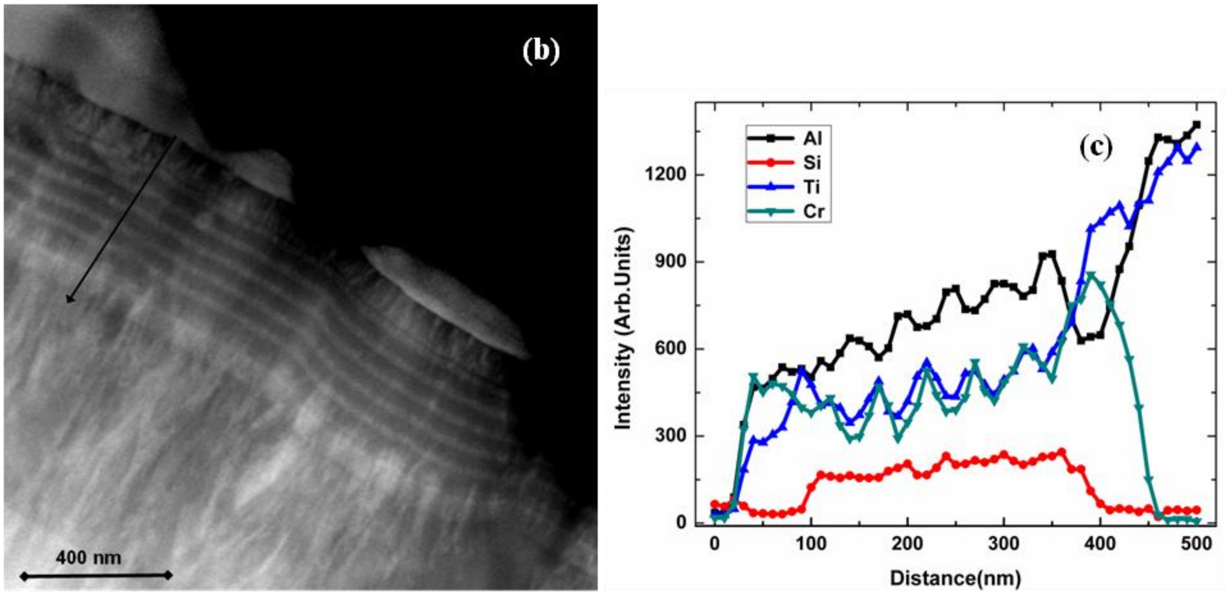

Fig. 8.10 (b) HAADF-STEM micrograph along with line scan across the nano-multi-layer and gradient regions and (c) EDS line scan showing the Cr and Si-rich layers along with the variation of Ti and Al across the layers. (The EDS line scan was done across the line profile shown in (b) with the arrow head marking the end of the scan)

8.5 Mechanical Properties

8.5.1 Modulus mapping of cross section

The cross section of the coating prepared for EBSD was also imaged by SPM in a Hysitron Triboindentor TI 950. The imaging was performed using a diamond Berkovich tip with a tip rounding of ~50 nm. The region was first selected by viewing the interface under the optical microscope and engaging the tip after a sample boundary was defined. A large area of 20 μm was chosen initially after setting an appropriate gain for the lock-in amplifier and an initial lateral dynamic force for the tip oscillation, along with a scan rate of 1 Hz. The scan size was then narrowed down to the coating substrate interface and a slower scan performed to obtain an image of the coating cross section as shown in Fig. 8.11 (a). The different layers within the multi-layer coating could be identified starting with the nano-multi-layers at the top, followed by a gradient layer of TiAlCrSiN, the thick TiAlN layer in the middle and the underlayer comprising of a gradient layer and TiN. The overall thickness of the coating was ascertained to be approximately 7 μm in accordance with measurements done in the SEM.

Fig. 8.11 (b) shows a high resolution modulus map of the nano-multi-layers obtained by scanning a smaller region within the coating at a higher gain and a lower scan rate as shown in the inset. A curvature within the layers could be noticed and the variation in composition between the individual alternate layers could also be observed as a change in the complex modulus in each layer. Fig. 8.11 (c) shows a graph indicating the variation in modulus along the line profile in Fig. 8.11 (b) in the area shown in the inset across the coating cross section starting from the TiAlN layer and ending in the nano-multi-layer region. The graph indicates that the TiAlN layer has an average modulus of ~400 GPa while the nano-multi-layers exhibit an oscillation between ~250 GPa and ~380 GPa in alternate layers corresponding to the layers with low Si% and high Si % respectively. The presence of alternating high and low moduli in the layers is known to lead to superior mechanical properties on account of enhanced crack resistance in the above coatings [19, 20].

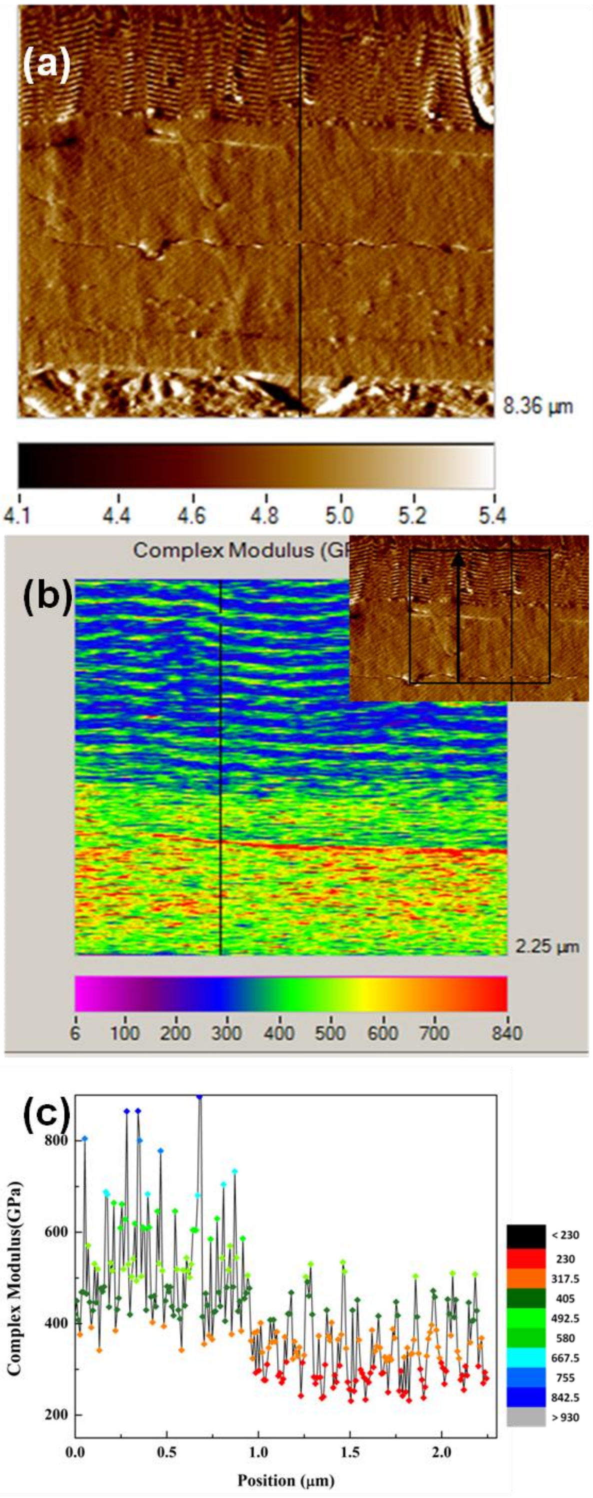

Fig. 8.11 (a) Scanning probe image showing contact force giving sample topography, (b) complex modulus map showing modulus variation in TiAlCrSiN multi-layers and TiAlN layer and (c) variation in modulus across the coating cross section along the line profile shown in (b).

8.5.2 Hardness and modulus

Nanoindentation was carried out on the 4 μm thick ML2 coating and the hardness and modulus recorded at different depths (Fig. 8.12) in the in-plane direction. There was a gradual drop in hardness from ~ 36 ± 2.9 GPa at 200 nm to 31 ± 1.8 GPa at 500 nm and 25 ± 1.6 GPa at 1 μm with the modulus following a similar trend. However, the effect of the sub-layers on the values could not be avoided as the depth of indentation could not be kept within 10 % of the layer thickness when sampling the various layers. The gradual transition in the hardness and modulus indicates a multi-layer coating with good interlayer bonding and a dense microstructure.

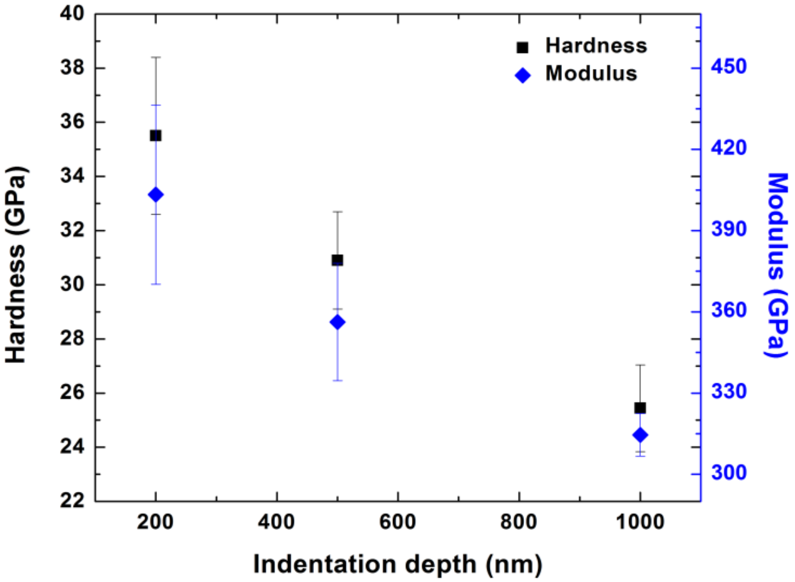

Fig. 8.12 Variation of hardness and modulus as a function of depth in coating ML2.

8.6 Performance evaluation of multi-functional, multi-layer coatings

The performance of the multi-functional, multi-layer coatings which were deposited using optimized compositions and architectures was evaluated by nano-impact testing and the effect of different layer configurations on impact resistance was studied. The seven coatings with various layer configurations as given in Table 8 were tested under identical conditions. The tests were carried out for 180 sec at loads ranging from 10 to 70 mN. 12 tests were carried out at each load in order to obtain a reliable value of the average impact depth. For the purpose of comparison, only tests at low loads of 10 mN and 20 mN and for shorter time durations are considered so as to identify changes in deformation at the initial stages. The variation in impact depth in the seven coatings at 10 mN and 20 mN is shown in Fig.8.13.

After taking into account the impact depths at both loads, the impact resistance in the seven coatings was found to be in the following descending order:

Coat GL > Coat 2 > Coat 3 > Coat 5 > Coat 4 > Coat 6 > Coat 1

Among these coatings, Coat 1 showed low impact resistance while Coat GL showed high impact resistance with a difference of ~ 22 % between the two. Coat 2 and Coat 3 showed similar depths. The difference in impact depth between Coat GL and Coat 2 and 3 was only 6.5 %, which is probably due to the similar architecture between the coatings with the small difference due to the presence of an extra gradient layer in case of Coat GL. Coat GL showed a 9 % increase in impact resistance over Coat 5 which has a similar architecture but without gradient layers. Coat GL showed ~ 15 % increase in impact resistance over Coat 6 and Coat 4.

Though gradient layers are absent in both Coat 5 and Coat 1, Coat 5 showed ~ 15 % increase in impact resistance over Coat 1. The better resistance is due to the presence of multi-layers of TiAlN and TiAlCrSiN in Coat 5 while Coat 1 is only comprised of monolithic TiAlN and TiAlCrSiN layers.

Thus, impact resistance is improved by both multi-layering and addition of gradient layers. While multi-layering delays crack propagation in the coatings due to the deflection of cracks at interfaces, the presence of gradient layers allows a gradual transition of stresses at the interfaces in coating layers and thus prevents any sharp spikes in stress which can lead to cracking induced failure.

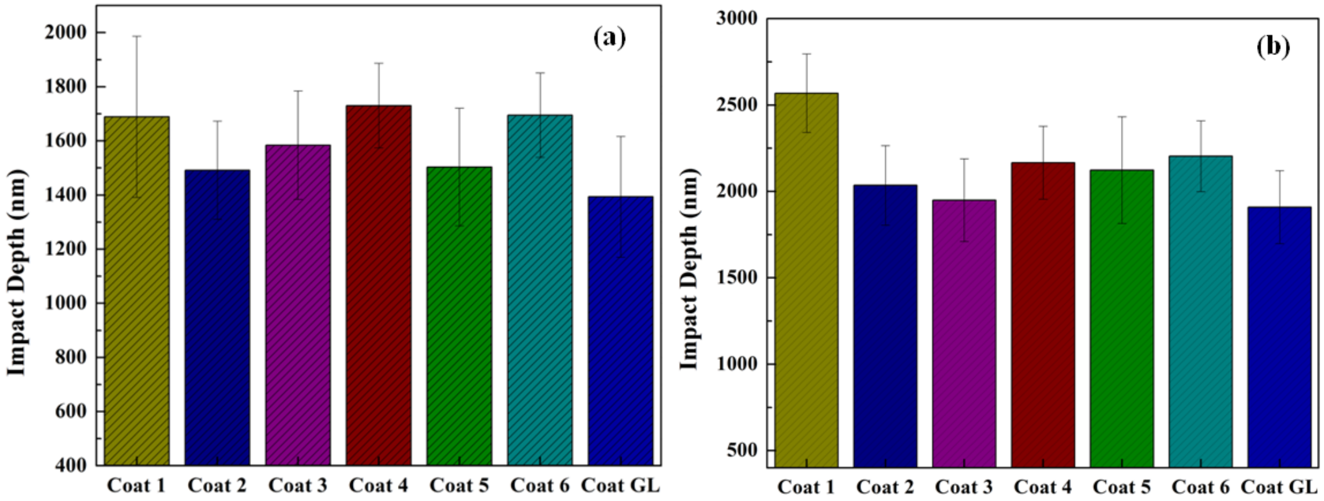

Fig. 8.13 Final impact depth in the multi-functional, multi-layer coatings at (a) 10 mN and (b) 20 mN.

When compared to real life machining tests, nano-impact testing simulates interrupted cutting operations such as milling with good correlation between nano-impact and actual machining tests reported [21]. Hence, the above multi-functional, multi-layered coatings which show good impact resistance in nano-impact tests can be expected to perform better in interrupted cutting tests such as milling.

8.7 Conclusions

Multi-functional, multi-layer coatings were deposited by choosing optimized configurations of TiAlN and TiAlCrSiN coatings which showed the best properties in terms of high-temperature toughness and hardness, respectively. A detailed analysis of the microstructure and mechanical properties of the multi-functional, multi-layered coatings was performed at multiple length scales.

Combined EDS and EBSD was carried out to ascertain the phase formation and further confirmed by SAED in the TEM. The phase formed in the middle layer of TiAlN was confirmed by both SAED and EBSD to be FCC $Ti_{0.5}Al_{0.5}N$ while the adhesion layer was found to have the tetragonal phase of Ti_2N. FIB and TEM have enabled obtaining valuable information on the features in the multi-layer coating and measuring their dimensions while SPM enabled a mapping of the modulus variation across the multi-layer coating.

The TiN layer comprises of large grains which progressively become finer with the addition of aluminium as seen in the TiAlN layer. Introduction of Cr does not significantly alter the columnar structure as seen in the gradient layer and the top most TiAlCrN layer while the introduction of Si disrupts the columnar growth as seen in the nano-multi-layered region due to the amorphous phase formation leading to a layered nano-composite structure. The compositional variation seen within the nano-multi-layers was found to lead to the alternating modulus variation in the layers which led to enhanced toughness and increased impact resistance.

Good interlayer bonding among all the multi-layers was observed. The alternating high and low moduli in the multi-layers, as confirmed by modulus mapping, led to enhanced crack resistance. The presence of multi-layers and gradient layers led to enhanced impact resistance. Hence, the multi-functional, multi-layer coatings developed and studied in this thesis can be expected to lead to improved tool properties and lead to enhanced cutting efficiencies in machining applications.

References

[1] Veprek, S., Zhang, R. F., Veprek-Heijman, M. G. J., Sheng, S. H., Argon, A. S. Superhard nanocomposites: Origin of hardness enhancement, properties and applications. Surface and Coatings Technology, 204(12), (2010) 1898-1906.

[2] Cselle T, Coddet O, Galamand C, Holubar P, Jilek M, Jilek J et al. TripleCoatings3-New Generation of PVD-Coatings for Cutting Tools. Journal of Machine Manufacturing, 1, (2009) 19-25.

[3] Vereschaka, A. A., Grigoriev, S. N., Vereschaka, A. S., Popov, A. Y., Batako, A. D. Nano-scale multilayered composite coatings for cutting tools operating under heavy cutting conditions. Procedia CIRP, 14, (2014) 239-244.

[4] Tabakov, V. P., Vereschaka, A. S. Development of Technological Means for Formation of Multilayer Composite Coatings, Providing Increased Resistance of Carbide Tools, for Different Machining Conditions, Key Engineering Materials, 581, (2014) 55-61.

[5] A. Vereshchaka, A. S. Vereshchaka ,O. Mgaloblishvili, M. N. Morgan, A. D. Batako Nano-scale multilayered-composite coatings for the cutting tools, Int J Adv Manuf Technol 72, (2014) 303–317.

[6] Çalışkan, H., Kurbanoğlu, C., Panjan, P., Čekada, M., Kramar, D., Wear behavior and cutting performance of nanostructured hard coatings on cemented carbide cutting tools in hard milling, Tribology International, 62 (2013) 215-222.

[7] Stueber M, Holleck H, Leiste H, Seemann K, Ulrich S, Ziebert C. Concepts for the design of advanced nanoscale PVD multilayer protective thin films. J. Alloys Compd. 483 (2009) 321-33.

[8] Wo PC, Zhao XL, Munroe PR, Zhou ZF, Li KY, Habibi D, Xie ZH. Extremely hard, damage-tolerant ceramic coatings with functionally graded, periodically varying architecture. Acta Materialia. 61 (2013) 193-204.

[9] Hidalgo JA, Montero-Ocampo C, Cuberes MT. Nanoscale Visualization of Elastic Inhomogeneities at TiN Coatings Using Ultrasonic Force Microscopy. Nanoscale Res Lett. 4, (2009) 1493–1501.

[10] Schwarzer RA, Field DP, Adams BL, Kumar M, Schwartz AJ. Present State of Electron Backscatter Diffraction and Prospective Developments. In: Schwartz AJ, Kumar M, Adams BL, Field DP, Editors. Electron Backscatter Diffraction in Materials Science, New York : Springer Science + Business Media, LLC; 2009, p.1-20.

[11] ICDD PDF4+ database JCPDS card no. 04-005-5251

[12] ICDD PDF4+ database JCPDS card no. 01-076-1834

[13] Huang CT, Duh JG. Deposition of (Ti, Al) N films on A2 tool steel by reactive RF magnetron sputtering. Surf. Coat. Technol. 71, (1995) 259-66.

[14] Field DP. Recent advances in the application of orientation imaging. Ultramicroscopy 67 (1-4), (1997) 1-9.

[15] Goldstein, J., Newbury, D. E., Echlin, P., Joy, D. C., Romig Jr, A. D., Lyman, C. E., Fiori, C, Lifshin, E. Scanning electron microscopy and X-ray microanalysis: a text for biologists, materials scientists, and geologists. Springer Science & Business Media; 2012, p.73.

[16] Lu C, Mai YW, Shen YG. Recent advances on understanding the origin of superhardness in nanocomposite coatings: A critical review. J. Mater. Sci. 41, (2006) 937–50.

[17] Jilek M, Cselle T, Holubar P, Morstein M, Veprek-Heijman MGJ, Veprek S. Development of Novel Coating Technology by Vacuum Arc with Rotating Cathodes for Industrial Production of nc-($Al_{1-x}Ti_x$)N/a-Si_3N_4 Superhard Nanocomposite Coatings for Dry, Hard Machining. Plasma Chem. and Plasma Process. 24, (2004) 493-510.

[18] Godinho V, Rojas TC, Trasobares S, Ferrer FJ, Delplancke-Ogletree MP, Fernandez A. Microstructural and Chemical Characterization of Nanostructured TiAlSiN Coatings with Nanoscale Resolution. Microsc. Microanal. 18, (2012) 568-81.

[19] Barshilia HC, Deepthi B, Rajam KS. Transition Metal Nitride–Based Nanolayered Multilayer Coatings and Nanocomposite Coatings as Novel Superhard Materials. In: Zhang S, editor. Nanostructured thin films and Coatings: Mechanical Properties, CRC Press, Taylor & Francis; 2010, p. 427-480.

[20] Holmberg, K., Matthews, A. Tribology of engineered surfaces. Wear: Materials, Mechanisms, and Practice, (2005) 123.

[21] Beake B. D., Fox-Rabinovich G. S., Veldhuis S. C., Goodes S. R., Coating optimisation for high speed machining with advanced nanomechanical test methods, Surface and Coatings Technology, 203(13) (2009) 1919-1925.

Chapter 9 Concluding remarks

9.1 Summary and conclusions

This thesis is the outcome of a detailed research study on the development of multi-functional, multi-layer nitride coatings based on TiAlN and TiAlCrSiN. The emphasis of the study was on studying the effect of composition and architecture on the phase constitution and microstructure of the various coating layers and their impact on the mechanical properties and coating life as evaluated by nanoindentation and nano-impact testing, respectively. A triple layer coating comprising an adhesive underlayer of TiN, a tough intermediate layer of TiAlN followed by a hard, wear resistant top layer of TiAlCrSiN was deposited by cathodic arc deposition. Each coating layer (TiN, TiAlN and TiAlCrSiN) was first individually optimized to achieve the desired properties in terms of its targeted function as mentioned above and the optimized coatings were finally combined to deposit the multi-functional, multi-layer coating.

The role of TiN as an adhesive underlayer was first studied by depositing TiAlN coatings with and without TiN as an underlayer, with the TiN underlayer thickness also being varied to study the differences in adhesion. The addition of a TiN layer was found to distinctly improve adhesion strength as determined from scratch testing with a 100 nm thick layer of TiN found to provide the best adhesion strength. This thickness was deemed to be optimum and kept constant for all subsequent coatings deposited and all the TiAlN coatings and the multi-functional, multi-layer coatings in this study were deposited with a 100 nm thick TiN underlayer for good adhesion and improved coating life.

The next part of the study focused on TiAlN and its role as a tough, impact resistant layer. Assessment of the effect of bias voltage was undertaken as a preliminary study in order to find an optimum value of substrate bias at which good mechanical properties could be achieved. An optimum value of hardness and residual stress was obtained at a bias voltage of – 50 V and this value was fixed during deposition of all subsequent coatings.

The effect of varying Al content on mechanical properties- hardness, fracture toughness and impact resistance of the $Ti_{1-x}Al_xN$ coatings was then specifically assessed and correlated with the crystal structure, phase constitution and microstructure. The Al content played a role in determining the residual stress and microstructure of the coatings that, in turn, affected their hardness and fracture toughness. The fracture toughness gradually increased with Al content with the maximum observed in $Ti_{0.47}Al_{0.53}N$ and was followed by a small drop in case of $Ti_{0.35}Al_{0.65}N$ due to the presence of the hexagonal phase of AlN. The impact resistance showed a close relation to the fracture toughness, with the coating showing highest fracture toughness also showing the highest impact resistance. It was found that a cubic structure along with a fine grain size contributed to fracture toughness enhancement while a nanocomposite structure limited the decrease in fracture toughness. Thus, design of a TiAlN coating with a high content of Al while retaining the cubic nature and a good control of the amount of second phase (amorphous AlN) to realize a nanocomposite structure can lead to coatings with high toughness and impact resistance.

Since the purpose of the TiAlN layer in the multi-functional, multi-layer coating is to impart improved fatigue and impact resistance, multi-layers based on $Ti_{1-x}Al_xN$ were deposited so as to further enhance the impact resistance and toughness of the TiAlN coating. Two sets of multi-layer coatings were studied, TiN-TiAlN ML (comprising of TiN and $Ti_{0.35}Al_{0.65}N$ layers) and $Ti_{1-x}Al_xN$ ML (comprising of $Ti_{0.7}Al_{0.3}N$ and $Ti_{0.47}Al_{0.53}N$ layers) with varying bi-layer period thicknesses (Λ) of 160,100, 80, and 40 nm (designated as Λ-160, Λ-100, Λ-80 and Λ-40). TiN-TiAlN ML was comprised of layers with a large difference in modulus while $Ti_{1-x}Al_xN$ ML was comprised of layers both of which had Al and the same crystal structure, though with lower modulus difference.

Among these multi-layer coatings, the TiN-TiAlN ML coatings showed a linear increase in hardness and modulus with reducing bi-layer period with a maximum of ~ 30 GPa at 40 nm which is above the composite hardness value of the individual layers by ~ 25 %. The $Ti_{1-x}Al_xN$ ML coatings did not show an increase in hardness and modulus with reducing bi-layer period, with all the coatings showing hardness values in the range 32-33 GPa which is close to the composite hardness of the individual layers. Λ-40 $Ti_{1-x}Al_xN$ ML coatings showed the highest impact resistance apart from a low cracking probability, although the coating did not display any hardness increase on account of multi-layering. It may also be noted that the hardness of the Λ-40 $Ti_{1-x}Al_xN$ ML coating is higher by about 3 GPa compared to the TiN-TiAlN ML coatings. This indicates that the above approach can be utilized to improve the impact resistance by increasing the number of interfaces in a coating even when the coating has a high hardness. From an industrial viewpoint, TiAlN coatings which have a high Al content are preferred for the purpose of high oxidation resistance. Hence, the $Ti_{1-x}Al_xN$ ML coatings are better suited than the TiN-TiAlN ML coatings which have TiN as one of the layers when tool quality deterioration due to oxidation is also a concern. It is relevant to point out that such multi-layer coatings can be conveniently deposited by programming an appropriate processing sequence to simplify the deposition protocol and also make it cost-effective for industrial applications.

The next part of the study focused on the synthesis of nanocomposite coatings of TiAlCrSiN with a desirable combination of high hardness, high-temperature resistance and toughness, by studying the role of composition and architecture on the microstructure and the resultant properties. Monolithic coatings of TiAlCrSiN were first synthesized with different elemental ratios and an optimum concentration of silicon arrived at to obtain high hardness and high temperature stability. A maximum hardness of ~37 GPa was obtained in the coatings at a silicon content of 9 at. %. This composition was also found to show the highest thermal stability as determined from TGA tests. The high hardness and thermal stability at this particular composition can be attributed to the desired nanocomposite structure in this coating where nanocrystalline grains of TiAlCrN were surrounded by a thin layer of amorphous Si_3N_4 as confirmed from HRTEM.

Multi-layer coatings of TiAlCrSiN were subsequently deposited by choosing two appropriate compositions from among the above monolithic coatings in order to achieve a good combination of hardness and toughness. Two layers, one with high hardness (TiAlCrSiN with 9 % Si) and the other a softer layer with low crack probability (TiAlCrSiN with 11 % Si) were chosen in order to achieve a multi-layer with a combination of toughness and wear resistance for enhanced life. The multi-layers were then deposited with bi-layer periods of 20, 40 and 80 nm and designated as Si ML Λ-20, Si ML Λ-40 and Si ML Λ-80, respectively. There was no hardness increase in the multi-layers over the composite value of the monolithic coating layers; however, the coating with 40 nm bi-layer period, Si ML Λ-40 showed a minor increase in hardness and modulus compared to the other two bi-layer periods. This could be attributed to the nature and volume of interfaces present. The TiAlCrSiN multi-layer coatings with an intermediate bi-layer period of 40 nm (Si ML Λ-40) also showed the best impact resistance even above the monolithic TiAlCrSiN coating which showed a nanocomposite structure (Si-9). There was a ~35 % improvement in impact resistance compared to Si-9. Si ML Λ-40 showed a nearly 55 % reduction in impact depth over Si ML Λ-80 coating and a ~66 % reduction in impact depth over Si ML Λ-20. This enhancement in impact resistance is most likely due to the presence of an optimum interface volume in the 40 nm bi-layer coating and the presence of sharp interfaces when compared to the 20 nm bi-layer coating. The presence of the softer amorphous layer (Si-11) along with the hard layer (Si-9) in the multi-layers reduces crack propagation and promotes crack re-direction where the hard layer limits deformation by providing stiffness and the softer layer accommodates plastic deformation, thereby slowing down crack growth. Thus, an optimum combination of layers and bi-layer period was identified and a TiAlCrSiN coating layer with a desirable combination of hardness and toughness that can enable enhanced performance was developed.

The final section of the thesis is focused on the optimized multi-functional, multi-layer coating which is a triple layer comprising of a TiN underlayer, a TiAlN intermediate layer, and a TiAlCrSiN top layer, where each of the layer is based on compositions and configurations that were earlier optimized for their targeted functions. As part of the preceding optimization studies, TiN which comprises the underlayer was optimized for adhesion while TiAlN which forms the middle layer was optimized for toughness and impact resistance and TiAlCrSiN which forms the top layer was optimized for hardness, thermal stability and durability. Seven different triple layer coatings were deposited using the optimized compositions and configurations which resulted from the above optimization studies and the coatings were evaluated. A detailed analysis of the microstructure and mechanical properties of the coatings was performed at multiple length scales. The performance of the coatings was then evaluated by nano-impact testing.

The TiN layer comprises of large grains which progressively become finer with the addition of aluminium as seen in the TiAlN layer. Introduction of Cr does not significantly alter the columnar structure as seen in the gradient layer and the TiAlCrN layer while the introduction of Si disrupted the columnar growth as seen in the nano-multi-layered region due to the amorphous phase formation leading to a layered nano-composite structure. The compositional variation seen within the nano-multi-layers was found to lead to the alternating modulus variation in the layers. Good interlayer bonding among all the multi-layers was observed.

Nano-impact studies showed that the triple layer coatings with the presence of multi-layers and gradient layers had distinctly improved impact resistance over triple layer coatings with simple monolithic structure and coatings without gradient layers. Thus, the impact resistance is improved by both multi-layering and the addition of gradient layers. While multi-layering delays crack propagation in the coatings due to the deflection of cracks at interfaces, the presence of gradient layers allows a gradual transition of stresses at the interfaces in coating layers and thus prevents any sharp spikes in stress which can lead to cracking-induced failure. The alternating high and low moduli in the multi-layers, as confirmed by modulus mapping, led to the enhanced crack resistance. The presence of multi-layers and gradient layers has led to the enhanced impact resistance. Hence, the multi-functional, multi-layer coatings developed and studied in this work can be expected to impart improved tool properties and to the enhanced cutting efficiencies in machining applications.

9.2 Scope for future work

The nitride coatings developed in this work have applications in industry for high speed machining, especially in cutting and drilling of hard to machine materials. There is scope for future work in aspects related to the structure and microstructure of the coatings, in high temperature properties of the coatings and in real time machining applications. The following studies could be carried out in order to gain additional understanding of the coatings and for further enhancement in coating performance:

- XTEM and nano-beam diffraction studies can be performed to study the interface between the TiN layer and the coatings and substrate to identify any intermetallic compounds that may be contributing to the adhesion.

- TiAlN coatings with high aluminium content and a cubic phase have been reported to show the best machining properties. A $Ti_{0.35}Al_{0.65}N$ coating could be deposited at slightly higher negative bias values (75 to 100 V) to suppress the growth of the hcp-AlN phase which leads to deterioration in mechanical properties and the resultant properties evaluated.

  - Cross sectional FIB studies of the nano-impact indents would enable observation of the variation in crack deflection with varying bi-layer period in the multi-layer coatings and help explain the differences in impact behaviour between various coating compositions.

  - Multi-layer coatings with low bi-layer periods have been reported to show epitaxial stabilization where a composition could be stabilized in the crystal structure of the other layer. TiN/AlN coatings have been reported to comprise of AlN layers stabilized in the cubic phase where TiN acts as a template for the AlN growth and prevents growth of the layer in its equilibrium hcp structure. $Ti_{0.35}Al_{0.65}N$ could be co-deposited with other TiAlN compositions and the deposition conditions controlled to obtain epitaxially stabilized multi-layers for enhanced mechanical properties.

  - XTEM studies could be performed on both the multi-layer coatings, TiN-TiAlN ML and $Ti_{1-x}Al_xN$ ML to study the orientation relationships between layers to predict any epitaxial growth.

  - EELS and EFTEM mapping of the nanocomposite TiAlCrSiN coatings would enable observation of the exact distribution of the Si_3N_4 phase around the TiAlCrN grains.

  - Nano-impact tests at high temperatures can be performed on the coatings to simulate the high temperatures to which the coated tools are exposed in actual machining tests.

  - Comparison studies of nano-impact tests on coatings deposited on tungsten carbide (WC) substrates vs the coatings on HSS substrates could be done to study the effect of varying load support due to the combinations of hard coating on a hard substrate (coatings on WC) and hard coating on soft substrate (coatings on HSS) .

- Machining studies on the optimized individual coating compositions and the final, optimized multi-functional, multi-layer coatings could be carried out to cross validate the nano-impact tests.